

UNIVERSIDADE FEDERAL DE MINAS GERAIS
INSTITUTO DE GEOCIÊNCIAS
PROGRAMA DE PÓS-GRADUAÇÃO EM GEOLOGIA

TESE DE DOUTORADO

Estudos de inclusões fluidas e de química mineral em depósitos de ferro e isotópicos U-Pb e Lu-Hf na Suíte Borrachudos na borda leste da Serra do Espinhaço meridional: implicações para a evolução metalogenética no fim do Precambriano

Autor: Sylvio Dutra Gomes

Orientação: Profa. Dra. Rosaline C. Figueiredo e Silva

Co-orientações:

Profa. Dra. Lydia Maria Lobato

Prof. Dr. Carlos A. Rosière

Prof. Steffen Hagemann

BELO HORIZONTE
28/06/2018

Nº 41

G633e

Gomes, Sylvio Dutra.

2018

Estudos de inclusões fluidas e de química mineral em depósitos de ferro e isotópicos U-Pb e Lu-Hf na Suite Borrachudos na borda leste da Serra do Espinhaço meridional [manuscrito] : implicações para a evolução metalogenética no fim do Precambriano /Sylvio Dutra Gomes. – 2018.

153 f., enc. (principalmente color.)

Orientadora: Rosaline Cristina Figueiredo e Silva.

Coorientadora: Lydia Maria Lobato.

Coorientador: Carlos Alberto Rosière.

Coorientador: Steffen Hagemann.

Tese (doutorado) – Universidade Federal de Minas Gerais, Instituto de Geociências, 2018.

Área de concentração: Geologia Econômica e Aplicada.

Inclui bibliografias.

Inclui anexos.

1. Geologia econômica – Minas Gerais – Teses.
 2. Tempo geológico – Teses.
 3. Inclusões fluidas – Teses.
 4. Minérios de ferro – Minas Gerais – Teses.
- I. Figueiredo e Silva, Rosaline Cristina. II. Lobato, Lydia Maria. III. Rosière, Carlos Alberto. IV. Hagemann, Steffen Gerd. V. Universidade Federal de Minas Gerais. Instituto de Geociências. VI. Título.

CDU: 553 (815.1)

Ficha catalográfica elaborada por Graciane A. de Paula – CRB6 3404



UNIVERSIDADE FEDERAL DE MINAS GERAIS

PROGRAMA DE PÓS-GRADUAÇÃO EM GEOLOGIA



FOLHA DE APROVAÇÃO

Estudos de inclusões fluidas e de química mineral em depósitos de ferro e isotópicos U-Pb e Lu-Hf do granito Borrachudos na borda leste da Serra do Espinhaço meridional

SYLVIO DUTRA GOMES

Tese submetida à Banca Examinadora designada pelo Colegiado do Programa de Pós-Graduação em GEOLOGIA, como requisito para obtenção do grau de Doutor em GEOLOGIA, área de concentração GEOLOGIA ECONÔMICA E APLICADA.

Aprovada em 28 de junho de 2018, pela banca constituída pelos membros:

Rosaline L. F. Lira

Profa. Rosaline Cristina Figueiredo e Silva - Orientadora
UFGM

Elton Luiz Dantas
Prof. Elton Luiz Dantas
UnB

Francisco Javier Rios
Prof. Francisco Javier Rios
CDTN/CNEN

Fábio Andrade Caxito
Prof. Fábio de Andrade Caxito

UFGM

Rafael Rodrigues de Assis
Prof. Rafael Rodrigues de Assis

USP

Belo Horizonte, 28 de junho de 2018.

SUMÁRIO

Capítulo 1: Introdução	1
1.1 Apresentação da tese	2
1.2 Localização e vias de acesso	3
1.3 Objetivos e justificativas	3
1.4 Metodologia de trabalho	4
Capítulo 2: Contexto geológico regional	8
Capítulo 3: 1º Artigo – Estudos de inclusões fluidas e química mineral	12
Capítulo 4: 2º Artigo - Estudos de geocronologia e isótopos Lu-Hf	82
Capítulo 5: Considerações finais	125
Capítulo 6: Referências bibliográficas	127
Anexo 1: Resultados de análises LA-ICP-MS em óxidos de ferro	129
Anexo 2: Resultados de análises LA-ICP-MS em inclusões fluidas	141

AGRADECIMENTOS

Gostaria de expressar os devidos agradecimentos a todas as pessoas e entidades que contribuíram para que este trabalho fosse desenvolvido, em especial agradeço:

- Ao Programa de Pós-Graduação em Geologia econômica da Universidade Federal de Minas Gerais (UFMG), e ao Centro de Pesquisas Professor Manoel Teixeira da Costa (CPMTC) pelo fornecimento de infra-estrutura;
- À minha orientadora profa. Rosaline Cristina Figueiredo e Silva por todo aprendizado e suporte, e aos co-orientadores profa. Lydia Lobato, prof. Carlos Rosière e prof. Steffen Hagemann. Obrigada por acreditarem na minha capacidade de desenvolver esse trabalho;
- Ao prof. João Orestes Schneider Santos que me auxiliou durante o estágio sanduíche no exterior com a aquisição das análises geocronológicas;
- Ao prof. Tony Kemp (UWA) que me auxiliou durante o estágio sanduíche no exterior com a aquisição das análises Lu-Hf;
- Ao Prof. David Banks (University of Leeds) que me auxiliou durante as análises LA-ICP-MS das inclusões fluidas;
- Ao grupo de pesquisadores do laboratório de metalogenia do Instituto de Geociências da UFMG, especialmente aos geólogos Milton Morales, Breno Martins e Jorge Roncato;
- À geóloga Nilza Quintão por fornecer as amostras de berilo utilizadas no estudo de incusões fluidas;

Aos amigos da UWA Jéssica Bogossian, Mayara Fraeda e Sun Xiang que tanto me ajudaram durante meu período de estágio.

O presente trabalho foi realizado com apoio da Coordenação de Aperfeiçoamento de Pessoal de Nível Superior - Brasil (CAPES) - Código de Financiamento 001

Resumo

Os depósitos Piçarrão e Liberdade contêm corpos de alto teor de ferro ($> 65\%$ Fe) hospedados em itabirito do Grupo Guanhães, que estão associados com corpos e veios de pegmatitos com esmeralda, relacionados à anatexia de granito da Suite Borrachudos. Estudos de inclusões fluidas nos veios de quartzo associados com os corpos de minério mostram que fluidos de média a alta salinidade (25-28 wt% NaCl eq.) e temperaturas (275-375 °C) estão relacionados ao processo de lixiviação de sílica que levou ao enriquecimento em ferro. Estudos de química mineral por LA-ICP-MS em óxidos de ferro demonstram que processos metassomáticos foram responsáveis pela transformação da magnetita para hematita e pela subsequente recristalização da hematita. Estes processos estão relacionados ao aumento do teor de ferro no itabirito e à formação dos corpos de alto teor. A oxidação da magnetita para martita é associada com um enriquecimento em P e As, e com empobrecimento em Mg, Ti e Co; o que foi observado nos cristais de martita quando comparados com seus respectivos núcleos de kenomagnetita. Por outro lado, Ti e Mo estão enriquecidos nos cristais de hematita que se formaram a partir da recristalização da martita. Neste caso, Ti se comporta como elemento imóvel, e seu enriquecimento é acompanhado por empobrecimento na maioria dos elementos traços. Um segundo estágio de magnetita se cristalizou junto com quartzo em veios discordantes, e está oxidada formando a martita-II. Estes veios de quartzo-martita-II contêm inclusões fluidas de baixas salinidade e temperatura, que registram um episódio de influxo de fluido meteórico. As análises LA-ICP-MS das inclusões fluidas nos veios de quartzo e pegmatitos indicam contribuição de fluido anatético.

Estudos isotópicos Lu-Hf e geocronológicos em zircões da Suite Borrachudos fornecem indícios dos eventos tectono-magmáticos que afetaram a borda sul do Craton São Francisco e que levaram à formação de depósitos de ferro e esmeraldas. O granito registra cristalização magmática entre 1740-1688 Ma e assinatura geoquímica tipo-A₂. Os cristais de zircão possuem áreas hidrotermais e anatáticas com idade Cambriana que estão relacionadas ao colapso gravitacional dos estágios finais do orógeno Brasiliense. Durante este evento o granito foi deformado e metamorfoseado em grau anfibolito, levando à anatexia e formação de grande quantidade de corpos de pegmatito. Os dados isotópicos Lu-Hf nas áreas hidrotermais/anatáticas indicam que durante o pico metamórfico do orógeno (ca. 610 Ma) pequenas quantidades de fusão parcial foram acompanhadas de fluidos hidrotermais enriquecidos em Hf radiogênico. Durante o Cambriano, estes fluidos contribuíram para elevar a quantidade de fusão parcial, levando à formação de grande quantidade de fusões hidratadas, pegmatitos, formação dos depósitos de esmeraldas e de corpos de alto teor de ferro nos depósitos Piçarrão-Liberdade.

Abstract

The Piçarrão and Liberdade deposits contain high-grade iron orebodies (> 65% Fe) hosted in the Guanhães Group itabirite, that are associated with emerald-bearing pegmatite veins and bodies related to the anatexis of the Borrachudos Granite. Fluid inclusion studies in quartz veins associated with the high-grade orebodies show that medium to high salinities (25-28 wt% NaCl eq.) and temperatures (275-375 °C) fluids are associated with the silica leaching that led to the iron enrichment. Mineral chemistry studies by LA-ICP-MS in the iron oxides demonstrate that metasomatic processes were responsible for the mineralogical transformations of magnetite to hematite and for subsequent hematite recrystallization. These processes are related to the iron upgrade in the itabirite and the formation of high-grade orebodies. The oxidation of the magnetite to martite is associated with an enrichment in P and As, and depletion in Mg, Ti and Co; as observed in martite crystals compared to their matching kenomagnetite rims. On the other hand Ti and Mo are enriched in hematite crystals that recrystallized from martite. In this case Ti behaved as an immobile element, and its enrichment is accompanied by the depletion of most of the trace elements. A second stage of magnetite formation precipitated with quartz in discordant veins and is oxidized to martite-II. These quartz-martite-II veins contain low salinity and temperature fluid inclusions that record an episode of meteoric fluid influx. The results of the LA-ICP-MS analyses on the fluid inclusions from pegmatite and quartz veins associated with the high-grade iron bodies indicate the contribution of anatetic fluids in the evolution of the metasomatic events.

Isotopic Lu-Hf and geochronological studies on the zircon grains of the Borrachudos Suite provide constraints of the tectono-magmatic events that affected the southern border of the São Francisco Craton and led to the formation of the associated iron and emerald deposits. The granite records magmatic crystallization in the 1740-1688 Ma time range, and A₂-type geochemical signature. Zircon grains present hydrothermal and anatetic areas with Cambrian age that are related to the gravitational collapse of the final stages Brasiliano orogen. During this event the granite was deformed and metamorphosed in the amphibolite grade, leading to anatexis and the formation of large amount of pegmatite bodies. The Hf isotope data on the hydrothermal/anatetic areas indicate that during the metamorphic peak of the orogen (ca. 610 Ma) small amounts of partial melting were accompanied by hydrothermal fluids enriched in radiogenic Hf. During the Cambrian these fluids contributed to the high degree of partial melting leading to the formation of large amounts of hydrous melts (pegmatite), the formation of the emerald deposits and the high-grade iron orebodies in the Piçarrão-Liberdade deposit.

Capítulo 1 – Introdução

A borda leste da Serra do Espinhaço Meridional (BLSEM) é uma faixa geográfica com cerca de 30 km de largura e 150 km de comprimento balizada a norte pela cidade de Serra Azul de Minas e a sul por Santa Maria do Itabira no centro leste do estado de Minas Gerais. Devido a procura por novas reservas de minério de ferro para além da região do quadrilátero ferrífero após 2005 a BLSEM passou a ser alvo de campanhas de exploração mineral, que visam principalmente as formações ferríferas englobadas no Grupo Serra da Serpentina ([Rolim et al., 2016](#)) e no Complexo Guanhães ([Grossi Sad et al., 1990a; Pedrosa-Soares et al., 1994](#)). Além disso, duas teses de doutorado e diversas dissertações de mestrado na UFMG tiveram como tema as formações ferríferas da região, o que contribuiu para ampliar os conhecimentos a respeito da estratigrafia, tectônica e do ambiente de deposição dessas rochas ([Braga, 2012; Rolim, 2016; Barrote, 2016; Oliveira, 2015](#)). Diferentes hipóteses tentam estabelecer a posição estratigráfica e a idade das sequências metassedimentares portadoras de formações ferríferas associadas ao Complexo Guanhães: (1) sequência metavulcanossedimentar do Arqueano; (2) porções mais profundas de bacias paleoproterozoicas correlatas ao supergrupo Minas, e (3) parte da bacia da borda leste da Serra do Espinhaço Meridional, isto é, correlatas ao Grupo Serra da Serpentina.

A presente tese de doutorado tem como foco de estudo três áreas de ocorrência de formações ferríferas associadas ao Complexo Guanhães: (1) depósito Liberdade-Piçarrão; (2) Serra do Morro Escuro; e (3) Guanhães e Dores de Guanhães. Nestas áreas as formações ferríferas e rochas metassedimentares associadas apresentam relação espacial com granito da Suíte Borrachudos e frequentes intrusões de pegmatito.

Os depósitos Liberdade e Piçarrão estão localizados a 10 km da cidade de Itabira e estão hospedados em uma unidade de formação ferrífera do Complexo Guanhães que se estende por 6 km na direção NNE. O depósito Liberdade representa a continuação NNE do depósito Piçarrão, o qual foi operado pela VALE entre 1976 e 1985 com reserva de 37 Mton de minério de ferro. O depósito Liberdade é atualmente explorado por uma empresa de pequeno porte (MARSIL mineração), e tem reservas estimadas em 5,3 Mton a 43% Fe. Estas reservas são compostas predominantemente por itabirito friável, e em menor quantidade por corpos maciços de alto teor de ferro.

A serra do Morro Escuro está localizada 5 km a NE da cidade de Santa Maria Itabira, na divisa com o município de Passabém, e se estende por 15 km na direção NE-SW. Nesta região aflora uma sequência metassedimentar portadora de formação ferrífera por uma faixa de 1 km de largura aproximadamente. [Carvalho et al. \(2014\)](#) e [Braga \(2012\)](#) definiram esta sequência como um bloco alóctone de idade Estateriana inserido entre rochas do Complexo Guanhães/Dona Rita de idade

Arqueana e subdividiram sua litoestratigrafia em 4 unidades: (1) unidade biotita-quartzo xisto; (2) unidade quartzito inferior; (3) unidade quartzito superior e (4) unidade formação ferrífera bandada. Trabalhos de exploração mineral identificaram pequenos corpos de alto teor de ferro ($> 66\%$) associados com a formação ferrífera da Serra do Morro Escuro.

As áreas de Guanhães e Dores de Guanhães apresentam unidades de formação ferrífera com espessuras que variam entre 10 a 100 m que afloram próximo as cidades de mesmo nome e estão inseridas em rochas do Complexo Guanhães. Nestes corpos, ocorre uma associação de formação ferrífera com xisto carbonático, dolomito, metachert e quartzito ferruginoso ([Grossi Sad et al., 1990b](#)).

1.1 Apresentação da tese

O texto desta tese de doutorado será apresentado na forma de artigos científicos, precedidos por capítulos contendo a apresentação do esquema da tese, um resumo da geologia regional da BLSEM e das principais metodologias utilizadas. Os trabalhos de campo e parte das análises LA-ICP-MS foram custeadas pelo projeto FAPEMIG APQ-0117815. O estágio de doutorado sanduíche na University of Western Australia (UWA) foi realizado através do programa Ciência Sem Fronteiras do CNPq. O Ciência Sem Fronteiras também custeou as análises SHRIMP e de isótopos de Hf. No Capítulo 1 – Introdução – consta a apresentação da tese, a localização e vias de acesso da área de estudo, e os objetivos e metodologias do trabalho.

O Capítulo 2 - Contexto geológico regional - apresenta uma descrição da geologia da borda leste da Serra do Espinhaço meridional.

O primeiro artigo, apresentado no Capítulo 3, está publicado no periódico *Ore Geology Reviews* e é intitulado "Oxide Geochemistry and Fluid inclusion constraints on the formation of itabirite-hosted iron ore deposits and associated pegmatites at the eastern border of the Southern Espinhaço Range, Brazil". Este artigo contém os resultados de mapeamento/geologia local das formações ferríferas na BLSEM, com ênfase na caracterização da paragênese dos óxidos de ferro, estudos de geoquímica de rocha e de química mineral, e estudos de inclusões fluidas em veios de quartzo e pegmatito associados aos corpos de minério de ferro.

O segundo artigo, intitulado "Zircon U-Pb ages and Hf isotope compositions of Açucena Granite (Borrachudos Suite): Implications for Statherian-Cambrian tectono-magmatic evolution of the southern border of the São Francisco Craton, Brazil", foi submetido ao periódico *Lithos*. Este artigo apresenta os resultados das análises geocronológicas e isotópicas pelo método Lu-Hf em zircão do granito Açucena - Suíte Borrachudos, as implicações para a evolução crustal da região e as

influências dos eventos tectono-termais Brasilianos na gênese dos depósitos minerais na BLSEM. O capítulo 5 apresenta as conclusões e considerações finais, e o capítulo 6 as referências bibliográficas citadas no texto, e que não estão citadas nos artigos.

1.2 Localização e vias de acesso

O acesso à área pode ser realizado a partir de Belo Horizonte pelas rodovias BR381 e MG129 até a cidade de Santa Maria Itabira. A partir desta cidade utilizam-se estradas vicinais não pavimentadas para acessar os depósitos Liberdade-Piçarrão e a serra do Morro Escuro. As cidades de Guanhães e Dores de Guanhães podem ser acessadas seguindo a rodovia MG120 a partir de Santa Maria Itabira (Fig. 1).

1.3 Objetivos e justificativas

Esta tese de doutorado tem como objetivo principal desenvolver um estudo metalogenético das ocorrências de corpos de alto teor de ferro hospedados nas formações ferríferas na borda leste da Serra do Espinhaço meridional (e.g. depósitos Liberdade-Piçarrão) com ênfase no entendimento dos processos hidrotermais/metamórficos que transformaram porções destas rochas em corpos de alto teor.

O estudo visa ainda, com base na correlação dos resultados de análises de química mineral de óxidos de ferro com análises de inclusões fluidas em veios de quartzo e pegmatito, investigar a fonte dos fluidos hidrotermais que foram responsáveis pela formação dos corpos de alto teor.

Da mesma forma, através de estudos geocronológico e isotópico na Suíte Borrachudos pretende-se investigar o processo de formação dos depósitos de esmeralda, berilo e outras gemas que estão hospedados em pegmatitos associados aos granitos da Suíte Borrachudos, e ao mesmo tempo contribuir para o entendimento da evolução crustal da área.

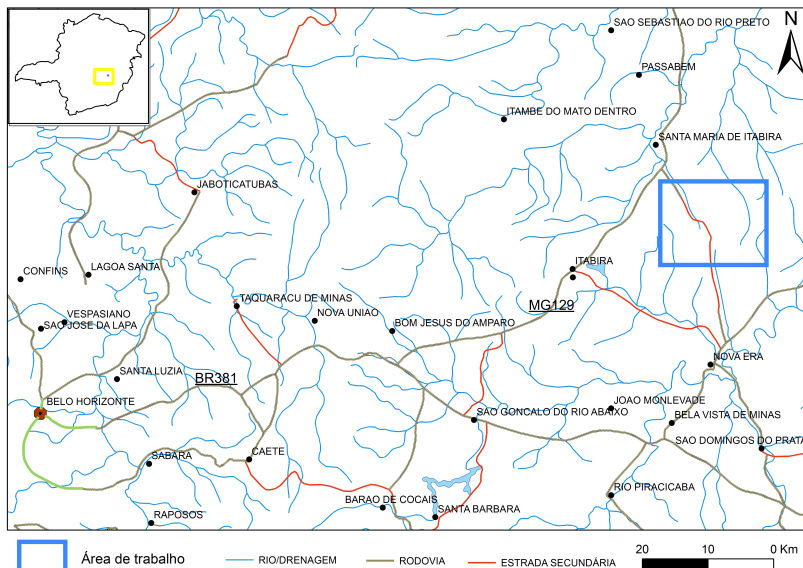


Figura 1. Mapa de localização da área de trabalho.

1.4 Metodologia de trabalho

As seguintes técnicas analíticas e métodos de trabalho foram desenvolvidos para atingir os objetivos propostos na tese:

Mapeamento e classificação de veios: Nas áreas de ocorrência de formação ferrífera foi realizado o mapeamento dos corpos de alto teor ($> 65\%$ em peso Fe), sua relação com as rochas hospedeiras (formação ferrífera) e a presença de veios. Os veios foram classificados de acordo com sua relação temporal e espacial com a rocha encaixante e a composição mineralógica. Nesta etapa também foram coletadas amostras do granito Açucena para estudos petrográficos, de geoquímica de rocha e concentração de minerais para separação de cristais de zircão.

Descrições petrográficas: Foram descritas 50 lâminas delgadas e polidas de amostras de formações ferríferas e rochas metassedimentares associadas, de corpos de alto teor de ferro compostos por martita e hematita (hematita maciça), e de granito da Suíte Borrachudos. As relações temporais de cristalização, recristalização e/ou oxidação entre os minerais magnetita e hematita foram utilizadas para descrever a evolução da paragênese dos óxidos de ferro durante os eventos metamórficos, hidrotermais e de enriquecimento em ferro que levaram a transformação da formação ferrífera em corpos de alto teor.

Geoquímica de rocha total: Análises de elementos maiores, traços e terras raras em rocha total foram realizadas em 30 amostras representativas de formação ferrífera, veios e corpos de hematita

maciça, e de três amostras de granito Borrachudos, no Activation Laboratories – Canadá. Carbono e enxofre foram analisados por espectroscopia de absorção IR, FeO por titrimetria e digestão em ácido frio. Elementos traço e terras raras foram analisados por ICP-MS e digestão ácida seguida por fusão em borato de lítio e água régia. O conteúdo em voláteis foi medido gravimetricamente por análises de perda ao fogo a 1000°C. A exatidão analítica para as amostras de formação ferrífera foi avaliada através de análises do padrão interno FeR-3 BIF ([Bau and Alexander, 2009](#)) e obteve-se valor de $\pm 1,25$ ppm. A precisão foi medida através de análises de amostras duplicatas e obteve-se valor de erro de ± 3 ppm.

Química mineral: Foram confeccionadas 41 lâminas delgadas e polidas de formação ferrífera e corpos de hematita maciça para descrição mineralógica, textural e paragenética ao microscópio petrográfico. Imagens de microscopia eletrônica de varredura foram realizadas no equipamento TESCAN VEGA3 no CMCA-UWA (Centre for Microscopy, Characterisation and Analysis - The University of Western Australia) e análises quantitativas foram efetuadas utilizando o sistema de Espectrometria de Energia Dispersiva (EDS). Estas imagens e análises foram utilizadas para a identificação em detalhe da mineralogia e microestrutura, e com isso determinar as porções quimicamente homogêneas dos cristais e apropriadas para as análises LA-ICPMS.

As análises laser-ablation inductively-coupled mass-spectrometry (LA-ICPMS) foram realizadas no equipamento ICPMS Agilent 7700x quadrupole acoplado com um sistema Resonetics M-50-LR 192 nm excimer laser ablation no John de Laeter Centre for Isotope Research - Curtin University (Perth – Australia). Os padrões USGS – GSD-1G, GSE1E e NIST-610 – foram analisados em duplicata no começo, no final e a cada 20 análises de amostra para calibração e correção de *drift*. Os resultados em contagem por segundo foram convertidos para concentração em ppm através do software SILLS ([Guillong et al., 2008](#)) utilizando a concentração estequiométrica de ferro em cada mineral (magnetite – 723691 ppm, hematite – 699530 ppm e goethite – 628631 ppm) como elemento padrão interno.

Mapeamento de inclusões fluidas-IFs: Para esta etapa de trabalho foram confeccionadas oito seções bipolidas que incluíram amostras de veios de quartzo, veios de quartzo-martita, veios de quartzo-feldspato e montagens de cristais de berilo de depósitos hospedados em granito Açucena. As seções foram descritas em microscópio petrográfico convencional para o mapeamento dos tipos de inclusões fluidas presentes. As inclusões foram classificadas de acordo com o tipo de cristal hospedeiro, o número de fases/composição; a razão entre as fases líquido/vapor; o tamanho/forma e a associação espacial/temporal. No mapeamento da distribuição e associação espacial/temporal das IFs, inclusões aprisionadas ao mesmo tempo, e que são, portanto contemporâneas, foram agrupadas em *Fluid Inclusion Assemblages*-FIAs ([Goldstein and Reynolds, 1994](#)).

Microtermometria de IFs: Os estudos de microtermometria foram realizados em platina automática Linkam THMSG600 com um controlador de temperatura TMS93 do laboratório de metalogenia do CPMTC-IGC-UFMG. Durante o estudo foram conduzidos ensaios de resfriamento (ate -140°C) e de aquecimento (até ~450°C). A platina foi calibrada com inclusões sintéticas de CO₂ fornecidas pela Linkam. A precisão das medidas é de ± 0,1°C para temperaturas negativas e de ± 1°C para as temperaturas entre 0-500°C. Os cálculos de salinidade e densidade foram realizados no programa MacFlinCor ([Brown and Hagemann, 1995](#)). As salinidades determinadas foram reportadas em peso percentual equivalente de NaCl (wt%NaCl_{eq}).

Análises LA-ICPMS em IFs: Estas análises foram realizadas no laboratório de inclusões fluidas da *University of Leeds* (Inglaterra). Através do método LA-ICPMS foram obtidas as composições químicas das IFs. Os procedimentos a respeito do desenvolvimento desta metodologia aplicada a estudos de inclusões fluidas, assim como protocolos analíticos e de calibração podem ser vistos em [Allan et al. \(2005\)](#). Inicialmente as inclusões fluidas são abertas pelo processo de ablação através de um feixe de laser ArF 193-nm (Geolas Q Plus excimer laser). O diâmetro do feixe de laser utilizado no procedimento de ablação foi de 20 um. Após a abertura da IF, todo o conteúdo (líquido, gás e sólido) é extraído e transportado para o plasma (ICP) na forma de aerosol junto com gás He. Este conteúdo é então analisado no ICP-MS Agilent 7500c quadrupolo, equipado com um octopole reaction cell. Estas análises foram calibradas utilizando o padrão NIST SRM 610.

Os dados obtidos no ICP-MS foram processados através do programa SILLS ([Guillong et al., 2008](#)), para a calibração, integração do sinal e correção de background e flutuação. Durante este procedimento, para garantir que os sinais das inclusões fluidas estão sendo processados sem a interferência do cristal hospedeiro, somente os espectros contendo sinais coincidentes do elemento Na com outros cátions foram processados. Neste processamento os resultados para cada elemento são obtidos em forma de razão com relação a Na (elemento/Na). A conversão desta razão para a concentração (ppm) de cada elemento é realizada utilizando-se a concentração em wt%NaCl_{eq} medida através da microtermometria.

Geocronologia U-Pb: A geocronologia U-Pb em zircão foi usada para determinar as idades de cristalização magmática e recristalização metamórfica/hidrotermal de 7 amostras de granito Açucena – Suíte Borrachudos. Inicialmente 10 amostras foram submetidas a procedimentos padrão para a preparação de concentrados de minerais pesados: (1) britagem e moagem; (2) peneiramento e seleção da fração fina; (3) concentração por bateia (4) separação por líquido denso – bromofórmio; e (4) separação magnética – Frantz. Esta preparação foi realizada no laboratório de preparação de amostras da UNESP-Rio Claro (SP). De cada amostra de concentrado foram selecionados entre 70 a 100 cristais de zircão para a confecção das seções polidas - *mounts*, junto com cristais dos padrões

M257 ([U] = 840 ppm - [Nasdala et al., 2008](#)) e OGC (3467 ± 3 Ma; [Stern et al., 2009](#)). Imagens de catodoluminescência e de elétrons retroespalhados foram utilizadas para identificar os domínios internos de textura nos cristais de zircão, e principalmente determinar áreas com perda de chumbo (metamitização e fraturamento) e zonas de sobrecrescimento. A partir destas imagens foram selecionados os sítios específicos (*spots*) para datação. Estas imagens foram realizadas no equipamento TESCAN VEGA3 do CMCA-UWA (Centre for Microscopy, Characterisation and Analysis - The University of Western Australia). A datação dos *spots* foi realizada por SIMS - SHRIMP na Curtin University (Perth – Australia) de acordo com os procedimentos analíticos descritos em [Nelson et al. \(2000\)](#). Os dados foram processados pelo software SQUID, e diagramas concordia plotados no Isoplot/Ex ([Ludwig, 2001](#)).

Estudos isótopicos Lu-Hf: As análises in-situ Lu-Hf por LA-ICP-MS (*Thermo Scientific Neptune PLUS multi-collector ICP-MS coupled to a Cetac Analyte G2 laser ablation sampling system*) foram realizadas na UWA (The University of Western Australia - School of Earth Sciences) sobre os *spots* com idades U-Pb previamente determinadas por SHRIMP.

Capítulo 2 – Contexto geológico regional

A área de estudo encontra-se no domínio geotectônico da Faixa de Dobramento Araçuaí ([Almeida, 1977](#)), que possui idade entre 630 a 490 Ma ([Pedrosa Soares et al., 2007](#)). Neste contexto geológico há ocorrência de formações ferríferas em duas unidades: (1) Grupo/Complexo Guanhães (~2,8 Ga), ([Grossi Sad et al., 1990; Noce et al., 2007](#)) e (2) Grupo Serra da Serpentina (~1,7 Ga), ([Uhlein, 1982; Grossi-Sad e Magalhães, 1989; Rolim et al., 2016](#)). Durante o orógeno Brasiliense a região foi submetida a uma tectônica compressiva leste-oeste na forma de falhas de empurrão com dobras associadas de direção norte-sul e vergência para leste. Estas falhas geraram um imbricamento tectônico de fatias de unidades litológicas segundo a direção NNE ([Rolim et al., 2016](#)) ([Fig. 2](#)). As seguintes unidades de rochas ígneas ocorrem na região: (1) Unidade Conceição do Mato Dentro (riolitos e dacitos) e os granítoides da Suíte Borrachudos de idade estateriana ([Dussin, 1994](#)), (2) Plutônitos Jacém e Dom Joaquim ([Knauer e Grossi-Sad, 1997](#)), (3) pequenos corpos graníticos associados com pegmatitos (~520 Ma; [Barrote, 2016](#)), (4) Meta-gabros e meta-diabásios da Suíte Pedro Lessa de idade neoproterozóica ([Machado et al., 1989, Silva et al, 1995](#)) e (5) diques de diabásio não metamorfizados. A seguir apresenta-se a descrição das principais unidades geológicas da área de estudo.

2.1 Complexo Guanhães

Segundo [Noce et al. \(2007\)](#) o Complexo Guanhães constitui o embasamento do orógeno Araçuaí e formou-se a partir da aglutinação de blocos crustais arqueanos durante uma orogênese Paleoproterozóica. Este embasamento sofreu variado grau de retrabalhamento durante a orogênese Brasiliense, de acordo com sua posição em relação ao Cráton São Francisco. No Complexo Guanhães ocorrem gnaisses e migmatitos com composição tonalito-trondjemito-granodiorítica (TTG) datados entre 2711 ± 11 e 2904 ± 9.8 Ma ([Silva et al. 2002; Barrote, 2016](#)), corpos graníticos de 2710 ± 6 Ma ([Silva et al. 2002](#)), faixas metavulcanossedimentares e sequências metassedimentares portadoras de formações ferríferas bandadas. Este conjunto de rochas foi inicialmente definido por [Grossi-Sad et al. \(1990a\)](#), reunindo as rochas graníticas e granodioríticas de uma sequência tipo TTG que afloram na borda leste da Serra do Espinhaço meridional.

O Grupo Guanhães foi definido por [Grossi Sad \(1990b\)](#) como um conjunto de rochas metavulcanosedimentares com padrão de deformação complexo e facies metamórfica anfibolito, e é constituído por três formações depositadas em ambiente marinho: Inferior (predomínio de metavulcânicas), Média (metassedimentos químicos e clásticos) e Superior (paragnaisses e

anfibolito). Na Formação Média ocorrem formação ferrífera, quartzito ferruginoso, mármore e rochas calciosilicáticas. As espessuras das unidades de formação ferrífera variam entre 15 a 60 metros. Análises geocronológicas em zircões detriticos provenientes de quartzitos associados às formações ferríferas do Grupo Guanhães, realizadas por [Barrote \(2016\)](#), determinou idade máxima de deposição estateriana.

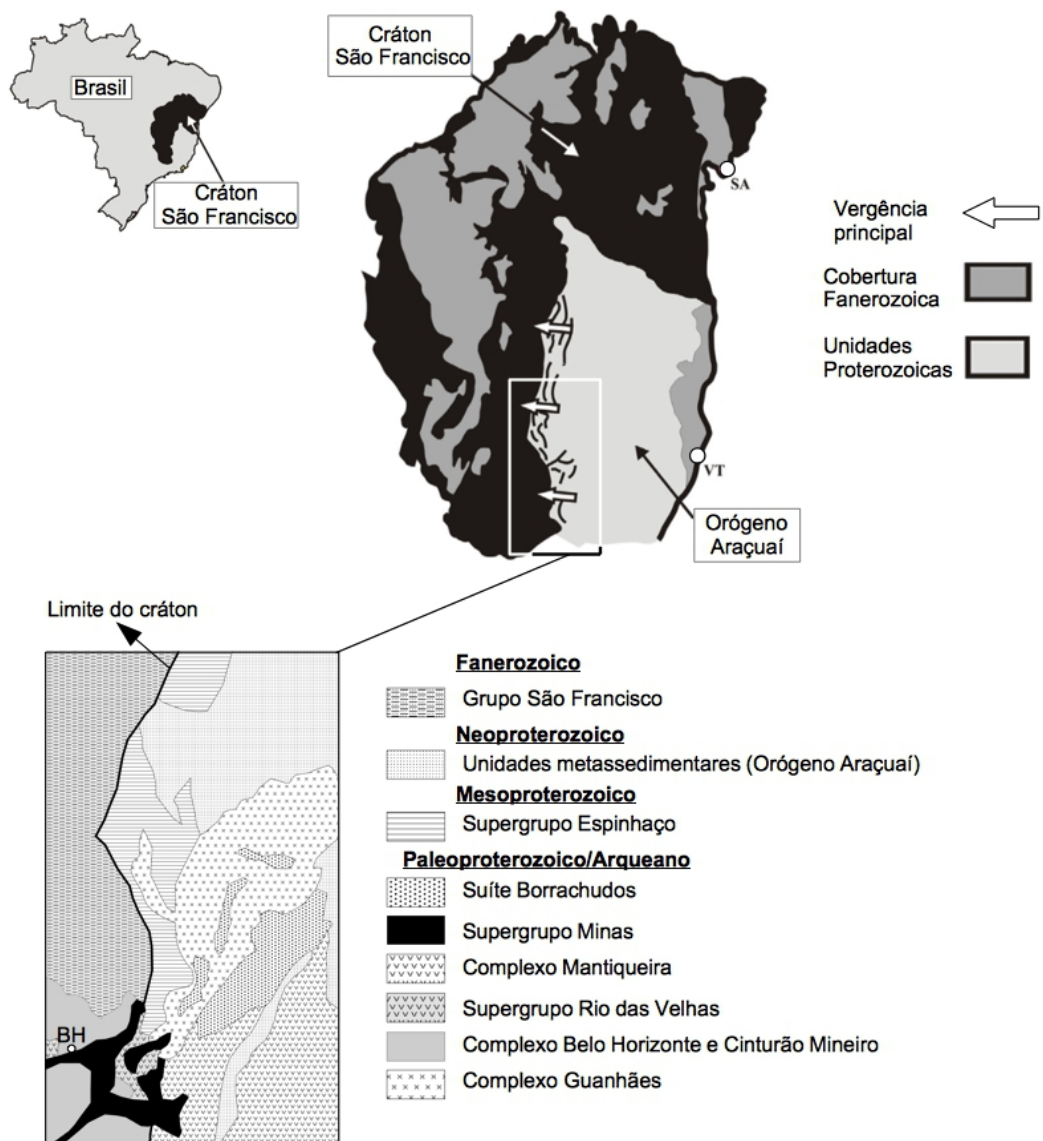


Figura 2. Contexto geológico da área de trabalho, mostrando o limite do orógeno Araçuaí com o Cráton São Francisco e as principais unidades geológicas. Cidades: BH – Belo Horizonte; VT- Vitória; SA- Salvador. Modificado de [Rolim et al. \(2016\)](#).

2.2 Suíte Borrachudos

A descrição original do termo granito Borrachudos foi definida por Dorr e Barbosa (1963), propondo esta denominação para as rochas granítoides de granulação muito grossa e textura foliada que afloram ao longo do vale do riacho dos Borrachudos, localizado na parte noroeste do sinclinal Dois Córregos, próximo a Itabira. Para estes autores a presença de fluorita e a lineação mineral da biotita são características que distinguem o Borrachudos de outras rochas graníticas do Quadrilátero Ferrífero. De acordo com a porcentagem relativa em feldspato potássico as rochas foram classificadas entre granito e monzogranito. Os granitos da Suíte Borrachudos ocorrem na forma de diversos plutons associados com rochas do Complexo Guanhães (Chemale Jr., 1987; Grossi Sad et al., 1990; Dussin, 1994; Fernandes, 2001); e foram datados por Silva et al. (2002) em 1740 ± 8 Ma (SHRIMP- U-Pb em zircão) e por Dossin et al. (1993) em 1729 ± 14 Ma (método de evaporação Pb em zircão). As características geoquímicas apontam para uma origem crustal (granito intra-placa – diagrama Rb vs. Y + Nb; Pearce et al., 1984) como fonte dos magmas (Dussin, 1994; Fernandes, 2001; Oliveira, 2002). Segundo Dossin e Dossin (1995) o magmatismo Borrachudos é do tipo anorogênico, associado à abertura do *rift* Espinhaço.

Durante o evento tectono-termal do orógeno Brasiliense, metamorfismo de grau anfibolito foi acompanhado de intensa anatexia e deformação nestes granitos (ver cap. 4). Desta fusão parcial, originaram-se localmente estruturas migmatíticas e uma grande quantidade de corpos de pegmatito que hospedam depósitos minerais de gemas variadas (e.g. esmeralda, berilo, alexandrita). Os depósitos de esmeralda da região de Itabira-Nova Era estão hospedados em rocha ultramáfica no contato com granito Borrachudos onde ocorreu a interação de fluidos hidrotermais e pegmatitos gerados por anatexia (Jordt Evangelista et al., 2016).

2.3 Grupo Serra da Serpentina

O Grupo Serra da Serpentina aflora na borda leste da Serra do Espinhaço meridional e é uma sequência sedimentar portadora de formação ferrífera com idade de deposição máxima orosiriana, que apresenta espessura variável entre 50 a 800 m (Rolim et al., 2016). De acordo com Rolim et al., 2016 esta sequência apresenta um ambiente deposicional de bacia tipo *sag*, epicontinental e com baixas atividade tectônica e taxa de subsidência.

Duas formações compõem o Grupo Serra da Serpentina: (1) Formação Meloso de composição psamo-pelítica e (2) Formação Serra do Sapo (Almeida-Abreu et al., 1989) composta por sedimentos químicos, formação ferrífera na base com espessura média de 80 m e camadas

descontínuas de dolomito no topo.

Diversos estudos atestam semelhanças químicas e geocronológicas que sugerem uma possível correlação entre as formações ferríferas do Grupo Guanhães e do Grupo Serra da Serpentina ([Braga et al., 2015](#); [Barrote, 2016](#); [Rolim et al., 2016](#)).

Capítulo 3 - 1º Artigo (publicado na Ore Geology Reviews)

Ore Geology Reviews 95 (2018) 821–848



Contents lists available at ScienceDirect

Ore Geology Reviews

journal homepage: www.elsevier.com/locate/oregeorev



Oxide chemistry and fluid inclusion constraints on the formation of itabirite-hosted iron ore deposits at the eastern border of the southern Espinhaço Range, Brazil



Sylvio D. Gomes^{a,*}, Sarah Berger^b, Rosaline C. Figueiredo e Silva^a, Steffen G. Hagemann^b, Carlos A. Rosière^a, David A. Banks^c, Lydia M. Lobato^a, Ana-Sophie Hensler^d

^a Universidade Federal de Minas Gerais, CPMTC, Instituto de Geociências, Av. Presidente Antônio Carlos, 6627 Pampulha, Belo Horizonte, MG, Brazil

^b University of Western Australia, Centre for Exploration Targeting, Nedlands, WA 6009, Australia

^c School of Earth and Environment, University of Leeds, Woodhouse Lane, Leeds LS2 9JT, United Kingdom

^d Institute of Mineral Resources Engineering, RWTH Aachen University, Aachen, Germany

ARTICLE INFO

ABSTRACT

Keywords:

Fluid inclusions
LA-ICP-MS
Iron ore

The Piçarrão and Liberdade deposits contain high-grade iron orebodies (> 65% Fe) hosted in the Guanhães Group itabirite, that are associated with pegmatite veins and bodies. Fluid inclusion studies in quartz veins associated with the high-grade orebodies show that medium to high salinities (25–28 wt% NaCl eq.) and temperatures (275–375 °C) fluids are associated with the silica leaching that led to the iron enrichment. Mineral chemistry studies by LA-ICP-MS in the iron oxides demonstrate that metasomatic processes were responsible for the mineralogical transformations of magnetite to hematite and for subsequent hematite recrystallization. These processes are related to the iron upgrade in the itabirite and the formation of high-grade orebodies. The oxidation of the magnetite to martite is associated with an enrichment in P and As, and depletion in Mg, Ti and Co; as observed in martite crystals compared to their matching kenomagnetite rims. On the other hand Ti and Mo are enriched in hematite crystals that recrystallized from martite. In this case Ti behaved as an immobile element, and its enrichment is accompanied by the depletion of most of the trace elements. A second stage of magnetite formation precipitated with quartz in discordant veins and is oxidized to martite-II. These quartz-martite-II veins contain low salinity and temperature fluid inclusions that record an episode of meteoric fluid influx. The results of the LA-ICP-MS analyses on the fluid inclusions from pegmatite and quartz veins associated with the high-grade iron bodies indicate the contribution of anatectic fluids in the evolution of the metasomatic events.

1. Introduction

High-grade (> 65 wt. % Fe) iron ore deposits are the most important Fe metal source (production and reserve) worldwide. These deposits are commonly hosted in banded iron formations (BIF), which are defined as chemical sedimentary rocks composed of chert layers (bands) and containing at least 15 wt. % of iron (Beukes and Gutzmer, 2008; Klein, 2005).

The iron formation-hosted iron ore system is defined as ore located and derived from BIF. The transformation of iron formation to high-grade iron ore is controlled by: (1) structural permeability; (2) hypogene alteration caused by ascending deep hydrothermal fluids (largely magmatic or basinal brines), and descending ancient meteoric water; and (3) supergene enrichment via weathering processes (Hagemann et al., 2016). The hypogene iron enrichment is characterized by silica and carbonate leaching, and changes in the iron oxides mineralogy and textures. The name itabirite is used to describe metamorphosed and deformed banded iron formations (Dorr, 1969). There are two main itabirite-hosted iron ore provinces in southeastern Brazil: Quadrilátero Ferrífero (QF) and the eastern border of the southern Espinhaço Range (SER). Both provinces are located at the southern portion of the São Francisco Craton (Almeida, 1977; Almeida et al., 2000) in Minas Gerais state (Fig. 1). The geology of QF is composed of three main units: granite–gneiss terranes; the Rio das Velhas greenstone belt, and Proterozoic metasedimentary sequences (Dorr, 1969), with the latter encompassing the Minas Supergroup, Itacolomi Group and Espinhaço Supergroup.

The Minas Supergroup is a metasedimentary unit containing a thick Lake Superior-type (Klein, 2005) sequence of iron formation which was metamorphosed during the Paleoproterozoic Transamazonian tectono-thermal orogenic event (Machado et al., 1992; Alkmim and Marshak, 1998). During this event, hydrothermal hypogene alteration, second order flexural and flexural-slip folds and reverse shear zones controlled the distribution of economically important itabirite-hosted high-grade iron ore deposits, typically >64 wt. % Fe (Rosière et al., 2008).

In the SER there are itabirite-bearing metasedimentary sequences that were deposited in a rift and rift-sag epicontinental environment; and that can be correlated with the Espinhaço Supergroup, Guanhães Group and with the Costa Sena Group (Grossi-Sad et al., 1997, Braga et al., 2015, Rolim et al., 2016). These sequences occur as thrust slices, associated with granitic-gneiss rocks of the Guanhães Complex, developed during the tectono-thermal Neoproterozoic-Early Paleozoic Brasiliano/Pan-African orogenic event (e.g., Alkmim et al., 2006).

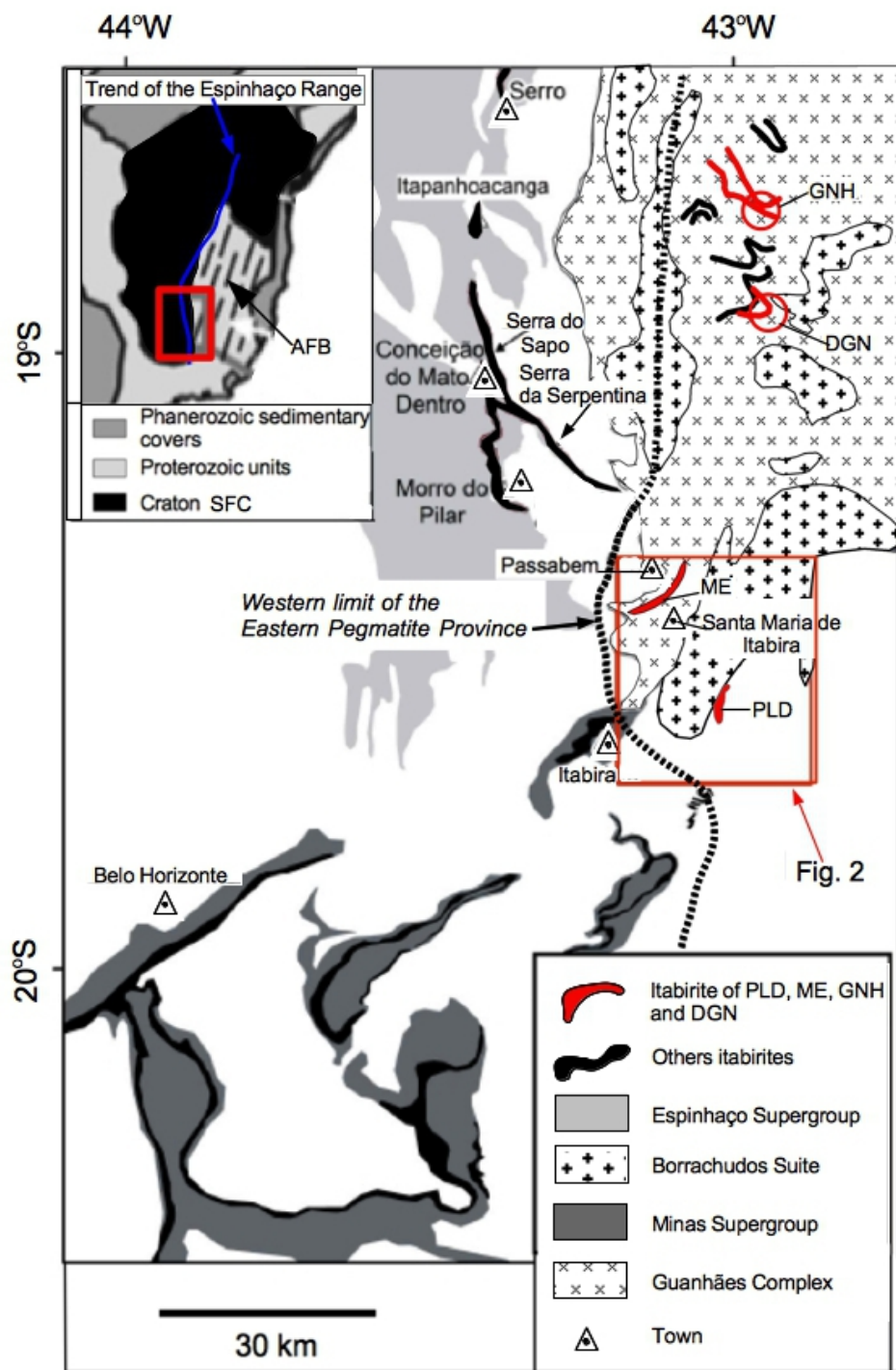


Figure 1. Geological setting of the Southern Espinhaço Range with the location of the studied areas (red box and two red circles). The western limit of the Eastern Pegmatite Province is also shown with a dashed line. PLD (Piçarrão-Liberdade deposit), ME (Morro Escuro ridge), GNH (Guanhães prospect), DGN (Dores de Guanhães prospect), SFC (São Francisco Craton), AFB (Araçuaí fold belt). Adapted from Grossi-Sad et al., 1997.

This area is located at the western portion of the Eastern Brazilian Pegmatite Province (Fig. 1), constituting the most important Brazilian gemological province (Correia Neves et al., 1986; Morteani et al., 2000). Pegmatites within SER have an anatetic origin and intruded during the Brasiliano orogen (Bilal et al., 1995; Marciano et al., 1993). The Ponte da Raiz beryl deposit is located 5 km NE of the town of Santa Maria de Itabira (Fig. 2) and is hosted in tabular shaped pegmatite intrusive in the gneiss of the Guanhães Complex.

Due to the increasing global demand for iron in the last 15 years, an intensive exploration program has been developed in the SER providing a large amount of new data through diamond drilling, detailed geological mapping and geophysical surveys. In 2014, Anglo American started production at the first iron mine in the Serra da Serpentina range (Anglo American, 2014).

The Piçarrão-Liberdade iron deposit (PLD) is located approximately 20 km NE of the town of Itabira and represents a resource of 5.31 Mt of iron ore at an average grade of 43.3 wt. % Fe (Centaurus, 2008). The PLD was mined by VALE from 1976 to the late 1980's, and contains high-grade, tabular-shaped iron orebodies, with 20 m thick layers, striking to the NE for 5 km. Pegmatites and quartz veins are commonly associated with the high-grade orebodies in this deposit. The Morro Escuro ridge is located at the northern limit of the town of Santa Maria de Itabira, and comprises a metasedimentary itabirite-bearing sequence forming a NE-striking thrust slice in the Guanhães Complex rocks (Carvalho et al., 2014; Braga et al., 2015). The itabirite layer is exposed along the ridge for about 20 km and has a 15 m average thickness. Both PLD and Morro Escuro ridge are located at the southern portion of the eastern border of the Espinhaço Range (Fig. 1).

Geological processes responsible for the hypogene upgrade of itabirite to high-grade iron deposits in the Espinhaço Range (Oliveira et al., 2017; Rolim, 2016) is controversial and the nature of the hydrothermal fluids involved is unknown. This study addresses this controversy by using detailed mineralogy and paragenetic studies, together with whole rock geochemistry, mineral chemistry and fluid inclusions techniques to investigate the composition of iron oxides and fluid inclusions from quartz veins and pegmatites located at the Piçarrão-Liberdade iron deposit and Morro Escuro ridge. Results from these analyses are used to propose a hydrothermal model that constrains mineralizing processes and fluid sources, which led to the enrichment of itabirite to high-grade iron ore. In addition, itabirite from the more northern Guanhães and Dores de Guanhães areas (Fig. 1) were studied in terms of their whole rock geochemistry and mineral chemistry in order to evaluate the similarities of the depositional and metamorphic/hydrothermal process over a wide geographical range within the Guanhães Group.

2. Geological setting of the southern Espinhaço Range

The southern Espinhaço Range is located at the external, western zone of the Neoproterozoic Araçuaí fold belt ([Almeida 1977](#); [Alkimim et al., 2006](#); [Pedrosa Soares et al., 2001, 2007](#)). This is a NS-trending and west-verging system of faults and folds on the southeastern edge of the São Francisco Craton that incorporates Archean-Paleoproterozoic basement and supracrustal rocks of the Espinhaço Supergroup (Fig. 1). In the external zone, the Archean-Paleoproterozoic basement is composed of the Guanhães Complex and the Borrachudos Suite ([Alkmim et al., 2006](#); [Noce et al., 2007](#)).

The São Francisco Craton is defined as a stable part of the South American platform. As a single continental block following the Paleoproterozoic it was not involved in the Brasiliano/Pan-African orogen during the Neoproterozoic, between 600 and 480 Ma ([Cordani et al., 2010](#)). The Craton has a long history of intracratonic and passive margin basin filling, magmatism and orogenic build-up ([Almeida, 1977](#); [Chemale et al., 1998](#); [Silveira et al., 2013](#)), and its basement records an important tectono-magmatic evolution during the Paleoproterozoic - Transamazonian/Eburnean orogen (2.2 to 2.0 Ga; [Barbosa and Sabaté, 2004](#); [Noce et al., 2007](#)).

The Espinhaço Basin forms part of a complex rift system, extending approximately 1090 km north-south (Fig. 1), that developed as an intracontinental rift-sag basin on the São Francisco Craton during the Paleo – Mesoproterozoic ([Martins-Neto, 2000](#); [Chemale et al., 2012](#); [Guadagnin et al., 2015](#)). This extensional event was accompanied by the emplacement of anorogenic granites of the Borrachudos Suite within granite-gneiss-migmatitic rocks of the Archean basement rocks grouped in the Guanhães Complex ([Dussin and Dussin, 1995](#)), and by the deposition of the Espinhaço Supergroup. The Espinhaço Supergroup comprises a more than 5000 m thick sequence of metasandstone, metaconglomerate, metapelite, bimodal volcanic and subordinate carbonate rocks ([Pflug, 1965](#); [Grossi-Sad et al., 1997](#); [Uhlein et al., 1998](#); [Martins-Neto, 2000](#)). The U-Pb detrital zircon dating established two rift stages for the Espinhaço Supergroup deposition ([Chemale Jr. et al., 2012](#)): a rift-sag sequence accumulated between 1192 and 906 Ma (Stenian-Upper Espinhaço); and a rift sequence accumulated between 1.68 and 1.80 Ga (Statherian-Lower Espinhaço).

During the Neoproterozoic, between 1000 and 850 Ma, a second episode of rifting occurred in the region with the development of a narrow ocean basin ([Pedrosa Soares et al., 2001](#)). The sedimentary fill of this Neoproterozoic basin comprises the Macaúbas Group ([Uhlein et al., 1998](#); [Martins-Neto and Hercos, 2002](#); [Pedrosa-Soares et al., 2000](#)).

During the Brasiliano orogen, the assembly of West Gondwana resulted in the closure of the rift basins (Espinhaço and Macaúbas), and the development of the Araçuaí fold belt (Fig. 1). At the

contact between the São Francisco Craton and the Araçuaí fold belt the basin rocks are deformed and portions of the reworked Archean and Paleoproterozoic basement are exposed (Dussin and Dussin, 1995; Uhlein et al., 1998; Pedrosa-Soares et al., 2001; Alkmim et al., 2006; Noce et al., 2007). The tectonic evolution of the Araçuaí belt is well documented with granitic magmatism in the 630 to 480 Ma time range: pre-collisional (G1 suite – 630 to 580 Ma); syn-collisional (G2 and G3 suites – 585 to 530 Ma); and post-collisional (539 to 480 Ma G4 and G5 suites). The post-collisional granites have been interpreted to be related to the gravitational collapse of the orogeny (Campos et al., 2016; Melo et al., 2017).

The Guanhães Complex is composed of tonalite-trondjemite-granodiorite (TTG) gneisses, migmatites and granites. Geochronological studies (SHRIMP U/Pb; Silva et al., 2002) on the TTG gneissic complex yield 2.7-2.8 Ga magmatic crystallization age, and 519-527 Ma metamorphic age. From $\delta^{18}\text{O}$ data on quartz/garnet/biotite, Muller et al. (1986a) deduced a temperature between 462 and 612 °C for the Brasiliano regional metamorphism at the Guanhães Complex. From the $\delta^{18}\text{O}$ data on the quartz/magnetite mineral pair from the itabirite of the Piçarrão mine, it was deduced a higher metamorphic temperature from 606 to 814 °C Muller et al. (1986b).

The Guanhães Complex is associated with discontinuous units of metasedimentary rocks of the Guanhães Group (Grossi-Sad et al., 1990b; 1997; Noce et al., 2007). This group of rocks were metamorphosed to amphibolite facies. Itabirite layers with a thickness from 15 to 60 m have variable contents of amphibole (5-20%), carbonate and chlorite (1-10%). According to Barrote (2016) the basal quartzite is 50 m thick, containing intercalations of sericitic, arkosic and iron-rich quartzites associated with layers of gneiss and schist. The upper unit has coarse-grained quartzite interlayered with centimetric to metric bands of garnet-rich amphibolite. Detrital zircon geochronological analyses from quartzite of the Guanhães Group established deposition no older than Rhyacian (maximum age of 2080 Ma; Barrote, 2016).

Several granitic plutons of the Borrachudos Suite occur in the Guanhães Complex (Grossi-Sad et al., 1990a; Dussin and Dussin, 1995). This denomination was first used by Dorr and Barbosa (1963) to describe a granitic pluton NW of Itabira. Geochronological and geochemical data of the Borrachudos Suite indicate magma genesis at 1.7 Ga in the anorogenic context of crustal extension and melting of lower crustal rocks related to the rift event that led to the deposition of the Espinhaço Supergroup (Dossin et al., 1993; Fernandes et al., 1994; Dussin, 1994; Dussin et al., 2000; Fernandes, 2001; Silva et al., 2002).

The Guanhães Complex and the Borrachudos Suite host a wide number of pegmatite bodies that are 1-10 m thick, generally tabular-discordant in shape, and that host beryl deposits and other types of gems (eg. alexandrite, emerald); these deposits are grouped in the Santa Maria de Itabira (or Nova

Era – Itabira – Ferros) pegmatite district ([Pedrosa Soares et al., 2011](#)). This district is part of the Brazilian eastern pegmatite province ([Marciano, 1995](#); [Morteani et al., 2000](#); [Preinfalk et al., 2002](#)) and have an anatetic origin during the Brasiliano tectono-thermal event according to the dating of igneous monazite (531 Ma; [Bilal et al., 1995](#)); muscovite (519 Ma; [Marciano et al., 1993](#)) and titanite (576 Ma; [Jordt-Evangelista et al., 2016](#)). In this portion of the pegmatite province, pegmatites were produced by partial melting of the basement. In the case of the Ponte da Raiz deposit the beryl crystals occur in the intermediate zone associated mainly with quartz and K-feldspar. This pegmatite-forming event is more or less coeval with the intrusion of the post-tectonic S-type granites, emplaced mainly in the eastern portion of the Araçuaí belt during the late stages of the Brasiliano orogen ([Pedrosa-Soares et al., 2011](#)).

The most important itabirite bearing metasedimentary sequences in the SER crops out at the Serra da Serpentina Range ([Almeida-Abreu and Renger 2002](#)). Based on detrital zircon dating and structural mapping, [Rolim et al. \(2016\)](#) established two itabirite-bearing metasedimentary sequences at this range: São José and Serra da Serpentina Groups. The São Jose Group was deposited on a tectonically active continental rift basin with a maximum depositional age of 1666 ± 32 Ma (Statherian); it is correlated with the Lower Espinhaço Supergroup and the early stages of the opening of the Espinhaço basin. The Serra da Serpentina Group was deposited on a sag basin with little tectonic activity with a maximum depositional age of 1990 ± 16 Ma (Orosirian) and is correlated with the pre-Espinhaço Costa Sena Group. This Orosirian sequence is separated from the overlying São José Group by an erosional unconformity. The itabirite layer thickness varies from 20 to 40 m in the São José Group, and from 15 to 350 m in the Serra da Serpentina Group. [Barrote \(2016\)](#) established the correlation between the Guanhães and Serra da Serpentina Groups based on the similar age distributions of detritic zircons.

3. Sampling and analytical methods

3.1. Whole rock geochemistry

Thirty representative samples (itabirite and ores) from all localities were analyzed for major oxide, trace element (TE) and rare earth elements (REE) whole rock geochemistry at the Activation Laboratories in Ontario, Canada. Martite-II crystals were extract from quartz-martite veins (Vp2) from the PLD deposit and analyzed separately.

Carbon and sulfur were analyzed by IR absorption spectroscopy and FeO through titration using a cold acid digestion of ammonium metavanadate and hydrofluoric acid. Trace elements and REE

were analyzed by both four acid digestion followed by ICP-MS and lithium borate fusion and aqua regia digestion followed by ICP-MS. Loss on ignition (LOI) at 1000° C was measured gravimetrically and gives an indication of the total weight of volatiles in each sample. Analytical accuracy was tested with an externally submitted powder of the FeR-3 BIF international standard ([Bau and Alexander, 2009](#)), with an achieved accuracy of ±1.25 %SD. Precision was measured by the analysis of identical duplicate samples with an error of ±3 %RSD.

3.2. Iron oxide LA-ICP-MS studies

Eighteen samples were selected for in-situ iron oxide chemistry using laser-ablation inductively-coupled mass-spectrometry (LA-ICP-MS) in order to provide a comprehensive data set of the complete paragenetic iron oxide sequence. Analyses were conducted using the Resonetics M-50-LR 193 nm excimer laser ablation system coupled to an Agilent 7700x quadrupole ICPMS at the John de Laeter Centre for Isotope Research at Curtin University. Samples were ablated in a He atmosphere (flow rate 0.68 L/min) and the aerosol mixed with Ar (flow rate 1 L/min) and N (flow rate 0.0028 L/min) carrier gas for transport to the ICP-MS. Laser energy was 100 mJ with a 75 µm spot size, pulse frequency of 7 hz with 46% attenuation and fluence of 7 J/cm². The ablation time was 30 s with a dwell time of 0.01 s. The sample was ablated to a depth of approximately 30 µm. The GSD-1G, GSE-1G and NIST-610 standards from USGS were ablated in duplicate at the beginning of each sample analysis, every 20 spots, and at the end of each analysis, for calibration and drift correction. The following isotopes were measured: ²⁴Mg, ²⁷Al, ²⁸Si, ³¹P, ⁴⁴Ca, ⁴⁵Sc, ⁴⁹Ti, ⁵¹V, ⁵²Cr, ⁵⁵Mn, ⁵⁹Co, ⁶⁰Ni, ⁶⁵Cu, ⁶⁶Zn, ⁷¹Ga, ⁷⁴Ge, ⁷⁵As, ⁸⁸Sr, ⁸⁹Y, ⁹⁰Zr, ⁹²Zr, ⁹³Nb, ⁹⁵Mo, ¹¹⁸Sn, ¹²¹Sb, ¹³⁷Ba, ¹³⁹La, ¹⁴⁰Ce, ¹⁴¹Pr, ¹⁴⁶Nd, ¹⁴⁷Sm, ¹⁵³Eu, ¹⁵⁷Gd, ¹⁶³Dy, ¹⁶⁵Ho, ¹⁶⁶Er, ¹⁷²Yb, ¹⁷⁵Lu, ¹⁸²W, ²⁰⁸Pb, ²⁰⁹Bi, ²³²Th, ²³⁸U. The counts per second data generated were reduced with the SILLS program ([Guillong et al., 2008](#)). Iron was used as the internal standard element using the stoichiometric Fe contents of magnetite and hematite (723691 and 699530 ppm respectively). The results and the summary statistics are provided in the Appendix B.

3.3. Fluid inclusion studies

The samples chosen for microthermometry are from the Piçarrão-Liberdade iron deposit (samples Vp1, Vp2, Vpe), the Morro Escuro ridge (samples Vmi, Vms) and the Ponte da Raiz pegmatite (sample Vb) (Table 1). Six doubly polished 100- to 200-µm-thick sections of quartz and two of beryl were examined petrographically and selected for microthermometric analysis. Detailed

petrographic description and mapping were undertaken using a Leica petrographic microscope to discriminate fluid inclusions (FIs) types (Table 2), sizes, morphologies and definition of fluid inclusion assemblages (FIAs).

Heating and freezing experiments on fluid inclusions were conducted using a fully automated Linkam THMSG600 heating and freezing stage with a TMS 93 temperature controller at the Laboratory of Metallogeny, Institute of Geosciences, at the Federal University of Minas Gerais, Brazil. The stage was calibrated between -56.6°C and 374.1°C with synthetic fluid inclusion standards supplied by Linkam (pure H_2O and mixed $\text{H}_2\text{O}-\text{CO}_2$). The cyclic technique ([Goldstein and Reynolds, 1994](#)) was used to acquire better precision in measurements of transition of temperature between carbonic phases.

The accuracy of the freezing measurement runs is about $\pm 0.1^{\circ}\text{C}$, and for heating runs $\pm 1^{\circ}\text{C}$ between 200 and 500°C . Final ice melting (T_{mice}), clathrate melting (T_{clath}), total homogenization (T_{htot}), CO_2 homogenization (T_{hCO_2}) and halite melting (T_{mhal}) temperatures were measured during the freezing and heating cycles, and are provided for each FI assemblage (Table 3). It was not possible to definitely determine the temperature of the eutectic melting temperature (T_e), and the observations have been omitted from the table; however, the estimation of the T_e of $\text{H}_2\text{O}-\text{NaCl}$ (-21.2°C) was used to discriminate the presence of other cations besides NaCl . The CO_2 melting temperature (T_{mCO_2}) is used to identify the presence of other volatiles besides CO_2 and H_2O . The microthermometric results are compiled in Table 3.

Due to the lack of independent geothermometric data for the studied veins, it was not possible to calculate isochores and apply pressure corrections to homogenization temperatures. Since no boiling evidence was described, the homogenization temperatures measured are considered as the minimum trapping temperature.

Apparent salinity has been reported in equivalent percentage weight of NaCl (% wt. NaCl_{eq}). Calculations of salinity and bulk CO_2 fractions (X_{CO_2}) were made using the MacFlinCor program ([Brown and Hagemann, 1995](#)). Equations of state by [Bodnar and Vityk \(1994\)](#) were applied for the $\text{H}_2\text{O}-\text{NaCl}$ system, and by [Bowers and Helgeson \(1983\)](#) for the $\text{H}_2\text{O}-\text{NaCl}-\text{CO}_2$ system.

Individual inclusions trapped in quartz from the Vp1, Vp2, Vpe, Vmi and Vms veins (Tables 1, 2) were analyzed by (LA-ICP-MS). These analyses were completed at the Laser Ablation ICP-MS laboratory at the University of Leeds, England. The samples were introduced into the sample chamber of the ArF 193-nm excimer laser Geolas Q Plus and were analyzed in steps of 300 s, during which several inclusions were opened by the laser ablation process (30 μm spot size). The entire content of inclusions extracted was transported as an aerosol together with He gas. The samples were then analyzed by ICP-MS Agilent 7500c quadrupole, equipped with an octopole

reaction cell. The analyses were calibrated using the NIST SRM 610 standard. The data collected from the ICP-MS were processed by the software SILLS ([Guillong et al., 2008](#)), for calibration, background correction and floating of the integration signal. During this procedure, to ensure that the fluid inclusion signals were being processed without the interference of the host crystal, only spectra containing signals coincident with Na and other cations were processed. The results are presented as the weight ratios relative to Na (internal standard element) for each inclusion analyzed. The element/Na ratios were converted into absolute concentrations in ppm using a charge-balance relationship against Cl⁻ concentrations ([Allan et al., 2005](#)), which was estimated from microthermometric measurements as described above. The average salinity of fluid inclusions in the FIA was used for the determination of Cl⁻ concentration instead of the individual salinities.

4. Geological setting of itabirite hosted Fe deposits

In this section, we provide descriptions of three itabirite sequences in terms of geological setting, mineralogy and veins type. These are (1) Liberdade-Piçarrão; (2) Morro Escuro; and (3) Dores de Guanhães and Guanhães (Figs. 1 and 2).

4.1. Piçarrão-Liberdade deposit

The Piçarrão-Liberdade deposit is hosted by an itabirite-bearing metasedimentary sequence comprising quartz schist and sillimanite-bearing banded paragneiss. Pegmatite veins composed of quartz, K-feldspar and plagioclase (Vpe, see Table 1) cut the sequence. The deposit is located close (< 1 km) to the contact between the metasedimentary sequence with the Borrachudos granite (Fig. 2).

The itabirite forms strongly folded and deformed lenticular bodies intercalated within biotite-quartz schist, and quartz-rich, sillimanite-garnet-biotite gneiss that strike 5 km in the NE direction. The banding of the itabirite (Fig. 3a) is flat lying to gently dipping (10°-15° NW), presents tight folds and is partially transposed. Two types of quartz veins are hosted in the itabirite: (1) concordant quartz veins, and (2) discordant quartz-martite veins (see section 4.1.2.).

High-grade iron (HGI) orebodies (~65 wt. % Fe) in itabirite are 5-30 m-thick, banded to compact, locally display foliated texture (Fig. 3c), and are locally positioned at the contact with pegmatite. Banded orebodies are rich in granoblastic hematite (Fig. 3b) and have subordinate tabular hematite, and the foliated orebodies are rich in tabular hematite (Fig. 3d) with subordinate granoblastic hematite. Compact orebodies have massive structure, and are composed of martite grains in

granoblastic hematite. The shape of the high-grade orebodies is totally or partially controlled by the banding of the itabirite protore. The genesis of the high-grade orebodies is probably related to syntectonic quartz leaching by pressure solution along thrust zones during the hydrothermal overprint that affected the entire Serra do Espinhaço fold-and-thrust belt during the Brasiliano orogen (Rolim and Rosière, 2011; Rolim et al., 2016). In this context, the foliated high-grade rocks represent the most-altered and recrystallized portions of the orebodies, and the compact and banded high-grade rocks represent the least-deformed areas.

Pegmatite occurs as lenticular bodies and boudins, with variable thickness, in the entire sedimentary sequence. The pegmatites are composed of quartz, K-feldspar and plagioclase.

Specular hematite is hosted in shear zones and quartz veins as elongated grains oriented parallel to each other, defining a strong foliation.

4.1.1. Itabirite: ore mineralogy and paragenesis

The dominant iron oxide in the itabirite is lamellar hematite, forming mesobands with quartz and idiomorphic martite (martite-I) crystals (~250 µm) overprinted by lamellar hematite (~330 µm) (Fig. 4a). Relicts of kenomagnetite (kenomagnetite-I) represent the earliest iron oxide, enclosed in martite-I and rarely in hematite in the itabirite (Figs. 4c, 5). Kenomagnetite is formed during the oxidation of the magnetite. This process involves mobilization of Fe²⁺ ions and their removal from the system, resulting in a relative Fe⁺²-poor kenomagnetite. The result of this process produce martite crystals, which are pseudomorphs of magnetite with hematite composition.

The high-grade iron ore is composed of granoblastic and tabular hematite, and 10 to 30% of martite-I (Figs. 4b, 4d) with a strong intragranular porosity. Kenomagnetite-I appears as relicts within martite-I grains. Banded high-grade orebodies are enriched in granoblastic hematite, whereas foliated, high-grade orebodies are enriched in tabular hematite. Granoblastic hematite overprints martite-I, itself overprinted by tabular hematite (Figs. 4c, 4d). Compact high-grade ore is composed of martite-I that is not overprinted by new crystals of hematite.

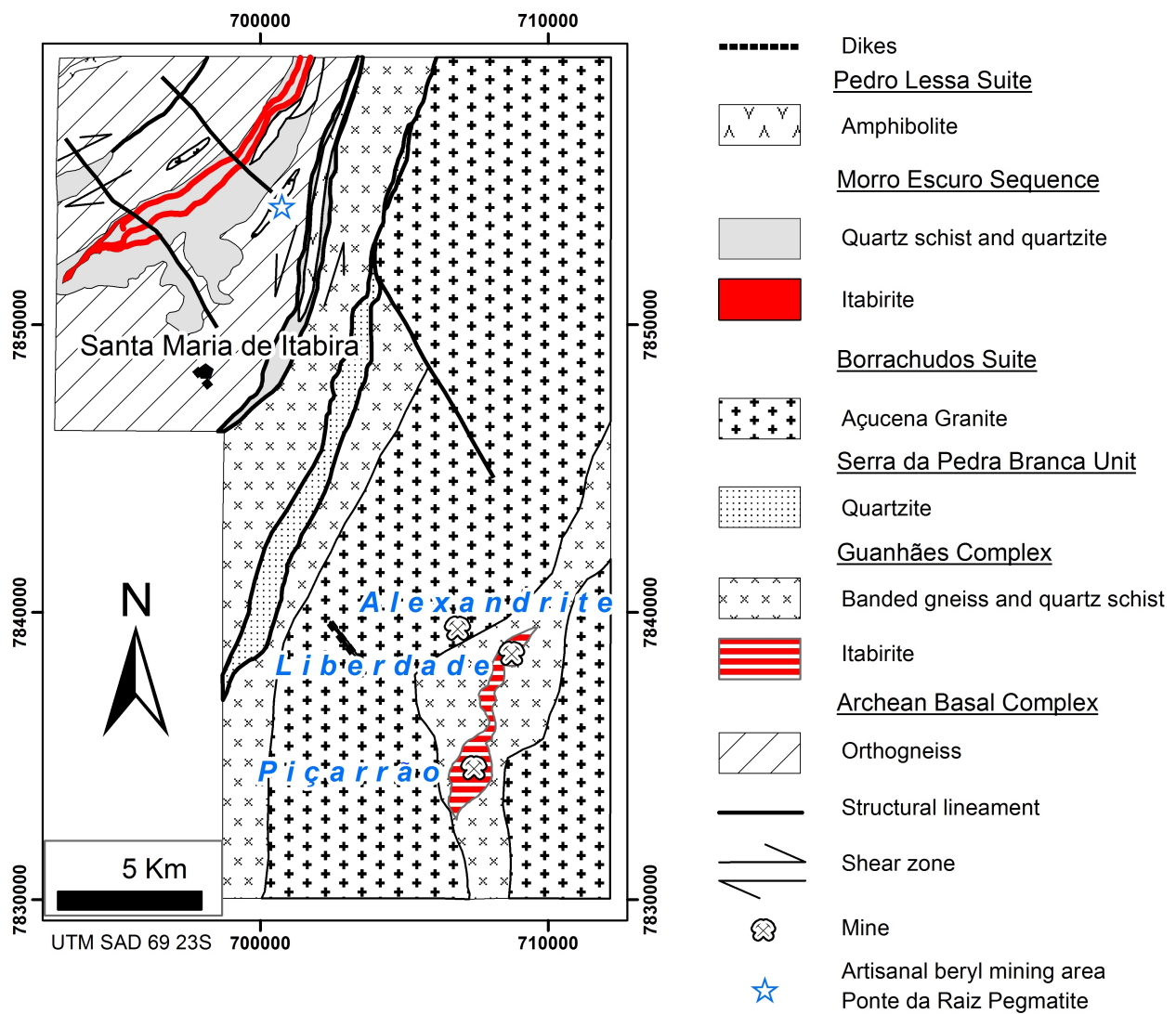


Figure 2. Geology of the Piçarrão-Liberdade iron and alexandrite-beryl pegmatite deposits, as well as the Morro Escuro ridge area. Adapted from Carvalho et al. (2014).

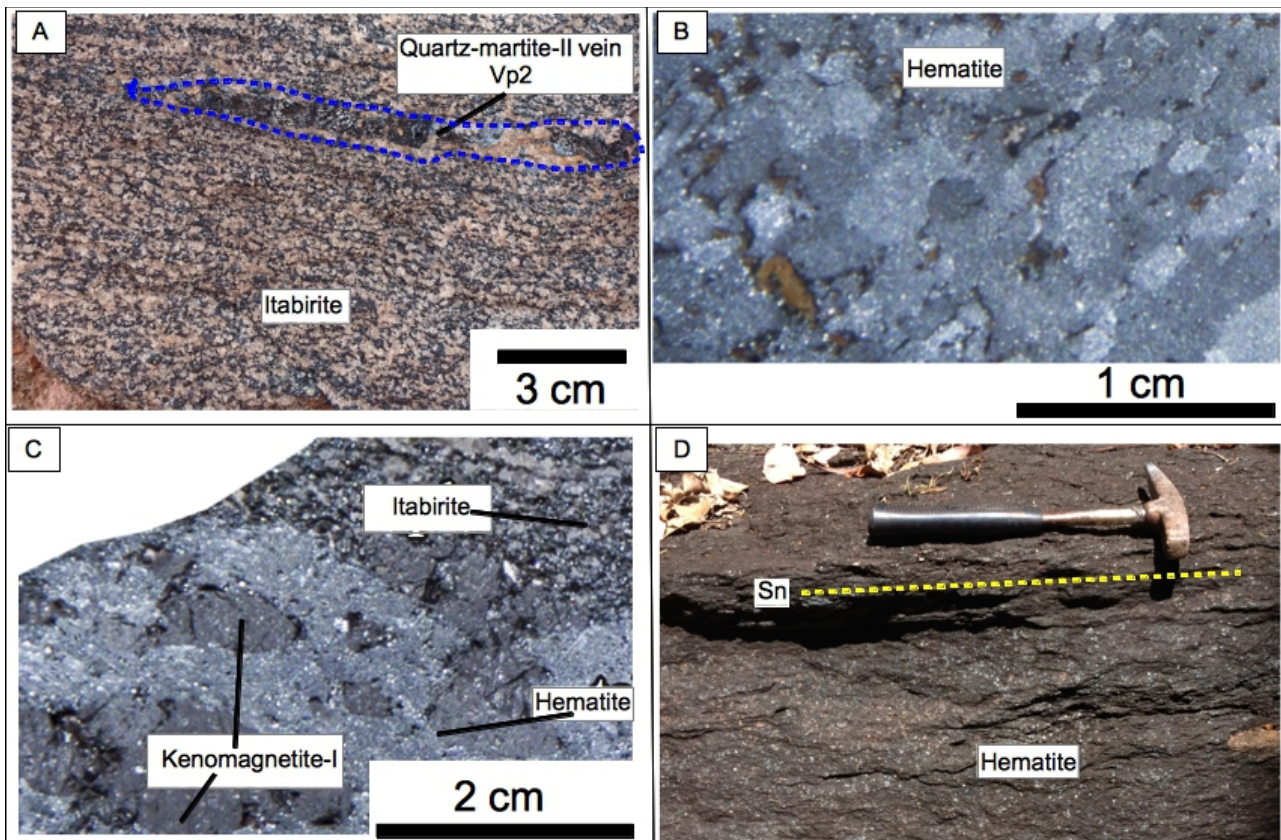


Figure 3. Photographs of hand specimens of the itabirite and ores from the Piçarrão-Liberdade deposit. A. s34a – non-mineralized itabirite with hematite and quartz microbands, schistose fabric and quartz-martite vein. B. s36b - high-grade iron ore with granoblastic hematite. C. s34b - high-grade iron ore with kenomagnetite-I and granoblastic hematite in contact with itabirite. D. ss1 – foliated, high-grade iron ore with tabular hematite. Sn: foliation. Vp2 veins classification: see section 4.1.2.

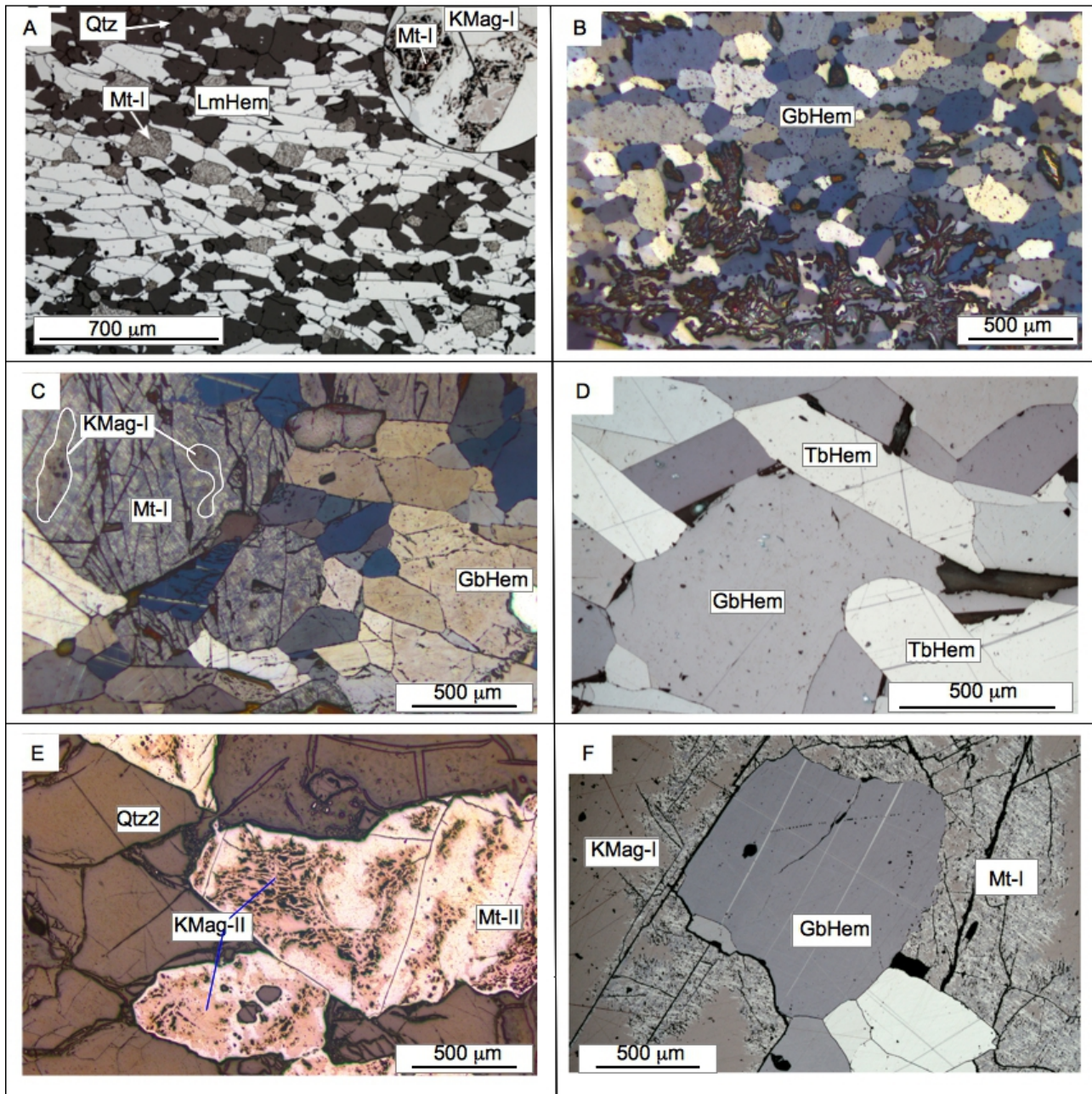


Figure 4. Photomicrographs (reflected, polarized light) showing itabirite mineralogy, in samples. A. s34a - non-mineralized itabirite with schistose fabric, showing martite-I with relic kenomagnetite (in circular blow up), lamellar hematite and quartz microbands; martite grains are overprinted by lamellar hematite. B. s36b - high-grade iron ore with granoblastic hematite. C. s34b - high-grade iron ore with kenomagnetite-I relicts in martite-I, martite grains are overprinted by granoblastic hematite. D. ss1 - high-grade iron ore with granoblastic hematite overprinted by tabular hematite. The tabular hematite shows a preferred orientation E. s35 - quartz-martite-II vein with kenomagnetite-II replaced by martite-II. F. ss2 – kenomagnetite-I overprinted by granoblastic hematite. Martitization of kenomagnetite is along grain boundary in contact with the granoblastic hematite. GbHem: granoblastic hematite; KMag: kenomagnetite; LmHem: lamellar hematite; Mt:

martite; Qtz: quartz; TbHem: tabular hematite.

A second generation of magnetite crystallized/precipitated during the formation of the discordant quartz-martite-II veins (Vp2). The oxidation of this magnetite generated the subhedral martite-II crystals with a well-developed octahedral cleavage. The martite-II crystals are preserved from the metamorphic recrystallization that formed granoblastic hematite from martite-I within high-grade orebodies and itabirite. Kenomagnetite-II appears as relicts within martite-II grains (Figs. 4e, 5, 6a).

4.1.2. Vein types

Three quartz-bearing vein types are identified at the PLD (Fig. 6a and Table 1): Vp1 - quartz-only vein hosted in high-grade orebodies; Vp2 - quartz-martite-II veins; and Vpe quartz-K-feldspar-plagioclase pegmatitic veins.

The Vp1 shows a sharp contact with the host rock and is folded with banding. Quartz (Qtz1) is fine to medium-grained, strongly fractured, with undulose extinction. This vein type varies from 2 to 5 cm in thickness. The Vp2 is hosted in itabirite, mostly discordant, crosscutting the itabirite foliation. It seems to develop a hematite enrichment halo in the contact with itabirite (Fig. 6a). The Vp2 is composed of medium to coarse-grained, subhedral quartz (Qtz2) with undulose extinction and martite-II. This vein type varies from 2 to 30 cm in thickness. The relationship of Vp1 and Vp2 with their host rock structures indicates that Vp1 vein is older than Vp2. The Vpe crosscuts the granite in the deposit area. It is composed of quartz-Qtz3 (40%), K-feldspar (30%) and plagioclase (30%) with hypidiomorphic texture. The Vpe thickness varies from 1 to 5 cm; its relation to Vp1 and Vp2 is not clear.

4.2. Morro Escuro ridge

The Morro Escuro (ME) ridge is an allochthonous shear zone-bound block that strikes 7 km in the NE-SW direction, located between slices of the Archean Basal Complex and the Paleoproterozoic Borrachudos Suite ([Carvalho et al., 2014](#)) (Fig. 2).

The Morro Escuro ridge supracrustal rocks were subdivided by [Braga et al. \(2015\)](#) in four lithostratigraphic units: (1) biotite schist, (2) lower and (3) upper quartzite and (4) itabirite. The itabirite unit occurs as NE-SW-striking layers with 15-60 m thickness, in gradational contact with 4 m thick ferruginous quartzite (Fig. 6b). Morro Escuro ridge lacks significant high-grade iron mineralization, and the itabirite Fe grade varies from 30 to 35 wt. %.

4.2.1. Itabirite mineralogy and paragenesis

Itabirite has a schistose fabric containing lamellar hematite crystals with irregular intergrowths and martite-I. Kenomagnetite-I appears as relicts in martite-I, or as subhedral crystals grown in a fine-banded lamellar hematite matrix in the itabirite (Fig. 5).

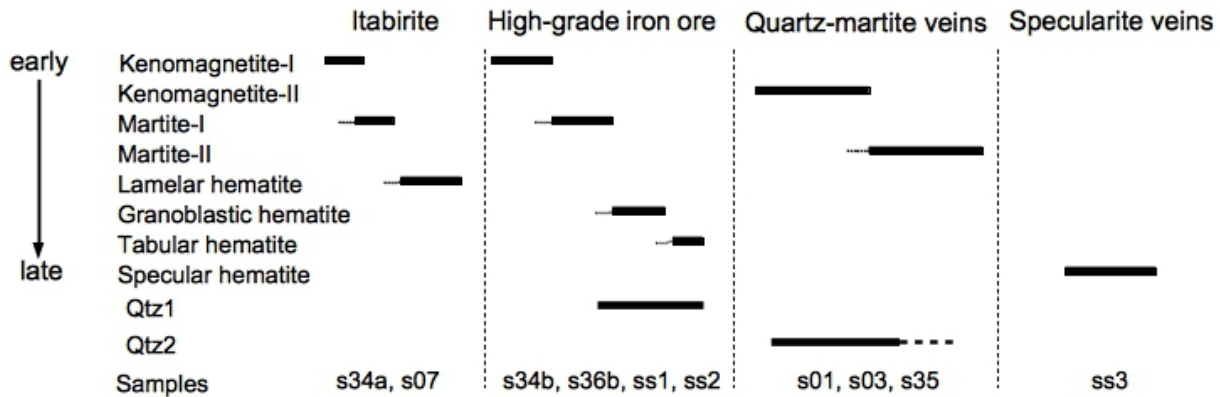


Figure 5. Iron oxide paragenetic sequence of itabirite-hosted iron ore at Piçarrão-Liberdade deposit, Morro Escuro ridge, Guanhães and Dores de Guanhães prospects. The classification of the quartz crystals used in the fluid inclusion studies is also shown. Qtz: quartz.

Table 1
Vein types classified at the studied areas.

Deposit/Area	Vein Type	Mineralogy	Host rock	Thickness	Geometry
Picarrão-Liberdade	Vp1	Quartz (Qtz1)	Quartz vein in high-grade Fe ore	Centimetric	Lenticular
Picarrão-Liberdade	Vp2	Quartz (Qtz2)-martite-II	Coarse-grained vein hosted in itabirite	Decimetric	Tabular-discordant
Picarrão-Liberdade	Vpe	Quartz (Qtz3)-K-feldspar-plagioclase	Pegmatite vein hosted in gneiss	Centimetric	Tabular-discordant
Morro Escuro	Vmi	Quartz (Qtz1a)	Quartz vein hosted in itabirite	Centimetric	Lenticular-concordant
Morro Escuro	Vms	Quartz (Qtz1a)	Quartz vein hosted in quartz schist	Decimetric	Lenticular-concordant
Ponte da Raiz Pegmatite	Vb	Quartz-K-feldspar-beryl	Pegmatite	Metric	Tabular-discordant

Small (<1 m thick), high-grade iron lenses consists of tabular-granoblastic hematite with strong intragranular porosity to compact granular kenomagnetite-I. Banded, high-grade lenses are enriched in granoblastic hematite, whereas foliated, high-grade lenses are enriched in tabular hematite. Granoblastic hematite overprints kenomagnetite-I, and is overprinted by tabular hematite. Compact high-grade lenses are composed of kenomagnetite-I that displays only minor martitization along fractures and cleavage planes and is not overprinted by hematite. Specular hematite is hosted in shear zones and quartz veins as elongated grains oriented parallel to each other, defining a strong foliation.

4.2.2. Vein types

Two types of quartz veins occur at the Morro Escuro ridge: Vmi hosted in itabirite and Vms hosted in quartz schist (Fig. 6b and Table 1). The Vmi vein is concordant to the foliation of the itabirite and is composed of medium-grained quartz with undulose extinction. The vein border is enriched in tabular hematite. The Vmi thickness varies from 1 to 3 cm (Fig. 6b). The Vms veins are boudinaged, parallel to the foliation of the quartz schist and comprise medium-grained quartz. The Vms thickness varies from 5 to 50 cm. In both Vmi and Vms, quartz crystals are highly deformed, with undulose extinction and recrystallized borders.

4.3. Dores de Guanhães (DGN) and Guanhães (GNH) prospects

The DGN prospect is located 35 km north of the Morro Escuro ridge within rocks of the Guanhães Complex (Fig. 1), and less than 1 km from the Borrachudos Suite granite. A lens of high-grade iron strikes N-S for approximately 1 km and dips sub-vertically with an average thickness of 3 m. ([Centaurus, 2014](#)).

The GNH prospect is located on the outskirts of the town of Guanhães. The geological units consist of TTG granites of the Guanhães Complex and dolomitic itabirite of the Guanhães Group. Itabirite appears as elongated and isolated segments within the Guanhães Complex (Fig. 1); it is folded, with the fold axes of the tight to isoclinal folds plunging between NW to NE ([Centaurus, 2014](#)).

4.3.1. Itabirite mineralogy and paragenesis

The dominant iron oxides in the banded high-grade iron lens at the DGN are granoblastic hematite and martite-I crystals in fine-grained goethite. Hematite overprints martite-I. Small (<10 cm) lenses of compact high-grade iron bodies occur at GNH where the dominant iron oxide is kenomagnetite-I locally overprinted by granoblastic hematite. Small (<10 cm) lenses of foliated high-grade iron bodies are composed of tabular hematite with subordinate granoblastic hematite.

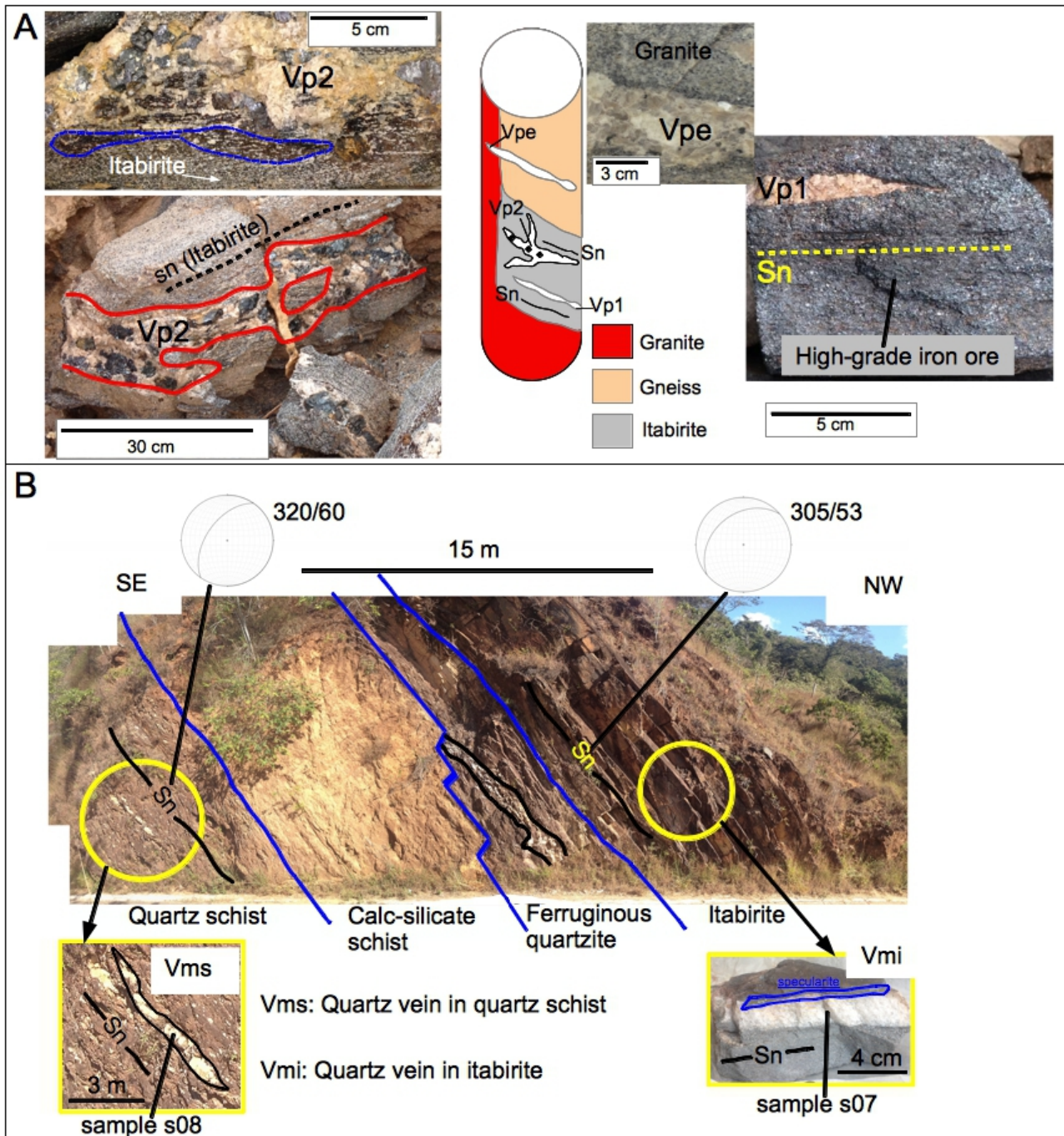


Figure 6. Schematic diagram illustrating the different vein types (Vp1, Vp2, Vpe, Vms, Vmi). A. Piçarrão-Liberdade deposit B. Morro Escuro ridge. Sn: foliation.

5. Whole rock geochemistry

5.1. Piçarrão-Liberdade deposit

Itabirite at the PLD consists mainly of Fe_2O_3 (52.9 wt. %) and SiO_2 (45.7 wt. %), with minor Al_2O_3 (0.2 wt. %). The Fe_2O_3 content of high-grade iron orebodies varies from 95 to 99 wt. %, with higher concentrations of Al_2O_3 (0.4 – 0.8 wt. %). The compact sample is the most enriched in martite and kenomagnetite, and it shows the highest FeO content (12.8 wt. %). The foliated, hematite-enriched samples present the lowest FeO content (1.2 and 4.2 wt. %) (Appendix A).

Normalized to the PAAS-(sn) (Post-Archaean Average Australian Sedimentary Rocks; [McLennan, 1989](#)), the itabirite REE + Y spidergram (Fig. 7) shows the typical HREE enrichment in relation to LREE, $\text{Pr/Yb}_{(\text{sn})} = 0.31$. The itabirite has a slight negative $\text{Eu}_{(\text{sn})}$ anomaly ($\text{Eu/Eu}^* = 0.89$), presents seawater-like Y/Ho ratios (> 40) (Fig. 8), and a positive $\text{Ce}_{(\text{sn})}$ anomaly (Fig. 9). The chondrite-normalized ([Taylor and McLennan, 1985](#)) $\text{Eu}_{(\text{cn})}$ anomaly is negative ($\text{Eu/Eu}^*_{(\text{cn})} = \text{Eu}_{(\text{cn})}/0.5\text{Sm}_{(\text{cn})} + 0.5\text{Gd}_{(\text{cn})} = 0.62$).

The banded sample shows anomalous enrichment in LREE, which is probably the result of supergene alteration (goethite enrichment), and subsequently not further discussed. Although foliated and compact samples present REE pattern similar to the itabirite, the foliated samples show depletion in LREE content, whereas the compact sample presents slight enrichment in REE content (Fig. 7). The foliated samples are also slightly enriched in V, Pb, Ni, Co, As and Hg; when compared to the itabirite.

5.2. Morro Escuro ridge

Two samples of itabirite from Morro Escuro ridge were analyzed; one from the SW extension and the other from the NE extension (Fig. 2). The major elements abundances for these two samples are very similar. Itabirite at the Morro Escuro ridge consists mainly of Fe_2O_3 (55 - 56 wt. %) and SiO_2 (42 – 45.5 wt. %), with minor Al_2O_3 (0.13 – 0.26 wt. %). High-grade banded lenses contain Fe_2O_3 (77.8 wt. %) and SiO_2 (19.7 wt. %), with higher concentrations of Al_2O_3 (0.5 wt. %). Foliated lenses have higher concentrations of Fe_2O_3 (99.1 wt. %) and is enriched in Al_2O_3 (1.29 wt. %). Compact samples are the most enriched in martite and kenomagnetite, they show the highest FeO content (6.5 and 9.5 wt. %) (Appendix A).

Normalized to the PAAS ([McLennan, 1989](#)), the two itabirite REE + Y spidergrams (Fig. 7) present

different LREE/HREE ratios ($\text{Pr/Yb}_{(\text{SN})} = 1.25$ and 0.31). Both itabirites have positive a $\text{Y}_{(\text{sn})}$ and $\text{Eu}_{(\text{sn})}$ anomaly ($\text{Eu/Eu}^* = 1.44$ and 1.34), present signatures of terrigenous input (shale field), as indicated by the low values of Y/Ho (under 35) (Fig. 8), and are HREE depleted. One itabirite presents a positive $\text{Ce}_{(\text{sn})}$ anomaly (Fig. 9), similar to the Ce-allanite itabirite of [Braga et al. \(2015\)](#). The chondrite-normalized ([Taylor and McLennan, 1985](#)) $\text{Eu}_{(\text{cn})}$ anomaly is close to 1.00 ($\text{Eu/Eu}^*_{(\text{cn})} = 0.96$ and 0.89). The foliated sample shows very pronounced HREE enrichment and slight enriched in Cr, Sr and V. In relation to the itabirite, the foliated and compact samples show slight depletion in REE content (Fig. 7).

5.3. Dores de Guanhães (DGN) and Guanhães (GNH) prospects

Dolomitic itabirite at GNH consists mainly of Fe_2O_3 (53.5 wt. %) and SiO_2 (44.8 wt. %), with minor MgO (0.07 wt. %). High-grade samples at DGN and GNH consist of Fe_2O_3 (95.6 to 97.9 wt. %) with variable concentrations of Al_2O_3 (0.1 to 1.24 wt. %). The compact sample is the most enriched in martite and kenomagnetite, and shows the highest FeO content (20.7 wt. %) (Appendix A). Normalized to the PAAS ([McLennan, 1989](#)), the itabirite REE + Y spidergram (Fig. 7) shows the typical HREE enrichment in relation to LREE, $\text{Pr/Yb}_{(\text{sn})} = 0.42$. The itabirite sample from GNH have a positive $\text{Eu}_{(\text{sn})}$ anomaly ($\text{Eu/Eu}^* = 1.77$), and presents a signature for a terrigenous input (shale field), indicated by the low values of Y/Ho (under 35) (Fig. 8). The chondrite-normalized ([Taylor and McLennan, 1985](#)) $\text{Eu}_{(\text{cn})}$ anomaly is also positive ($\text{Eu/Eu}^*_{(\text{cn})} = 1.22$). In relation to the itabirite, the foliated and compact samples show depletion in REE content, and the banded sample presents enrichment in REE content (Fig. 7). Compact and foliated samples are enriched in As and Pb, whereas banded sample is enriched in As, Cr, Pb and Sr.

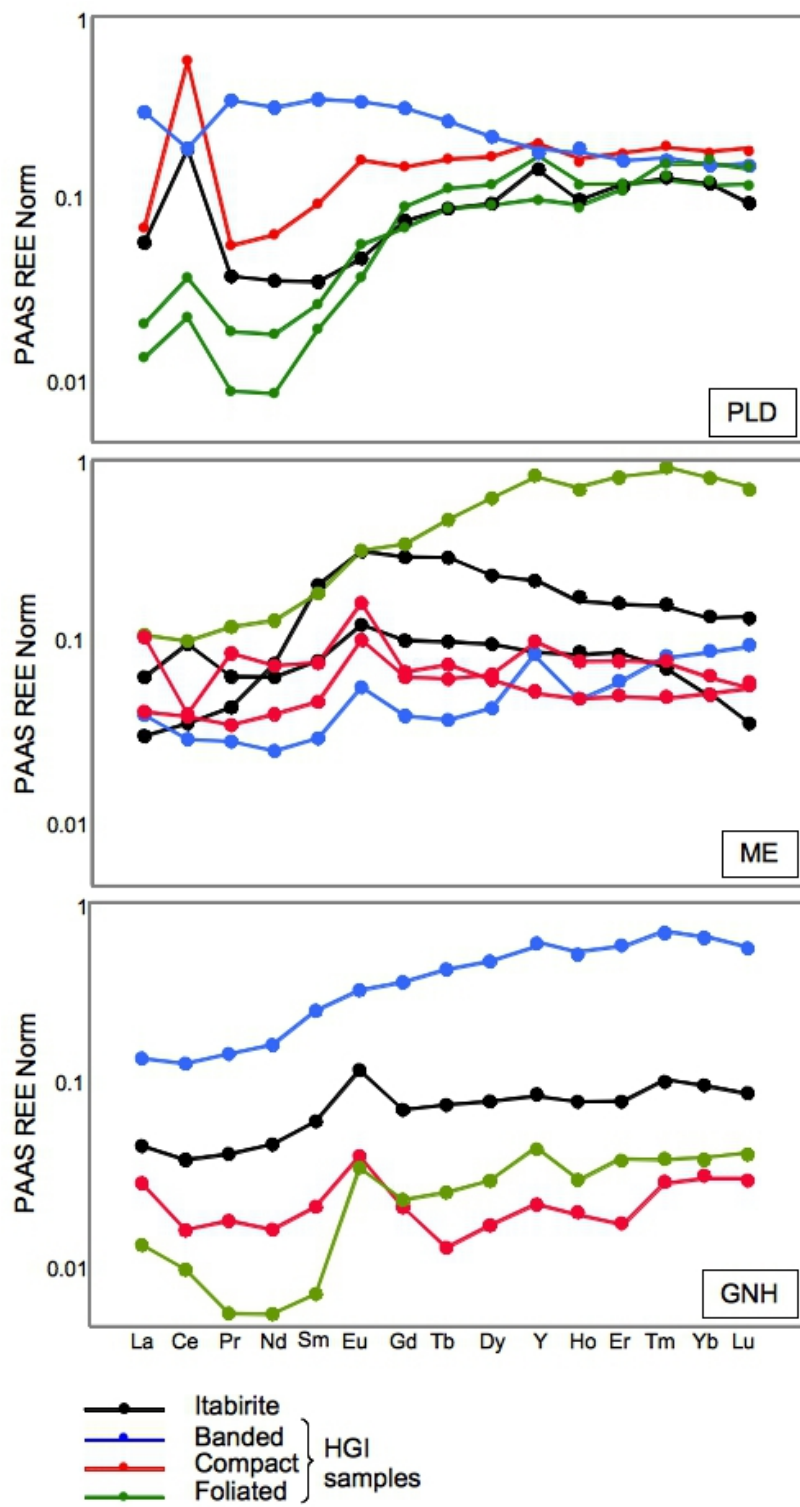


Figure 7. Results of whole-rock geochemical analyses of itabirite-hosted high-grade iron rock. Distribution pattern of the REE + Y values of the hematite and itabirites normalized to the values of PAAS (McLennan, 1989) in relation to itabirite for each deposit. PLD (Piçarrão-Liberdade deposit); ME (Morro Escuro ridge); GNH (Guanhães and Dores de Guanhães prospects). HGI: high-grade iron.

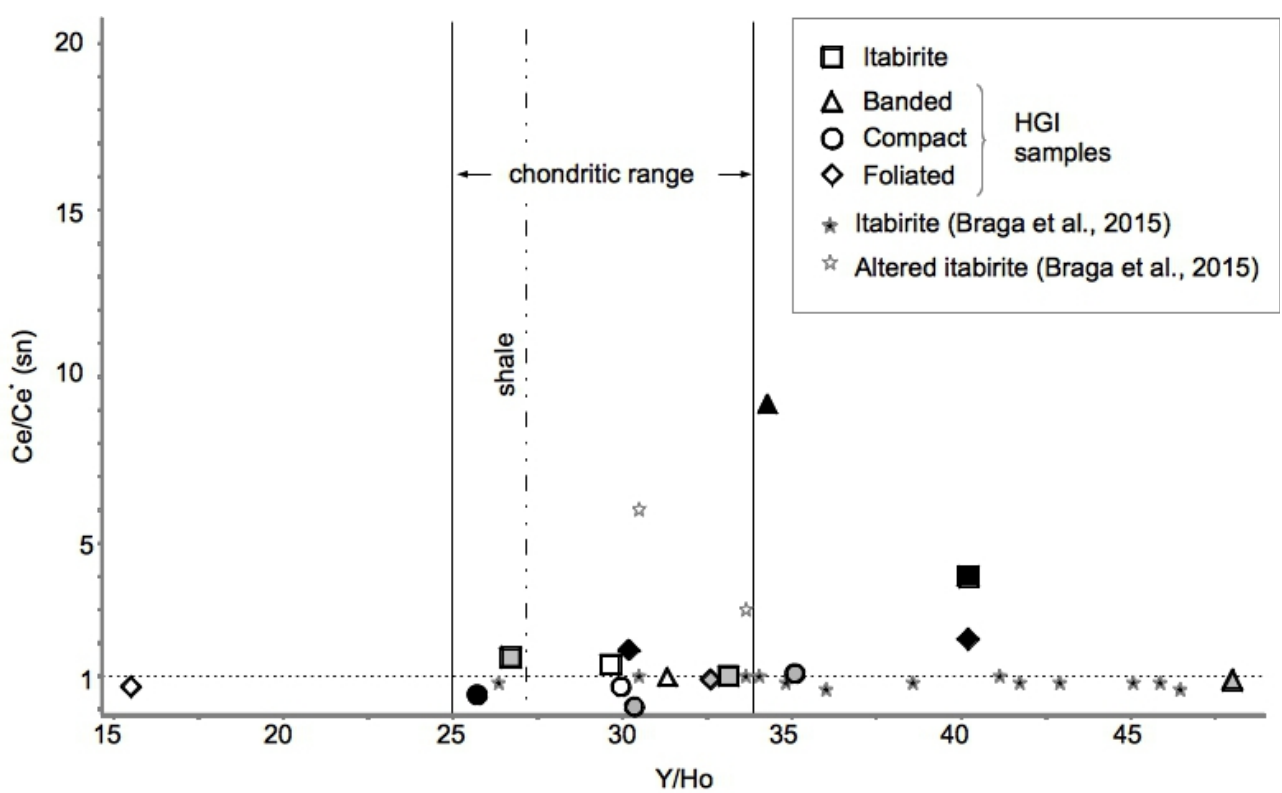


Figure 8. Ce/Ce*(SN) vs.Y/Ho diagram showing a comparison of trace element data derived from whole-rock geochemical analyses of itabirite-hosted high-grade iron rock (Pecoits, 2010). Symbols: Black (Piçarrão-Liberdade); gray (Morro Escuro); white (Guanhães-Dores de Guanhães). HGI: high-grade iron.

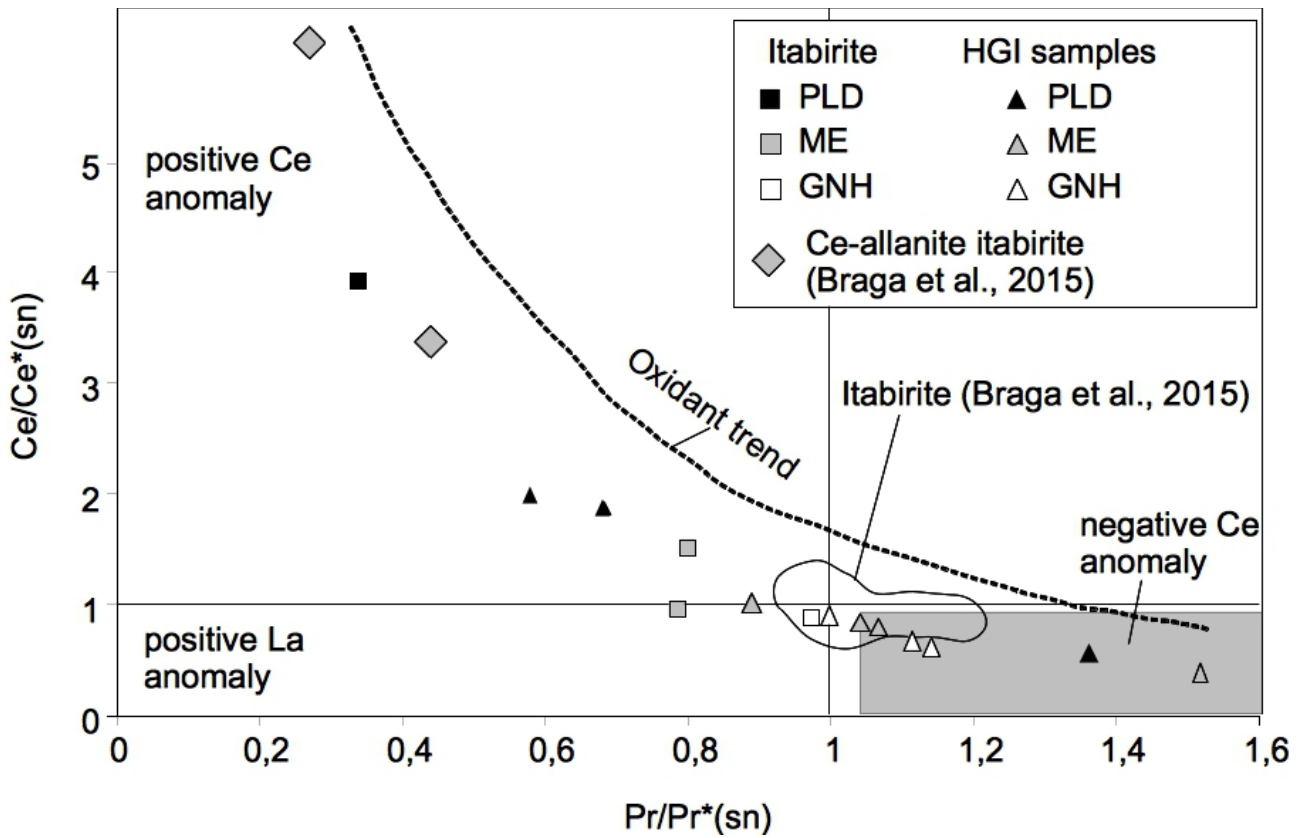


Figure 9. Discrimination diagram, derived from whole-rock geochemical analyses, of $\text{Ce}/\text{Ce}^*(\text{SN})$ vs. $\text{Pr}/\text{Pr}^*(\text{SN})$ for La and Ce anomalies ([Bau and Dulsky, 1996](#)). It shows a variation from positive Ce anomaly in the itabirites to negative Ce anomaly in the HGIs. PLD (Piçarrão-Liberdade), ME (Morro Escuro), GNH (Guanhães-Dores de Guanhães). HGI: high-grade iron.

6. Iron oxide LA-ICP-MS studies

6.1. Piçarrão-Liberdade deposit

Itabirite-bearing kenomagnetite-I and lamellar hematite show similar chemical patterns with considerable amounts of Al (1100-1200 ppm), Ti (80-120 ppm), V (30-35 ppm) and Cr (5-10 ppm). Second-stage martite-II in quartz-martite-II veins contains mainly Mg (625 ppm), Al (861 ppm), P (156 ppm), V (40 ppm), Cr (10 ppm) and Mn (1004 ppm). Other trace elements such as Ti, Co, Ni, Zn, Ga, As and Mo have concentrations of <5 ppm. The REE concentrations of martite-II (Vp2) are the highest of all other iron oxides (Fig. 10), and its PAAS-normalized diagram exhibits slight HREE enrichment and positive Ce anomaly (Fig. 11a, Appendix B).

Kenomagnetite-I in high-grade orebodies contains high amounts of Mg (697 ppm), Al (743 ppm), V

(55 ppm), Cr (15 ppm) and Mn (815 ppm). In relation to itabirite iron oxides, kenomagnetite-I is enriched in all elements except Al, Ti and Mo, REE are below the detection limits. Martite-I alteration of kenomagnetite-I is accompanied by significant depletions in Mg, Ti, V, Cr, Mn, Co and Ni with enrichment in Al, P and As. The PAAS-normalized diagram for martite-I exhibits HREE enrichment and positive Ce anomaly (Figs. 10 and 11a).

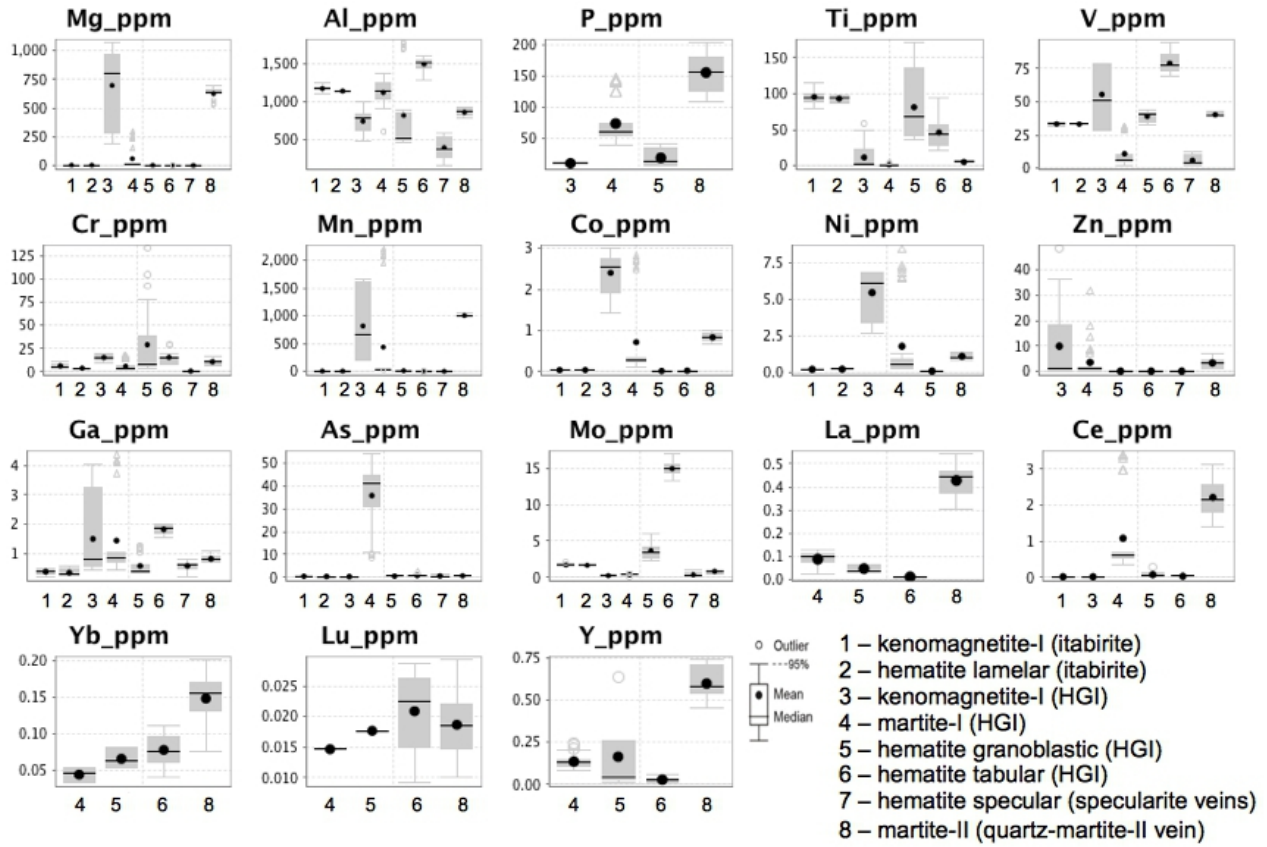


Figure 10. Box-and-whisker plots of minor and trace elements in ppm from mineral chemistry LA-ICP-MS data. The results are grouped by iron oxide mineral for the Piçarrão-Liberdade deposit. The upper and lower margins of the box represent the upper and lower 50 percentile of the data. The whiskers represent the upper and lower threshold values (95 percentile of the data). Median values are shown as solid black lines and mean values as solid black circles. See Fig. 4 for oxide paragenetic sequence. HGI: high-grade iron.

Granoblastic hematite contains mainly Al (819 ppm), P (18 ppm), Ti (81 ppm), V (39 ppm), and Cr (29 ppm). Other trace elements such as Mg, Co, Ni, Zn, Ga, As and Mo have concentrations <5 ppm, and together with Mn are depleted in relation to paragenetically older martite-I, whereas Mo,

Ti and Cr are enriched. No REE >1 ppm were detected. Paragenetically younger tabular hematite is less abundant than granoblastic hematite in P, Ti, Cr, and Mn, whereas Al, V, Ga and Mo are relatively enriched. Shear zone- and vein-hosted specular hematite is significantly depleted in most trace elements and REE, containing only Al (399 ppm) and V (6 ppm) in significant amounts.

6.2. Morro Escuro ridge

Martite-I of the least altered itabirite represents the paragenetically earliest oxide at Morro Escuro ridge, and has considerable amounts of Mg (56 ppm), Al (845 ppm), P (564 ppm), V (33 ppm), Cr (6 ppm), Mn (17831 ppm), Co (31 ppm), Ni (164 ppm), Zn (129 ppm), Ga (5 ppm), and As (15 ppm). Other trace elements such as Ti and Mo, as well as REE, are not present in concentrations >2 ppm other than Ce (3 ppm) and Y (3 ppm). The REE concentrations are the highest in all other iron species, and the PAAS-normalized diagram for martite-I exhibits HREE enrichment and positive Ce anomaly (Figs. 12 and 11b). Paragenetically younger lamellar hematite is depleted in most trace elements and REE other than Al, V and Cr, and enriched in Ti (142 ppm).

Kenomagnetite-I in high-grade orebodies contains mostly Mg (26 ppm), Al (66 ppm), P (37 ppm), V (94 ppm), Mn (1106 ppm), Ni (11 ppm), and Zn (129 ppm) with other trace elements and REE present in concentrations <5 ppm. Relative to paragenetically younger kenomagnetite-I, tabular hematite is depleted in Mn, Co, Ni, Zn; and enriched in Al (3694 ppm), Ti (1967 ppm), Cr and Mo. Compact kenomagnetite-I in high-grade orebodies has high concentrations of Mg (24679 ppm), significant amounts of Al (1359 ppm), Ti (117 ppm), V (75 ppm), Cr (9 ppm), Mn (3627 ppm), Ni (7 ppm) and Zn (7 ppm); concentrations of other trace elements and REE do not exceed 2 ppm. Relative to kenomagnetite-I overprinted by tabular hematite, compact kenomagnetite-I is enriched in Mg, Al, Ti, and depleted in P and Zn. Shear zone- and vein-hosted specular hematite is characterized by Al (696 ppm), P (9 ppm), Ti (42 ppm), V (37 ppm) and Mn (15 ppm). Other elements such as Mg, Cr, Co, Ni, Zn and REE were not detected in concentrations >2 ppm.

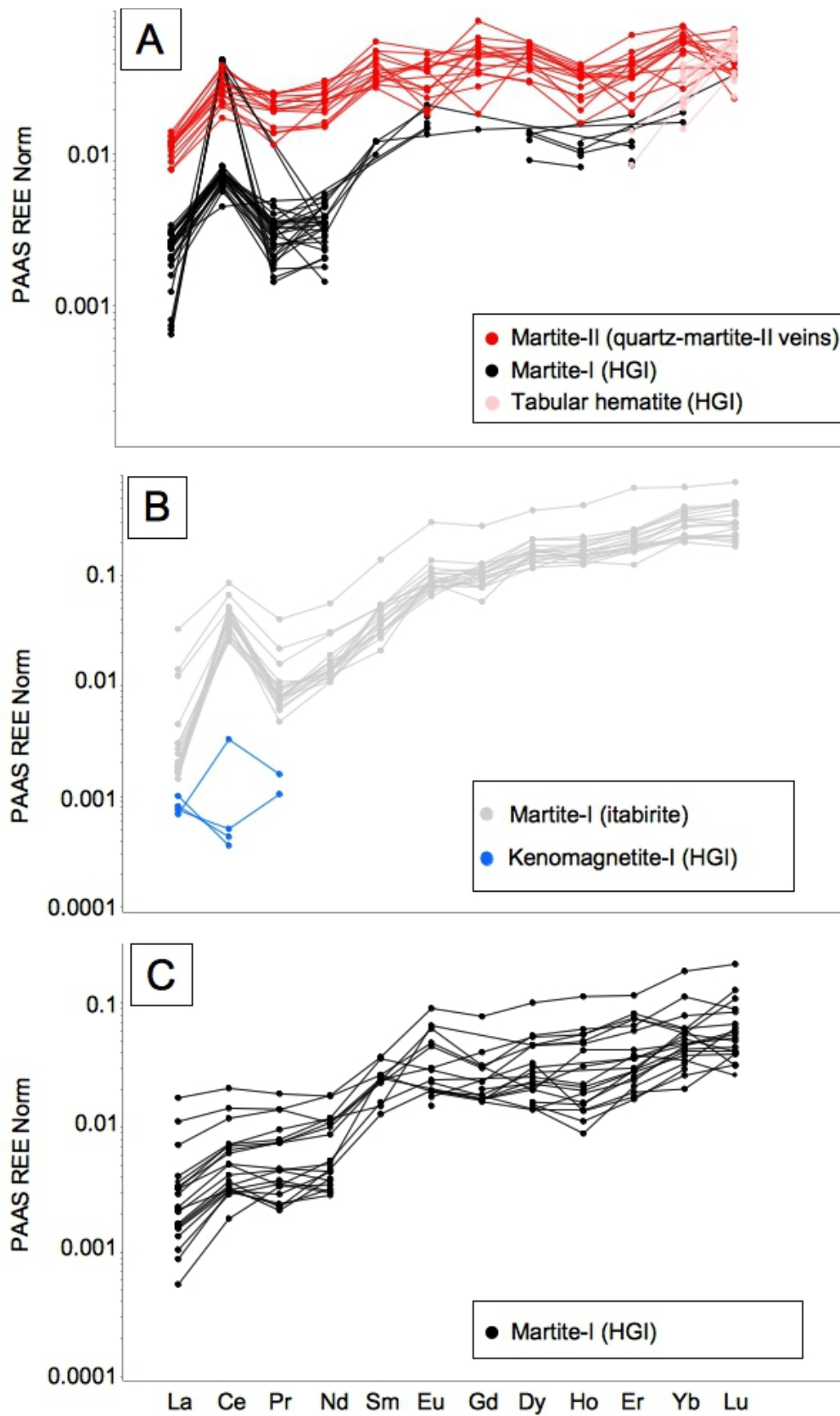


Figure 11. Rare earth element PAAS-normalized (McLennan, 1989) spider plot of iron oxide mineral chemistry data from A. Piçarrão-Liberdade deposit; B. Morro Escuro ridge, and C. Dores de Guanhães and Guanhães prospects. HGI: high-grade iron.

6.3. Dores de Guanhães (DGN) and Guanhães (GNH) prospects

Kenomagnetite-I from banded, high-grade lens represents the earliest paragenetically iron oxide species at GNH. It is characterized by high concentrations of Mg (38545 ppm), and considerable Al (1838 ppm), Ti (19 ppm), V (56 ppm), Cr (32 ppm), Mn (4215 ppm), Co (29 ppm), Ni (68 ppm), Zn (8 ppm) and Ga (7 ppm) (Fig. 13). Arsenic and Mo as well as REE were not present in concentrations >1 ppm. Paragenetically younger granoblastic hematite is relatively depleted in Mg, Mn, Co, Ni, Zn and Ga when compared to kenomagnetite-I, and enriched in Ti (2635 ppm) and Mo. compact kenomagnetite-I is depleted in P, Cr, Co and Ni in relation to kenomagnetite-I from banded, high-grade lens.

Granoblastic hematite from banded, high-grade lens at DGN is relatively depleted in Mg and Ti when compared to granoblastic hematite from GNH, and enriched in P, Cr and Ga. Martite-I from banded, high-grade lens at DGN is relatively enriched with respect to most trace elements when compared to granoblastic hematite at DGN, other than Al (3750 ppm) (Fig. 12). The REE are slightly enriched, and the PAAS-normalized diagram for martite-I exhibits HREE enrichment and positive Eu anomaly (Fig. 11c).

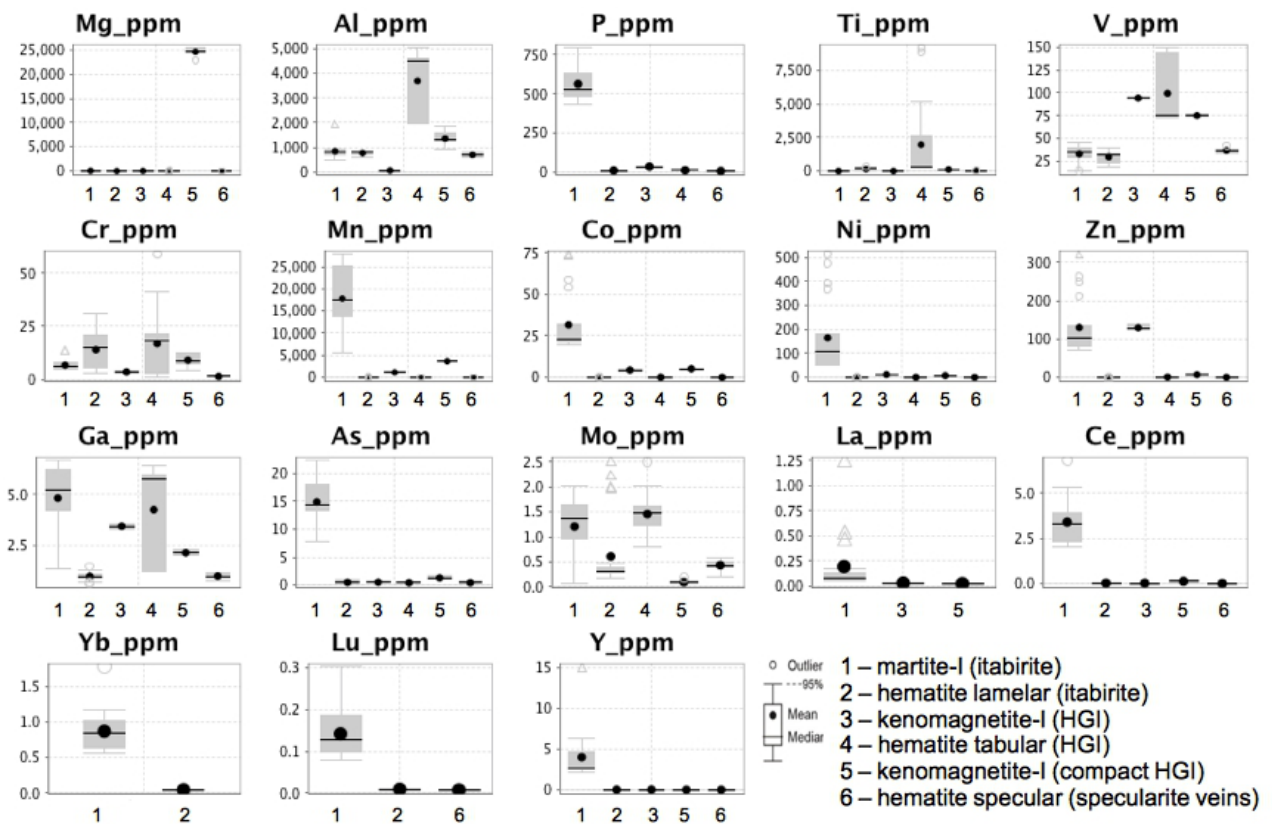


Figure 12. Box-and-whisker plots, derived from mineral chemistry LA-ICP-MS data, of minor and trace elements in ppm grouped by iron oxide mineral for Morro Escuro ridge. The upper and lower margins of the box represent the upper and lower 50 percentile of the data. The whiskers represent the upper and lower threshold values (95 percentile of the data). Median values are shown as solid black lines and mean values as solid black circles. See Fig. 4 for oxide paragenetic sequence. HGI: high-grade iron.

7. Fluid inclusion studies at the Piçarrão-Liberdade (PLD) iron deposit, the Morro Escuro ridge itabirite sequence and the Ponte da Raiz beryl-bearing pegmatite

The samples used in the fluid inclusion studies at PLD and ME areas were selected according to the vein classification in sections 4.1.2. and 4.2.2. In the following sections the areas selected for microthermometry are described in terms of its fluid inclusions content (Figs. 14, 15, 16, 17).

Table 2

Analyzed fluid inclusion types. PLD: Piçarrão-Liberdade deposit; ME: Morro Escuro ridge.

Deposit/Area	Samples	Vein Type	Mineral	Fluid inclusion type	Timing	Microthermometry	LA-ICP-MS
Piçarrão-Liberdade	s31	Vp1	Quartz (Qtz1)	Type 1 – Aqueous Type 2 – Aqueous-carbonic	S PS	x	x
Piçarrão-Liberdade	s01, s03	Vp2	Quartz (Qtz2)	Type 1 – Aqueous Type 1 – Aqueous	PS	x	x
Piçarrão-Liberdade	s47	Vpe	Quartz (Qtz3)	Type 1 – Aqueous Type 1 – Aqueous	S PS	x	x
Morro Escuro	s07	Vmi	Quartz (Qtz1a)	Type 1 – Aqueous Type 2 – Aqueous-carbonic	PS	x	
Morro Escuro	s08	Vms	Quartz (Qtz1a)	Type 1 – Aqueous Type 2 – Aqueous-carbonic	PS	x	x
Ponte da Raiz	Be1	Vb	Beryl	Type 2a – Aqueous-carbonic Type 2b – Aqueous-carbonic Type 2c – Aqueous-carbonic	P PS	x	

Abbreviations: PS = pseudosecondary, S = secondary

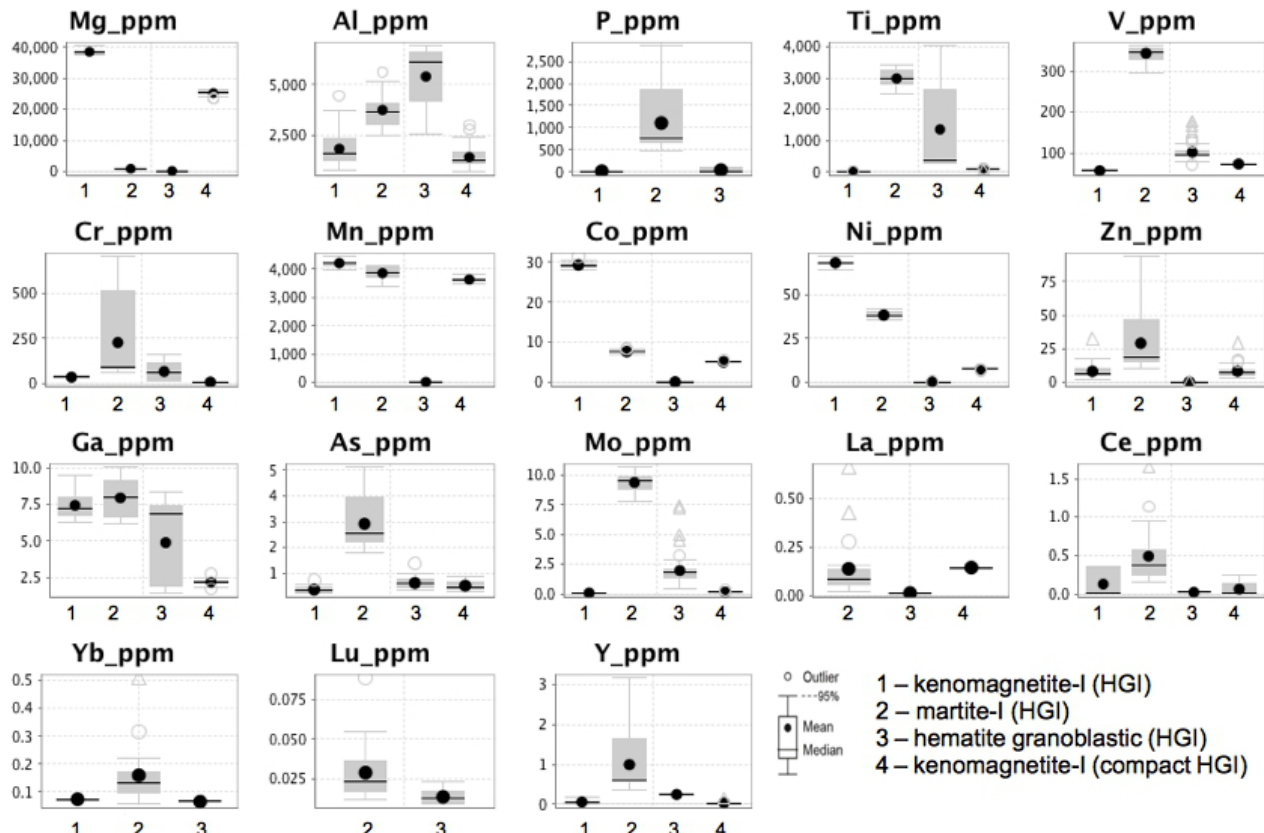


Figure 13. Box-and-whisker plots of minor and trace elements in ppm from mineral chemistry LA-ICP-MS data. The results are grouped by iron oxide mineral for Dores de Guanhães and Guanhães prospects. The upper and lower margins of the box represent the upper and lower 50 percentile of the data. The whiskers represent the upper and lower threshold values (95 percentile of the data). Median values are shown as solid black lines and mean values as solid black circles. See Fig. 4 for oxide paragenetic sequence. HGI: high-grade iron.

7.1. Fluid inclusions trapped in quartz from the Piçarrão-Liberdade (PLD) iron deposit

Vein samples from itabirite (40% Fe), high-grade iron ore (>55%Fe) and gneiss were chosen from the PLD for microthermometry and LA-ICP-MS analyses (Table 2).

7.1.1. Fluid inclusions types and assemblages

7.1.1.1. Vp1 veins

The Qtz1 crystals from the quartz vein in the high grade iron ore (Vp1; Figs. 5 and 6) host fluid inclusion assemblages that form three-dimensional clusters and trails. They are interpreted as pseudosecondary in nature because of the confinement of the cluster and trails to individual crystal (Roedder, 1984) (Fig. 14a). Secondary trails of inclusions are also observed, but not considered here for data interpretation due to their unclear relationship with the mineralization process. According to the number, nature, and volume proportions of phases present at room temperature, two types of fluid inclusion are classified in these Qtz1 crystals: Type 1, two-phase (L-V) aqueous; and type 2, four-phase (L-L-V-S) aqueous-carbonic (Fig. 14f) with aqueous-saline phase, liquid CO₂, vapor and solid phases (daughter crystals).

Type 1 FIs have a high liquid/vapor ratio (average 85% liquid, 15% vapor), and form irregularly shaped to rounded inclusions in secondary trails. Type 2 FIs have highly variable H₂O/CO₂ ratio (volume fraction of CO₂ varies from 30 to 80 vol. %), average size between 25-35 µm and form irregularly shaped to rounded inclusions. Locally, negative crystal shape was observed in type 2 inclusions.

7.1.1.2. Vp2 veins

Coarse-grained Qtz2 crystals from the itabirite-hosted quartz-martite-II veins (Vp2; Figs. 5 and 6) contain only type 1 two-phase (L-V) aqueous FIs, with constant L/V ratios (5-15% vapor) and smaller average size (10-20 µm) than Qtz1 FIs. These type 1 FIs are irregularly shaped to rounded inclusions, form three-dimensional clusters and internal trails, and are interpreted as pseudosecondary inclusions (Fig. 15). Secondary trails of inclusions are also observed, but not considered here for data interpretation due to their unclear relationship with the mineralization process.

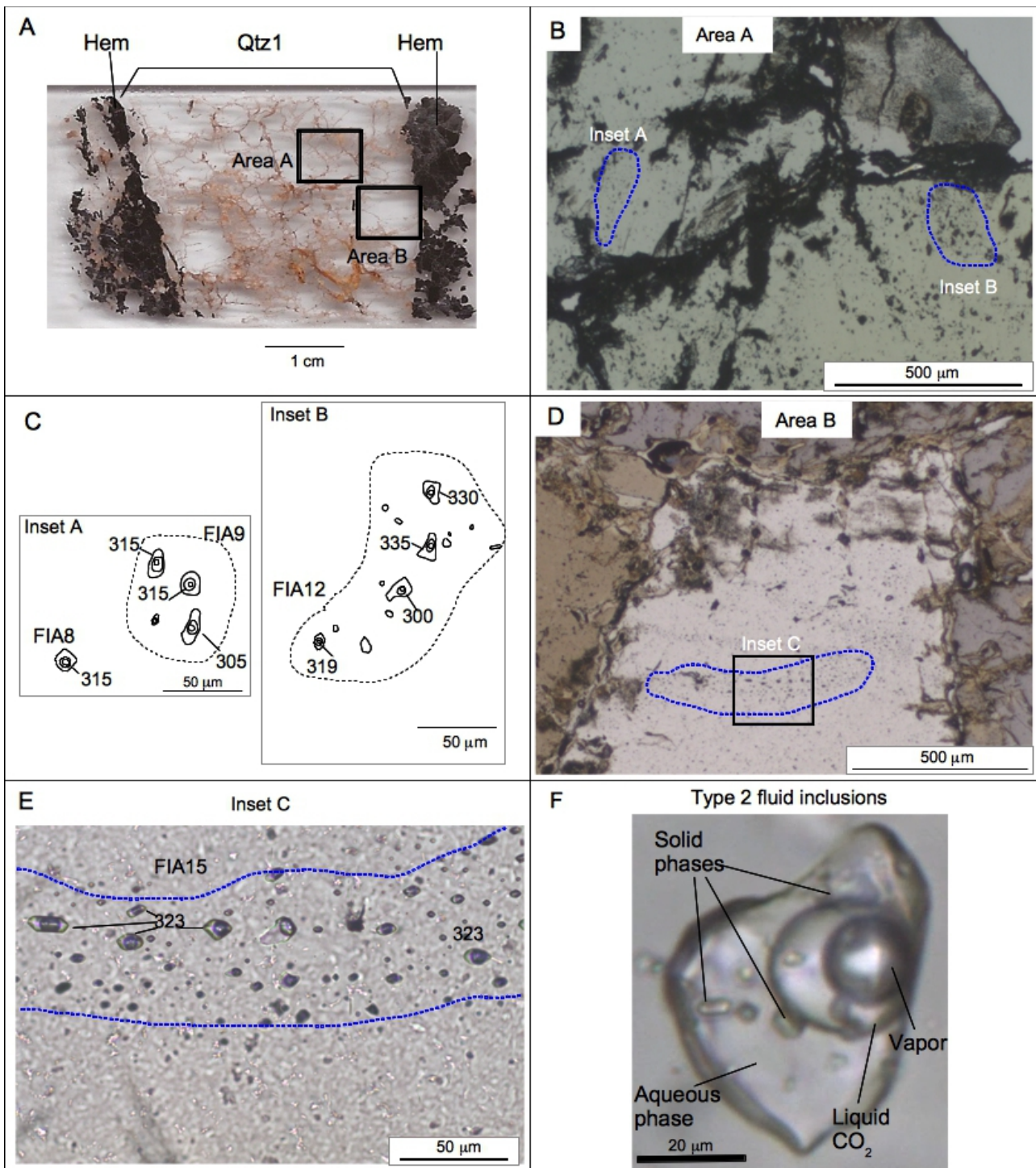


Figure 14. Fluid inclusion samples, and fluid inclusion maps showing analyzed fluid inclusion assemblages hosted by Vp1 veins from the Piçarrão-Liberdade iron deposit. A. sample s31 - thin section surface of Vp1 quartz (Qtz1) vein with border of granoblastic hematite (Hem). B. Photomicrograph of Qtz1 showing selected fluid inclusion areas for microthermometric analyses. C. Insets displaying fluid inclusion maps with FI assemblage number. D. Photomicrograph of Qtz1 showing pseudosecondary trail selected for microthermometric analyses. E. Photomicrograph of the selected trail displaying fluid inclusion map with assemblage number. F. Type 2 inclusion trapped

in Qtz1 from Area A. FIA: Fluid Inclusion Assemblage.

7.1.1.3. Vpe veins

The Qtz3 crystals from the granite-hosted pegmatite vein (Vpe; Fig. 6) share some similarities with Qtz2 in terms of their FIs content and contain only type 1, two-phase (L-V) aqueous FIs, with more constant L/V ratios (5-15% vapor), and average size between 10-20 μm . These type 1 FIs form three-dimensional clusters and/or internal trails and are interpreted as pseudosecondary (Fig. 16).

7.1.2. Microthermometry

7.1.2.1. Vp1 veins

Freezing experiments on the CO₂-rich assemblages (type 2 FIs) demonstrate that the nine fluid inclusion assemblages have internally consistent eutectic temperatures (Te) that range from - 30 to - 3 9 °C, suggesting other cations besides Na. Melting temperatures of clathrate (Tclath) define a maximum ranging from 7.5 to 9.0 °C (Table 3). Within fluid assemblages Tclath determinations vary by 0.8 °C. The formation of hydrohalite crystals was observed during the freezing experiments, between -8 and -1 °C. Melting temperatures of CO₂(s) - TmCO₂ - are between -57.9 to -56.6 °C, suggesting CO₂ to have been the most abundant gas species. The bulk CO₂ fraction (XCO₂) varies from 0.1 to 0.54 (H₂O – 0.9 to 0.46), and the CO₂-rich phase homogenized (ThCO₂) over a wide range of temperatures, from 25 to 31.5 °C.

Type 2 inclusion assemblages homogenize by the disappearance of liquid-(CO₂) over a wide range of temperatures, from 270 to 373 °C although ThTot values for individual fluid inclusion assemblages vary only by 15 °C (Table 3). Inclusions with the highest content of CO₂ (XCO₂) present the highest ThTot. These ThTot data represent a minimum trapping temperature since no boiling evidence was observed. Two types of solid phases (daughter crystals) were observed, sylvite and halite. Sylvite crystals are slight pleochroic (Fig. 14f) and dissolve between 15 and 35 °C. Halite appears as non pleochroic square shaped crystals with higher dissolution temperatures between 70 and 87 °C. The salinity values display small variations between 26.5 to 27.6 wt. % NaCl equiv. (Fig. 18), and was calculated based on the halite dissolution temperature (Tmhal).

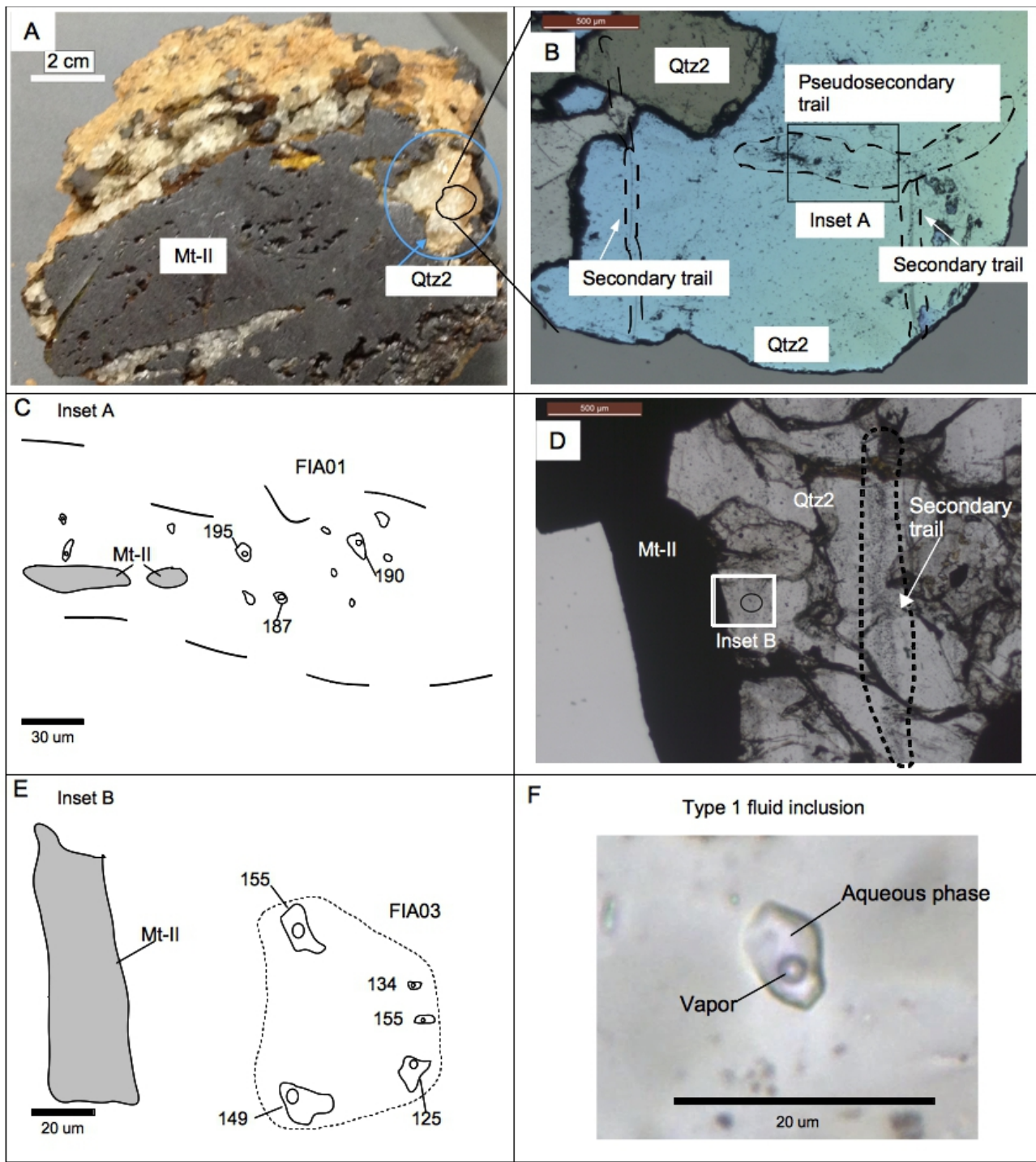


Figure 15. Fluid inclusion samples and fluid inclusion maps showing analyzed fluid inclusion assemblages hosted by Vp2 veins from the Piçarrão-Liberdade iron deposit. A. sample s01 - quartz-martite-II vein (Vp2) and location of double-polished thin section used for microthermometry. B. Photomicrograph of quartz (Qtz2) with pseudosecondary and secondary FI trails. C. Inset A that shows a map of fluid inclusions analyzed, displaying fluid inclusion sample map with assemblage number. D. sample s03 - photomicrograph of Qtz2 and martite-II with secondary fluid inclusion trail and one area where pseudosecondary fluid inclusion are observed (see inset B). E. Inset B

displaying pseudosecondary fluid inclusions and assemblage number. F. Type 1 fluid inclusion trapped in Qtz2 from FIA01. FIA: Fluid Inclusion Assemblage.

7.1.2.2. Vp2 veins

Freezing experiments on type 1 two-phase (L-V) aqueous FIs demonstrate that the seven fluid inclusion assemblages have internally consistent eutectic temperatures (T_e) that range from -30 to -40 °C, suggesting other cations besides Na. Melting temperatures of ice (T_{mice}) are variable and define a maximum T_{mice} ranging from -0.7 to -8.5 °C (Fig. 18). Within fluid assemblages T_{mice} determinations vary by 3 °C. Type 1 inclusion assemblages homogenize by the disappearance of vapor bubbles over a wide range of temperatures, from 144 to 260 °C, although ThTot (L) values for individual fluid inclusion assemblages vary only by 20 °C (Table 3).

7.1.2.3. Vpe veins

Freezing experiments on type 1 two-phase (L-V) aqueous FIs demonstrate that the three fluid inclusion assemblages have internally consistent eutectic temperatures (T_e) that range from -30 to -40 °C, suggesting other cations besides Na. Melting temperatures of ice (T_{mice}) are variable and define a maximum T_{mice} ranging from -2.1 to -6.1 °C (Fig. 18). Within fluid assemblages T_{mice} determinations vary by 1.6 °C. Type 1 inclusion assemblages homogenize by the disappearance of vapor bubbles over a wide range of temperatures, from 156 to 348 °C, although ThTot (L) values for individual fluid inclusion assemblages vary only by 55 °C (Table 3).

7.1.3. Quantitative estimation of fluid inclusion composition based on LA-ICP-MS data

Analytical results for inclusions from Vp1, Vp2 and Vpe veins show that Na, K, Ca and Fe are the dominant components (Table 4). Type 1 two-phase (L-V), aqueous FIs were analyzed in Qtz2 from Vp2 veins, and in Qtz3 from Vpe vein; and type 2 four-phase (L-L-V-S) aqueous-carbonic FIs were analyzed in Qtz1 from Vp1 vein.

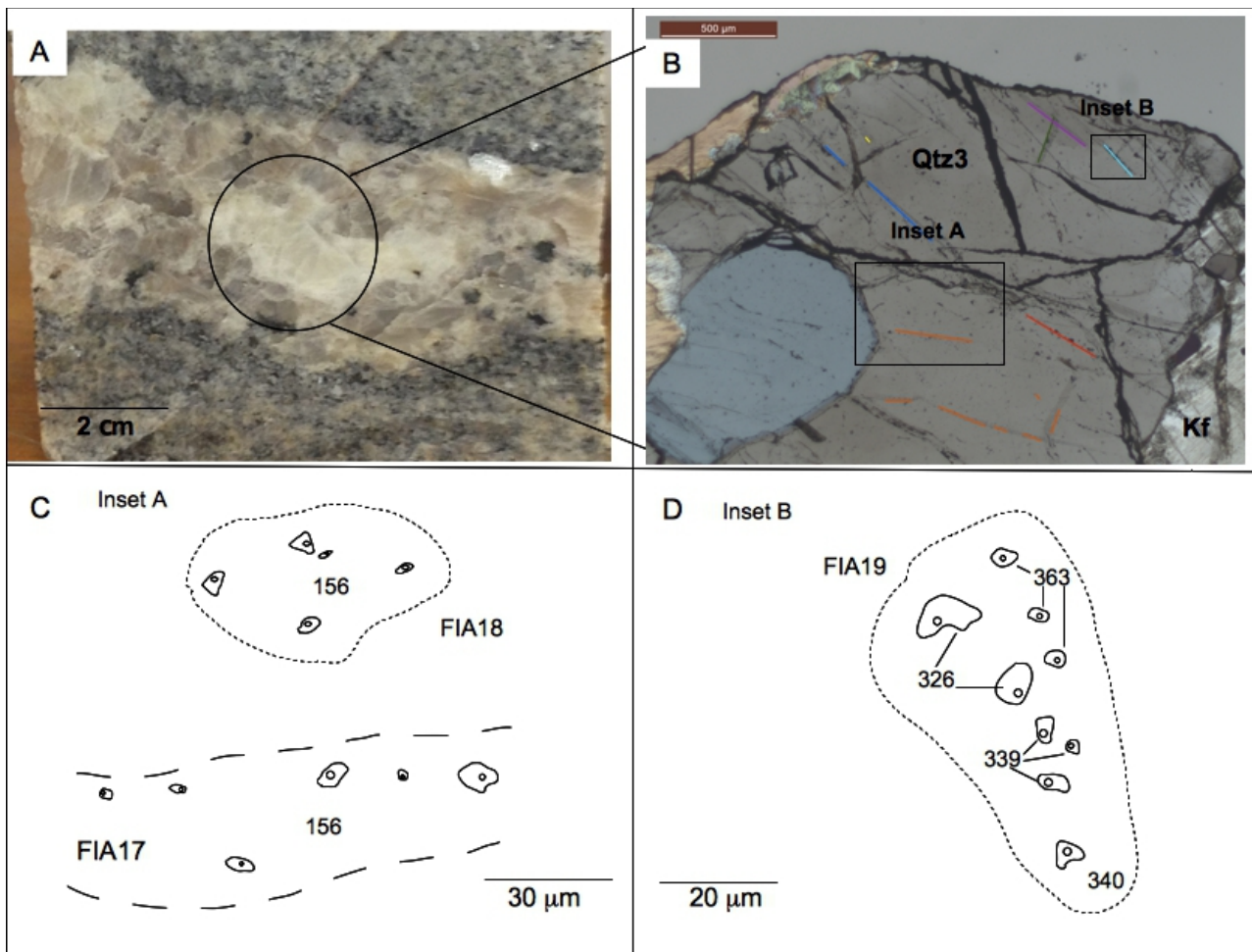


Figure 16. Fluid inclusion samples, and fluid inclusion maps showing analyzed fluid inclusion assemblages hosted by Vpe veins from the Piçarrão-Liberdade iron deposit. A. sample s47 - diamond drill core (31m depth) displaying Vpe vein and sampling location. B. Photomicrograph of quartz (Qtz3) showing map of fluid inclusions. C and D. Insets displaying fluid inclusion sample map with assemblage number. FIA – Fluid Inclusion Assemblage. Kf: K-feldspar.

Table 3

Microthermometric results of pseudosecondary fluid inclusion assemblages. PLD: Piçarrão-Liberdade deposit; ME: Morro Escuro ridge.

Vein/host mineral	Deposit/Area	Phase(s)	Assemblage	n	TmIce (°C)	Tclath (°C)	TmCO ₂ (°C)	ThCO ₂ (°C)	XCO ₂	ThTot (°C)	Tm(hal)(°C)	Salinity (wt% NaCl equiv.)
Vp1	PLD	L-L-V-S	8	1	9	-56.7	30.9	0.086	315	86.5	27.6	
Quartz (Qtz1)	PLD	L-L-V-S	9	3	8.5	-56.7	27.5 ± 3	0.215	310 ± 5	87	27.6	
	PLD	L-L-V-S	10	2	7.5 ± 0.5	-56.7	31.2 ± 0.1	0.086	305 ± 10	87	27.6	
	PLD	L-L-V-S	11	5	9.1 ± 0.5	-57.9	28.5 ± 3.3	0.213	315 ± 15	83 ± 10	27.5	
	PLD	L-L-V-S	12	7	9.0 ± 0.8	-56.6	25 ± 1.5	0.305	329 ± 15	70 ± 10	26.5 ± 1	
	PLD	L-L-V-S	13	2	8.6	-56.6	31.5	0.086	373	70 ± 10	27.2 ± 1	
	PLD	L-L-V-S	14	5	8.5 ± 0.8	-56.6	31 ± 1.5	0.086	315 ± 15	72 ± 10	27.2	
	PLD	L-L-V-S	15	5	8.2 ± 0.5	-56.6	27.6 ± 5.4	0.215	323 ± 15	80 ± 10	27.4	
	PLD	L-L-V-S	16	5	8.2 ± 0.7	-56.6	27.3 ± 6	0.215	270	83	27.5	
Vp2	PLD	L-V	1	3	-0.9 ± 0.1					190 ± 5	1.5	
Quartz (Qtz2)	PLD	L-V	2	3	-8.5 ± 0.5					244 ± 5	12.7 ± 1.5	
	PLD	L-V	3	5	-3 ± 2.5					144 ± 20	4.96	
	PLD	L-V	4	6	-8.5 ± 1.5					260 ± 5	12.7 ± 1	
	PLD	L-V	5	2	-1.8 ± 1.2					160	3.06	
	PLD	L-V	6	10	-1.6 ± 0.4					145 ± 5	2.74 ± 1.5	
	PLD	L-V	7	8	-0.7 ± 0.1					152.7 ± 14.7	1.23	
Vpe	PLD	L-V	17	6	-2.1 ± 1.6					156 ± 10	3.55	
Quartz (Qtz3)	PLD	L-V	18	5	-2.4 ± 0.9					156 ± 10	4.03	
	PLD	L-V	19	9	-6.1 ± 0.6					348 ± 55	9.34 ± 1	
Vmi	ME	L-L-V-S	20	2	7.6 ± 2	-56.6	27.6 ± 2	0.287	290	51 ± 5	26.8	
Quartz (Qtz1a)	ME	L-L-V-S	21	5	8.0 ± 3	-56.6	29.7 ± 3	0.027	340 ± 20	58 ± 5	26.9 ± 1	
	ME	L-L-V-S	22	1	7.7	-56.6	32	0.128	310	35	26.6	
	ME	L-L-V-S	23	1	8.2	-56.6	22.4	0.142	300	37	26.6	
	ME	L-V	24	5	-1.8 ± 0.6					157 ± 15	4.55 ± 1	
Vms	ME	L-L-V-S	25	3	9.8 ± 2	-56.6	30	0.058	250	58 ± 4	26.9	
Quartz (Qtz1a)	ME	L-V	26	2	-2.5 ± 0.3					140	4.18	
	ME	L-L-V-S	27	5	9.3 ± 0.5	-56.6	31 ± 1.5	0.128	230 ± 10	58.8 ± 10	26.9	
	ME	L-L-V	28	4	5.0 ± 0.5	-56.6	15.4	0.126	235		9	
	ME	L-L-V	29	6	6.1 ± 0.5	-56.6	25 ± 4	0.126	230 ± 10		7 ± 2	
	ME	L-V	30	3	-11 ± 1					130	14.97	
Vb	Ponte da	L-L-V-S	32	7	6.0 ± 0.3	-56.6	25	0.021	220		7	
Beryl	Ponte da	L-L-V-S	33	3	4.6 ± 1.2	-57.7	31.4 ± 0.6	0.128	315		135 ± 40	29.2
	Raiz											
	Ponte da	L-L-V-S	34	4	9.2 ± 0.6	-56.6	31 ± 0.8	0.058	315		126 ± 15	28.7
	Raiz											

Fluid inclusions trapped in Qtz1 (Vp1 veins) are enriched in Ca (av. Ca/Na = 0.514), Mn, Cu, Zn, Pb, Sr and Ag when compared to Qtz2 and Qtz3 (Table 4, Fig. 19). Only 1/3 of the analyzed FIs show Fe above the limit of detection, but for these FIs the Fe concentration is high. Bivariate and ternary diagrams (Fig. 20) show good correlation between Cu versus Zn and Sr versus Ca, but no correlation of Fe with other major components, such as K or Ca.

Fluid inclusions trapped in Qtz2 (Vp2 veins) are rich in K and Fe relative to Na (K/Na = 1.44; Fe/Na = 0.418). The Fe concentration is high, similar to type 2 FIs trapped in Qtz1 (Table 4, Fig. 19). The other analyzed cations show very low values that are close to the limit of detection. Bivariate diagrams of Zn versus Cu and Sr versus Ca show good correlation, but in the Fe versus K diagram there is a wide dispersion in data.

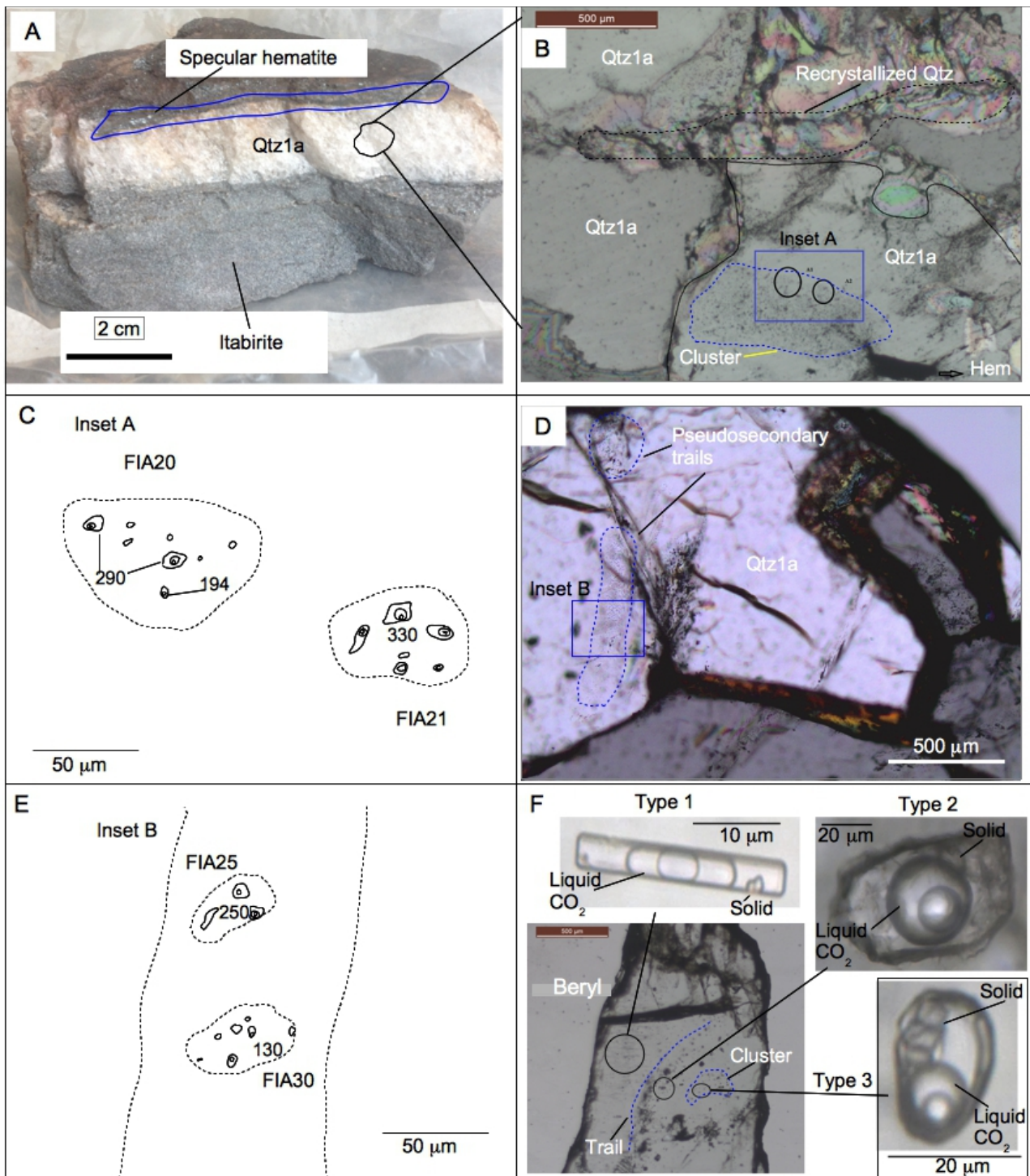
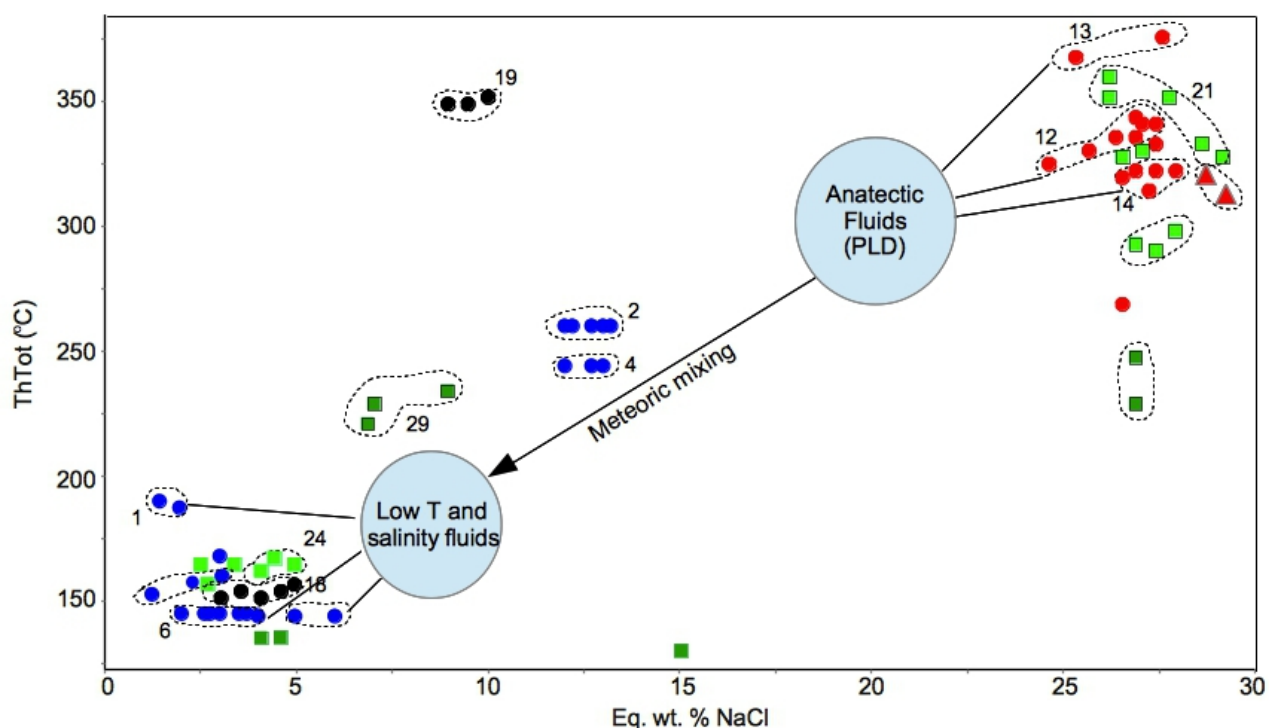


Figure 17. Fluid inclusion samples, and fluid inclusion maps showing analyzed fluid inclusion assemblages hosted by Vmi and Vms veins from Morro Escuro ridge as well as beryl samples from Ponte da Raiz pegmatite. A. sample s07 displaying Vmi vein and sampling location. B. Photomicrograph of quartz (Qtz1a) from Vmi showing mapping of fluid inclusions (hematite - Hem). C. Inset displaying fluid inclusion sample map with assemblage number. D. sample s08 - photomicrograph of Qtz1a from Vms showing mapping of fluid inclusions. E. Inset displaying fluid inclusion sample map with assemblage number. F. Photomicrograph of beryl (sample Be01)

showing mapping of fluid inclusion types. FIA – Fluid Inclusion Assemblage.



Vein type	Aqueous	Aqueous-carbonic
Vp1		●
Vp2	●	
Vpe	●	
Vmi	■	■
Vms	■	■
Vb		▲

Figure 18. Salinity (eq. wt. % NaCl) versus homogenization temperature (°C) data for fluid inclusion assemblages trapped in quartz (Vp1, Vp2, Vpe, Vmi and Vms veins) and beryl (Vb). Dashed lines represent fluid inclusion assemblages.

7.2. Fluid inclusions trapped in quartz from the Morro Escuro ridge

From the Morro Escuro ridge, vein samples from itabirite (40% Fe) and quartz schist were chosen for microthermometry and LA-ICP-MS analyses (Table 2).

7.2.1. Fluid inclusions types and assemblages

7.2.1.1. Vmi veins

The Qtz1a crystals from the quartz vein in the itabirite (Vmi) host fluid inclusion assemblages that form three-dimensional clusters and internal trails. They are interpreted as pseudosecondary because of the confinement of the cluster/trails to individual crystals according to criteria proposed by Roedder (1984) (Fig. 17b). No FIs are observed in recrystallized quartz crystals. Secondary trails of inclusions are also observed, but are not considered here for data interpretation due to their unclear relationship with the mineralization process.

Table 4

Summary of LA-ICP-MS analysis on fluid inclusion. Element/Na weight ratios and element concentrations in ppm, calculated using the salinity of the fluid inclusions. RSD (relative standard deviation). sd (standard deviation). bdl (below detection limit).

Vp1				Vp2				Vpe							
Ratio (mean)	RSD	ppm (mean)	sd	n	Ratio (mean)	RSD	ppm (mean)	sd	n	Ratio (mean)	RSD	ppm (mean)	sd	n	
Na	1	0	44,730	21,202	36	1	0	7641	6054	73	1	0	6745	2352	33
K	0.483	43	9731	9851	22	1.44	48	6060	6931	50	0.676	47	3159	2026	28
Ca	0.514	47	12,136	9660	27	0.438	48	2134	2217	58	0.364	53	1479	1099	25
Mg	0.108	66	1841	2813	17	0.223	86	1066	1695	47	0.224	81	1049	1107	26
Mn	0.015	76	84	277	6	0.025	164	30	83	20	0.027	41	28	79	6
Fe	0.332	81	2731	5296	11	0.418	69	1852	2320	49	0.215	72	759	827	22
Cu	0.255	57	4770	4881	22	0.086	85	226	294	45	0.140	51	561	554	22
Zn	0.105	64	2060	2191	23	0.048	116	151	139	55	0.146	71	876	665	33
Sr	0.002	51	87	63	33	0.002	75	14	19	59	0.002	61	14	11	32
Ag	0.001	84	11	23	11	0.0003	126	0.277	10.36	9	0.0008	91	.84	2.05	8
Ba	0.011	77	298	332	27	0.004	79	14	22	46	0.006	66	35	28	29
Pb	0.02	66	462	508	24	0.004	72	13	16	45	0.008	72	29	40	19
Li	0.049	55	537	1062	10	< LOD					0.02	54	24	79	5
Vmi															
Vms															
Ratio (mean)	RSD	ppm (mean)	sd	n	Ratio (mean)	RSD	ppm (mean)	sd	n	Ratio (mean)	RSD	ppm (mean)	sd	n	
Na	1	0	27,107	12,492	27	1	0	26,121	7525	36					
K	2.17	47	45,437	15,231	27	1.91	25	43,603	14,465	35					
Ca	0.444	54	8215	4634	25	0.440	38	9636	4717	33					
Mg	0.111	47	1979	1860	22	0.293	78	4124	4871	24					
Mn	0.004	83	21	51	8	0.002	86	13	32	10					
Fe	0.155	53	4039	4020	25	0.057	63	1370	1110	33					
Cu	0.020	43	261	335	17	0.021	47	386	338	27					
Zn	0.009	40	159	212	19	0.018	62	458	287	36					
Sr	0.001	44	34	31	23	0.001	51	38	22	34					
Ag	0.0002	83	1.57	3.8	8	0.0002	128	0.77	4.24	4					
Ba	0.003	56	24	51	10	0.0008	55	13	15	23					
Pb	0.001	48	20	20	17	0.003	61	98	74	35					
Li	< LOD					0.025	149	59	328	4					

According to the number, nature, and volume proportions of phases present at room temperature, two types of fluid inclusion are classified in these Qtz1a crystals: Type 1 two-phase (L-V) aqueous; and type 2 four-phase (L-L-V-S) aqueous-carbonic with aqueous-saline phase, liquid CO₂, vapor and solid phases (daughter crystals). Type 1 FIs have a high liquid/vapor ratio (average 85% liquid, 15% vapor) and form irregularly shaped to rounded inclusions in separate assemblages (FIA 24 – Table 3). Type 2 FIs have highly variable H₂O/CO₂ ratio (volume fraction of CO₂ varies from 30 to 80 vol. %), average size between 35-45 µm, and are irregularly shaped to rounded inclusions. Type 2 inclusions locally display a negative crystal shape.

7.2.1.2. Vms veins

The Qtz1a crystals from the quartz vein in the quartz schist (Vms) host fluid inclusions assemblages that form three-dimensional clusters and internal trails. They are interpreted as pseudosecondary because of the confinement of the cluster/trails to individual crystal according to criteria by Roedder (1984) (Fig. 17d). Secondary trails of inclusions are also observed, but are not considered here for data interpretation due to their unclear relationship with the mineralization process. Three types of FIs are defined in Vms veins (Table 2): Type 1 two-phase (L-V) aqueous; type 2 four-phase (L-L-V-S) aqueous-carbonic with aqueous-saline phase, liquid CO₂, vapor and solid phases (daughter crystals), and type 3 three-phase, (L-L-V) aqueous-carbonic with aqueous-saline phase, liquid CO₂, and vapor.

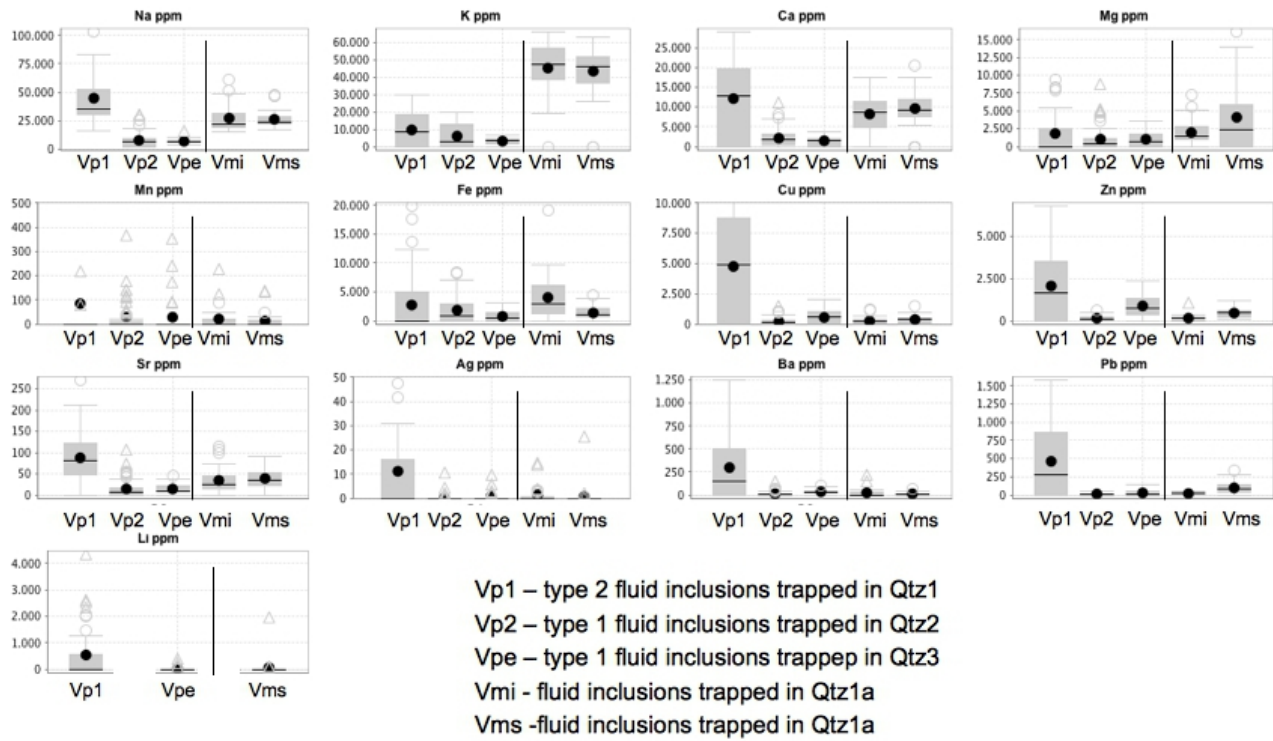


Figure 19. Diagrams showing metal concentrations (ppm) obtained from LA-ICP-MS analyses on individual fluid inclusions. The shaded box is the 25th and 75th percentiles, with the median value (horizontal lines) and mean value (black circle). The lower and upper horizontal lines are the 5th and 95th percentiles; outliers are individual points.

7.2.2. Microthermometry

7.2.2.1. *Vmi* veins

Freezing experiments on aqueous (type 1 FIs) and CO₂-rich (type 2 FIs) assemblages demonstrate that the fluid inclusion assemblages have internally consistent eutectic temperatures (Te) that range from -38 to -45 °C, suggesting the presence of other cations besides Na. Melting temperatures of ice (Tmice) of one type 1 two-phase (L-V) aqueous fluid assemblage have a maximum Tmice of -1.8 °C that vary by 0.6 °C. This type 1 inclusion assemblage homogenizes by the disappearance of vapor bubbles at 145 °C (Table 3). This data represents a minimum trapping temperature since no boiling evidence was observed.

Melting temperatures of clathrate (Tclath) of four CO₂-rich fluid inclusion assemblages define a maximum ranging from 7.6 to 8.2 °C (Table 3). Within fluid assemblages Tclath determinations vary by 3 °C. All the measured melting temperatures of CO₂(s) (TmCO₂) are coincident at -56.6 and °C, suggesting that CO₂ is the most abundant gas species. The bulk CO₂ fraction (XCO₂) varies from 0.03 to 0.3, and the CO₂-rich phase homogenize (ThCO₂) from 22.4 to 32 °C. These type 2 inclusion assemblages homogenize by the disappearance of liquid-(CO₂) over a wide range of temperatures, from 290 to 340 °C, and ThTot values for individual fluid inclusion assemblages vary by 20 °C (Table 3). Inclusions with the higher content of CO₂ (XCO₂) present the highest ThTot. These ThTot data represent a minimum trapping temperature since no boiling evidence was observed. The dissolution temperatures of the solid phases are between 20 and 30 °C for sylvite crystals and between 35 and 58 °C for halite crystals. The salinity values display small variations between 26.6 to 26.9 wt. % NaCl equiv. (Fig. 18), and were calculated based on halite dissolution temperature (Tmhal).

7.2.2.2. *Vms* veins

Freezing experiments demonstrate that the 26 fluid inclusion assemblages have internally consistent eutectic temperatures (Te) that range from -38° to -45 °C, suggesting the presence of other cations besides Na. Melting temperatures of ice (Tmice) are variable and define a maximum Tmice ranging from -2.5 to -11 °C. Individual fluid assemblages have Tmice determinations that vary by 1 °C. These type 1 inclusion assemblages homogenize by the disappearance of vapor bubbles over a low range of temperatures, from 130 to 140 °C. These ThTot data represent a minimum trapping temperature since no boiling evidence is observed.

Melting temperatures of clathrate (Tclath) of five CO₂-rich fluid inclusion assemblages define a maximum ranging from 5.0 to 9.3 °C (Table 3). Within fluid assemblages Tclath determinations vary by 2 °C. All the measured melting temperatures of CO₂(s) (TmCO₂) are coincident at -56.6 and °C, suggesting that CO₂ is the most abundant gas species. The CO₂-rich phase homogenizes (ThCO₂) over a wide range of temperatures from 15 to 31 °C. These types 2 and 3 inclusion assemblages homogenize by the disappearance of liquid-(CO₂) over a low range of temperatures, from 220 to 250 °C, and ThTot values for individual fluid inclusion assemblages vary by 10 °C (Table 3). The solid phases in type 2 FIs (sylvite and halite) have similar dissolution temperatures as type 2 FIs of the Vmi veins. The salinity of type 2 FIs was calculated based on halite dissolution temperature (Tmhal), and the salinity of type 3 FIs based on clathrate melting (Tclath).

7.2.3. Quantitative estimation of fluid inclusion composition - LA-ICP-MS

Analytical results for inclusions from Vmi and Vms veins show that K, Na, Ca, Fe and Mg are the dominant components (Table 4). Only type 2 four-phase (L-L-V-S), aqueous-carbonic inclusion assemblages were analyzed in Qtz1a from Vmi and Vms veins. Both Vmi and Vms veins show K as the main cation component, and similar values of Na and Ca concentrations. Relative to Vms, FIs trapped in Qtz1a from Vmi has higher concentration of Fe, and lower concentration of Mg and Zn. The bivariate diagrams (Fig. 21), show good correlation between Ca versus Sr, Cu versus Zn and Ca versus K. Compared to the PLD, FIs data from ME veins shows small variations in the ternary diagrams Fe-K-Ca and Fe-K-Mg, and the relation between the main components K and Na is inverted; K>Na at ME and Na>K at PLD (Figs. 19 and 21). The same trend in the Fe-Cu-Zn diagram is observed in both PLD and ME.

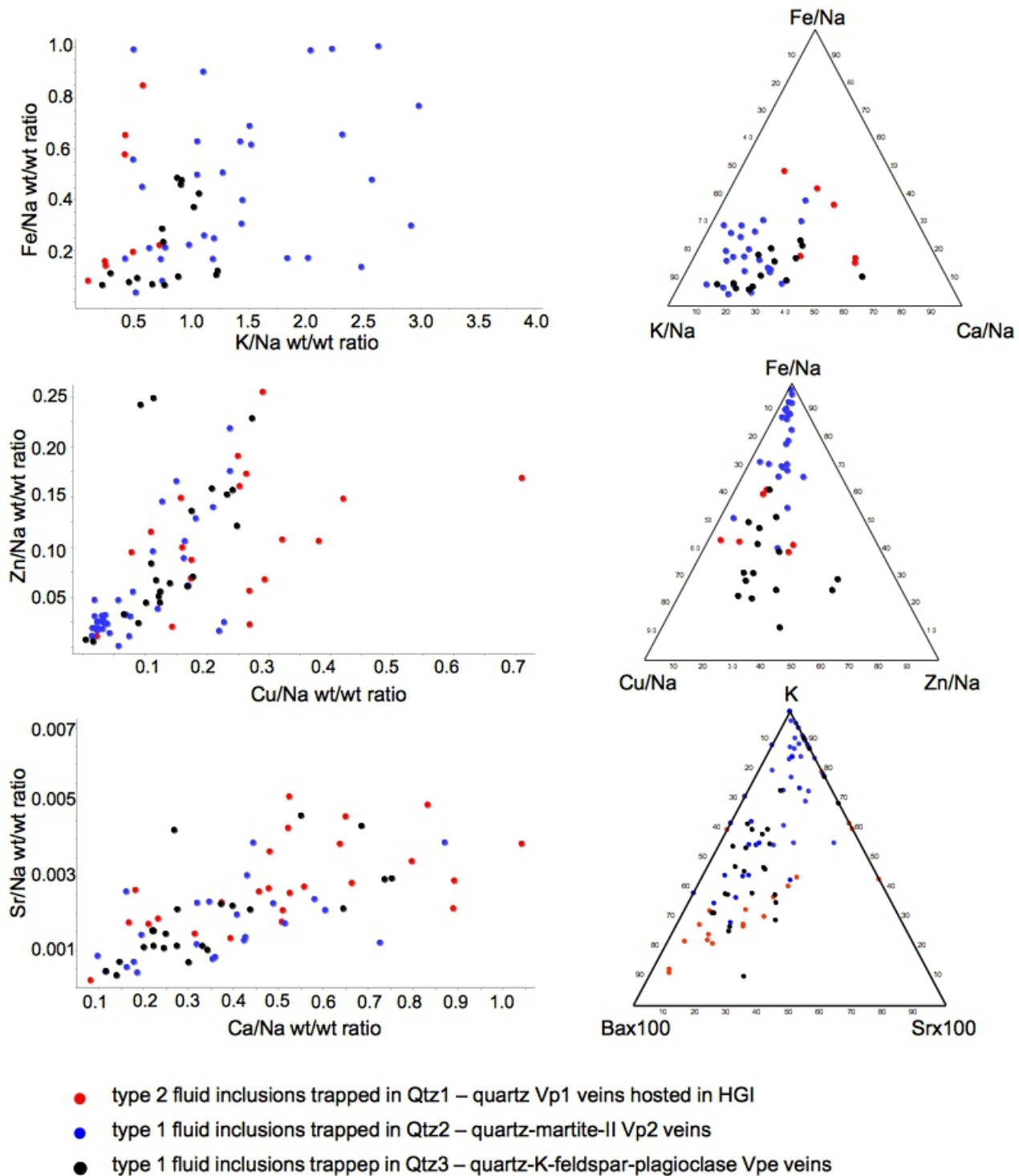


Figure 20. Bivariate and ternary plots of LA-ICP-MS element ratios (alkali and alkaline earths and transition metals) of individual fluid inclusions trapped in quartz from Vp1, Vp2, and Vpe veins at Piçarrão-Liberdade deposit.

7.3. Fluid inclusions trapped in beryl from the Ponte da Raiz pegmatite

7.3.1. Fluid inclusions types and assemblages

Fluid inclusions were studied in two beryl samples, Be1 and Be2, both from the Ponte da Raiz pegmatite (Table 2). Beryl-(Be1) is green and contains abundant fluid inclusion. Three types of inclusions are described, all with the same composition at room temperature – aqueous-carbonic, four-phase (L-L-V-S) with aqueous-saline phase, liquid CO₂, vapor and halite daughter crystals. Halite daughter crystals were identified by dissolution temperature and square shape. However, these three types present distinct shapes and orientation with respect to the beryl crystallographic axes (Fig. 17f): Type 2a FIs show tubular shape and is interpreted to be primary because they are always oriented parallel to some of the crystallographic axes. Type 1 is the most abundant in number and volume. Type 2b FIs show tabular-rounded shape, are the largest (>50 µm), and are associated with pseudosecondary trails that do not cross the crystal boundaries. Type 2c FIs show square shape, are smaller than Type 2, and form pseudosecondary clusters inside the crystal. Beryl-(Be2) is light yellow and has rare FIs. Only Type 2c FIs are observed in Be2, but it was not possible to analyze them because they are necked.

7.3.2. Microthermometry

Eutectic temperatures (Te) estimation vary slightly from -24° to -26 °C for all inclusions assemblages on Be1, suggesting low concentrations of other cations besides Na. Freezing experiments on the CO₂-rich assemblages (types 1, 2 and 3) demonstrate that the 14 fluid inclusions analyzed have consistent melting temperatures of CO₂(s) (T_mCO₂) that range between -57.7 to -56.6 °C, suggesting that CO₂ is the most abundant gas species. The CO₂-rich phase homogenization temperature (ThCO₂) also varies slightly from 28.5 to 31.4 °C . Melting temperatures of clathrate (T_{clath}) are variable and define a range from 4.3 to 9.2 °C, although individual fluid assemblages have T_{clath} determinations that vary by 1.2 °C (table 3).

Inclusion assemblages homogenize by the disappearance of liquid-(CO₂) over a low range of temperatures, from 315 to 320 °C (Table 3). These ThTot data represent a minimum trapping temperature since no boiling evidence is observed. The salinity values display small variations between 28.7-29.2 wt. % equiv. NaCl and was calculated based on halite dissolution temperature (T_{mhal}).

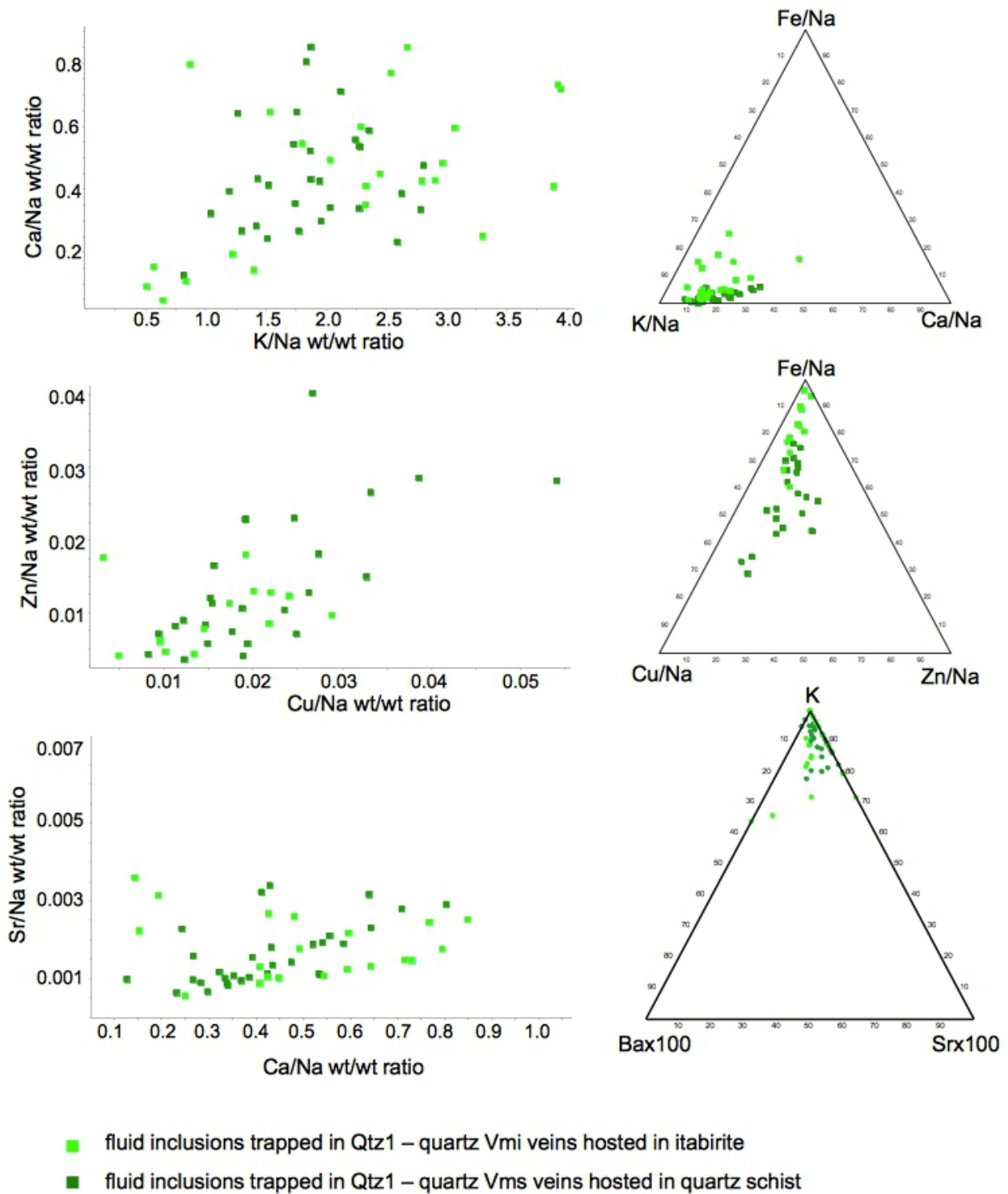


Figure 21. Bivariate and ternary plots of LA-ICP-MS element ratios (alkali and alkaline earths and transition metals) of individual fluid inclusions trapped in quartz from Vmi and Vms veins at Moro Escuro ridge.

8. Discussion

8.1. Least-altered itabirite features at Piçarrão-Liberdade, Morro Escuro and Guanhães areas

The itabirite samples (Appendix A) from each area are considered the least-altered rocks in the sequence of high-grade iron samples. Therefore, their chemistry and mineralogy are used to evaluate depositional environment features, and to compare chemical changes during itabirite iron upgrade. Metamorphic and hydrothermal alteration affected these rocks to some extent.

For example, the positive Ce_(sn) anomaly observed in PLD itabirite and some HGI samples (Fig. 9) is probably the result of hydrothermal alteration and does not reflect the redox conditions of the depositional environment. A similar Ce_(sn) anomaly, associated with the generation of REE-bearing minerals, was described by [Braga et al. \(2015\)](#) in ME itabirite. Itabirite alteration at PLD did not produce the strong Eu_(sn) anomaly observed in ME and GNH (Fig. 7), suggesting a different composition of the hydrothermal fluids between these areas and-or redox condition of the depositional environment. Even though only one itabirite was analyzed, the different depositional environment at PLD is also supported by the lack of clastic contamination, as shown by the Y/Ho ratio (Fig. 8). The evidence of clastic contamination (low Y/Ho; Fig. 8) and the lack of negative Ce_(sn) anomaly (Fig. 9) present in itabirite from GNH and ME areas suggest that these sediments precipitated on a shallow marine environment, with strong influence of continental input. Similar results were found in the previous studies of Morro Escuro and Guanhães itabirites ([Braga et al., 2015](#); [Barrote, 2016](#)).

8.2. Chemical changes during itabirite iron upgrade

The chemical changes between different iron oxide species in the paragenetic sequence can be interpreted with respect to different hypogene alteration and mineralization processes. The evolution of the trace elements and REE chemistry through the paragenetic sequence can be linked to specific ore forming processes. These processes include: (1) oxidation of magnetite to martite; (2) transformation of martite to hematite; (3) recrystallization of granoblastic to tabular hematite; (4) emplacement of quartz vein-hosted specular hematite; (5) emplacement of quartz vein-hosted martite-II.

8.2.1. Oxidation of magnetite (martitization)

Chemical changes during the transformation of magnetite to martite in high-grade orebodies at the PLD deposit is accompanied by the enrichment of Al, P and As in martite-I, and depletion in Mg, V, Cr, Mn, Co, Ni and Zn when compared to the kenomagnetite-I relicts (Fig. 10 and 4c). According to [Hensler et al. \(2015\)](#), the removal of Fe^{2+} and Mg (and other mobile elements) in magnetite may result in the relative enrichment of the less mobile elements in martite, in this case Al, P and As. A similar chemical change is observed in magnetite-martite alteration at GNH and DGN prospects and their relative enrichment of Ti, P, As and Mo (Fig. 13).

Kenomagnetite-I from compact HGI bodies at Me and GNH, which is not associated with martite and hematite, presents a higher content of Mg, suggesting that it has the closest composition of the original magnetite in the Guanhães Group.

At the PLD deposit REE are present in very low concentrations in both kenomagnetite-I (other than Ce) and martite-I. The positive Ce PAAS-normalized anomaly displayed by martite-I indicates an oxidizing fluid, due to the preferential precipitation of Ce when oxidized from Ce^{3+} to Ce^{4+} . The same REE pattern is observed in martite-I from itabirite at the Morro Escuro ridge and martite-I from high-grade orebodies at DGN, Ce anomaly and HREE enrichment (Fig. 11b-c).

[Bau \(1996\)](#) discuss the behaviour of Y/Ho in magmatic and aqueous systems and defines a primitive chondrite-like “CHARAC” (from Charge and Radius Control) signature characterized by $24 < \text{Y/Ho} < 34$ and a seawater-like signature by $44 < \text{Y/Ho} < 74$ (Fig. 22). The low Y/Ho ratios (< 34) detected in martite-I from Morro Escuro ridge and DGN suggest the role of hydrothermal fluids in the oxidation of magnetite to martite, resetting the itabirite – seawater-like - HREE signature. A positive PAAS-normalized Eu anomaly is documented for martite-I from Morro Escuro ridge and DGN (Fig. 22); corroborating the whole rock geochemical results of Morro Escuro ridge and DGN (Fig. 7).

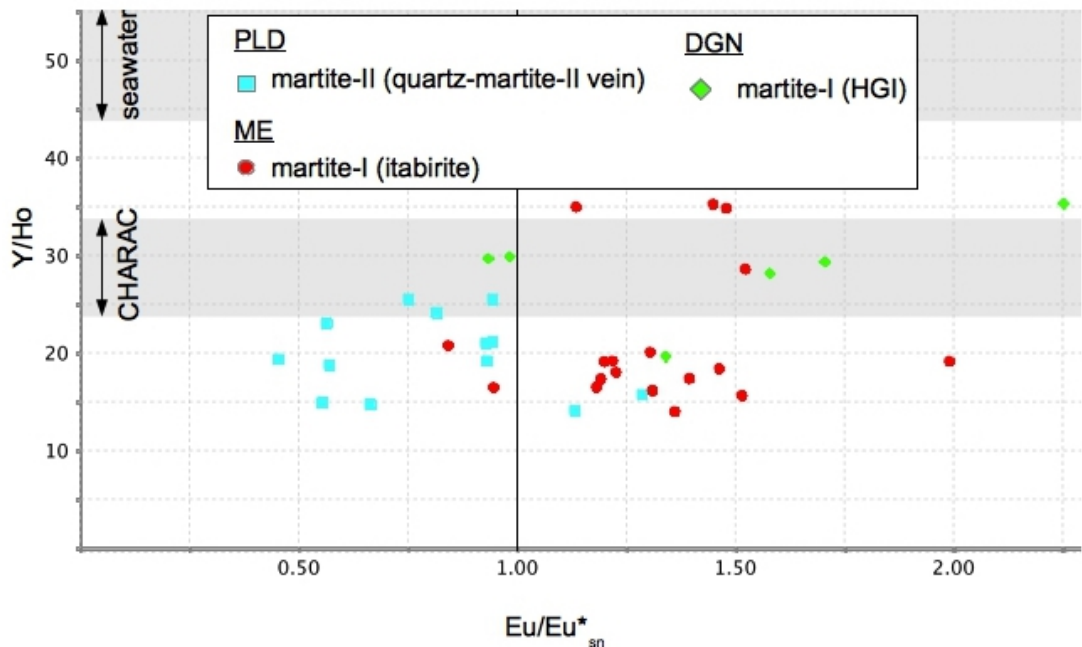


Figure 22. Binary plot illustrating Eu anomalies and the Y/Ho ratios derived from mineral LA-ICP-MS analyses. The Eu anomaly is calculated $\text{Eu}/\text{Eu}_{\text{sn}} = (\text{Eu}_{\text{PAAS}}/(0.5 \times \text{Sm}_{\text{PAAS}} + 0.5 \times \text{Gd}_{\text{PAAS}}))$. The shadowed areas define the behavior of Y/Ho ratios of modern seawater and the chondritic-like CHARAC field (Bau, 1996). (HGI: high-grade iron; PLD – Piçarrão-Liberdade; ME Morro Escuro; DGN Dores de Guanhães).

8.2.2. Transformation of martite to hematite in high-grade bodies

Granoblastic hematite recrystallized from martite-I from high-grade bodies at the PLD deposit is significantly enriched in Ti and Mo (and to a lesser extent Al, V and Cr); and depleted in Mg, Al, P, Mn, Co, Ni, Zn, Ga and As (Fig. 10). The REE are strongly depleted in hematite relative to martite-I (Fig. 11a). Tabular hematite recrystallized from kenomagnetite-I at Morro Escuro ridge is also enriched in Ti, Al, Cr and Mo, and depleted in Mn, Co, Ni and Zn (Fig. 12). Granoblastic hematite at the GNH prospect shows the same chemical changes when compared to kenomagnetite-I (Fig. 13).

According to Hensler et al. (2015) the exclusion of Mg and Mn during recrystallization of hematite is likely due to the poor compatibility of Mg^{2+} and Mn^{2+} in hematite in comparison to martite. Purtov and Kotel'nikova (1993) state that titanium is commonly regarded as immobile in aqueous solutions during metasomatic processes. In this case, the removal of the mobile elements result in the relative enrichment of the titanium; and others immobile elements such as Al, V, Cr and Mo (residual enrichment).

8.2.3. Recrystallization of granoblastic hematite to tabular hematite in high-grade iron bodies

The texture transformation of hematite (granoblastic to tabular) is related to the iron enrichment during the formation of the high-grade iron bodies. This transformation shows good inheritance of mineral chemistry, suggesting an isochemical process, a continuation of the recrystallization under similar physico-chemical conditions and fluid chemistry (martite - granoblastic hematite - tabular hematite; Figs. 10, 12, 13). The same pattern is observed in all three areas.

8.2.4. Formation of vein-hosted specular hematite at PLD and ME

Vein-hosted specular hematite and paragenetically older tabular hematite from the high-grade iron bodies share a similar depletion of trace elements; indeed all trace elements and REE are even more depleted in specular hematite (Figs. 10 and 12). This suggests that specular hematite was the last iron oxide to precipitate. The REE are more likely to have been concentrated in the earlier crystallizing hematite and the fluid was depleted in these elements during the crystallization of the last generation of hematite.

8.2.5. Formation of vein-hosted martite-II at PLD

Comparison of martite-II from quartz-martite-II veins (Vp2) with martite-I from high-grade bodies shows that martite-II is enriched in Mg, P, V, Mn, and REE, but strong depleted in As. However, compared to kenomagnetite-I from HGI, martite-II presents similar trace elements content but is relatively REE enriched (Figs. 10 and 11). The low Y/Ho ratios (<34) detected in martite-II (Fig. 22) suggest the role of hydrothermal fluids in the precipitation of the original magnetite, and this Y/Ho ratios is similar to the highly evolved granite-pegmatite systems described by [Bau \(1996\)](#). A negative PAAS-normalized Eu anomaly (Fig. 22) also suggests significant variation in redox-sensitive Eu during the formation of the Vp2 veins, when compared to the Eu anomaly of the itabirite and HGI (REE whole rock diagram, Fig. 7). Thus, precipitation of magnetite in the Vp2 veins probably occurred in a different physico-chemical context compared to the high-grade iron bodies.

8.3. Model for the paleo fluid system

The occurrence of fluid inclusions with different proportions of CO₂ and H₂O (variable XCO₂ and CO₂ Vol%), and different homogenization temperatures (Table 3) observed within type 2 fluid inclusion assemblages trapped in Qtz1 suggest that the cooling of a homogenous fluid ([Roedder, 1984](#); [Diamond, 1990](#)) was the major processes to explain these heterogeneous fluid chemistry and trapping conditions during Vp1 formation. On the other hand, trapping inclusions with different homogenization temperatures and salinity in Qtz2 and Qtz3 (Table 3; Fig. 18) suggests that Vp2 and Vpe veins were formed by trapping of two or more homogeneous fluids as a result of partial mixing ([Anderson et al., 1992](#)); probably representing mixing between low-temperature, low-salinity meteoric waters and higher-temperature, higher-salinity brines (the latter fluids are possibly related to anatexis). Although the Vp1 and Vpe have different total concentrations of NaCl equiv., they have comparable element ratios (specially Cu and Zn) determine by LA-ICP-MS (Figs. 18 and 20; Table 4). The similar element ratios between FIs trapped in Vp1 and Vpe is evidence of the contribution of anatetic fluids to the Vp1 veins. Indeed, fluid inclusions trapped in beryl crystals show similar fluid inclusion phases and phase ratios (aqueous-carbonic), and overlapping temperatures as FIs trapped in Qtz1 from Vp1 veins at the PLD deposit (Table 4; Fig. 19).

The results of the FIs studies suggest that the interaction of anatetic fluids with PLD itabirite during the metamorphic event of the Brasiliano orogen led to the silica leaching and iron enrichment of the itabirite, resulting in high-grade iron orebodies. Loss of silica bands in the itabirite coincided with the local crystallization of quartz-rich veins in some parts of these high-grade iron orebodies. Silica leaching and the transformation of magnetite to hematite are probably a contemporaneous processes, and as hematite is depleted in mobile trace element (Figs. 10, 12, 13; Appendix B), the fluids that formed Vp1 veins became trace element enriched. The high temperature, salinity and trace element enrichment of the FIs trapped in Vp1 veins (Figs. 18 and 19; table 4) suggest that these veins formed as a result of the removal of quartz-rich bands from the itabirite.

Concentrations of Fe in pseudosecondary fluid inclusions trapped in Qtz1 range from 2,731 to 19,775 ppm (Table 4). These results are similar to those found by [Figueiredo e Silva et al. \(2013\)](#) at Carajás iron ore deposits (82–17,507 ppm Fe) and by [Thorne et al. \(2014\)](#) at Paraburadoo 4E Deposit, Hamersley Province (2,349-27,796 ppm Fe).

The formation of the Vp2 veins probably occurred at a lower crustal level during the mixing of the Vp1 fluids with meteoric water, and the precipitation of magnetite (transformed to martite-II) which is enriched in trace elements (Figs. 10 and 11). The low concentration of trace elements in FIs from

the Vp2 veins (Fig. 19; Table 4) results from its precipitation during the crystallization of magnetite (martite-II). The low salinity and temperature of Vp2 FIs (Fig. 18), and the different redox environment for martite-II (Fig. 22) support this evolution. Also, the good correlation between trace elements ratios (Fig. 20) supports the cogenetic relation between the fluids trapped in Vp1, Vp2 and Vpe veins.

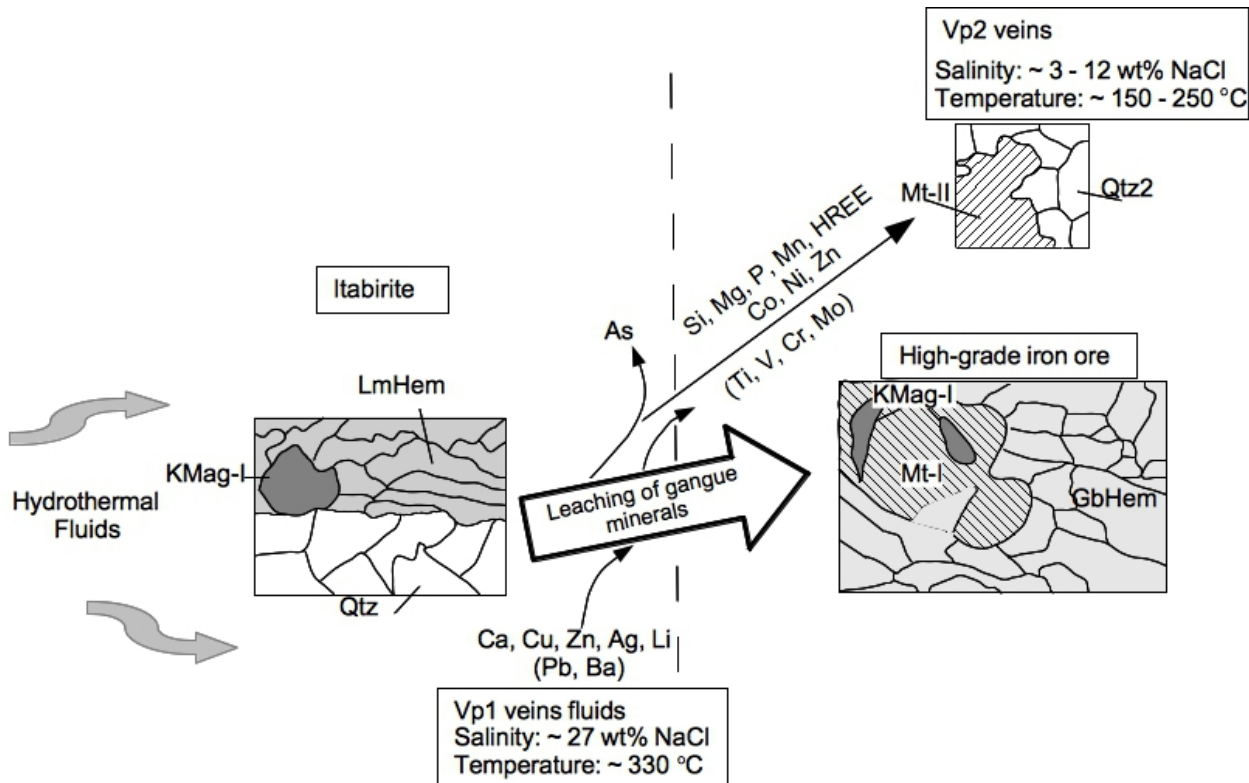


Figure 23. Schematic illustration showing the interaction of high salinity and temperature fluids during the leaching of gangue minerals (silica), and the formation of high-grade iron orebodies and Vp1 veins. The Vp2 veins present martite enriched in trace elements, and lower salinity and temperature fluids trapped in the Qtz2. Kmag: kenomagnetite; LmHem: lamellar hematite; Mt: martite. GbHem: granoblastic hematite; Qtz: quartz.

The Vmi and Vms veins at Morro Escuro ridge are related to the same event, since both present FIs with similar compositions and temperatures (Figs. 19 and 21). The metal content of FIs trapped in both Vmi and Vms veins is depleted when compared to the FIs composition trapped in Qtz1 from Vp1 veins with similar salinities and homogenization temperatures (Table 3 and 4; Figs. 19). This suggests that due to the lower silica leaching, Vmi was formed with depleted trace element content

as well as lower fluid/rock ratio at ME when compared to the PLD deposit. The good correlation between the major components of the fluids (Fig. 21), also supports the low fluid/rock ratios in the ME veins. The lack of high-grade iron orebodies at ME corroborate these conclusions.

9. Conclusions

According to the mineral chemistry of the iron oxides paragenesis, and the fluid inclusion studies in the pegmatite and quartz veins associated with the high-grade iron bodies of the PLD deposit, it is possible to conclude that:

1. In the Piçarrão-Liberdade deposit-PLD, the paragenetic sequence of the iron oxides show three major chemical trends: (i) oxidation of kenomagnetite to hematite is followed by depletion of Mg, Co and Ni; and enrichment of As and REE; (ii) recrystallization of granoblastic hematite is commonly accompanied by enrichment in immobile elements (Ti, Al, V, Cr and Mo) due to removing of mobile elements (Mg, Mn, and As); (iii) late-stage specular hematite has very low concentrations of most trace elements relative to paragenetically early-stage iron oxides, similar to previous analyses on shear vein-hosted specular hematite from another iron deposits ([Hensler et al., 2015](#); [Oliveira et al., 2015](#)).
2. The iron enrichment in the high-grade orebodies of the PLD deposit is related to the same anatetic event of the Borrachudos-hosted pegmatites; and could be explained by the following processes (Fig. 23): (i) Influx of anatetic fluids during the metamorphic event of the Brasiliano orogen and formation of the high-grade orebodies through silica leaching; (ii) Hematite crystallization in high-grade orebodies during silica and trace elements leaching and the formation of Vp1 veins; (iii) A second-stage of magnetite crystallization (martite-II) during the the lowering of the pressure and the formation of the Vp2 veins.

According to the whole rock geochemical analyses, itabirites from Morro Escuro ridge, Guanhães and Dores de Guanhães prospects show evidences of a shallow marine depositional environment and secondary hydrothermal alteration; while the itabirite and HGI orebodies from PLD show a different hydrothermal alteration evolution and depositional environment.

Acknowledgments

This paper contains results of the PhD thesis of the first author at the Universidade Federal de Minas Gerais-UFMG, Brazil, who received a scholarship from Coordenação de Aperfeiçoamento de Pessoal de Nível Superior — CAPES. The main research funds were provided by FAPEMIG (grant APQ-0117815), and a project with joint resources from the Brazil's National Council of Technological and Scientific Development — CNPq and Vale.

Appendix A. Chemical composition of the itabirite and high-grade samples. PLD: Piçarrão-Liberdade deposit; ME: Morro Escuro ridge; GNH: Guanhães prospect; DGN: Dores de Guanhães prospect; HGI: high-grade iron; LOI: loss on ignition; LOD: limit of detection; bdl: below detection limit; sd: standard deviation.

Sample Area/ deposit	LOD	ME2B	PB2A	GU1	LI3SUL	LI1	LI4SUL	L1S4E	LI7A	PB1A	ME2A	PB3A	PB4A	GB	DG2	GI3
Rock type wt%		Itabirite	Itabirite	Itabirite	Itabirite	Compact HGI	Banded HGI	Foliated HGI	Compact HGI	Compact HGI	Banded HGI	Foliated HGI	Compact HGI	Banded HGI	Foliat ed HGI	
SiO ₂	0.01	42.02	45.52	44.86	45.71	1.3	0.82	0.22	3.93	0.23	0.8	19.66	0.21	0.29	0.31	0.53
Al ₂ O ₃	0.01	0.26	0.14	0.17	0.23	0.79	0.47	0.39	0.31	0.44	0.52	0.51	1.29	0.5	1.24	0.17
Fe ₂ O ₃ (Total)	0.01	56.07	55.1	53.54	52.94	98.78	96.1	99.67	95.31	96.3	96.89	77.84	99.18	95.63	97.98	97.85
MgO	0.01	0.02	0.02	0.07	0.01	0.1	0.19	0.04	0.03	3.55	0.04	0.03	0.03	3.81	0.03	0.02
CaO	0.01	bdl	bdl	bdl	bdl	bdl	bdl	bdl	bdl	bdl	bdl	bdl	bdl	0.13	bdl	bdl
Na ₂ O	0.01	bdl	bdl	bdl	bdl	bdl	bdl	bdl	bdl	bdl	bdl	bdl	bdl	bdl	bdl	0.01
K ₂ O	0.01	bdl	bdl	bdl	bdl	bdl	bdl	bdl	bdl	bdl	bdl	bdl	bdl	bdl	0.01	bdl
TiO ₂	0.01	0.008	0.01	0.006	0.008	0.044	0.015	0.023	0.009	0.021	0.032	0.01	0.066	0.022	0.063	bdl
MnO	0.01	0.035	0.12	0.032	0.015	0.084	0.033	0.019	0.086	0.413	0.112	0.017	0.015	0.436	0.017	0.018
P ₂ O ₅	0.01	0.03	0.03	0.01	bdl	0.05	0.17	0.02	bdl	0.06	0.24	0.13	0.11	0.03	0.09	0.01
Sum	0.01	98.48	100.9	98.67	100.6	100.7	98.49	100.4	99.32	98.62	98.76	100.3	100.9	98.34	100.7	100.7
LOI	0.06	0	0	1.69	0	0.71	0.05	0	0	0.1	2.11	0.04	0	0.95	2.1	
FeO	0.1	0.9	1	1	1.6	12.8	6.3	1.2	4.2	6.5	9.5	0.9	0.8	20.7	1.8	2.2
Fe ₂ O ₃ ppm	0.01	55.07	53.99	52.43	51.16	84.54	89.1	98.34	90.64	89.07	86.33	76.84	98.07	72.61	95.98	95.4
La	0.05	2.53	1.21	1.77	2.25	0.81	11.6	2.7	0.53	4.18	1.64	1.57	4.29	1.11	5.33	0.51
Ce	0.05	8.02	2.94	3.1	15.2	3.01	15.3	46	1.83	3.31	3.21	2.42	8.29	1.28	10.4	0.78
Pr	0.01	0.59	0.4	0.37	0.34	0.17	3.1	0.5	0.08	0.79	0.32	0.26	1.1	0.16	1.3	0.05

Appendix A (cont.)

Nd	0.05	2.25	2.66	1.6	1.24	0.63	10.9	2.2	0.3	2.59	1.41	0.89	4.58	0.55	5.6	0.19
Sm	0.01	0.45	1.17	0.35	0.2	0.15	1.98	0.53	0.11	0.44	0.27	0.17	1.05	0.12	1.41	0.04
Eu	0.005	0.138	0.348	0.13	0.052	0.062	0.373	0.179	0.041	0.182	0.114	0.063	0.351	0.044	0.354	0.038
Gd	0.01	0.49	1.4	0.34	0.36	0.33	1.49	0.71	0.43	0.33	0.31	0.19	1.64	0.1	1.69	0.11
Tb	0.01	0.08	0.23	0.06	0.07	0.07	0.21	0.13	0.09	0.06	0.05	0.03	0.37	0.01	0.33	0.02
Dy	0.01	0.47	1.11	0.38	0.45	0.44	1.04	0.81	0.57	0.3	0.32	0.21	2.93	0.08	2.21	0.14
Ho	0.01	0.09	0.18	0.08	0.1	0.09	0.19	0.16	0.12	0.05	0.08	0.05	0.69	0.02	0.51	0.03
Er	0.01	0.25	0.48	0.23	0.34	0.32	0.47	0.51	0.35	0.15	0.23	0.18	2.32	0.05	1.64	0.11
Tm	0.005	0.03	0.067	0.042	0.054	0.064	0.067	0.08	0.055	0.021	0.033	0.035	0.374	0.012	0.273	0.016
Yb	0.01	0.15	0.4	0.28	0.35	0.47	0.44	0.51	0.36	0.15	0.19	0.26	2.28	0.09	1.79	0.11
Lu	0.002	0.016	0.06	0.039	0.042	0.066	0.067	0.08	0.052	0.026	0.027	0.043	0.303	0.013	0.241	0.018
							15.55									
Σ REE		4	12.655	8.771	21.048	6.682	47.227	55.099	4.918	12.579	8.204	6.371	30.568	3.639	33.078	2.162
As	0.1	3.2	2.3	0.5	bdl	1.9	1.7	0.2	3.4	5.6	3.8	1.5	1	2.1	1.4	21.8
Co	0.1	0.8	2.9	0.7	0.5	3.4	7.1	1.6	1.1	4.8	4.9	0.7	0.2	5.3	0.3	0.7
Cr	0.5	58	38.5	40.1	24.9	37.5	48.3	101	40.5	19.3	25	80.4	74.2	19.2	109	19.2
Cu	0.2	2.2	2.8	3.9	7.1	6.4	23.7	4.8	13.3	3.8	13.8	11	2.4	5.9	2.7	7.4
Hg (ppb)	10	bdl	bdl	bdl	40	210	270	130	60	bdl	bdl	20	bdl	bdl	bdl	350
Ni	0.5	4.4	4.1	3.6	2.7	7.9	7.2	4	5.2	7.9	10.7	2.4	2.1	7.6	2.7	4.1
Pb	0.5	41.3	0.9	0.6	0.6	4.6	8.5	2.5	1.7	4	2.1	9.2	5.2	2.8	4.1	1.3
Sr	0.2	2.1	7.6	1.3	0.9	0.9	6.8	1.3	0.9	2.4	21.7	1.4	24	1.3	19.8	1.1
Th	0.05	0.47	0.21	0.08	0.31	0.25	0.22	0.36	bdl	0.48	0.09	0.29	0.33	0.19	0.24	bdl
U	0.01	0.83	0.86	1.15	0.24	1.92	3.59	2.02	0.75	3.63	2.99	1.77	1.77	2.11	1.56	0.17
V	5	34	45	88	37	79	56	116	66	68	89	27	94	64	97	12
W	0.5	23.8	4.2	2	6.8	2.8	4	12.4	5.8	13.7	6.4	4.6	3.6	9.4	4	2.8
Y	0.5	2.4	6	2.4	4	2.7	4.9	5.5	4.8	1.5	2.8	2.4	22.5	0.6	16	1.2

Appendix A (cont.)

Ce/Ce*													
(sn)	1.51	0.96	0.88	3.92	1.87	0.59	9.08	2.00	0.42	1.02	0.86	0.88	0.68
Eu/Eu*													
(sn)	1.44	1.34	1.77	0.89	1.19	1.05	1.38	0.73	2.14	1.95	1.75	1.14	2.17
Eu/Eu*													
(cn)	0.96	0.89	1.22	0.63	0.88	0.69	0.96	0.54	1.51	1.29	1.15	0.87	1.29
Pr/Yb													
(sn)	1.26	0.32	0.42	0.31	0.12	2.25	0.31	0.07	1.68	0.54	0.32	0.15	0.57
Ce/Ce*(sn)=Ce(sn)/(0.5Pr(sn) + 0.5La(sn)); Eu/Eu*(sn)=Eu(sn)/(0.67Sm(sn) + 0.33Tb(sn)); Eu/Eu*(cn) = Eu(cn)/(0.5Sm(cn) +0.5Gd(cn)). sn: PAAS													
normalized (McLennan, 1989); cn: chondrite normalized (Taylor and McLennan, 1985).													

Appendix B1. iron oxide compositions determined by LA-ICP-MS at Piçarrão-Liberdade deposit. HGI: High-grade iron bodies. sd: standard deviation.

	kenomagnetite-I (itabirite)			lamellar hematite (itabirite)			kenomagnetite-I (HGI)			Martite-I (HGI)			Hematite granoblastic (HGI)		
	ppm (mean)	sd	n	ppm (mean)	sd	n	ppm (mean)	sd	n	ppm (mean)	sd	n	ppm (mean)	sd	n
Mg	2.54	0.681	9	2.47	0.34	2	697	322	21	58	96	31	1.99	1.07	26
Al	1171	30.02	18	1139	4.23	4	743	148	21	1119	154	31	819	473	26
P	<LOD	0		<LOD	0		9.58	0	1	73	33	31	18	15	4
Ti	95.49	8.50	18	93	5.03	4	11	18	21	1.45	1.34	17	81	46	26
V	33.35	0.65	18	33	0.48	4	55	20	21	11	9.94	31	39	3.62	26
Cr	6.24	2.33	18	3.84	0.33	4	15	3.3	21	5.95	5.26	31	29	36	26
Mn	3.24	0.57	5	3.34	0.61	3	815	568	21	433	831	31	9	4.40	26
Co	0.04	0.002	2	0.04	0.001	2	2.4	0.46	21	0.71	0.97	31	0.02	0.004	12
Ni	0.19	0.31	4	0.20	0	1	5.44	1.56	21	1.77	2.67	31	0.08	0.01	6
Zn	<LOD	0		<LOD	0		9.92	14	17	3.56	6.7	31	0.15	0.05	6
Ga	0.38	0.084	18	0.35	0.15	4	1.5	1.32	21	1.44	1.34	31	0.57	0.3	26
As	0.43	0.12	12	0.34	0	1	0.3	0.05	5	35	14	31	0.51	0.16	22
Mo	1.73	0.155	18	1.66	0.13	4	0.25	0.12	20	0.35	0.07	31	3.69	1.15	26
Ce	0.016	0	1	<LOD	0		0.01	0.006	3	1.08	1.07	31	0.07	0.09	8

Appendix B1 (cont.)

Hematite tabular (HGI)			Hematite Specular (shear vein)			Martite-II (Vp2 veins)			
	ppm (mean)	sd	n	ppm (mean)	sd	n	ppm (mean)	sd	n
Mg	1.81	0.49	18	0.61	0.24	12	625	46	15
Al	1489	76	18	399	142	13	861	43	15
P	<LOD	0		<LOD	0		156	29	15
Ti	46	22	18	<LOD	0		5.14	1.29	15
V	78	7	18	6	3.75	13	40	1.37	15
Cr	15	6	18	0.75	0.2	6	10	2.83	15
Mn	3.98	0.83	18	1.17	0.29	2	1004	17	15
Co	0.02	0	1	<LOD	0		0.83	0.09	15
Ni	<LOD	0		<LOD	0		1.08	0.18	15
Zn	0.15	0.044	8	0.13	0.01	3	3.33	1.66	15
Ga	1.82	0.15	18	0.58	0.16	13	0.81	0.11	15
As	0.72	0.48	18	0.57	0.42	9	0.65	0.19	14
Mo	15	1.04	18	0.36	0.31	8	0.83	0.19	15
Ce	0.03	0.022	2	<LOD	0		2.21	0.49	15

Appendix B2. iron oxide compositions determined by LA-ICP-MS at Morro Escuro ridge. HGI: High-grade iron bodies. sd: standard deviation.

	Martite-I (itabirite)			Lamelar Hematite (itabirite)			kenomagnetite-I (HGI)			Hematite tabular (HGI)			kenomagnetite-I (compact HGI)		
	ppm (mean)	sd	n	ppm (mean)	sd	n	ppm (mean)	sd	n	ppm (mean)	sd	n	ppm (mean)	sd	n
Mg	56	21	18	1.61	0.68	25	26	2.06	4	21	23	17	24679	735	9
Al	845	295	18	776	79	25	66	25	4	3694	1294	17	1359	276	9
P	564	93	18	12	0	1	37	0	1	14	0	1	<LOD		0
Ti	3.91	0	1	142	78	25	1.21	0.33	4	1967	2979	17	117	3	9
V	33	9.21	18	29	6.51	25	94	1	4	99	34	17	75	0.68	9
Cr	6.72	1.99	18	14	8.56	25	3.5	0.53	4	17	15	17	9	2.76	9
Mn	17831	7588	18	37	13	25	1106	20	4	11	9	17	3627	68	9
Co	31	18	18	0.07	0.11	17	4.4	0.08	4	0.06	0.03	12	5	0.11	9
Ni	164	154	18	0.45	0.77	17	11	0.45	4	0.23	0.12	6	7	0.2	9
Zn	129	75	18	0.28	0.22	18	129	6	4	0.86	0.66	8	7	1.95	9
Ga	4.83	1.78	18	0.98	0.18	25	3.44	0.1	4	4.26	2.28	17	2.14	0.1	9
As	15	4.13	18	0.50	0.22	14	0.54	0.1	4	0.44	0.1	2	1.3	0.31	3
Mo	1.2	0.63	18	0.60	0.71	25	<LOD		0	1.45	0.39	17	0.09	0.03	9
Ce	3.4	1.2	18	0.04	0.04	2	0.03	0.005	3	<LOD		0	0.13	0.17	2

Appendix B2 (cont.)

ME Hematite Specular
(shear veins)

	ppm (mean)	sd	n
Mg	0.31	0.14	12
Al	696	95	12
P	9	0	1
Ti	42	3.66	12
V	37	2.18	12
Cr	1.4	0.22	12
Mn	15	3.41	12
Co	0.01	0.0007	2
Ni	0.11	0.03	2
Zn	0.13	0.03	6
Ga	0.99	0.1	12
As	0.44	0.15	6
Mo	0.43	0.1	12
Ce	0.01	0	1

Appendix B3. iron oxide compositions determined by LA-ICP-MS. GNH: Guanhães prospect. GDN: Dores de Guanhães prospect. HGI: High-grade iron bodies. sd: standard deviation.

	kenomagnetite-I (HGI) (GNH)			Martite-I (HGI) (DGN)			Hematite granoblastic (HGI) (GNH)			kenomagnetite-I (compact HGI) (GNH)			Hematite granoblastic (HGI) (DGN)		
	ppm (mean)	sd	n	ppm (mean)	sd	n	ppm (mean)	sd	n	ppm (mean)	sd	n	ppm (mean)	sd	n
Mg	38545	771	32	908	122	20	402	136	29	25231	791	31	8.23	2.5	36
Al	1838	894	32	3750	814	20	4013	610	29	1425	566	31	6513	292	36
P	16	0	1	1106	693	20	9.08	0	1	<LOD	0	57	64	2	
Ti	19	4.52	32	2987	266	20	2635	893	29	108	12	31	323	19	36
V	56	0.93	32	344	16	20	112	27	29	73	1.21	31	94	2.5	36
Cr	32	5	32	226	231	20	21	6.9	29	5.5	1.16	31	99	34	36
Mn	4215	121	32	3863	219	20	30	6.1	29	3637	91	31	9.43	3.2	36
Co	29	0.7	32	7.67	0.39	20	0.18	0.06	28	5.14	0.12	31	0.04	0.01	26
Ni	68	1.73	32	38	1.77	20	0.25	0.08	29	7	0.30	31	0.15	0.04	21
Zn	8	5.88	32	29	20	20	0.24	0.07	20	8	5	31	0.25	0.25	13
Ga	7	0.86	32	8	1.21	20	1.84	0.26	29	2.15	0.2	31	7.33	0.32	36
As	0.35	0.12	16	2.91	0.95	20	0.44	0.08	11	0.51	0.16	22	0.67	0.21	33
Mo	0.07	0.008	4	9	0.74	20	2.09	1.79	29	0.15	0.07	17	1.83	0.17	36
Ce	0.12	0.19	3	0.49	0.36	20	0.02	0.005	4	0.06	0.1	5	0.02	0	1

References

- AngloAmerican, 2014. Anglo American delivers first ore on ship from Minas Rio. <http://www.angloamerican.com/media/press-releases/2014/27-10-2014>. (accessed oct-2017).
- Alkmim, F.F. and Marshak, S., 1998. Transamazonian orogeny in the southern São Francisco craton region, Minas Gerais Brazil: evidence for Paleoproterozoic collision and collapse in the Quadrilátero Ferrífero. *Precambrian Res.*, 90, 29–58.
- Alkmim, F.F., Marshak, S., Pedrosa-Soares, A.C., Peres, G.G., Cruz, S.C.P., Whittington, A., 2006. Kinematic evolution of the Araçuaí-West Congo Orogen in Brazil and Africa: nutcracker tectonics during the neoproterozoic assembly of Gondwana. *Precambrian Res.*, 149, 43-64.
- Allan, M.M., Yardley, B.W.D., Forbes, L.J., Shmulovich, K.I., Banks, D.A., Shepherd, T.J., 2005. Validation of LA-ICP-MS fluid inclusion analysis with synthetic fluid inclusions. *Am Mineral.* 90, 1767-1775.
- Almeida-Abreu, P.A., Renger, F.E., 2002. Serra do Espinhaço Meridional: Um Orógeno de Colisão do Mesoproterozóico, *Revista Brasileira de Geociências*; 32(1), 1-14.
- Almeida, F.F.M. 1977. O Cráton do São Francisco. *Revista Brasileira de Geociências*, 7, 349-364.
- Almeida, F.F.M., Brito Neves, B.B., Carneiro, C.D.R., 2000. The origin and evolution of the South American Platform. *Earth-Science Rev.* 50, 77-111.
- Anderson, M.R., Rankin, A.H., and Spiro, B., 1992, Fluid mixing in the generation of mesothermal gold mineralisation in the Transvaal Sequence, Transvaal, South Africa. *European Journal of Mineralogy.* 4, 933–948.
- Barrote, V.R., 2016. A sequência portadora de formações ferríferas de Guanhães, Minas Gerais, Brasil. Dissertação (Mestrado). Belo Horizonte. Instituto de Geociências da UFMG, p.103.
- Barbosa, J.S.F. and Sabate, P., 2004. Archean and Paleoproterozoic crust of the São Francisco Craton, Bahia Brazil: geodynamic features. *Precamb. Res.* 133, 1–27.

Bau M., Alexander, B., 2009. Distribution of high field strength elements (Y, Zr, REE, Hf, Ta, Th, U) in adjacent magnetite and chert bands and in reference standards FeR-3 and FeR-4 from the Temagami iron-formation, Canada, and the redox level of the Neoarchean ocean. *Precambrian Research*. 174, 337-346.

Bau, M., 1996. Controls on the fractionation of isovalent trace elements in magmatic and aqueous systems: evidence from Y/Ho, Zr/Hf, and lanthanide tetrad effect. *Contrib. Mineral. Petrol.* 123, 323–333.

Bau, M., Dulski, P., 1996. Distribution of yttrium and rare-earth elements in the Penge and Kuruman Iron-Formations, Transvaal Supergroup, South Africa. *Precambrian Res.* 79, 37-55.

Beukes, N.J., Gutzmer, J., 2008. Origin and paleoenvironmental significance of major iron formations at the Archean–Paleoproterozoic boundary. *Rev. Econ. Geol.* 15, 5–47.

Bilal E., Marciano V.R.P.R.O., Fuzikawa K., Correia Neves J.M., Giret, A., 1995. Datação de monazitas do Distrito Pegmatítico de Santa Maria de Itabira, MG. In: SBG/ Núcleo MG, Simp. Geol. Minas Gerais, 8, Diamantina, Boletim, 13:46-47.

Bodnar, R.J., Vityk, M.O., 1994. Interpretation of microthermometric data for H₂O-NaCl fluid inclusions. In: de Vivo, B., Frezzotti, M.L. (Eds.), *Fluid Inclusions in Minerals: Methods and Applications*. Short Course IMA, p.117–130.

Bowers, T.S., Helgeson, H.C., 1983. Calculation of the thermodynamic and geochemical consequences of nonideal mixing in the system H₂O–CO₂–NaCl on phase relations in geological systems: equation of state for H₂O–CO₂–NaCl fluids at high pressures and temperatures. *Geochim. Cosmochim. Acta*. 47, 1247-1275.

Brown, P.E., Hagemann, S.G., 1995. MacFlinCor and its application to fluids in Archaean lode-gold deposits. *Geochim. Cosmochim. Acta* 59, 3943–3952.

Braga, F.C.S., Rosiere, C.A., Queiroga, G.N., Rolim, V.K., Santos, J.O.S., McNaughton, N.J., 2015. The Statherian itabirite-bearing sequence from the Morro Escuro Ridge, Santa Maria de Itabira, Minas Gerais, Brazil. *J. S. Am. Earth Sci.* 58, 33-53.

Campos, C.P., Medeiros, S.R., Mendes, J.C., Pedrosa-Soares, A.C., Dussin, I., Ludka, I.P., Dantas, E.L., 2016, Cambro-Ordovician Magmatism in the Araçuaí Belt (SE Brazil): snapshots from a post-collisional event. *Journal of South American Earth Sciences*, v. 68, p. 248-268.

Carvalho, R.P., Rosiere, C.A., Rolim, V.K., Lana, C.C., Santos, J.O.S., 2014. A sequência orosiriana-estateriana e geometria transpressiva na região de Santa Maria de Itabira-MG. *Rev. Inst. Geociências-USP* 14 (2), 101-120.

Centaurus Metals Ltd., 2008. Initial JORC Resource for Liberdade Project, Perth: ASX Release.

Centaurus Metals Ltd., 2014. September 2014 Quarterly Activities Report, Perth: ASX Release.

Chemale Jr., F., Quade H., Schmus W.R.V, 1998. Petrography, geochemistry and geochronology of the Borrachudos and Santa Bárbara metagranites, Quadrilátero Ferrífero, Brazil. *Zbl. Geol. Palaont*, Stuttgart, I, 3-6, 739-750.

Chemale Jr., F., Dussin, I.A., Alkmim, F.F., Martins, M.S., Queiroga, G., Armstrong, R., Santos, M.N., 2012. Unravelling a Proterozoic basin history through detrital zircon geochronology: the case of the Espinhaço Supergroup, Minas Gerais, Brazil. *Gondwana Research*, 22(1), 200-206.

Cordani, U.G., Fraga, L.M., Reis, N., Tassinari, C.C.G., Brito-Neves, B.B., 2010. On the origin and tectonic significance of the intra-plate events of Grenvillian-type age in South America: a discussion. *Journal of South American Earth Sciences* 29, 143–159.

Correia Neves, J.M., Pedrosa Soares, A.C., Marciano, V.R.P.da R.O., 1986. A província pegmatítica oriental do Brasil à luz dos conhecimentos atuais. *Rev. Bras. Geoc.* 16 (1), 106-118.

Diamond, L.W., 1990, Fluid inclusion evidence for P-V-T-X evolution of hydrothermal solutions in late-Alpine gold-quartz veins at Brusson, Val d'Ayas, northwest Italian Alps. *American Journal of Science*. 290, 912–958.

Dorr, J.V.N., Barbosa, A.L.M., 1963. Geology and ore deposits of the Itabira District Minas Gerais, Brazil: U. S. Geological Survey Professional Paper 341-C, p110.

Dorr, J.V.N., 1969. Physiographic, stratigraphic and structural development of the Quadrilatero Ferrifero, Minas Gerais, Brazil. United States Geological Survey. Professional Paper, 110-641.

Dossin, I.A., Dossin, T.M., Charvet, J., Cocherie, A., Rossi, P., 1993. Single-zircon dating by step-wise Pb-evaporation of Middle Proterozoic Magmatism in the Espinhaço Range, Southeastern São Francisco Craton (Minas Gerais, Brazil). In: Simpósio do Craton do São Francisco, 2, Salvador, Anais, p39-42.

Dussin, T.M., 1994. The Borrachudos Suite, Mezoproterozoic A-type Granitic Magmatism in the São Francisco Craton (SE Brazil). In: Associacions vulcano- plutoniques de l'Espinhaço Meridional (SE - Brésil). Université d'Orleans, Orléans. PhD Thesis.

Dussin, I.A., Dussin, T.M., 1995. Supergrupo Espinhaço: modelo de evolução geodinâmica. Geonomos, 3(1), 19-26.

Dussin, T. M., Duarte, P., Dussin, I.A., 2000. Registro da tectônica Brasiliiana na região de Guanhães (SE, Brasil): Deformação e metamorfismo das rochas de idade pós-Transamazônicas. Geonomos, 8(2), 55-59.

Fernandes M. L. S., Marciano V. R. P. R., Oliveira R. C., Correia Neves J. M., Dilascio M. V., 1994. Granitos Borrachudos: um exemplo de granitogênese anorogênica na porção central do estado de Minas Gerais. Belo Horizonte. Geonomos, 2,2. 23-29.

Fernandes, M.L.S., 2001. O Granito Borrachudos entre Guanhães e Dores de Guanhães (Plutônito Morro do Urubu): Gênese e Evolução. PhD thesis. Departamento de Geologia, Universidade Federal do Rio do Janeiro, p. 187.

Figueiredo e Silva, R.C., Hagemann, S.G., Lobato, L.M., Rosière, C.A., Banks, D.A., Davidson, G.J., Vennemann, T.W., Herget, J.M., 2013. Hydrothermal fluid processes and evolution of the giant Serra Norte jaspilite-hosted iron ore deposits, Carajás Mineral Province, Brazil. Econ. Geol. 108, 739-779.

Goldstein, R.H., Reynolds, T.J., 1994. Systematics of fluid inclusions in diagenetic minerals. SEPM Short Course 31. The Mineralogical Association of Canada, Tulsa, p199.

Grossi-Sad J.H., Chiod Filho C., Santos J.F., Magalhães J.M.M., Carelos P.M., 1990a. Duas Suítes Graníticas do Bordo Sudeste do Cráton Sanfrasciscano, em Minas Gerais: Petroquímica e Potencial Metalogenético. SBG, Congr. Bras. de Geol., 36, Natal, Anais, 4: 1836-1848.

Grossi-Sad, J.H., Chiodi Filho, C., Santos, J.F., Magalhães, J.M.M., Carelos, P.M., 1990b. Geoquímica e origem da formação ferrífera do Grupo Guanhães, Distrito de Guanhães, MG, Brasil. SBG, Congr. Bras. de Geol., 36, Natal, Anais, 3: 1241-1253.

Grossi-Sad, J.H., Mourão, M.A.A., Guimarães, M.L.V., Knauer, L.G., 1997. Geologia da Folha Conceição do Mato Dentro. In: Grossi-Sad, J.H., Lobato, L.M., Pedrosa- Soares, A.C., Soares-Filho, B.S. (Eds.), Projeto espinhaço Em CD-ROM (textos, mapas e anexos). COMIG e Companhia Mineradora de Minas Gerais, Belo Horizonte, pp. 2533-2693.

Guadagnin, F., Chemale Jr., F., Magalhães, A.J.C., Santana, A., Dussin, I., Takehara, L., 2015. Age constraints on crystal-tuff from the Espinhaço Supergroup — Insight into the Paleoproterozoic to Mesoproterozoic intracratonic basin cycles of the Congo–São Francisco Craton. *Gondwana Research*, 27, 363–376.

Guillong M.M., Maier D.L., Allan M.M., Heinrich C.A., 2008. SILLS: a MATLAB based program for the reduction of laser ablation ICPMS data of homogeneous materials and inclusions. Sylvester P (ed) *Laser Ablation ICPMS in the Earth Sciences. Current Practices and Outstanding Issues*, 328-333.

Hagemann, S.G., Angerer, T., Duuring, P., Rosière, C.A., Figueiredo e Silva, R.C., Lobato, L.M., Hensler, A.S., Walde, D.H.G., 2016. BIF-hosted iron mineral system: A review. *Ore Geol. Rev.* 76, 317–359.

Hensler, A.S., Hagemann, S.G., Rosière, C.A., Angerer,T., Gilbert, S., 2015. Hydrothermal and metamorphic fluid-rock interaction associated with hypogene “hard” iron ore mineralisation in the Quadrilátero Ferrífero, Brazil: Implications from in-situ laser ablation ICP-MS iron oxide chemistry. *Ore Geology Reviews*. 69, 325-351.

Jordt-Evangelista, H., Lana, C., Delgado, C.E.R, Viana, D.J., 2016, Age of the emerald mineralization from the Itabira Nova Era District, Minas Gerais, Brazil, based on LAICPMS

geochronology of cogenetic titanite. Brazilian Journal of Geology, 46(3), 427-437.

Klein, C., 2005. Some Precambrian banded iron-formations (BIFs) from around the world: their age, geologic setting, mineralogy, metamorphism, geochemistry, and origin. Am. Mineral. 90, 1473–1499.

Marciano, V.R.P.R.O, Svisero, D.P, Correia-Neves, J.M., 1993, Dados geocronológicos de pegmatitos da borda oriental do Craton do São Francisco. Anais do Simp. sobre o Craton do São Francisco: Sua evolução tectônica e metalogenética. Salvador, SBG-Ba, SE/SGM, 362-365.

Marciano, V.R.P.R.O., 1995. O distrito pegmatítico de Santa Maria de Itabira, MG. Mineralogia, geoquímica e zoneografia. PhD Thesis. Inst. Geoc. Univ. São Paulo, p216.

Martins-Neto, M.A., 2000. Tectonics and sedimentation in a paleomesoproterozoic rift-sag basin (Espinhaço basin, southeastern Brazil). Precambrian Res. 103, 147-173.

Martins-Neto, M.A., and Hercos, C.M., 2002. Sedimentation and tectonic setting of Early Neoproterozoic glacial deposits in southeastern Brazil. International Association of Sedimentologists, Special Publication, 33: 383-403.

McLennan, S.M., 1989. Rare earth elements in sedimentary rocks: influence of provenance and sedimentary processes. In: Lipin, B.R., McKay, G.A. (Eds.), Geochemistry and Mineralogy of Rare Earth Elements, Reviews in Mineralogy. 21, 169-200.

Melo, M.G., Lana, C., Stevens, G., Pedrosa_Soares, A.C., Gerdes, A.A., Leonardo, A., Nalini, H.A., Alkmim, F.F., 2017, Assessing the isotopic evolution of S-type granites of the Carlos Chagas Batholith, SE Brazil: Clues from U?Pb, Hf isotopes, Ti geothermometry and trace element composition of zircon. Lithos, 284-285, 730-750.

Morteani, G., Preinfalk, C., Horn, A.H., 2000. Classification and mineralisation potential of the pegmatites of the Eastern Brazilian Pegmatite Province. Mineral. Deposita, 35, 638-655.

Müller G., Höhndorf A., Lauenstein H.J., Lenz H., 1986a. Petrological and Geochemical data on a high-metamorphic Archean BIF - bearing rock sequence near Guanhães, Minas Gerais, Brazil.

Müller, G., Schuster, A.K., Hoefs, J., 1986b. The metamorphic grade of banded iron formations: Oxygen isotope and petrological constraints: *Fortschritte der Mineralogie*, 64, 163-185.

Noce, C.M., Pedrosa-Soares, A.C., Silva, L.C., Armstrong, R., Piuzana, D., 2007. Evolution of polycyclic basement complexes in the Araçuaí Orogen, based on U-Pb SHRIMP data: Implications for Brazil–Africa links in Paleoproterozoic time, *Precambrian Res.*, 159, 60-78.

Oliveira, L.A.R., Rosière, C.A., Rios, F.J., Andrade, S., Moraes, R., 2015. Chemical fingerprint of iron oxides related to iron enrichment of banded iron formation from the Cauê Formation - Esperança Deposit, Quadrilátero Ferrífero, Brazil: a laser ablation ICP-MS study. *Revista Brasileira de Geociências*, v. 45, p. 193-216.

Oliveira, L.A.R., Rios, F.J., Rosière, C.A., Wölle, M., Ortelli, M., Kouzmanov, K., 2017. Nature and evolution of fluids associated with specularite-bearing Fe and Au-PGE (Jacutinga) mineralization during the Brasiliano orogeny in the eastern São Francisco Craton, Minas Gerais, Brazil. *Ore Geology Reviews* 86, 130–153.

Pecoits, E., 2010. Ediacaran Iron Formations and Carbonates of Uruguay: Palae-oceanographic, Palaeoclimatic and Palaeobiologic Implications. PhD thesis. University of Alberta, p.230.

Pedrosa-Soares, A.C., Cordani, U., Nutman, A., 2000. Constraining the age of Neoproterozoic glaciation in eastern Brazil: First U-Pb SHRIMP data from detrital zircons. *Rev. Bras. de Geociênc.*, 30: 58-61.

Pedrosa-Soares, A.C., Noce, C.M., Wiedemann, C.M., Pinto, C.P., 2001. The Araçuaí-West Congo orogen in Brazil: An overview of a confined orogen formed during Gondwanaland assembly. *Precamb. Res.*, 110, 307–323.

Pedrosa-Soares, A.C., Noce, C.M., Alkmim, F.F., Silva, L.C., Babinski, M., Cordani, U., Castañeda, C., 2007. Orógeno Araçuaí: síntese do conhecimento 30 anos após Almeida 1977. *Geonomos*, 15(1), 1-16.

Pedrosa-Soares, A.C., Campos, C.P., Noce, C., Silva, L.C., Novo, T., Roncato, J., Medeiros, S., Castaneda, C., Queiroga, G., Dantas, E., Dussin, I.A., Alkmim, FF. 2011. Late Neoproterozoic–Cambrian granitic magmatism in the Araçuaí orogen (Brazil), the Eastern Brazilian Pegmatite Province and related mineral resources. Geological Society, London, Special Publications, 350, 25–51.

Pflug, R., 1965. A geologia da parte meridional da Serra do Espinhaço e zonas adjacentes, Minas Gerais. DNPM/DGM, Bol. 226., Rio de Janeiro, p.1-51.

Preinfalk, C., Kostitsyn, Y., Morteani, G., 2002. The pegmatites of the Nova Era - Itabira - Ferros pegmatite district and the emerald mineralisation of Capoeirana and Belmont (Minas Gerais, Brazil): geochemistry and Rb-Sr dating. Jour. South Am Earth Scienc., 14, 867-887.

Purtov, V.K., Kotelnikova, A.L., 1993. Solubility of titanium in chloride and fluoride hydrothermal solutions. Int. Geol. Rev. 35, 279-287.

Roedder, E., 1984. Fluid inclusions. Rev. Mineral. 12. Mineralogical Society of America, p. 646.

Rolim, V.K., 2016. As Formações Ferríferas da Região de Conceição do Mato Dentro – MG: Posicionamento Estratigráfico, Evolução Tectônica, Características Geoquímicas e Gênese dos Minérios (Ph.D. thesis). Universidade Federal de Minas Gerais, Brazil, 242pp.

Rolim, V.K., Rosière, C.A., 2011. The Conceição do Mato Dentro Iron Formation Province in southeastern Brazil. In: Let's Talk Ore Deposits: Proceedings of the 11th Biennial SGA Meeting, Antofagasta, Chile. https://sga.conference-services.net/resources/1054/2590/pdf/SGA2011_0237.pdf. (accessed 24.11.2016).

Rolim, V.K., Rosière, C.A., Santos, J.O.S., McNaughton, N.J., 2016. The Orosirian-Statherian banded iron formation-bearing sequences of the southern border of the Espinhaço Range, Southeast Brazil. J. S. Am. Earth Sci. 65, 43-66.

Rosière, C.A., Spier, C.A., Rios, F.J., Suckau, V.E., 2008. The itabirites of the quadrilatero ferrifero and related high-grade iron ore deposits: an overview. Rev. Econ. Geol. 15, 223-254.

Silva, L.C., Armstrong, R., Noce, C.M., Carneiro, M.A., Pimentel, M.M., Pedrosa- Soares, A.C., Leite, C.A., Vieira, V.S., Silva, M.A., Paes, V.J.C., Cardoso-Filho, J.M., 2002. Reavaliação da evolução geológica em terrenos pre cambrianos brasieiros com base em novos dados U-Pb SHRIMP, parteII: Orógeno Araçuaí, Cinturão Mineiro e Cráton São Francisco Meridional. Rev. Bras. Geociênc. 32, 513-528.

Silveira, E.M., Söderlund, U., Oliveira, E.P., Ernst, R.E., Menezes Leal, A.B., 2013. First precise U-Pb baddeleyite ages of 1500 Ma mafic dykes from the São Francisco Craton, Brazil, and tectonic implications. *Lithos* 174, 144–156.

Taylor, S.R. and McLennan, S.M., 1985. *The Continental Crust: Its Composition and Evolution*. Blackwell, London.

Thorne, W.S., Hagemann, S.G., Sepe, D., Dalstra, H.J., Banks, D.A., 2014. Structural control, hydrothermal alteration zonation, and fluid chemistry of the concealed, high-grade 4EE iron orebody at the Paraburdoo 4E Deposit, Hamersley Province, Western Australia. *Econ. Geol.* 109, 1529-1562.

Uhlein, A., Trompette, R.R., Egydio-Silva, M., 1998. Proterozoic rifting and closure, SE border of the São Francisco Craton, Brazil. *J. South Am. Earth Sci.* 11, 191-203.

Capítulo 4 - 2º Artigo (submetido)

Zircon U-Pb ages and Hf isotope compositions of Açucena Granite (Borrachudos Suite): Implications for Statherian-Cambrian tectono-magmatic evolution of the southern border of the São Francisco Craton, Brazil

Sylvio D. Gomes^{a*}, Rosaline C. Figueiredo e Silva^a, Anthony I. S. Kemp^b, João Orestes S. Santos^b, Steffen G. Hagemann^b, Lydia M. Lobato^a, Carlos A. Rosière^a

^a Universidade Federal de Minas Gerais, CPMTC-Instituto de Geociências, Av. Presidente Antônio Carlos, 6627, Pampulha, Belo Horizonte, MG, Brazil

^b School of Earth Sciences, University of Western Australia, Centre for Exploration Targeting, WA 6009, Australia

* Corresponding author

E-mail address: sylvio.gomes@gmail.com

Keywords:

Zircon

Hafnium isotopes

São Francisco Craton

Araçuaí belt

Crustal anatexis

Abstract

Isotopic Lu-Hf and geochronological studies on the zircon grains of the Borrachudos Suite provide constraints on the evolution of the tectono-magmatic events that affected the southern border of the São Francisco Craton and led to the formation of the associated iron and emerald deposits. The granite records magmatic crystallization in the 1740-1688 Ma time range, and A₂-type geochemical signature. Zircon grains present hydrothermal and anatetic areas with Cambrian age that are related to the gravitational collapse of the final stages Brasiliano orogen. During this event the granite was deformed and metamorphosed in the amphibolite grade, leading to anatexis and the formation of large amount of pegmatite bodies. The Hf isotope data on the hydrothermal/anatetic areas indicate that during the metamorphic peak of the orogen (ca. 610 Ma) small amounts of partial melting were accompanied by hydrothermal fluids enriched in radiogenic Hf. During the Cambrian these fluids contributed to the high degree of partial melting leading to the formation of large amounts of hydrous melts (pegmatites), the formation of the emerald deposits and the high-grade iron orebodies.

1. Introduction

The A-type granitoids constitute important intrusive units in most post-Archean continental landmasses on Earth (e.g., Dall'Agnol et al., 2012), despite their minor volumetrical importance (Bonin, 2007). Their diverse compositions require large differences in magma source and evolutionary paths from source region to emplacement site (Zhang et al., 2015). Petrogenetic models include crustal anatexis (Frost and Frost, 1997; King et al., 1997; Wu et al., 2002; Dall'Agnol and Oliveira, 2007; Huang et al., 2011), differentiation of basaltic magmas derived from the mantle (Mushkin et al., 2003; Namur et al., 2011), and coupled contributions from crustal and mantle sources (Kemp et al., 2005; Yang et al., 2006; Zhang et al., 2012).

Due to the low diffusivity of trace elements within distinct growth zones, zircon crystals preserve isotopic and chemical variations during geological processes that affected the parent magma or rock. Once incorporated into the zircon lattice, U-Pb and Lu-Hf systems are not easily disturbed (e.g., Cherniak et al., 1997). Also, its Hf isotopic composition can be utilized as a geochemical tracer of the host rock, providing constraints on the source rocks of the magmas (e.g., Patchett et al., 1981). Zircon is an ideal mineral for U-Th-Pb dating and Lu-Hf isotopic measurements, because it contains moderate U, Th concentrations, but very low common Pb, and high Hf (~ 1 wt.%) and very low $^{176}\text{Lu}/^{177}\text{Hf}$ (typically < 0.001).

The integration of U-Pb age and Hf isotope data measured in zircon crystals is a powerful approach to the study of magmatic and crustal evolution (Stevenson and Patchett, 1990; Corfu and Noble, 1992). The calculation of ϵHf values may allow an estimate of crustal residence times and crustal growth/reworking episodes (Hawkesworth and Kemp, 2006a).

In this study, the age and Hf isotopic composition of zircon crystals from the Açucena Granite is investigated. The Açucena pluton is a 200 km-scale (Fig. 1), A-type granite that is part of the Borrachudos Suite (Dussin, 1994), emplaced during the Paleoproterozoic in the southeastern border of the São Francisco Craton (SFC). The Borrachudos Suite records U-Pb crystallization ages of ca. 1700–1730 Ma, shows evidence of a metamorphic overprint, and is associated with gem deposits hosted in pegmatite dikes dated at 480-530 Ma (Jordt Evangelista et al., 2016). The pegmatite deposits belong to the western portion of the Eastern Brazilian Pegmatite Province (Itabira-Nova Era Emerald District), which is the most important Brazilian gemstone province (Correia Neves et al., 1986; Morteani et al., 2000). Brazilian emerald deposits account presently for 10-20% of world emerald production, which ranks Brazil second after Colombia (Schwarz and Giuliani, 2002; Groat et al., 2008). The pegmatites have an anatetic origin during the Brasiliano orogen (Bilal et al., 1995; Marciano et al., 1993).

In the Piteiras and Belmont mines (Fig. 1) the metasomatic, schist-type emerald mineralization is associated with alkaline, metasomatized pegmatite bodies in deformation zones close to the contact between meta-mafic and -ultramafic rocks of the Guanhães Complex and granite of the Borrachudos Suite. Fluid inclusions studies, combined with geological and tectonic characteristics support a metamorphic origin for emerald mineralization at the Piteiras Mine ([Lynch et al., 2014](#)).

[Gomes et al. \(2018\)](#) also conducted fluid inclusions studies with evidence for the contribution of anatetic melts from the Açucena Granite in the formation of high-grade iron orebodies that are associated with pegmatites in the Piçarrão-Liberdade deposit (Fig. 1).

Many episodes of juvenile continental crust accretion from 2470 to 2000 Ma (Minas accretionary orogeny, [Teixeira et. al, 2015](#)) during Trans-Amazonian orogen are well documented in the southern part of the SFC and adjacent areas ([Noce et al., 2007](#), [Barbosa et al., 2015, 2018](#)). However, the tectonic setting of the late Paleoproterozoic magmatic episode represented by the Borrachudos Suite still remains poorly constrained, in spite of the wide occurrence of this suite (Fig. 1) and association with Fe and pegmatite mineral deposits.

This paper will apply a combination of U-Pb geochronology, combine with Hf isotope compositions of single zircon crystals, to provide important constraints on the crustal processes (e.g., magmatic crystallization) that constrained the evolution of the Açucena Granite. In addition, the constraints on the igneous processes, e.g., magmatic crystallization, that formed the Açucena Granite, and the subsequent metamorphic/hydrothermal overprint, will be used to advance the understanding of the genesis of the spatially and genetically associated itabirite-hosted iron and emerald deposits.

2. Geological setting

The São Francisco Craton (SFC) is defined as a stable part of the South American Platform. As a single continental block, it was not involved in the Brasiliano/Pan-African orogen between 600 and 480 Ma ([Brito Neves and Cordani, 1991](#); [Cordani et al., 2010](#)). The Brasiliano orogen formed during the convergence of the Amazonian, São Francisco-Congo, Paranapanema (Rio de La Plata) cratons, and smaller allochthonous blocks, leading to the assembly of West Gondwana and the development of many fold and thrust belts (e.g. Brasilia belt, [Pimentel, 2016](#); Ribeira belt, [Valeriano et al., 2016](#); Araçuaí belt, [Pedrosa Soares, et al., 2001](#); Araguaia and Paraguay belts).

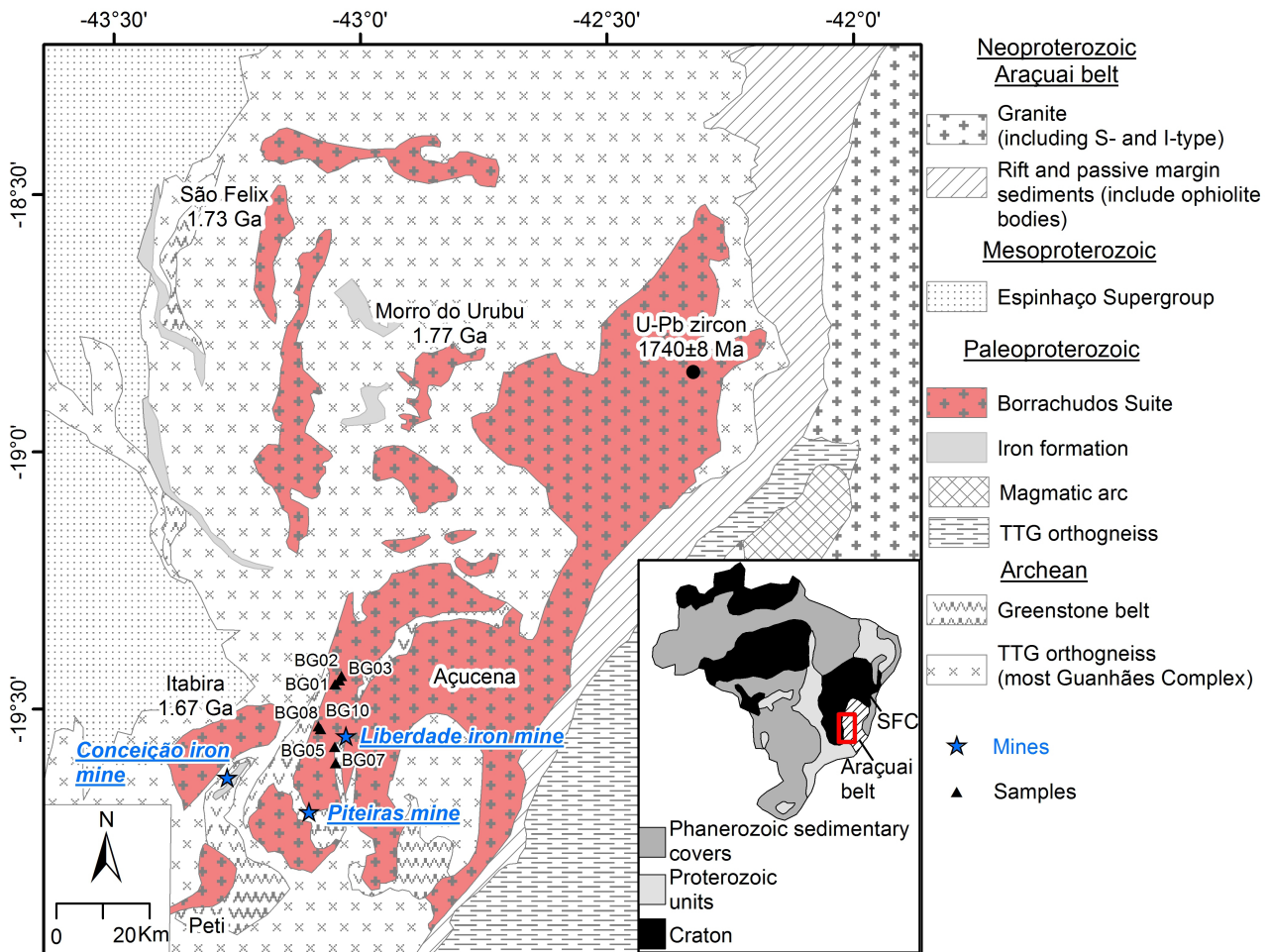


Figure 1. Geological setting of the eastern border of the southern Espinhaço Range with the location of various Borrachudos Suite plutons, Piçarrão-Liberdade and emerald mines. Geochronological data: Itabira granite ([Chemale Jr. et al., 1998](#)); Morro do Urubu granite ([Fernandes et al., 2000](#)); São Felix granite ([Dossin et al., 1993](#)), and Açucena granite ([Silva et al., 2002](#)). SFC: São Francisco craton. Based on Heineck et al., 2003.

The SFC has a long history of intracratonic and passive margin basin filling, magmatism and orogenic build up ([Almeida, 1977](#); [Marshak and Alkmim, 1989](#); [Silveira et al., 2013](#)). The Craton basement records an important tectono-magmatic evolution during the Paleoproterozoic - Trans-Amazonian/Eburnean orogenic cycle (2.2 to 1.9 Ga; [Barbosa and Sabaté, 2004](#); [Noce et al., 2007](#)). The Espinhaço basin forms part of a complex rift system, extending approximately 1090 km north-south (Fig. 1), which developed as an intracontinental rift-sag basin on the São Francisco Craton during the Paleo-Mesoproterozoic ([Martins Neto, 2000](#); [Alkmim and Martins Neto, 2012](#); [Guadagnin et al., 2015](#)). The Espinhaço Supergroup was formed in two stages of basin filling: (1) the lower Espinhaço basin, marked by a volcano-sedimentary sequence with alluvial, fluvial and

eolian deposits formed from 1.80 to 1.68 Ga; (2) the overlying sequence, called the upper Espinhaço basin, represents 85% the Espinhaço Supergroup thickness; it is a rift-sag basin with a younger detritic zircon peak at 1192 Ma, which is the maximum age for deposition of the upper units (Chemale et al., 2012). Between 1000 and 850 Ma, a second rifting event gave rise to the development of a narrow ocean basin (Pedrosa Soares et al., 2001), filled by sediments that now comprise the Macaúbas Group (Uhlein et al., 1998; Martins Neto and Hercos, 2002; Pedrosa Soares et al., 2000).

The closure of the Espinhaço and Macaúbas rift basins during the Brasiliano orogen resulted in the development of the Araçuaí fold belt (Fig. 1). The basin rocks are deformed near the contact between the SFC and the Araçuaí fold belt, with portions of the reworked Archean and Paleoproterozoic basement being exposed (Marshak and Alkmim, 1989; Dussin and Dussin, 1995; Uhlein et al., 1998; Noce et al., 2007). The tectonic evolution of the Araçuaí belt is well documented, with granitic magmatism in the 630-480 Ma time range. The G1 suite (630 to 580 Ma) is considered to be pre-collisional; G2 and G3 suites (585 to 530 Ma) syn-collisional; and G4 and G5 suites (539 to 480 Ma) as post-collisional. The latter granites are interpreted to be related to the gravitational collapse of the orogeny (Figueiredo, 2009; Campos et al., 2016; Melo et al., 2017).

The Borrachudos Suite batholiths (Fig. 1) are located in the external western zone of the Neoproterozoic Araçuaí belt (Almeida 1977; Alkmin et al., 2006; Pedrosa Soares et al., 2007). This is a NS-trending zone and west-verging system of faults and folds on the eastern edge of the SFC, which incorporates Archean-Paleoproterozoic basement and supracrustal rocks of the Espinhaço Supergroup. In the external zone, the Archean-Paleoproterozoic basement is composed of the Guanhães Complex and the Borrachudos Suite.

The Guanhães Complex is composed of TTG (tonalite-trondhjemite-granodiorite) gneisses, migmatites and granites. Geochronological studies (SHRIMP U-Pb; Silva et al., 2002) on the TTG gneissic complex yield 2700-2800 Ma magmatic crystallization, and 519-527 Ma metamorphic ages, respectively. The TTGs are polymetamorphic and experienced enrichments in alkalis (K, Rb) and other incompatible elements in the course of the Rhyacian and Brasiliano-age orogen (Machado, 1998).

The Guanhães Complex is associated with discontinuous units of metasedimentary and metavolcanic rocks of the Guanhães Group (Grossi Sad et al. 1990b; 1997; Noce et al., 2007). Muller et al. (1986) demonstrated that the Guanhães Group metasedimentary sequence was metamorphosed under granulite facies conditions based on O isotopic studies.

Several granitic plutons of the Borrachudos Suite occur in the Guanhães Complex (Grossi Sad et al., 1990a; Dussin and Dussin, 1995). This denomination was first used by Dorr and Barbosa (1963)

to describe a granite suite (Borrachudos granite) NW of the town of Itabira (Fig. 1), with Açuçena being the largest plutonic unit of the suite. Geochronological and geochemical data of the Borrachudos Suite indicate magma genesis at 1700 Ma in the anorogenic context of crustal extension and melting of lower crustal rocks related to the rift event that led to the lower Espinhaço basin deposition (Dussin et al., 2000). The occurrence of metavolcanic (rhyolitic) rocks with U-Pb age in the 1700-1770 Ma time range in the eastern portion of the area also suggests a correlation with rift-related magmatism (Brito Neves et al., 1979; Machado et al., 1989). According to Dussin (1994), the Borrachudos magma has A-type geochemical signature, high temperature of crystallization ($\sim 850^\circ \text{C}$ – hypersolvus), is enriched in fluorine and high-field strength (HFS) elements, and is relatively dry.

The Sm-Nd isotopes of the Itabira Granite (Chemale Jr. et al., 1998), São Félix and Morro do Urubu granites (Dussin et al., 1997) show Borrachudos Suite initial ϵ_{Nd} values (back-calculated to 1730 Ma) to be between -11.3 to -8.8 ($^{147}\text{Sm}/^{144}\text{Nd}$ range from 0.11 to 0.13), and T_{DM} model ages from 3.27 to 2.6 Ga. Previous single-zircon dating by step-wise Pb evaporation yields an age of 1729 ± 14 Ma for São Félix (Dossin et al., 1993), 1770 ± 30 Ma for Morro do Urubu (Fernandes et al., 2000), and 1670 ± 32 Ma for Itabira granites (Chemale Jr. et al., 1998). The magmatic crystallization SHRIMP U-Pb zircon age of the Açuçena Granite is 1740 ± 8 Ma (Silva et al., 2002). Titanite with an U-Pb age of 507 Ma is probably related to the tectono-thermal Brasiliano orogen, and the post-collisional (G4 and G5) granitic magmatism of the Araçuaí belt (Fernandes et al., 2000; Richter et al., 2016).

The Guanhães Complex and the Borrachudos Suite host a wide number of pegmatite bodies, which are generally tabular-discordant (1-10m thick) and host beryl deposits and other types of gems (eg. alexandrite, emerald); these are grouped in the Santa Maria de Itabira pegmatite district (Pedrosa Soares et al., 2011). This district is part of the Brazilian eastern pegmatite province (Marciano, 1995; Morteani et al., 2000; Preinfalk et al., 2002), and was formed by partial melting of the basement during the late Brasiliano tectono-thermal event according to monazite (531 ± 22 Ma – Bilal et al., 1995); muscovite (519 Ma – Marciano et al., 1993) and titanite dating from the emerald host rock at the Piteiras Mine (576 ± 7 Ma, – Jordt Evangelista et al., 2016). The pegmatite-forming event is more or less coeval with the intrusion of the post-collisional S-type granites in the late Brasiliano orogen (G4 and G5) emplaced mainly in the eastern portion of the Araçuaí belt (500 – 540 Ma, Pedrosa Soares et al., 2011).

3. Samples and analytical procedures

Samples used in this study were collected from the Açucena Granite and their location is shown in Fig. 1. Whole-rock geochemical analyses from three samples were conducted at ACME Labs using the Inductively Coupled Plasma Emission Spectrometry (ICP-ES) method for major oxide elements and the Inductively Coupled Plasma Mass Spectroscopy (ICP-MS) method for trace elements.

Seven rock samples were crushed and milled at the Sample Preparation Laboratory for Geochemistry and Geochronology of the Universidade Estadual Paulista (UNESP). The large pegmatite veins were avoided during the procedure of sample preparation, but it was not possible to separate the smallest veinlets (Fig. 2). Zircon concentrates were extracted using conventional gravimetric and magnetic (Frantz isodynamic separator) techniques. The most translucent zircon crystals were picked by hand under binocular microscope, mounted in a custom-size epoxy resin with reference zircons M257 and OGC, and polished up to mid-section to expose the grain centers at the Mineral Separation Laboratory of the University of Western Australia (UWA). The mounts were imaged using a camera system on a binocular microscope, and further imaged using SEM fitted with a cathodoluminescence (CL) and backscattered electron (BSE) detectors in order to identify internal structures and choose potential target sites for U-Pb and Hf analyses. The CL and BSE images were acquired by TESCAN VEGA3 scanning electron microscope at the CMCA (Centre for Microscopy, Characterization and Analysis) UWA, coupled to an energy-dispersive X-ray spectroscopy (EDS) detector.

The zircons analyzed for Hf isotopes in this study were dated by secondary ion mass spectrometry (SIMS – SHRIMP II) at Curtin University, Perth, following techniques described by [Nelson et al. \(2000\)](#). The $^{207}\text{Pb}/^{206}\text{Pb}$ zircon ages were corrected for common lead by measurement of ^{204}Pb and assuming a Pb isotope composition of Broken Hill lead following [Compston et al. \(1992\)](#), and the radiogenic Pb is shown as $^{207}\text{Pb}^*$ and $^{206}\text{Pb}^*$ (Appendix A). The data have been processed using SQUID, and concordia diagrams were plotted using Isoplot/Ex software ([Ludwig, 2001](#)).

Hafnium isotope measurements ($n=29$) were acquired with a Thermo Scientific Neptune PLUS multi-collector ICP-MS coupled to a Cetac Analyte G2 laser ablation sampling system in the School of Earth Sciences at the University of Western Australia. Laser ablation was carried out for 60 seconds, following a 30 second on-peak baseline, at repetition rates of 4 Hz and laser fluence of $\sim 5 \text{ J/cm}^2$. Spot sizes of 35 μm , 40 μm , or 50 μm diameter were employed, depending on the available polished area of the zone of interest in the crystal. Ablation was conducted in a two-volume Helex sample cell, with the He carrier gas exiting the cell being combined with Ar prior to transport into the ICP-MS via nylon tubing. A small ($\sim 0.008 \text{ l/min}$) N2 flow was introduced into the

Ar carrier gas to enhance sensitivity (Hawkesworth and Kemp, 2006b; Iizuka and Hirata, 2005). The isobaric interference of Lu and Yb on ^{176}Hf was corrected by monitoring the interference-free ^{171}Yb and ^{175}Lu intensities during the analysis and then deriving ^{176}Yb and ^{176}Lu using $^{176}\text{Yb}/^{171}\text{Yb} = 0.897145$ (Segal et al., 2003) and $^{176}\text{Lu}/^{175}\text{Lu} = 0.02655$ (Vervoort et al., 2004). Yb isotope ratios were normalized to $^{173}\text{Yb}/^{171}\text{Yb} = 1.130172$ (Segal et al., 2003) and Hf isotope ratios to $^{179}\text{Hf}/^{177}\text{Hf} = 0.7325$ (Patchett and Tatsumoto, 1981) using an exponential law. The instrumental mass fractionation of Lu was assumed to follow that of Yb. Data were processed offline using a Microsoft Excel spreadsheet. Hf isotope data quality was monitored for each analytical session by analysis of reference zircons Temora 2 and Penglai. These yielded mean $^{176}\text{Hf}/^{177}\text{Hf}$ values of 0.282694 ± 17 (2 SD, n = 13) and 0.282929 ± 21 (2 SD, n = 4), identical to those determined by solution analysis (0.282906 ± 0.0000010 (2s) for Penglai - Li et al., 2010; 0.282686 ± 8 for Temora 2 - Woodhead and Herdt, 2005). All zircon Hf isotope data are normalized to the solution $^{176}\text{Hf}/^{177}\text{Hf}$ value of Mud Tank zircon (0.282507 ± 6 , Woodhead and Herdt, 2005), reported relative to JMC 475 $^{176}\text{Hf}/^{177}\text{Hf} = 0.282160$ (Vervoort et al., 1999), using the laser ablation data generated from this zircon in the same analytical session (0.282496 ± 11 , 2 SD, n = 13). Uncertainties in $^{176}\text{Hf}/^{177}\text{Hf}$ quoted for sample zircons include the external precision of the Mud Tank zircon measurements, added in quadrature.

Initial $^{176}\text{Hf}/^{177}\text{Hf}$ ratios, $^{176}\text{Hf}/^{177}\text{Hf}(t)$ and $\epsilon\text{Hf}(t)$, are calculated at the time of zircon crystallization in the magma, using the decay constant of 1.867×10^{-11} year $^{-1}$ for ^{176}Lu (Söderlund et al., 2004) and the chondritic ratios of Bouvier et al. (2008), $^{176}\text{Hf}/^{177}\text{Hf}$ (0.282785) and $^{176}\text{Lu}/^{177}\text{Hf}$ (0.0336).

Two stage depleted-mantle model ages (T_{DM}) were calculated using the measured $^{176}\text{Lu}/^{177}\text{Hf}$ ratios in the zircon, referred to a model depleted mantle with a present-day $^{176}\text{Hf}/^{177}\text{Hf} = 0.28325$ and $^{176}\text{Lu}/^{177}\text{Hf} = 0.0384$ (Griffin et al., 2002). These T_{DM} ages represent a minimum age for the source of the host magma of the zircon.

4. Petrography and geochemistry of the Açucena Granite

The Açucena Granite mainly intrudes Archean rocks of the Guanhães Complex (Fig. 1). Machado (1998) demonstrated that the Açucena Granite was metamorphosed under amphibolite facies conditions ($460^\circ - 670^\circ\text{C}$). The Sm-Nd dating of garnets from one shear zone, associated with hydrothermal alteration crosscutting the Açucena Granite, provided an age of 519 ± 31 Ma (Oliveira, 2002).

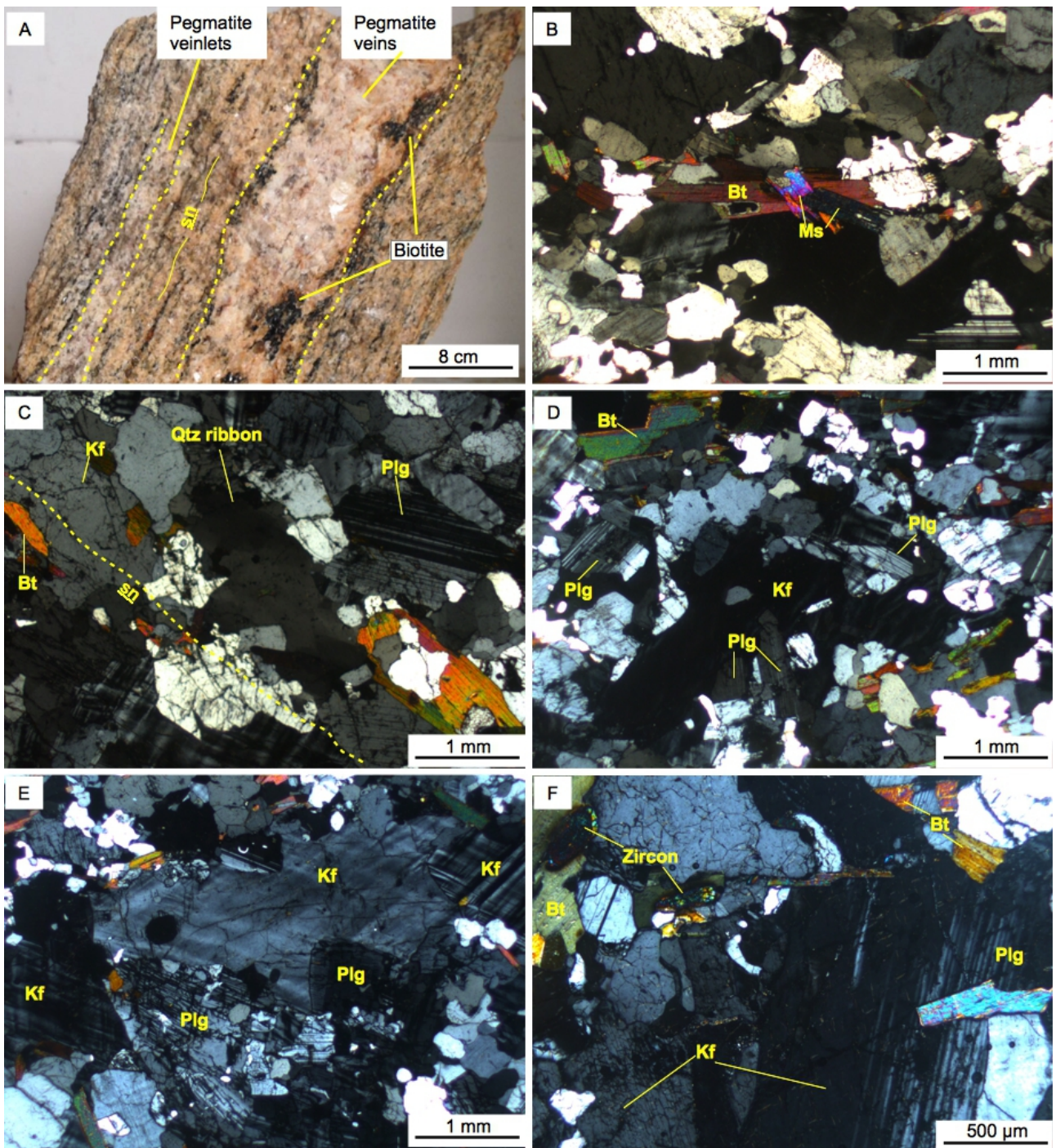


Figure 2. A: Representative sample from Açucena granite. Foliated granite with pegmatic (leucosome) veins and veinlets with biotite concentration on the borders. Photomicrographs: B: Secondary muscovite overgrowth on biotite. C: Recrystallized quartz ribbon defining the main foliation with biotite. D: K-feldspar overgrowth on plagioclase crystals. Plagioclase show euhedral relict texture. E: K-feldspar overgrowth on plagioclase crystals. F: Zircon crystals showing pleochroic halos on biotite. Bt: biotite, Kf: K-feldspar (microcline), Qtz: quartz, Ms: muscovite, Plg: plagioclase, sn: foliation.

4.1 Petrographic studies

The pluton consists of medium- to coarse-grained rocks with variable plagioclase content, and its composition varies from alkali-feldspar granite to granodiorite (Fig. 3). Concordant pegmatite veins are common, and represent up to 20 vol. % of the granite (Fig. 2a). The veins thickness varies from 1 to 5 cm, and are composed by quartz (20-30 %) and K-feldspar (70-80 %). The main minerals are K-feldspar (microcline – 30-40 %), plagioclase (albite – 20-30 %), quartz (20-30 %), iron-rich biotite (10-20 %), with subordinate (less than 5 %) muscovite, fluorite, allanite, titanite, ilmenite, zircon, monazite and magnetite (Fig. 2b,f). Perthite crystals are common, with K-feldspar as the host and albite as the lamellae. Biotite is the last mineral to crystallize. A strong tectonic foliation is defined by biotite aggregates and recrystallized quartz ribbons (Fig. 2c). Evidences of metasomatism include potassic alteration (Fig. 2d, e) and weak biotite chloritization.

4.2. Whole-rock geochemical results

Major element analyses (Appendix 1) indicate a felsic composition ($\text{SiO}_2 = 73.3$ to 75.3 wt. %) and moderate alkali contents ($\text{K}_2\text{O} = 4.4$ to 5.6 wt. %, $\text{Na}_2\text{O} = 2.8$ to 4.0 wt. %) with high $\text{K}_2\text{O}/\text{Na}_2\text{O}$ (1.1 to 1.6) and $\text{FeO}/(\text{FeO} + \text{MgO})$ (0.9 to 1.0) ratios.

The granite has peraluminous to metaluminous affinity ($\text{Al}_2\text{O}_3 / (\text{Na}_2\text{O} + \text{K}_2\text{O} + \text{CaO})$ molar = 0.99 to 1.30); low CaO content (0.1 to 0.6 wt. %), MgO (0.01 to 0.54 wt. %), TiO_2 (0.1 to 0.2 wt. %), P_2O_5 (below detection), and is enriched in Ga (32 to 41 ppm). Primitive mantle-normalized ([Taylor and McLennan, 1985](#)) patterns show its enrichment in REE and most incompatible elements (Cs, Rb, Th, U, K, Ta, Nb, Hf, Zr) with exception of Ba, Sr and Ti; and depletion in V, Cr and Ni. The ΣREE values range from 346 to 1969 ppm, LREE/HREE ratios from 2.8 to 7.0, $(\text{La}/\text{Yb})_{\text{N}}$ from 1.4 to 8.7, and Eu/Eu^* from 0.7 to 0.16 (normalized according to C1 chondrite, [Taylor and McLennan, 1985](#)). These geochemical signatures are similar to previous Açucena studies by [Oliveira \(2002\)](#) and [Braga et al. \(2015\)](#). In the REE spidergram (normalized to C1 chondrite of [Sun and McDonough, 1989](#)), the samples show a similar pattern with a negative Eu anomaly, but less pronounced HREE depletion compared to the [Oliveira \(2002\)](#) and [Braga et al. \(2015\)](#) results (Fig. 4). Borrachudos samples show A-type signature (Fig. 5a), however according to the discrimination diagrams from [Eby \(1992\)](#) the Borrachudos samples show an A₂-type signature (Fig 5b and c), which is typical of magmas derived from continental crust or underplated crust that has been through a cycle of continent-continent collision, or island-arc magmatism.

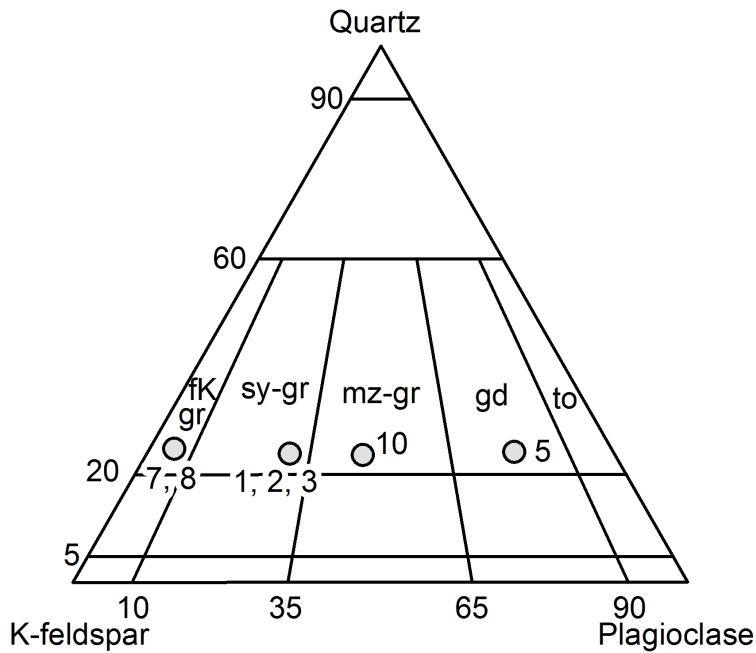


Figure 3. Classification of igneous rocks from the Açuçena pluton in the Q-A-P diagram (Streckheisen, 1967). Abbreviations: fK gr = alkali feldspar granite, sy-gr = syenogranite, mz-gr = monzogranite, gd = granodiorite, to = tonalite.

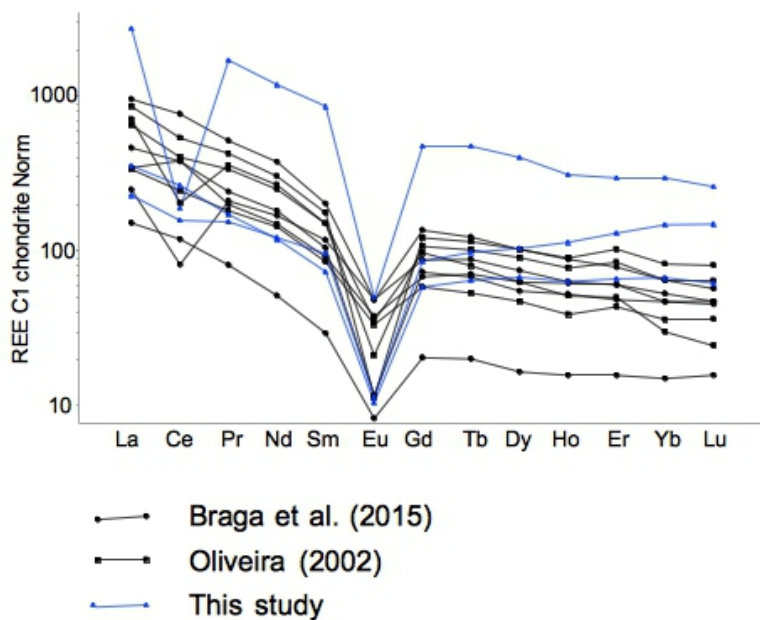


Figure 4. Chondrite-normalized REE patterns for samples BG2, BG5 and BG10 compared to the previous results on Açuçena Granite. Chondrite values are from Sun and McDonough (1989).

5. Zircon morphology and U-Th-Pb SHRIMP results

Considerable complexity is observed in the zircon population of all samples. The dominant zircon type is euhedral to irregular shaped, displays an oscillatory-zoned magmatic core, and overgrowth-recrystallized areas with variable size and shapes (Fig. 6), no inherited zircon (xenocrysts) was found. According to [Li et al., 2013](#), possible mechanisms of zircon growth and/or recrystallization in metamorphosed rocks include: (1) subsolidus metamorphic reactions of decomposing Zr-bearing minerals; (2) precipitation from metamorphic aqueous fluid; (3) crystallization from hydrous melt during crustal anatexis; (4) solid-state and replacement recrystallization of preexisting zircon (magmatic areas) by diffusion-reaction process; and (5) recrystallization of preexisting zircon by a coupled dissolution-reprecipitation process.

Three types of zircon crystallization mechanism were identified in the Açuçena samples: (1) magmatic crystallization (Fig. 6); (2) hydrothermal areas due to replacement recrystallization (e.g. transgressive recrystallization; [Hoskin and Black, 2000](#)), where metamorphic fluid is accessible to fractures and margins (Fig. 6); and (3) anatetic zircons-areas, where new growth areas surrounds euhedral magmatic cores without replacement textures (Fig. 6), due to crystallization from hydrous melt during crustal anatexis (see section 7.2 for further evidence). In some zircons, the magmatic domains have been resorbed by aqueous fluid or hydrous melt before the 1 and 2 mechanisms of zircon crystallization.

Pure metamorphic reactions (subsolidus and/or solid-state reactions) is not a possible interpretation because the metamorphic temperatures established for Açuçena Granite (amphibolite facies) are lower than the most common zircon crystallization temperature in the granulite facies ([Rubatto, 2002](#)).

The zircon crystals are colorless and transparent with intense fractures, and their lengths range from 150 to 450 µm, with length/width ratios from 2:1 to 4:1. Sector zoning, planar banding and more complex, irregular microstructures are also observed (Fig. 6). The CL images reveal internal structures, mainly magmatic textures (e.g. zoning), while BSE images, associated with qualitative EDS microanalyses, are most effective to distinguish metamict zones and to reveal hydrothermal-anatetic areas and associated minerals (e.g. xenotime in sample BG7; Fig. 6). Hydrothermal-anatetic areas present brighter BSE signals, due to its higher U content (Appendix A) compared to magmatic areas (Fig. 6). The magmatic cores present higher Th/U ratios from 0.25 to 1.3 (Fig. 7, Appendix A), bright luminescence, oscillatory-zoned pattern, and are intensely fractured. On the other hand the hydrothermal-anatetic areas present low Th/U ratios from 0.1 to 0.01 (Fig. 7, Appendix A), no luminescence, and sealing of the pre-existing fractures (Fig. 6).

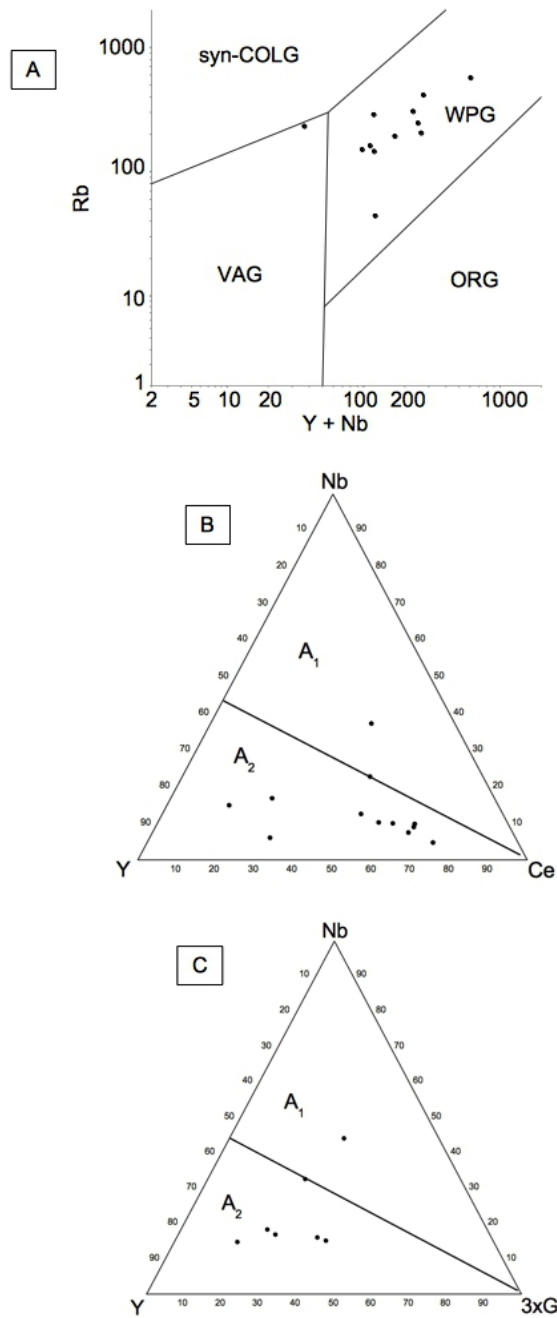


Figure 5. (A) Tectonic discriminant diagram of Pearce et al. (1984). (B) and (C) triangular plots for distinguishing between A_1 and A_2 granitoids of Eby (1992). WPG - within-plate granites; COLG - collisional granites; VAG - volcanic-arc granites; ORG - ocean-ridge granites. See text for discussion.

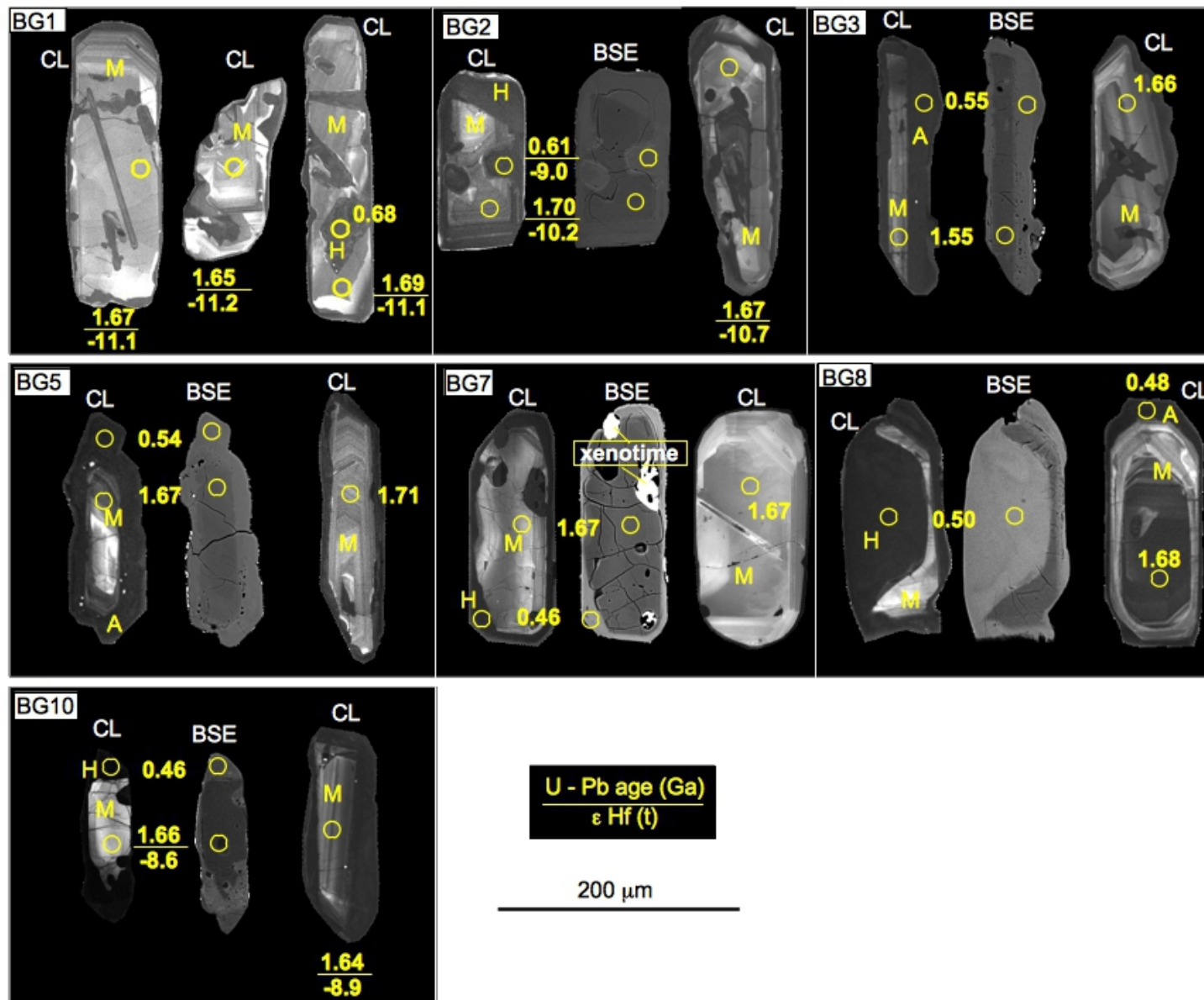


Figure. 6. Representative CL and BSE images of zircon grains for analyzed samples. Sample BG7 shows xenotime crystal associated with zircon. M: magmatic areas; H: hydrothermal areas; A: anatetic areas.

One hundred and fifteen spots were analyzed for U-Pb isotopes in 90 zircon grains (Appendix A), returning three age populations: (1) around 1700 Ma, interpreted as the magmatic crystallization age; (2) between 687-572 Ma, interpreted as the hydrothermal only event, without anatetic crystallization; and (3) between 553-465 Ma, interpreted as the anatetic event, with both hydrothermal and anatetic crystallization. Since the pegmatite veins were avoided during the sampling of the granite, the zircons with anatetic areas are probably related to the domains of the rock enriched in pegmatite veinlets (Fig. 2a), and the occurrence of hydrothermal areas in the 553-465 Ma time range are probably related to the areas of the rock not affected by the anatexis but with influence of anatetic and/or metamorphic fluids. Some of these analyses yield discordant results due to lead-loss. The distribution of these data on the concordia diagram of samples BG2, BG8 and BG10 (Fig. 8) is consistent with episodic lead-loss around 500 Ma.

Fourteen analyses were carried out on the zircon grains from BG1 (Appendix A), thirteen located in magmatic cores and one in hydrothermal overprint. Seven of these analyses in magmatic areas are more than 10% discordant. The distribution of these data along the discordia line results in the upper intercept age of 1698 ± 16 Ma ($n=10$, MSWD=7.5, Fig. 8), with recent lead loss at 130 ± 89 Ma. The analysis in the hydrothermal area yields apparent $^{206}\text{Pb}/^{238}\text{U}$ age of 687 ± 17 Ma, with +24% of discordance (Appendix A).

Nine magmatic cores, one hydrothermal area and one anatetic area were analyzed in the zircon grains from BG2. The distribution of the data along the discordia line results in the upper intercept age of 1670 ± 14 Ma ($n=9$, MSWD=3.9), with a lower intercept of 549 ± 59 Ma. The analyses in the anatetic and hydrothermal areas yield concordant, apparent $^{206}\text{Pb}/^{238}\text{U}$ ages of 548 ± 12 Ma and 614 ± 14 Ma, respectively.

Thirteen analyses in magmatic cores of the zircon grains from BG3 are distributed along the discordia line with upper intercept age of 1657 ± 20 Ma ($n=8$, MSWD=3.1). One analysis in the anatetic area yields a concordant $^{206}\text{Pb}/^{238}\text{U}$ age of 551 ± 12 Ma (Fig. 8).

Eleven analyses on magmatic cores in the zircon grains from BG5 yield U-Pb results on a line that intercepts the concordia curve at 1688 ± 20 Ma (MSWD=8.7). Analyses in one anatetic and one hydrothermal areas yield concordant to sub-concordant apparent $^{206}\text{Pb}/^{238}\text{U}$ ages of 572 ± 13 Ma and 545 ± 12 Ma, respectively.

Eight analyses on the magmatic cores of the zircon grains from BG7 define a concordia age of 1688 ± 5 Ma (MSWD=0.74), and the ages on the hydrothermal areas range from 465 ± 5 Ma to 511 ± 7 Ma (Fig. 8).

The analyses on the magmatic cores of the zircon grains extracted from the samples BG8 and BG10 yield upper intercept ages of 1701 ± 12 Ma ($n=14$, MSWD=3.7), and 1690 ± 16 Ma ($n=7$, MSWD=2.5), respectively. The lower intercept of the discordia lines are 455 ± 45 Ma for BG8, and 528 ± 23 Ma for BG10. These lower intercepts coincide with the ages from hydrothermal-anatectic domains, which range from 469 ± 6 Ma to 553 ± 5 Ma, and are thus interpreted to reflect lead loss during these thermal events (Fig. 8).

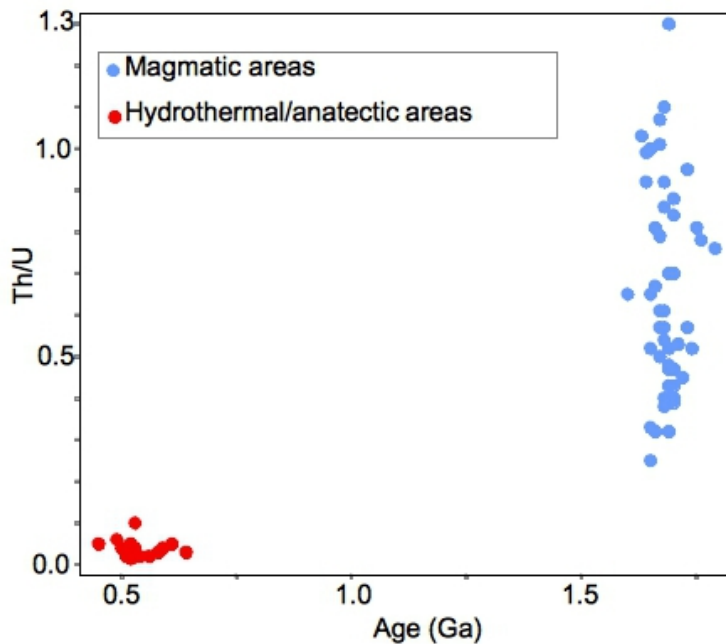


Figure 7. Th/U ratio vs. age of analyzed zircon, discriminating the metamorphic areas with low Th/U ratios from the magmatic zircons with wide variation in the Th/U ratios. See text for discussion.

6. Zircon Hf isotopes

The analyses on magmatic cores from sample BG1 show $^{176}\text{Lu}/^{177}\text{Hf}$ ratios ranging from 0.0008 to 0.0015, and $^{176}\text{Hf}/^{177}\text{Hf}$ ratios from 0.28143 to 0.28146. The $\epsilon\text{Hf}(t)$ values, back-calculated to the U-Pb age of the same area of the zircon, range from -10.2 to -11.2 (Table 1).

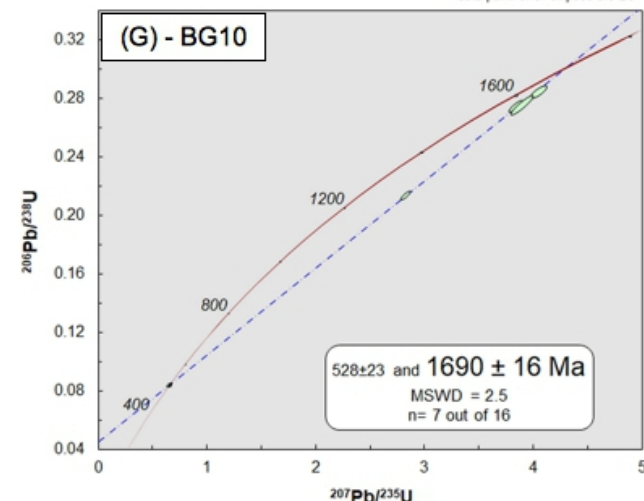
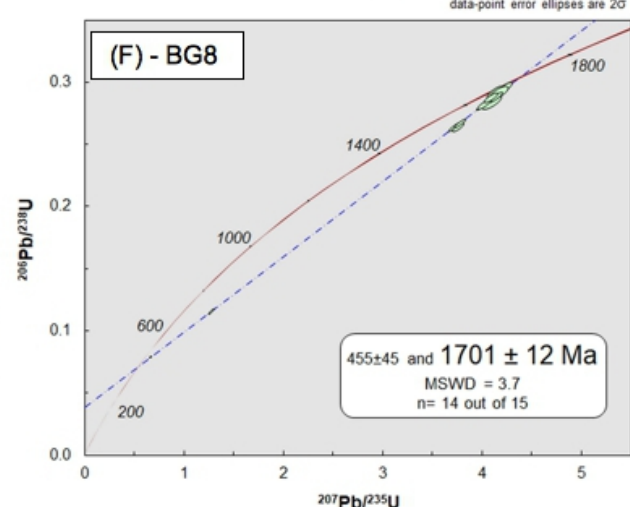
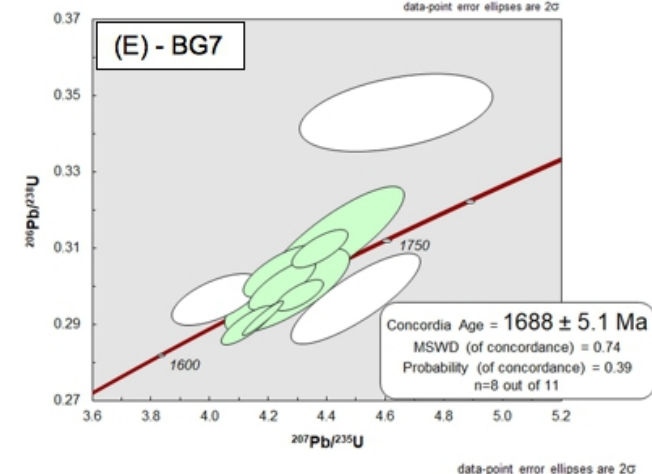
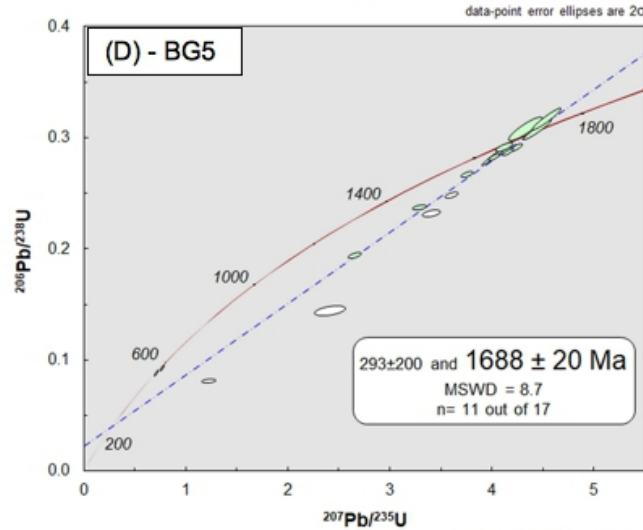
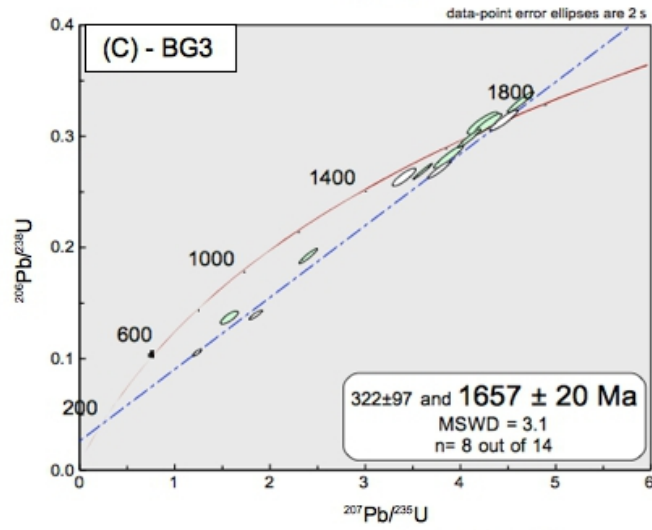
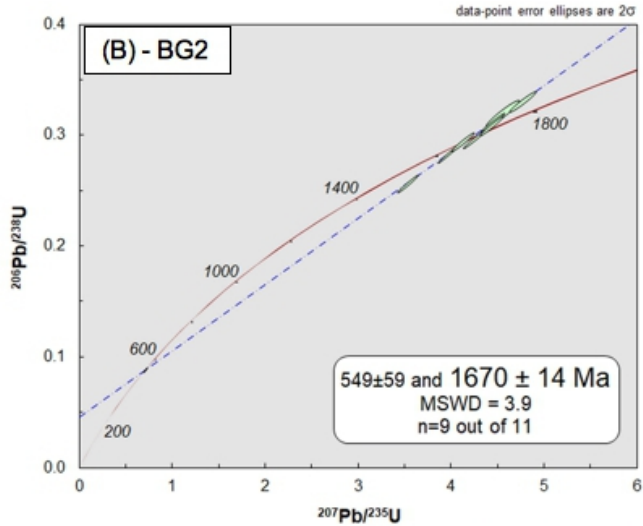
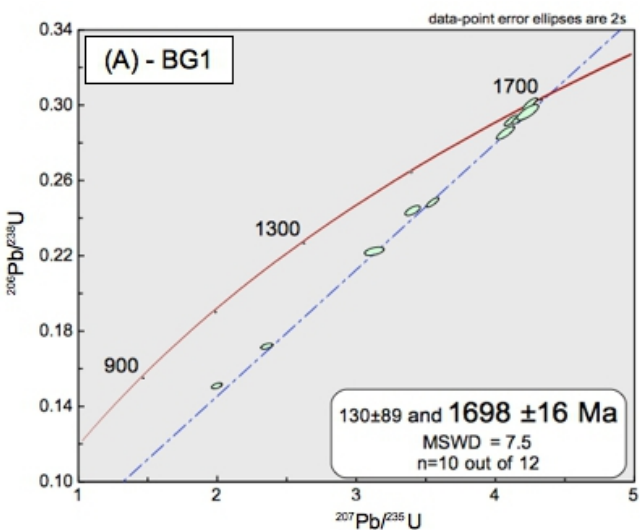


Figure 8. U–Pb concordia plots and age determination for analyzed samples. For sample location see Fig. 1.

Zircon magmatic cores from BG2 show similar Lu–Hf isotope features to zircons of BG1. They have $^{176}\text{Lu}/^{177}\text{Hf}$ ratios from 0.00069 to 0.00207, $^{176}\text{Hf}/^{177}\text{Hf}$ ratios of 0.28144 to 0.28148, and $\epsilon\text{Hf(t)}$ values varying from -9.0 to -11.8. One Hf analysis on hydrothermal area crystallized at 614 ± 14 Ma yields a higher $^{176}\text{Hf}/^{177}\text{Hf}$ (0.282154) ratio, but similar $\epsilon\text{Hf(t)}$ value of -9.0.

Zircon grains analyzed from BG8 have magmatic cores with slight lower $^{176}\text{Lu}/^{177}\text{Hf}$ (0.00054 – 0.00167) and $^{176}\text{Hf}/^{177}\text{Hf}$ (0.28135 - 0.28141) ratios, and slight lower $\epsilon\text{Hf(t)}$ values from -11.3 to -13.7.

Analytical Hf results for magmatic zircon cores from BG10 yield similar $^{176}\text{Hf}/^{177}\text{Hf}$ ratio (0.28149 - 0.28156), and slight higher $\epsilon\text{Hf(t)}$ values (-6.8 to -9.5). One anatetic area crystallized at 520 ± 6 Ma presents a much lower $\epsilon\text{Hf(t)}$ value of -34.3.

Most calculated T_{DM} ages vary from 2.38 to 2.61 Ga, one hydrothermal area from BG2 present T_{DM} age of 1.52 Ga (Table 1).

Due to the age complexity of the zircon grains in all samples, six analyses on hydrothermal/anatetic areas resulted in mixed signals, where the laser sampled material of different age. These mixed analyses yield higher $^{176}\text{Hf}/^{177}\text{Hf}$ (0.28215) ratios and much younger calculated T_{DM} ages from 2.12 to 0.79 Ga, and these are not considered further.

7. Discussion

7.1. Geochronological framework of the Açucena Granite

Since the early 1990s, the Borrachudos Suite has been the focus of geochronological and petrological studies. [Dossin et al. \(1993\)](#), [Chemale Jr. et al. \(1998\)](#), and [Fernandes et al. \(2000\)](#) reported Pb-evaporation ages from 1670 to 1770 Ma. However, due to the age complexity and hydrothermal overgrowth in these zircons, most of the analyses yielded discordant results, and the exact duration of the Borrachudos magmatism could not be determined. [Silva et al. \(2002\)](#) reported a high-precision SHRIMP zircon U-Pb age of 1740 ± 8 Ma for Açucena batholith, but the sample location is unclear.

In combination with previously published data, the new U–Pb ages support a geochronological framework for the Açucena magmatic crystallization evolution (Appendix A). The lack of inherited zircons can be explained by the high temperature ($\sim 850^\circ \text{C}$, [Dussin, 1994](#)) of the magma that

dissolved any zircon grains assimilated from the source rocks.

Table 1. Zircon Lu–Hf isotope data for BG1, BG2, BG8, and BG10.

Spot	Age (Ma)	$^{176}\text{Yb}/^{177}\text{Hf}$	2σ	$^{176}\text{Lu}/^{177}\text{Hf}$	2σ	$^{176}\text{Hf}/^{177}\text{Hf}$	2σ	$^{176}\text{Hf}/^{177}\text{Hf}$ (t)	$\epsilon\text{ Hf}$ (t)	T_{DM} (Ga)
BG1										
S15	1702	0.051040	0.0024	0.001528	0.0001	0.281461	0.0000	0.281412	-10.2	2.50
S12	1697	0.039960	0.0021	0.001128	0.0001	0.281427	0.0000	0.281391	-11.1	2.53
S7	1654	0.025781	0.0002	0.000767	0.0001	0.281440	0.0000	0.281416	-11.2	2.50
S4	1677	0.039370	0.0019	0.001094	0.0001	0.281438	0.0000	0.281403	-11.1	2.52
S3	1700	0.029136	0.0005	0.000848	0.0001	0.281429	0.0000	0.281402	-10.6	2.52
BG2										
S11	1700	0.032710	0.0006	0.001006	0.0000	0.281478	0.0000	0.281446	-9.1	2.46
S9	1690	0.059192	0.0015	0.001766	0.0000	0.281459	0.0000	0.281403	-10.8	2.52
S8	1655	0.036324	0.0007	0.001083	0.0000	0.281444	0.0000	0.281410	-11.4	2.51
S7	614	0.030695	0.0022	0.000978	0.0001	0.282154	0.0000	0.282142	-9.0	1.52
S6	1707	0.031508	0.0003	0.000908	0.0000	0.281440	0.0000	0.281411	-10.2	2.51
S5	1650	0.066536	0.0016	0.002065	0.0001	0.281465	0.0000	0.281401	-11.8	2.52
S4	1714	0.066536	0.0016	0.002065	0.0001	0.281465	0.0000	0.281398	-10.4	2.52
S2	1685	0.049536	0.0002	0.001481	0.0000	0.281438	0.0000	0.281391	-11.4	2.53
S1	1679	0.023147	0.0002	0.000690	0.0000	0.281435	0.0000	0.281413	-10.7	2.50
BG8										
S15	1676	0.022442	0.0009	0.000673	0.0000	0.281352	0.0000	0.281330	-13.7	2.61
S9	1694	0.027517	0.0008	0.000868	0.0000	0.281414	0.0000	0.281386	-11.3	2.54
S7	1678	0.055038	0.0015	0.001671	0.0001	0.281411	0.0000	0.281358	-12.7	2.58
S6	1690	0.017084	0.0006	0.000536	0.0000	0.281357	0.0000	0.281340	-13.1	2.60
S5	1662	0.028710	0.0031	0.000843	0.0001	0.281403	0.0000	0.281377	-12.4	2.55
S4	1696	0.033165	0.0038	0.000960	0.0001	0.281372	0.0000	0.281341	-12.9	2.60
S3	1710	0.017444	0.0004	0.000543	0.0000	0.281357	0.0000	0.281339	-12.6	2.60
S2	1686	0.018433	0.0003	0.000576	0.0000	0.281381	0.0000	0.281363	-12.3	2.57
BG10										
S16	1669	0.037370	0.0033	0.001147	0.0001	0.281491	0.0000	0.281454	-9.5	2.45
S14	520	0.059857	0.0034	0.001790	0.0001	0.281505	0.0000	0.281487	-34.3	2.40
S8	1681	0.034913	0.0021	0.001077	0.0000	0.281495	0.0000	0.281461	-9.0	2.44
S7	1648	0.072779	0.0046	0.002062	0.0001	0.281549	0.0001	0.281484	-8.9	2.41
S4	1763	0.029156	0.0017	0.000909	0.0001	0.281499	0.0000	0.281469	-6.8	2.43
S3	1661	0.052552	0.0008	0.001666	0.0000	0.281536	0.0000	0.281484	-8.6	2.41
S2	1609	0.063465	0.0030	0.001911	0.0001	0.281560	0.0000	0.281502	-9.2	2.38

The Borrachudos A₂-type magmatism started at 1740±8 Ma, and lasted until 1688±5 Ma, indicating a long-lived magmatic event coeval with the onset of the lower Espinhaço basin ([Martins Neto, 1998; Alkmim and Martins Neto, 2012; Chemale et al., 2012; Guadagnin et al., 2015](#)).

This study reports the first zircon $^{206}\text{Pb}/^{238}\text{U}$ hydrothermal/anatetic ages for Borrachudos Suite related to the Brasiliano orogen (650-500 Ma), and these range from ca. 690 to 450 Ma (Appendix A). The large spread in ages is interpreted to represent incomplete re-setting of the U-Pb isotopic compositions due to varying degrees of partial recrystallization. This could be the reason for the frequent mixed signals in the Hf isotope analyses (see section 6). The youngest ages represent the new growth portions of the zircons, and provide the timing of the anatetic event. The age of this anatetic event is in agreement with U-Pb ages of: metamorphic titanite (507 Ma, for Morro do Urubu Granite, [Fernandes et al., 2000](#); 512 \pm 4 Ma, for Açucena Granite, [Braga, 2018](#)); zircon from pegmatite dikes ([Bilal et al., 1995](#); [Braga, 2018](#)); and titanite from migmatites (512 \pm 5 Ma, [Machado et al., 1989](#)). These suggest that huge amounts of hydrothermal fluids accompanied the partial melting episodes during the late Brasiliano tectono-thermal event in this portion of the Araçuaí belt (hydrous melt). This anatetic event are coeval with the titanite crystallization in the emerald host rock at the Piteiras Mine (Fig. 1; 576 \pm 7 Ma – U-Pb in titanite; [Jordt Evangelista et al., 2016](#)), suggesting that the partial melts of the Açucena Granite are the source of the pegmatite magmas and the beryllium-rich fluids that formed the emerald crystals.

7.2. Source and evolution of the magmas and fluids

Magmatic zircon cores from the Açucena Granite display low $\epsilon\text{Hf(t)}$ values, typical of magmas derived from ancient continental crust (-13.7 to -6.8, Table 1, Fig. 9). These magmatic zircons yield T_{DM} ages ranging from 2.38 to 2.61 Ga. These data demonstrate that the granitic magmas derived from partial melting of old continental crust.

Partial melting and assimilation of rocks from the Guanhães Complex probably contributed to the formation of the Borrachudos Suite, because it is the main lithologic unit in the area, and the geochronological data show that it was mainly formed during the Neoarchean (2.80 to 2.53 Ga; [Silva et al., 2002](#)). Thus, these ages are in general agreement with the T_{DM} ages of magmatic zircon from the Açucena granite. Also, these T_{DM} ages are just bit younger than the period of exceptional rates of crustal growth at 2.7 Ga ([Hawkesworth et al., 2010](#)).

The $\epsilon\text{Hf(t)}$ values range from -13.7 to -6.8 in the magmatic areas of the zircons for all samples. However, zircons from individual samples show less pronounced variation. Sample BG8 presents the lowest values of $\epsilon\text{Hf(t)}$ (between -11.3 to -13.7), and sample BG10 the highest (-6.8 to -9.5). Also, BG10 presents the most variable results. These indicate that magmas crystallized from isotopically heterogeneous crustal anatetic melts. The assimilation (contamination) of crust during the ascent of the magmas from the lower crust could also explain the heterogeneity in the isotope

composition.

The identification of open-system processes that elevate the $^{176}\text{Hf}/^{177}\text{Hf}$ ratio of the melt from which the zircons precipitated can be accomplished by pairing the Hf isotope variations with trace element ratios (such as Th/U) that are proxies for the degree of differentiation (Kemp et al., 2007). In the cases of samples BG1, BG2, and BG8, the ϵHf values of the zircons broadly decrease with Th/U (Fig. 10). This suggests a progressive reduction in the $^{176}\text{Hf}/^{177}\text{Hf}$ ratio during the magmatic evolution of each suite, as could be induced by the addition of an unradiogenic (continental crust-like) component. Sample BG10 exhibit isotopic reversal in the pluton, when the ϵHf values increase while the Th/U decrease, and also presents the highest and most variable $\epsilon\text{Hf(t)}$. This could suggest that the evolution of the Açuçena pluton was punctuated by juvenile magma replenishments that reworked the supracrustal materials.

Metamorphic zircons can be formed by dissolution and re-precipitation of pre-existing zircon in anatectic melts or fluids (Flowerdew et al., 2006; Wu et al., 2007; Zheng, 2009); and/or by solid-state recrystallization of zircon grains (Hoskin and Black, 2000). These processes may affect the Hf isotope composition of the zircon crystals (Chen et al., 2015). When compared to older magmatic domains, the new overgrowth (or recrystallized) zones derived from melts and/or external fluid interaction generally exhibits elevated initial $^{176}\text{Hf}/^{177}\text{Hf}$ values (Chen et al., 2015; Ge et al., 2013).

Anatectic zircon crystallization with Cambrian age (ca. 480-550 Ma) is probably related to a crustal anatexis event that produced large amounts of pegmatite dikes and fluids during the gravitational collapse of the Brasiliano orogen (Pedrosa Soares et al., 2011) (Fig. 11). The anatectic new zircon growth is characterized by similar Hf isotope values (Fig. 9b) compared to the magmatic areas, suggesting that the high degree of partial melting did not affected the Hf composition of the melt.

In the time range 687-572 Ma only hydrothermal recrystallization was detected in the Açuçena zircon grains. These hydrothermal age are probably related to the metamorphic peak of the Brasiliano orogen. One hydrothermal area in this time range (614 Ma) present low $^{176}\text{Lu}/^{177}\text{Hf}$ values and high $^{176}\text{Hf}/^{177}\text{Hf}$ ratios (Fig. 9b, Table 1), implying ^{176}Hf input into the system at this time. Chen et al. (2015) attributed the higher initial $^{176}\text{Hf}/^{177}\text{Hf}$ values in zircon rim (hydrothermal and/or anatectic) compared to the relict cores to interaction with melt and/or fluid enriched in Hf. In the hydrothermal recrystallized border of the Borrachudos zircon, this enrichment could be caused by small amounts partial melting reactions involving breakdown of REE-rich mineral such as apatite or titanite, which elevated the $^{176}\text{Hf}/^{177}\text{Hf}$ ratios into the system.

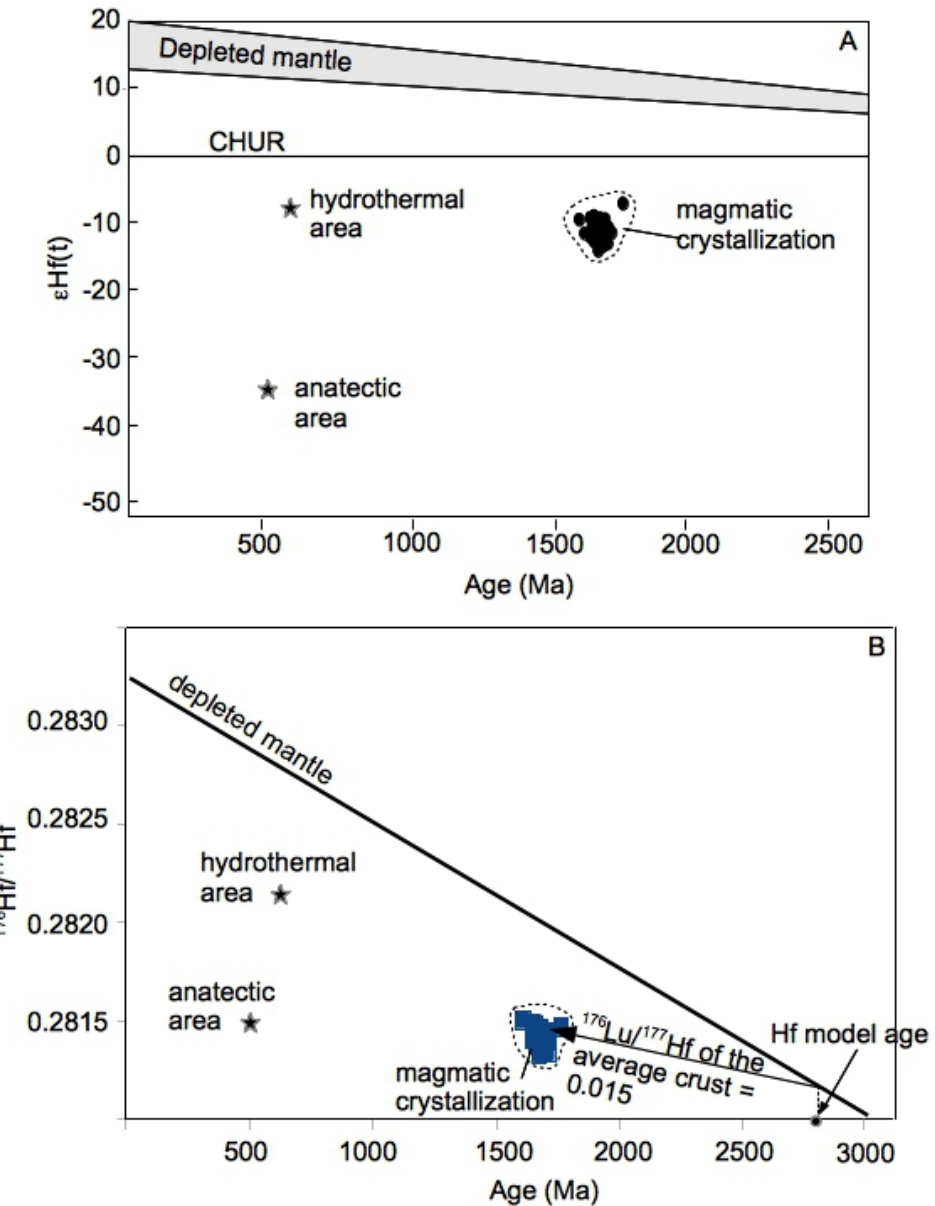


Figure 9. (A) $\epsilon\text{Hf}(t)$ vs. age plot showing the $\epsilon\text{Hf}(t)$ values of magmatic zircon cores and metamorphic zircon rims. CHUR: chondrite uniform reservoir. Depleted mantle evolution is calculated by using $\epsilon\text{Hf}(t) = 16.9$ at $t=0$ Ma and $\epsilon\text{Hf}(t) = 6.4$ at $t = 3.0$ Ga. (B) $^{176}\text{Hf}/^{177}\text{Hf}$ vc. age plot showing the calculated Hf model age of the magmatic zircon areas according to $^{176}\text{Lu}/^{177}\text{Hf}$ ratio of the average crust (0.015). The hydrothermal and anatetic areas show contrasting values of $^{176}\text{Hf}/^{177}\text{Hf}$ ratio, one similar and the other elevated ratio compared to magmatic areas.

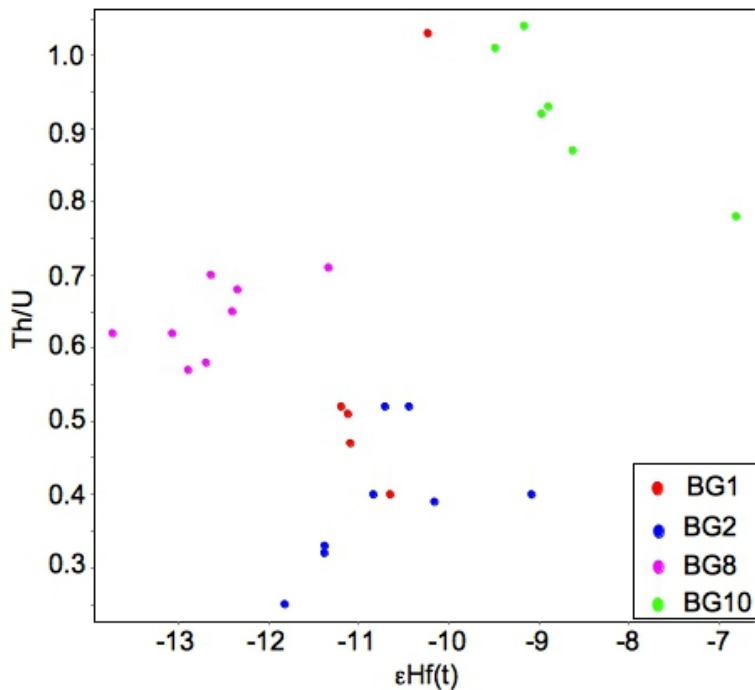


Figure 10. Hf isotopic compositions of magmatic areas (~ 1700 Ma) of the zircons from BG1, BG2, BG8, and BG10 samples plotted against the Th/U ratio measured for the same part of the crystal.

This hydrothermal/anatectic event is well documented in the south border of the CSF. [Martins et al. \(2016\)](#) report late Brasiliano, Cambrian age imprint (518 ± 9 Ma; U-Pb SHRIMP on xenotime) associated with the gold host rock of the Archean-age Lamego gold deposit in the adjacent Quadrilátero Ferrífero mineral province. Also, [Cabral et al. \(2015\)](#) describe mineralization of palladiferous gold in specular hematite-rich lodes at the Conceição Fe-ore deposit (Fig. 1), that are associated with monazite of late Cambrian age (495 ± 2 Ma). These ages corroborate an orogen-scale hydrothermal overprint at later stages of the Brasiliano event.

7.3. The role of the Açuçena Granite in the formation of the genetically and/or spatially associated iron, emerald, and gold-palladium deposits

Regional metamorphic remobilization and precipitation processes in a fluid-rich system is a prerequisite for both, the crystallization of emerald in the ultramafic host rock at Piteiras and Belmont mines ([Lynch et al., 2014](#)), and the enrichment of iron in the Piçarrão-Liberdade deposit ([Gomes et al., 2018](#)). Mineral chemistry studies of emerald from [Machado \(1998\)](#) also suggested the role of metasomatic processes in the genesis of emerald deposits associated with Açuçena Granite. Gold-Palladium mineralized veins along the Espinhaço range present hydrothermal minerals (monazite, xenotime, rutile, tourmaline), U-Pb Cambrian age (520-485 Ma, in monazite,

xenotime, and rutile), and highly evolved Sm-Nd composition ($\varepsilon_{\text{Nd}}(495) = -17 \pm 1$ in monazite) (Cabral et al., 2017; Gonçalves et al., 2017; Cabral and Zeh 2015).

This Cambrian age hydrothermal event is related to the gravitational collapse of the Brasiliano orogen in the Araçuaí belt, and the generation and emplacement of post-collisional granites (G5 suite; Pedrosa Soares et al., 2011). The new coupled U-Pb age and Hf composition in the recrystallized/new growth zircon from the Açuena Granite corroborate these conclusions and suggest that a long-lived thermal event (ca. 480-600 Ma) is related to anatexis and intense hydrothermal fluid flow in the southern SFC and adjacent areas. Gomes et al. (2018) also described anatetic signatures in the fluid inclusions trapped in quartz crystals from pegmatite and quartz veins associated with the high-grade iron bodies in the Picarrão-Liberdade mine.

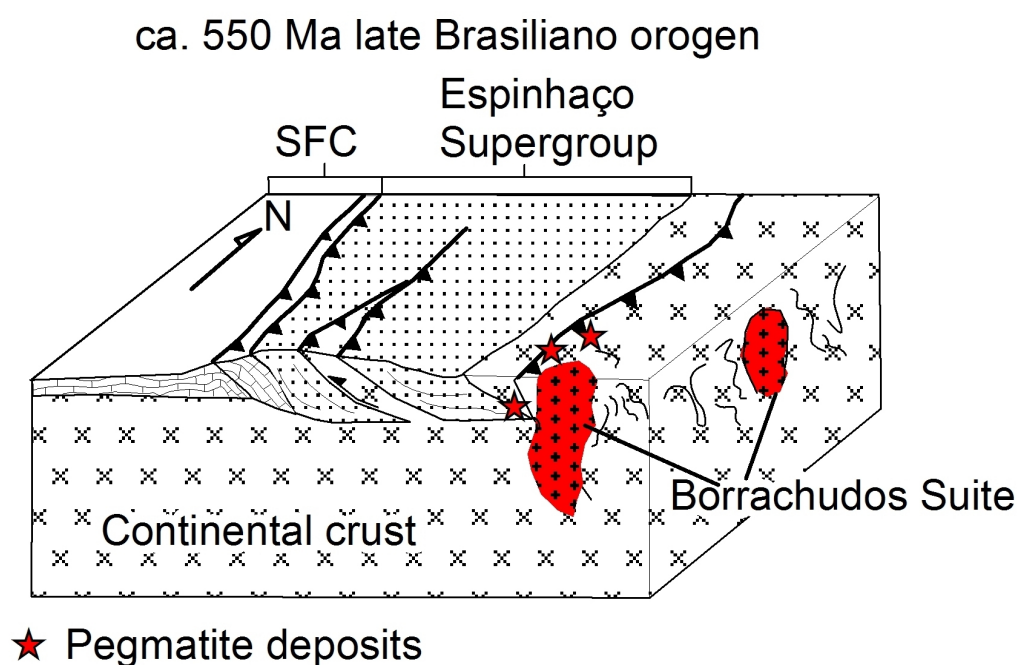


Figure 11. Brasiliano orogen and the formation of the pegmatite deposits. SFC: São Francisco craton. (see text for discussion).

The enrichment in radiogenic Hf in the Cambrian zircon border indicate that a low-degree melting (anatexis) episode in the Borrachudos Suite (and probably also in the Guanhães Complex) generate

large amounts of hydrothermal fluids and driven the formation of the iron and emerald deposits. The hydrothermal fluids, channelized by shear or fault zones, facilitated fluid-rock reactions responsible for the upgrade of itabirite to high grade iron ore (cf. [Hagemann et al., 2016](#)) and the formation of emerald deposits.

8. Conclusions

The Açuçena Granite consists of a differentiated pluton that recorded a long-lived magmatic episode, starting at 1740 ± 8 Ma and last until 1657 ± 20 Ma. Their variable and unradiogenic zircon Hf indicate a dominantly old crustal source for the magmas, with juvenile mantle contributions. The presence of heterogeneous zircon crystals with differing age and Hf isotope components indicate that the Borrachudos Suite have long and complex thermal histories.

Metamorphic overprint during the Brasiliano orogen (~ 500 Ma) yielded anatetic melts and fluids from partial melting of the Açuçena Granite and probably also Guanhães Complex. The tectono-thermal evolution of this part of the Araçuaí belt and adjacent areas in the SFC during the late stages of the Brasiliano orogen is characterized by very large amounts of hydrothermal fluid circulation that originated from the radiogenic Hf enriched partial melts of the basement rocks of the Guanhães Complex and Borrachudos Suite. These magmatic hydrothermal fluids are temporally and spatially linked to the upgrade of itabirite to high grade iron ore and emerald formation in the Guanhães Complex.

Acknowledgments

This paper contains results of the PhD thesis of the first author at the Universidade Federal de Minas Gerais-UFMG, Brazil, who received a scholarship from 'Coordenação de Aperfeiçoamento de Pessoal de Nível Superior' - CAPES. The main research funds were provided by the Science Without Borders project from the Brazil's National Council of Technological and Scientific Development – CNPq. The authors acknowledge the facilities, and the scientific and technical assistance of the Australian Microscopy & Microanalysis Research Facility at the Centre for Microscopy, Characterisation & Analysis, The University of Western Australia, a facility funded by the University, State and Commonwealth Governments; and Prof. Peter C. Hackspacher for the facilities and assistance in the sample preparation laboratory for geochemistry and geochronology of the 'Universidade Estadual Paulista' (UNESP).

Appendix A. SHRIMP zircon U–Pb data for BG1, BG2, BG3, BG5, BG7, BG8, BG10.

Sample Spot name	Element (ppm)	$^{232}\text{Th} / ^{238}\text{U}$	^{206}Pb ppm (4-corr)	^{206}Pb %com (4-corr)	Isotope ratio (4-corr)										Apparent age (Ma) (4- corr)				% Discor- -dant
					Isotope ratio (4-corr)					Isotope ratio (4-corr)					Apparent age (Ma) (4- corr)				
					U	Th	$^{207}\text{Pb} / ^{206}\text{Pb}$	% err	$^{207}\text{Pb} / ^{235}\text{U}$	%err	$^{206}\text{Pb} / ^{238}\text{U}$	%err	err corr	$^{208}\text{Pb}/^{232}\text{U}$	%err	^{206}Pb $/^{238}\text{U}$	1 σ	^{207}Pb $/^{206}\text{Pb}$	1 σ
BG1 (monzogranite)																			
S4	425	210	0.51	106	0.044	0.10292	0.52	4.1208	0.95	0.2904	0.80	0.835	0.0676	1.23	1643	12	1677	10	+2
S5	821	1136	1.43	118	0.696	0.10137	1.31	2.3377	1.52	0.1673	0.76	0.502	0.0199	1.72	997	7	1649	24	+43
S6	337	594	1.82	71	0.082	0.10484	0.63	3.5484	1.04	0.2455	0.83	0.799	0.0161	1.35	1415	11	1711	11	+19
S7	182	91	0.52	46	0.205	0.10165	0.90	4.1088	1.40	0.2932	1.07	0.766	0.0835	1.76	1657	16	1654	17	-0
S8	164	378	2.37	36	0.572	0.10565	2.16	3.7312	2.84	0.2561	1.86	0.653	0.0173	7.41	1470	24	1726	40	+17
S9	165	69	0.43	40	0.005	0.10433	0.76	4.0795	1.29	0.2836	1.04	0.806	0.0838	1.64	1609	15	1703	14	+6
S10	311	153	0.51	65	0.436	0.10222	1.02	3.4010	1.33	0.2413	0.85	0.643	0.0394	3.19	1394	11	1665	19	+18
S11	334	117	0.36	63	0.922	0.10332	1.67	3.1218	1.88	0.2191	0.87	0.464	0.0645	4.33	1277	10	1685	31	+27
S12	301	137	0.47	75	-0.047	0.10404	0.60	4.1827	1.05	0.2916	0.87	0.821	0.0841	1.29	1649	13	1697	11	+3
S13	342	179	0.54	88	-0.020	0.10315	0.54	4.2592	1.00	0.2995	0.84	0.840	0.0872	1.15	1689	12	1682	10	-0
S14	319	412	1.34	40	0.543	0.09823	1.41	1.9740	1.65	0.1457	0.86	0.520	0.0118	2.99	877	7	1591	26	+48
S15	121	121	1.03	31	-0.082	0.10432	0.95	4.2412	1.50	0.2949	1.16	0.774	0.0866	2.10	1666	17	1702	17	+2
S16	1035	56	0.06	100	0.000	0.06860	0.72	1.0628	2.64	0.1124	2.54	0.962	0.0473	3.56	687	17	887	15	+24
S17	1675	196	0.12	167	0.531	0.07368	1.29	1.1796	2.60	0.1161	2.26	0.869	0.0470	7.45	708	15	1033	26	+33
BG2 (monzogranite)																			
S1	166	83	0.52	46	0.088	0.10302	1.00	4.5483	3.27	0.3202	3.11	0.952	0.0898	3.46	1791	49	1679	18	-8
S2	821	255	0.32	220	-0.005	0.10336	0.37	4.4495	2.32	0.3122	2.28	0.987	0.0883	2.39	1752	35	1685	7	-4
S3	1504	60	0.04	115	0.000	0.05828	0.68	0.7130	2.37	0.0887	2.27	0.958	0.0284	3.28	548	12	540	15	-1
S4	269	136	0.52	64	0.067	0.10497	1.05	4.0171	2.94	0.2775	2.74	0.935	0.0762	3.17	1579	38	1714	19	+9
S5	1385	335	0.25	338	0.059	0.10140	0.34	3.9694	2.44	0.2839	2.42	0.990	0.0814	2.59	1611	34	1650	6	+3
S6	411	156	0.39	117	-0.012	0.10460	0.59	4.7685	2.43	0.3306	2.35	0.970	0.0941	2.55	1841	38	1707	11	-9
S7	1312	38	0.03	113	-0.014	0.06116	0.75	0.8425	2.49	0.0999	2.37	0.954	0.0322	4.95	614	14	645	16	+5
S8	550	178	0.33	139	0.035	0.10170	0.52	4.1287	2.38	0.2944	2.32	0.976	0.0857	2.51	1664	34	1655	10	-1
S9	981	379	0.40	251	0.017	0.10361	0.40	4.2484	2.32	0.2974	2.28	0.985	0.0852	2.38	1678	34	1690	7	+1
S10	1312	532	0.42	290	0.072	0.09985	0.45	3.5363	2.53	0.2569	2.49	0.984	0.0763	2.71	1474	33	1621	8	+10
S11	519	202	0.40	138	-0.008	0.10421	0.47	4.4367	2.36	0.3088	2.31	0.980	0.0874	2.44	1735	35	1700	9	-2

Appendix A (cont.)

BG3 (monzogranite)

S1	145	151	1.08	38	0.085	0.10215	1.21	4.2892	2.82	0.3045	2.55	0.903	0.0877	2.88	1714	38	1664	22	-3
S2	348	154	0.46	97	-0.038	0.10360	0.76	4.6424	2.50	0.3250	2.38	0.952	0.0909	2.76	1814	38	1690	14	-8
S3	88	85	1.00	23	0.178	0.10066	1.57	4.2377	3.14	0.3053	2.72	0.866	0.0859	3.19	1718	41	1636	29	-6
S4	113	96	0.88	25	0.106	0.09652	1.52	3.3975	3.02	0.2553	2.62	0.865	0.0732	3.43	1466	34	1558	28	+7
S5	1190	48	0.04	91	-0.037	0.05851	1.42	0.7201	2.69	0.0892	2.28	0.849	0.0313	5.26	551	12	549	31	-0
S6	164	84	0.53	43	0.037	0.10511	1.06	4.4638	2.75	0.3080	2.54	0.923	0.0859	2.98	1731	39	1716	19	-1
S7	256	299	1.21	58	-0.024	0.10435	0.84	3.7700	2.57	0.2620	2.43	0.945	0.0689	2.62	1500	32	1703	15	+13
S8	108	51	0.49	12	0.827	0.08899	2.99	1.5402	4.88	0.1255	3.86	0.790	0.0587	5.11	762	28	1404	57	+48
S9	338	327	1.00	84	0.016	0.10202	0.68	4.0936	2.45	0.2910	2.36	0.961	0.0916	2.47	1647	34	1661	13	+1
S10	116	46	0.41	27	0.078	0.10230	1.14	3.8704	3.35	0.2744	3.15	0.940	0.0771	3.72	1563	44	1666	21	+7
S11	468	343	0.76	38	0.919	0.09273	1.90	1.1939	3.33	0.0934	2.73	0.821	0.0251	4.09	575	15	1482	36	+64
S12	333	406	1.26	37	0.407	0.10261	1.27	1.8145	2.94	0.1282	2.65	0.901	0.0288	3.13	778	19	1672	24	+57
S13	1088	688	0.65	244	0.148	0.09987	0.44	3.5922	2.32	0.2609	2.27	0.982	0.0790	2.37	1494	30	1622	8	+9
S14	285	180	0.65	45	0.118	0.09456	1.07	2.3782	3.20	0.1824	3.01	0.942	0.0804	4.26	1080	30	1519	20	+31

BG5 (granodiorite)

S1	109	86	0.81	27	0.111	0.10235	1.00	4.1148	1.57	0.2916	1.21	0.769	0.0834	1.69	1649	18	1667	19	+1
S2	190	99	0.54	48	0.000	0.10530	0.71	4.2293	1.22	0.2913	1.00	0.816	0.0838	1.43	1648	14	1719	13	+5
S3	174	177	1.06	35	1.505	0.10615	1.80	3.3951	2.07	0.2320	1.02	0.494	0.0533	2.24	1345	12	1734	33	+25
S4	266	176	0.68	57	0.650	0.10512	1.16	3.6008	1.48	0.2484	0.91	0.615	0.0635	2.24	1430	12	1716	21	+19
S5	272	101	0.38	67	0.022	0.10488	0.57	4.1530	1.04	0.2872	0.87	0.837	0.0809	1.40	1628	13	1712	11	+6
S6	784	300	0.40	97	5.874	0.12091	4.49	2.4042	5.08	0.1442	2.37	0.466	0.0888	4.51	868	19	1970	80	+60
S7	1164	487	0.43	81	9.222	0.10881	4.27	1.2174	4.50	0.0811	1.43	0.318	0.0329	5.39	503	7	1780	78	+74
S8	379	206	0.56	87	0.071	0.10188	0.90	3.7494	1.21	0.2669	0.80	0.666	0.0763	1.12	1525	11	1659	17	+9
S9	1367	627	0.47	278	0.728	0.10047	1.40	3.2828	1.57	0.2370	0.73	0.461	0.0650	1.94	1371	9	1633	26	+18
S10	278	154	0.57	67	0.115	0.10308	0.65	4.0185	1.09	0.2827	0.87	0.804	0.0810	1.28	1605	12	1680	12	+5
S11	802	440	0.57	134	1.753	0.09869	1.54	2.6428	1.94	0.1942	1.18	0.608	0.0490	3.62	1144	12	1600	29	+31
S13	297	140	0.49	78	0.000	0.10479	0.75	4.4426	2.52	0.3075	2.41	0.954	0.0852	2.66	1728	37	1711	14	-1
S14	1113	35	0.03	89	-0.043	0.05951	0.99	0.7612	2.49	0.0928	2.29	0.917	0.0332	6.87	572	13	586	22	+2
S15	87	86	1.03	23	0.061	0.10176	1.41	4.3214	3.09	0.3080	2.75	0.889	0.0856	3.15	1731	42	1656	26	-5
S16	506	159	0.32	123	0.019	0.10248	0.53	4.0095	2.38	0.2838	2.32	0.975	0.0856	2.50	1610	33	1670	10	+4
S17	1410	61	0.04	107	0.176	0.05749	1.06	0.6993	2.56	0.0882	2.33	0.911	0.0255	9.40	545	12	510	23	-7
S18	206	87	0.44	56	0.000	0.10355	0.79	4.5283	2.54	0.3172	2.42	0.951	0.0911	2.71	1776	38	1689	15	-6

Appendix A (cont.)

BG7 (alkali feldspar granite)

S1	51	38	0.77	13.0	-0.76	0.10997	2.29	4.4975	4.01	0.2966	3.30	0.821	0.0879	5.54	1675	49	1799	42	+8
S2	346	97	0.29	45.7	2.92	0.08866	8.27	1.8789	8.80	0.1537	3.02	0.343	0.0911	16.32	922	26	1397	159	+36
S3	86	81	0.97	22.2	-0.25	0.10354	2.71	4.2648	4.08	0.2987	3.05	0.748	0.0817	5.86	1685	45	1688	50	+0
S4	184	119	0.66	13.2	8.65	0.09062	10.08	1.0419	10.74	0.0834	3.70	0.344	0.0445	7.31	516	18	1439	192	+67
S5	92	69	0.78	20.8	0.56	0.10429	2.17	3.7995	2.59	0.2642	1.41	0.546	0.0631	3.27	1511	19	1702	40	+13
S6	74	52	0.72	21.9	1.01	0.09732	5.25	4.6360	5.78	0.3455	2.41	0.417	0.0927	7.02	1913	40	1573	98	-25
S7	149	159	1.10	38.1	-0.07	0.10494	1.05	4.3056	1.55	0.2976	1.14	0.736	0.0858	1.59	1679	17	1713	19	+2
S8	66	43	0.67	16.7	0.33	0.09842	2.43	4.0225	3.07	0.2964	1.88	0.613	0.0822	3.75	1674	28	1594	45	-6
S9	53	41	0.80	13.9	0.00	0.10133	1.74	4.2465	2.55	0.3039	1.87	0.733	0.0846	4.98	1711	28	1649	32	-4
S10	115	110	0.99	30.7	-0.08	0.10245	1.19	4.3752	1.77	0.3097	1.30	0.736	0.0855	2.75	1739	20	1669	22	-5
S11	1114	21	0.02	79	-0.032	0.05938	1.78	0.6736	2.39	0.0823	1.60	0.669	0.0315	37.55	510	8	581	39	+13
S12	39	33	0.86	10	0.000	0.10257	1.31	4.2461	2.21	0.3002	1.78	0.804	0.0855	5.40	1692	26	1671	24	-1
S13	112	96	0.88	30	-0.114	0.10281	2.37	4.4269	4.34	0.3123	3.63	0.838	0.0869	5.41	1752	56	1676	44	-5
S14	2022	36	0.02	130	0.217	0.05789	1.10	0.5971	1.50	0.0748	1.01	0.675	0.0278	28.50	465	5	526	24	+12
S15	2433	46	0.02	172	0.028	0.05766	1.26	0.6557	1.92	0.0825	1.45	0.754	0.0210	8.20	511	7	517	28	+1
S16	80	67	0.86	20	0.134	0.10336	1.00	4.1269	1.74	0.2896	1.42	0.817	0.0850	2.02	1639	21	1685	19	+3
S17	681	271	0.41	144	0.018	0.10055	0.33	3.4245	1.09	0.2470	1.04	0.953	0.0822	1.34	1423	13	1634	6	+14
S18	400	505	1.30	100	0.041	0.10404	0.43	4.1813	1.36	0.2915	1.29	0.949	0.0812	1.44	1649	19	1697	8	+3

BG8 (alkali feldspar granite)

S1	450	149	0.34	102	0.043	0.10196	0.41	3.7086	1.15	0.2638	1.07	0.934	0.0765	1.44	1509	14	1660	8	+10
S2	97	63	0.68	25	0.022	0.10342	0.88	4.2107	1.61	0.2953	1.35	0.837	0.0846	2.62	1668	20	1686	16	+1
S3	67	46	0.70	16	0.044	0.10474	1.17	4.0918	1.94	0.2833	1.55	0.798	0.0807	2.47	1608	22	1710	21	+7
S4	562	312	0.57	141	0.038	0.10396	0.41	4.1822	1.15	0.2918	1.07	0.934	0.0814	1.52	1650	16	1696	8	+3
S5	138	87	0.65	35	0.078	0.10205	0.73	4.1093	1.45	0.2921	1.26	0.865	0.0827	1.76	1652	18	1662	13	+1
S6	96	58	0.62	24	0.135	0.10361	1.31	4.1600	1.98	0.2912	1.49	0.752	0.0807	2.69	1647	22	1690	24	+3
S7	609	340	0.58	147	0.025	0.10295	0.36	3.9885	1.12	0.2810	1.06	0.946	0.0806	1.25	1596	15	1678	7	+6
S8	1394	20	0.02	97	0.000	0.05788	0.52	0.6497	1.25	0.0814	1.14	0.908	0.0227	4.82	505	6	525	11	+4
S9	231	158	0.71	57	0.013	0.10383	0.60	4.1258	1.32	0.2882	1.18	0.890	0.0833	1.55	1632	17	1694	11	+4
S10	1084	481	0.46	108	0.279	0.07926	0.66	1.2628	1.89	0.1156	1.78	0.938	0.0383	2.08	705	12	1179	13	+42
S11	1113	582	0.54	252	0.254	0.10332	0.71	3.7533	1.30	0.2635	1.09	0.837	0.0682	1.74	1508	15	1685	13	+12
S12	1534	75	0.05	104	0.270	0.06022	0.92	0.6548	1.37	0.0789	1.02	0.742	0.0151	12.43	489	5	611	20	+21

Appendix A (cont.)

S13	335	258	0.80	77	0.014	0.10243	0.46	3.7711	1.20	0.2670	1.10	0.922	0.0809	1.32	1526	15	1669	9	+10
S14	128	60	0.49	31	0.033	0.10319	0.71	4.0158	1.46	0.2822	1.27	0.874	0.0802	4.08	1603	18	1682	13	+5
S15	404	242	0.62	100	0.043	0.10284	0.68	4.0826	1.28	0.2879	1.08	0.846	0.0826	1.31	1631	16	1676	13	+3
BG10 (sienogranite)																			
S1	173	150	0.90	33.3	1.19	0.10341	4.04	3.1988	4.97	0.2244	2.89	0.581	0.0587	4.21	1305	34	1686	75	+25
S2	81	82	1.04	19.9	0.35	0.09921	2.49	3.8872	2.90	0.2842	1.49	0.514	0.0809	2.37	1612	21	1609	46	-0
S3	64	54	0.87	17.2	0.00	0.10200	1.43	4.3830	2.18	0.3117	1.64	0.755	0.0896	3.43	1749	25	1661	26	-6
S4	104	79	0.78	25.4	-0.26	0.10780	1.46	4.2189	1.97	0.2839	1.32	0.671	0.0846	2.24	1611	19	1763	27	+10
S5	308	558	1.87	39.8	2.14	0.09798	3.00	2.0365	5.22	0.1507	4.27	0.818	0.0237	5.55	905	36	1586	56	+46
S6	126	106	0.87	20.5	2.24	0.10542	3.95	2.7507	4.16	0.1892	1.29	0.310	0.0447	5.68	1117	13	1722	73	+38
S7	247	221	0.93	58	0.086	0.10129	0.61	3.8326	1.31	0.2744	1.15	0.883	0.0811	1.81	1563	16	1648	11	+6
S8	234	208	0.92	57	0.049	0.10309	0.88	4.0431	1.53	0.2844	1.25	0.816	0.0851	1.76	1614	18	1681	16	+4
S9	1060	55	0.05	76	0.081	0.05590	0.96	0.6430	1.56	0.0834	1.23	0.788	0.0230	6.30	517	6	448	21	-16
S10	594	326	0.57	109	0.106	0.09571	0.63	2.8182	1.28	0.2136	1.11	0.869	0.0769	1.78	1248	13	1542	12	+21
S11	979	51	0.05	61	-0.022	0.05802	0.69	0.5842	1.35	0.0730	1.16	0.858	0.0240	3.58	454	5	531	15	+15
S12	1083	52	0.05	78	0.073	0.05732	1.01	0.6586	1.45	0.0833	1.03	0.713	0.0227	5.15	516	5	504	22	-2
S13	2016	200	0.10	155	0.291	0.05794	1.53	0.7150	1.84	0.0895	1.03	0.558	0.0194	10.17	553	5	527	34	-5
S14	850	50	0.06	61	0.085	0.05718	0.78	0.6629	1.41	0.0841	1.18	0.833	0.0192	5.71	520	6	498	17	-5
S15	1128	815	0.75	73	3.372	0.05748	2.70	0.5979	3.02	0.0754	1.36	0.451	0.0104	6.38	469	6	510	59	+8
S16	149	146	1.01	35	0.213	0.10245	0.82	3.8891	2.14	0.2753	1.98	0.924	0.0818	2.23	1568	28	1669	15	+7

References

- Alkmim, F.F., Marshak, S., Pedrosa-Soares, A.C., Peres, G.G., Cruz, S.C.P., Whittington, A., 2006. Kinematic evolution of the Araçuaí-West Congo Orogen in Brazil and Africa: nutcracker tectonics during the neoproterozoic assembly of Gondwana. *Precambrian Res.*, 149, 43-64.
- Alkmim, F.F. and Martins-Neto, M.A., 2012. Proterozoic first-order sedimentary sequences of the São Francisco craton, eastern Brazil. *Mar. Pet. Geol.* 33, 127–139.
- Almeida, F.F.M. (1977). O Cráton do São Francisco. *Revista Brasileira de Geociências*, 7, 349-364.
- Bouvier, A., Vervoort, J.D., Patchett, P.J., 2008. The Lu–Hf and Sm–Nd isotopic composition of CHUR: constraints from unequilibrated chondrites and implication for the bulk composition of terrestrial planets. *Earth Planet. Sci. Lett.* 273, 48–57.
- Barbosa, J.S.F. and Sabate, P., 2004. Archean and Paleoproterozoic crust of the São Francisco Craton, Bahia Brazil: geodynamic features. *Precamb. Res.* 133, 1–27.
- Barbosa, N.S., Teixeira, W., Ávila, C.A., Montecinos, P.M., Bongiolo, E.M., 2015. 2.17–2.09 Ga crust forming episodes in the Mineiro belt, São Francisco craton, Brazil: U-Pb ages and geochemical constraints. *Precambr. Res.* 270, 204–225.
- Barbosa, N.S., Teixeira, W., Ávila, C.A., Montecinos, P.M., Bongiolo, E.M., Vasconcelos, F.F., 2018. U-Pb geochronology and coupled Hf-Nd-Sr isotopic-chemical constraints of the Cassiterita Orthogneiss (2.47–2.41-Ga) in the Mineiro belt, São Francisco craton: Geodynamic fingerprints beyond the Archean Paleoproterozoic Transition. *Precambr. Res.*
- <https://doi.org/10.1016/j.precamres.2018.01.017>.
- Bilal E., Marciano V.R.P.R.O., Fuzikawa K., Correia Neves J.M., Giret, A., 1995. Datação de monazitas do Distrito Pegmatítico de Santa Maria de Itabira, MG. In: SBG/ Núcleo MG, Simp. Geol. Minas Gerais, 8, Diamantina, Boletim, 13:46-47.
- Bonin, B., 2004. Do coeval mafic and felsic magmas in post-collisional to within-plate regimes necessarily imply two contrasting, mantle and crustal, sources? A review. *Lithos* 78, 1–24.

Bonin, B., 2007. A-type granites and related rocks: Evolution of a concept, problems and prospects. *Lithos* 97 (2007) 1-29

Bouvier, A., Vervoort, J.D., Patchett, P.J., 2008. The Lu–Hf and Sm–Nd isotopic composition of CHUR: constraints from unequilibrated chondrites and implication for the bulk composition of terrestrial planets. *Earth Planet. Sci. Lett.*, 273, 48–57.

Braga, F.C.S., Rosiere, C.A., Queiroga, G.N., Rolim, V.K., Santos, J.O.S., McNaughton, N.J., 2015. The Statherian itabirite-bearing sequence from the Morro Escuro Ridge, Santa Maria de Itabira, Minas Gerais, Brazil. *J. S. Am. Earth Sci.* 58, 33-53.

Braga, F.C.S., 2018. Gênese e controle dos depósitos magnetíticos-hematíticos encaixados no Complexo Cristalino, leste do Cráton do São Francisco. PhD qualification. UFMG.

Brito Neves, B.B., Kawashita K., Delhal J. 1979. A evolução geocronológica da Cordilheira do Espinhaço: dados novos e integração. *Rev. Bras. Geociências*, 9(1), 71-85.

Brito Neves, B.B., Cordani U.G. 1991. Tectonic evolution of South America during the late Proterozoic. *Precamb. Research*, 53(1-2), 23-40.

Cabral, A.R., Zeh, A., 2015. Detrital zircon without detritus: a result of 496-Ma-old fluid–rock interaction during the gold-lode formation of Passagem, Minas Gerais, Brazil. *Lithos*, 212-215, 415-427

Cabral, A.R., Zeh, A., Galbiatti, H.F., Lehmann, B., 2015. Late Cambrian Au-Pd mineralization and Fe enrichment in the Itabira district. Minas Gerais, Brazil, at 496 Ma: Constraints from U-Pb monazite dating of a Jacutinga lode. *Econ. Geology*, 110, 263-272.

Cabral, A.R., Tupinambá, M., Zeh, A., Lehmann, B., Wiedenbeck, M., Brauns, M., Kwitko Ribeiro, R., 2017. Platiniferous gold–tourmaline aggregates in the gold–palladium belt of Minas Gerais, Brazil: implications for regional boron metasomatism. *Mineralogy and Petrology*, 111, 807-819

Campos, C.P., Medeiros, S.R., Mendes, J.C., Pedrosa-Soares, A.C., Dussin, I., Ludka, I.P., Dantas, E.L., 2016. Cambro-Ordovician Magmatism in the Araçuaí Belt (SE Brazil): snapshots from a post-

collisional event. *Journal of South American Earth Sciences*, v. 68, p. 248-268.

Chen, Y.X., Gao, P., Zheng, Y.F., 2015. The anatetic effect on the zircon Hf isotope composition of migmatites and associated granites. *Lithos* 238, 174–184.

Chemalle Jr., F; Quade, H. ; Schumus, W.R. V. 1998. Petrography, Geochemistry and Geochronology of the Borrachudo Granite, Minas Gerais, Brazil. *Zentralblatt für Geologie und Paläontologie*. Teil 2, Paläontologie, Stuttgart, v. 3-6, p. 739-750.

Chemale Jr., F., Dussin, I.A., Alkmim, F.F., Martins, M.S., Queiroga, G., Armstrong, R., Santos, M.N., 2012. Unravelling a Proterozoic basin history through detrital zircon geochronology: the case of the Espinhaço Supergroup, Minas Gerais, Brazil. *Gondwana Research*, 22(1), 200-206.

Cherniak, D.J., Hanchar, J.M., Watson, E.B., 1997. Rare-earth diffusion in zircon. *Chemical Geology* 134, 289–301.

Cordani, U.G., Fraga, L.M., Reis, N., Tassinari, C.C.G., Brito-Neves, B.B., 2010. On the origin and tectonic significance of the intra-plate events of Grenvillian-type age in South America: a discussion. *Journal of South American Earth Sciences* 29, 143–159.

Corfu, F. and Noble, S.R., 1992. Genesis of the southern Abitibi Greenstone belt, Superior Province, Canada: evidence from zircon Hf isotope analysis using a single filament technique. *Geochimica et Cosmochimica Acta* 56, 2081–2097.

Correia Neves, J.M., Pedrosa Soares, A.C., Marciano, V.R.P.da R.O., 1986. A província pegmatítica oriental do Brasil à luz dos conhecimentos atuais. *Rev. Bras. Geoc.* 16 (1), 106-118.

Dall'Agnol, R. and Oliveira, D.C., 2007. Oxidized, magnetite-series, rapakivi-type granites of Carajás, Brazil: implications for classification and petrogenesis of A-type granites. *Lithos*, 93, 215–233.

Dall'Agnol, R., Frost, C.D., Rämö, O.T., 2012. IGCP Project 510 “A-type granites and related rocks through time”: project vita, results, and contribution to granite research. *Lithos*, 151, 1–16.

Dorr, J.V.N. and Barbosa, A.L.M., 1963. Geology and ore deposits of the Itabira District Minas Gerais, Brazil: U. S. Geological Survey Professional Paper 341-C, p110.

Dossin, I.A.; Dossin, T.M.; Charvet, J.; Cocherie ,A., Rossi, P. 1993 . Single-zircon dating by step-wise Pb-evaporation of Middle Proterozoic Magmatism in the Espinhaço Range, Southeastern São Francisco Craton (Minas Gerais, Brazil). In: Simpósio do Cráton do São Francisco, 2. Anais, 39-42.

Dussin, T.M., 1994. The Borrachudos Suite, Mezoproterozoic A-type Granitic Magmatism in the São Francisco Craton (SE Brazil). In: *Associacions vulcano- plutoniques de l'Espinhaço Meridional* (SE - Brésil). Université d'Orleans, Orléans. PhD Thesis.

Dussin, I.A. and Dussin, T.M., 1995. Supergrupo Espinhaço: modelo de evolução geodinâmica. *Geonomos*, 3(1), 19-26.

Dussin, T.M., Dussin, I.A., Noce, C.M., Rossi, P., Charvet, J., 1997. Tectonic setting and origin of the Mesoproterozoic Borrachudos granites (MG, Brazil). In: South-American Symposium on Isotope Geology, Campos do Jordão, Brazil. Extended Abstracts, 104-106.

Dussin, T. M., Duarte, P., Dussin, I.A., 2000. Registro da tectônica Brasiliiana na região de Guanhães (SE, Brasil): Deformação e metamorfismo das rochas de idade pós-Transamazônicas. *Geonomos*, 8(2), 55-59.

Eby, G.N., 1992. Chemical subdivision of the A-type granitoids: Petrogenetic and tectonic implications. *Geology*, 20, 641-644.

Fernandes, M.L.S., Pedrosa Soares, A.C., Noce, C.M., Wiedemann, C., Correia Neves, J.M., 2000. U-Pb geochronology of the Borrachudos Suite: evidence of Brasilian tectonism recorded by late Paleoproterozoic anorogenic granites (Araçuaí belt, Minas Gerais, Brazil). XXXI International congress.

Figueiredo, C.M.S., 2009. O arco magmático Brasiliano na conexão dos orógenos Araçuaí e Ribeira, região de Muriaé - MG. Diss. Mestrado. IGC-UFMG.

Flowerdew, M.J., Millar, I.L., Vaughan, A.P.M., Horstwood, M.S.A., Fanning, C.M., 2006. The

source of granitic gneisses and migmatites in the Antarctic Peninsula: a combined U–Pb SHRIMP and laser ablation Hf isotope study of complex zircons. *Contrib. Mineral. Petrol.* 151, 751–768.

Frost, C.D. and Frost, B.R., 1997. Reduced rapakivi-type granites: the tholeiite connection. *Geology* 25, 647–650.

Ge, R., Zhu, W., Wu, H., He, J., Zheng, B., 2013. Zircon U–Pb ages and Lu–Hf isotopes of Paleoproterozoic metasedimentary rocks in the Korla Complex, NW China: implications for metamorphic zircon formation and geological evolution of the Tarim Craton. *Precambrian Research* 231, 1–18.

Gomes, S.D., Berger, S., Figueiredo e Silva, R.C., Hagemann, S.G., Rosière, C.A., Banks, D.A., Lobato, L.M., Hensler, A.S., 2018. Oxide chemistry and fluid inclusion constraints on the formation of itabirite-hosted iron ore deposits at the eastern border of the southern Espinhaço Range, Brazil. *Ore Geology Reviews*, 95, 821–848.

Gonçalves, G.O., Lana, C., Buick, I.S., Alkmim, F.F., Scholz, R., 2017. Post-orogenic hydrothermal fluid-flow in the eastern São Francisco craton: implications for ore mineralization. Goldschmidt 2017, abstract.

Griffin, W.L., Wang, X., Jackson, S.E., Pearson, N.J., O'Reilly, S.Y., Xu, X., Zhou, X., 2002. Zircon chemistry and magma mixing, SE China: in-situ analysis of Hf isotopes, Tonglu and Pingtan igneous complexes. *Lithos*, 61, 237–269.

Groat, L.A., Giuliani, G., Marshall, D.D. and Turner, D., 2008. Emerald deposits and occurrences: a review. *Ore Geology Reviews*, 34, 87–112.

Grossi-Sad J.H., Chiod Filho C., Santos J.F., Magalhães J.M.M., Carelos P.M., 1990a. Duas Suítes Graníticas do Bordo Sudeste do Cráton Sanfrasciscano, em Minas Gerais: Petroquímica e Potencial Metalogenético. SBG, Congr. Bras. de Geol., 36, Natal, Anais, 4: 1836–1848.

Grossi Sad, J.H., Chiodi Filho, C., Santos, J.F., Magalhães, J.M.M., Carelos, P.M., 1990b. Geoquímica e origem da formação ferrífera do Grupo Guanhães, Distrito de Guanhães, MG, Brasil. SBG, Congr. Bras. de Geol., 36, Natal, Anais, 3: 1241–1253.

Grossi Sad, J.H., Mourão, M.A.A., Guimarães, M.L.V., Knauer, L.G., 1997. Geologia da Folha Conceição do Mato Dentro. In: Grossi-Sad, J.H., Lobato, L.M., Pedrosa- Soares, A.C., Soares-Filho, B.S. (Eds.), Projeto espinhaço Em CD-ROM (textos, mapas e anexos). COMIG e Companhia Mineradora de Minas Gerais, Belo Horizonte, pp. 2533-2693.

Guadagnin, F., Chemale Jr., F., Magalhães, A.J.C., Santana, A., Dussin, I., Takehara, L., 2015. Age constraints on crystal-tuff from the Espinhaço Supergroup — Insight into the Paleoproterozoic to Mesoproterozoic intracratonic basin cycles of the Congo–São Francisco Craton. *Gondwana Research*, 27, 363–376.

Hagemann, S.G., Angerer, T., Duuring, P., Rosière, C.A., Figueiredo e Silva, R.C., Lobato, L.M., Hensler, A.S., Walde, D.H.G., 2016. BIF-hosted iron mineral system: A review. *Ore Geol. Rev.* 76, 317–359.

Hawkesworth, C.J., Dhuime, B., Pietranik, A.B., Cawood, P.A., Kemp, A.I.S., Storey, C.D., 2010. The generation and evolution of the continental crust. *J. Geol. Soc.* 167, 229–248.

Hawkesworth, C.J. and Kemp, A.I.S., 2006a. Using hafnium and oxygen isotopes in zircon to unravel the record of crustal evolution. *Chemical Geology* 226, 144–162.

Hawkesworth, C.J. and Kemp, A.I.S., 2006b. Evolution of the continental crust. *Nature*, 443, 811–817.

Heineck C.A., Leite C.A.S., Silva M.A., Vieira V.S. 2003. Mapa geológico do Estado de Minas Gerais, Escala 1:1.000.000. COMIG/CPRM, Belo Horizonte. http://www.codemig.com.br/wp-content/uploads/2016/08/mapa_geologico_estado_minas_gerais.pdf

Hoskin, P.W. and Black, L.P., 2000. Metamorphic zircon formation by solid-state recrystallization of protolith igneous zircon. *Journal of Metamorphic Geology* 18, 423–439.

Huang, H.Q., Li, X.H., Li, W.X., Li, Z.X., 2011. Formation of high $\delta^{18}\text{O}$ fayalite-bearing A-type granite by high-temperature melting of granulitic metasedimentary rocks, southern China. *Geology* 39, 903–906.

Iizuka, T. and Hirata, T., 2005. Improvements of precision and accuracy in situ Hf isotope microanalysis of zircon using the laser ablation-MC-ICPMS technique. *Chemical Geology*, 220, 121-137.

Jordt Evangelista, H., Lana, C., Delgado, C.E.R., Viana, D.J. 2016. Age of the emerald mineralization from the Itabira-Nova Era District, Minas Gerais, Brazil, based on LA-ICP-MS geochronology of cogenetic titanite. *Brazilian Journal of Geology*, 46-3, 427-437.

Kemp, A.I.S., Wormald, R.J., Whitehouse, M.J., Price, R.C., 2005. Hf isotopes in zircon reveal contrasting sources and crystallization histories for alkaline to peralkaline granites of Temora, southeastern Australia. *Geology* 33, 797–800.

Kemp, A.I.S., Hawkesworth, C.J., Foster, G.L., Paterson, B.A., Woodhead, J.D., Herdt, J.M., Gray, C.M., and Whitehouse, M.J., 2007. Magmatic and Crustal Differentiation History of Granitic Rocks from Hf-O Isotopes in Zircon: *Science*, 315, 980-983.

King, P.L., White, A.J.R., Chappell, B.W., Allen, C.M., 1997. Characterization and origin of aluminous A-type granites from the Lachlan Fold Belt, Southeastern Australian. *Journal of Petrology* 38, 371–391.

Litvinovsky, B.A., Tsygankov, A.A., Jahn, B.M., Katzir, Y., Be'eri-Shlevin, Y., 2011. Origin and evolution of overlapping calc-alkaline and alkaline magmas: the Late Palaeozoic Post-collisional Igneous Province of Transbaikalia (Russia). *Lithos* 125, 845–874.

Li, X.H., Long, W.G., Li, Q.L., Liu, Y., Zheng, Y.F., Yang, Y.H., Chamberlain, K.R., Wan, D.F., Guo, C.H., Wang, X.C., 2010. Penglai zircon megacrysts: a potential new working reference material for microbeam determination of Hf O isotopes and U Pb age. *Geostandards and Geoanalytical Research*, 34, 117-134.

Li, W.C., Chen, R.X., Zheng, Y.F., Li, Q., Hu, Z., 2013. Zirconological tracing of transition between aqueous fluid and hydrous melt in the crust: Constraints from pegmatite vein and host gneiss in the Sulu orogen. *Lithos*, 162-163, 157-174.

Ludwig, K.R., 2001. Isoplot/Ex Rev. 2.49. Berkeley Geochronology Centre, Special Publication 1a.

Lynch, E.P., Costanzo, A., Feely, M., Blamey, N.J.F., Pironon, J., Lavin, P., 2014. The Piteiras emerald mine, Minas Gerais, Brazil: fluid-inclusion and gemmological perspectives. *Mineralogical Magazine*, 78(7), 1571–1587.

Machado G.A.A., 1998. Jazidas de esmeralda de Capoeirana e Belmont – MG: Geologia, petrogênese e metalogênese. PhD Thesis, Instituto de Geociências, Universidade de São Paulo, São Paulo, p294.

Machado N., Schrank A., Abreu F.R., Knauer L.G., Almeida-Abreu P.A., 1989. Resultados preliminares da geocronologia U/Pb na Serra do Espinhaço Meridional. In: SBG, Simp. Geol. Núcleo M.G., 5, e Simp. Geol. Núcleo Brasília, 1, Belo Horizonte, Anais, 1:171-174.

Marciano, V.R.P.R.O, Svisero, D.P, Correia-Neves, J.M., 1993, Dados geocronológicos de pegmatitos da borda oriental do Craton do São Francisco. *Anais do Simp. sobre o Craton do São Francisco: Sua evolução tectônica e metalogenética*. Salvador, SBG-Ba, SE/SGM, 362-365.

Marciano, V.R.P.R.O., 1995. O distrito pegmatítico de Santa Maria de Itabira, MG. Mineralogia, geoquímica e zoneografia. PhD Thesis, Instituto de Geociências, Universidade de São Paulo, São Paulo, p216.

Marshak, S., Alkmim, F.F., 1989. Proterozoic contraction/extension tectonics of the southern São Francisco region, Minas Gerais, Brazil. *Tectonics* 8, 555–571.

Martins, B.S., Lobato, L.M., Rosière, C.A., Hagemann, S.G., Santos, J.O.S., Villanova, F.L.S.P., Silva, R.C.F., Lemos, L.H.A., 2016. The Archean BIF-hosted Lamego gold deposit, Rio das Velhas greenstone belt, Quadrilátero Ferrífero: evidence for Cambrian structural modification of an Archean orogenic gold deposit. *Ore Geol. Rev.*, 72, 963–988.

Martins Neto, M.A., 2000. Tectonics and sedimentation in a paleomesoproterozoic rift-sag basin (Espinhaço basin, southeastern Brazil). *Precambrian Res.* 103, 147-173.

Martins Neto, M.A., and Hercos, C.M., 2002. Sedimentation and tectonic setting of Early Neoproterozoic glacial deposits in southeastern Brazil. *International Association of Sedimentologists, Special Publication*, 33: 383-403.

Melo, M.G., Lana, C., Stevens, G., Pedrosa_Soares, A.C., Gerdes, A.A., Leonardo, A., Nalini, H.A., Alkmim, F.F., 2017. Assessing the isotopic evolution of S-type granites of the Carlos Chagas Batholith, SE Brazil: Clues from U/Pb, Hf isotopes, Ti geothermometry and trace element composition of zircon. *Lithos*, 284-285, 730-750.

Morteani, G., Preinfalk, C., Horn, A.H., 2000. Classification and mineralisation potential of the pegmatites of the Eastern Brazilian Pegmatite Province. *Mineral. Deposita*, 35, 638-655.

Müller G., Höhndorf A., Lauenstein H.J., Lenz H., 1986. Petrological and Geochemical data on a high-metamorphic Archean BIF - bearing rock sequence near Guanhães, Minas Gerais, Brazil. *Geol. Jb.*, 3-20.

Mushkin, A., Navon, O., Halicz, L., Hartmann, G., Stein, M., 2003. The petrogenesis of A-type magmas from the Amram Massif, southern Israel. *Journal of Petrology* 44, 815–832.

Namur, O., Charlier, B., Toplis, M.J., Higgins, M.D., Housell, V., Liegeois, J.P., Auwera, J.V., 2011. Differentiation of tholeiitic basalt to A-type granite in the Sep Iles layered intrusion. Canada. *Journal of Petrology* 52, 487–539.

Nelson, R.D., Bruce W. Robinson, W.B., Myers, S.J., 2000. Complex geological histories extending for ≥ 4.0 Ga deciphered from xenocryst zircon microstructures. *Earth and Planetary Science Letters*, 181 (1–2), 89-102.

Noce, C.M., Pedrosa Soares, A.C., Silva, L.C., Armstrong, R., Piuzana, D., 2007. Evolution of polycyclic basement complexes in the Araçuaí Orogen, based on U–Pb SHRIMP data: Implications for Brazil–Africa links in Paleoproterozoic time, *Precambrian Res.*, 159, 60-78.

Oliveira, A.Z.K., 2002. Estruturação e alteração metassomática do ortognaisse Açucena (Série Borrachudos) na região de Ipatinga, Minas Gerais. Masters dissertation. Departamento de Geologia, Universidade Federal de Minas Gerais, p. 90.

Patchett, P.J., Kouvo, O., Hedge, C.E., Tatsumoto, M., 1981. Evolution of Continental Crust and Mantle Heterogeneity: Evidence from Hf Isotopes. *Contrib. Mineral. Petrol.*, 78, 279-297.

Patchett, P.J. and Tatsumoto, M., 1981 A routine high-precision method for Lu-Hf isotope geochemistry and chronology. *Contrib. Mineral. Petrol.*, 75, 263-267.

Pearce J.A., Harris N.B.W., Tindle A.G., 1984. Trace element discrimination diagrams for the tectonic interpretation of granitic rocks. *J. Petrol.*, 25, 956-983.

Pedrosa Soares, A.C., Cordani, U., Nutman, A., 2000. Constraining the age of Neoproterozoic glaciation in eastern Brazil: First U-Pb SHRIMP data from detrital zircons. *Rev. Bras. de Geociênc.*, 30, 58-61.

Pedrosa Soares, A.C., Noce, C.M., Wiedemann, C.M., Pinto, C.P., 2001. The Araçuaí-West Congo orogen in Brazil: An overview of a confined orogen formed during Gondwanaland assembly. *Precamb. Res.*, 110, 307–323.

Pedrosa Soares, A.C., Noce, C.M., Alkmim, F.F., Silva, L.C., Babinski, M., Cordani, U., Castañeda, C., 2007. Orógeno Araçuaí: síntese do conhecimento 30 anos após Almeida 1977. *Geonomos*, 15(1), 1-16.

Pedrosa Soares, A.C., Campos, C.P., Noce, C., Silva, L.C., Novo, T., Roncato, J., Medeiros, S., Castaneda, C., Queiroga, G., Dantas, E., Dussin, I.A., Alkmim, F.F., 2011. Late Neoproterozoic–Cambrian granitic magmatism in the Araçuaí orogen (Brazil), the Eastern Brazilian Pegmatite Province and related mineral resources. *Geological Society, London, Special Publications*, 350, 25–51.

Pimentel, M.M., 2016. The tectonic evolution of the Neoproterozoic Brasília Belt, central Brazil: a geochronological and isotopic approach. *Brazilian Journal of Geology*, 46, 67-82.

Preinfalk, C., Kostitsyn, Y., Morteani, G., 2002. The pegmatites of the Nova Era - Itabira - Ferros pegmatite district and the emerald mineralisation of Capoeirana and Belmont (Minas Gerais, Brazil): geochemistry and Rb-Sr dating. *J. South Am Earth Sci.*, 14, 867-887.

Richter, F.; Lana, C.; Stevens, G.; Buick, I.; Pedrosa-Soares, A.C.; Alkmim, F.F.; Cutts, K., 2016. Sedimentation, metamorphism and granite generation in a back-arc region: Records from the Ediacaran Nova Venécia Complex (Araçuaí Orogen, Southeastern Brazil). *Precambrian Research*,

272, 78-100.

Rubatto, D., 2002. Zircon trace element geochemistry: partitioning with garnet and the link between U–Pb ages and metamorphism. *Chemical Geology*, 184, 123–138.

Santos M.N., Chemale Jr. F., Dussin I.A., Martins M.S., Queiroga G., Pinto R.T.R., Santos A.N., Armstrong R., 2015. Provenance and paleogeographic reconstruction of a mesoproterozoic intracratonic sag basin (Upper Espinhaço Basin, Brazil). *Sedimentary Geology*, 318, 40–57.

Segal, I., Halicz, L., Platzner, I.T., 2003. Accurate isotope ratio measurements of ytterbium by multiple collection inductively coupled plasma mass spectrometry applying erbium and hafnium in an improved double external normalization procedure. *Journal of Analytical Atomic Spectrometry*, 18, 1217-1223.

Silva, L.C., Armstrong, R., Noce, C.M., Carneiro, M.A., Pimentel, M.M., Pedrosa- Soares, A.C., Leite, C.A., Vieira, V.S., Silva, M.A., Paes, V.J.C., Cardoso-Filho, J.M., 2002. Reavaliação da evolução geológica em terrenos pre cambrianos brasieiros com base em novos dados U-Pb SHRIMP, parteII: Orógeno Araçuaí, Cinturão Mineiro e Cráton São Francisco Meridional. *Rev. Bras. Geociênc.* 32, 513-528.

Silveira, E.M., Söderlund, U., Oliveira, E.P., Ernst, R.E., Menezes Leal, A.B., 2013. First precise U–Pb baddeleyite ages of 1500 Ma mafic dykes from the São Francisco Craton, Brazil, and tectonic implications. *Lithos* 174, 144–156.

Söderlund, U., Patchett, J.P., Vervoort, J.D., Isachsen, C.E., 2004. The ^{176}Lu decay constant determined by Lu–Hf and U–Pb isotope systematics of Precambrian mafic intrusions. *Earth Planet. Sci. Lett.* 219, 311–324.

Stevenson, R.K. and Patchett, P.J., 1990. Implications for the evolution of continental crust from Hf isotope systematics of Archaean detrital zircons. *Geochimica et Cosmochimica Acta* 54, 1683–1697.

Streckeisen, A.L., 1967. Classification and nomenclature of igneous rocks. *N. Jb. Miner.*, 107, 144-240.

Sun, S.S. and McDonough, W.F., 1989. Chemical and isotopic systematics of oceanic basalts: implications for mantle composition and processes. In: Saunders, A.D. & Norry, M.J. (eds) Magmatism in the Ocean Basins. Geological Society, London, Special Publications, 42, 313–345.

Schwarz, D. and Giuliani, G., 2002. South America: Colombia. ExtraLapis English, 2, 36 45.

Teixeira, W., Ávila, C.A., Dussin, I.A., Corrêa Neto, A.V., Bongiolo, E.M., Santos, J.O., Barbosa, N.S., 2015. A juvenile accretion episode (2.35–2.32 Ga) in the Mineiro belt and its role to the Minas accretionary orogeny: Zircon U–Pb–Hf and geochemical evidences. Precambrian Res. 256, 148-169.

Taylor, S.R. and McLennan, S.M., 1985. The Continental Crust: Its Composition and Evolution. Blackwell, London.

Uhlein, A., Trompette, R.R., Egydio-Silva, M., 1998. Proterozoic rifting and closure, SE border of the São Francisco Craton, Brazil. J. South Am. Earth Sci. 11, 191-203.

Valeriano, C., Mendes, J., Tupinambá, M., Bongiolo, E.M., Heilbron, M., Junho, M.C.B., 2016. Cambro-Ordovician post-collisional granites of the Ribeira belt, SE-Brazil: A case of terminal magmatism of a hot orogen. Journal of South American Earth Sciences, 68, 269-281.

Vervoort, J.D., Patchett, P.J., Blichert-Toft, J., Albarède, F., 1999. Relationships between Lu Hf and Sm Nd isotopic systems in the global sedimentary system. Earth and Planetary Science Letters, 168, 79-99.

Vervoort, J.D., Patchett, P.J., Söderlund, U., Baker, M., 2004 Isotopic composition of Yb and the determination of Lu concentrations and Lu/Hf ratios by isotope dilution using MC ICPMS. Geochemistry, Geophysics, Geosystems, 5.

Yang, J.H., Wu, F.Y., Chung, S.L., Wilde, S.A., Chu, M.F., 2006. A hybrid origin for the Qianshan A-type granite, northeast China: geochemical and Sr–Nd–Hf isotopic evidence. Lithos 89, 89-106.

Woodhead, J.D. and Hergt, J. M., 2005. A preliminary appraisal of seven natural zircon reference

materials for in situ Hf isotope determination. *Geostandards and Geoanalytical Research*, 29, 183–195.

Wu, F.Y., Sun, D.Y., Li, H.M., Jahn, B.M., Wilde, S.A., 2002. A-type granites in northeastern China: age and geochemical constraints on their petrogenesis. *Chemical Geology* 187, 143–173.

Wu, Y.B., Zheng, Y.F., Zhang, S.B., Zhao, Z.F., Wu, F.Y., Liu, X.M., 2007. Zircon U–Pb ages and Hf isotope compositions of Migmatite from the North Dabie Terrane in China: constraints on partial melting. *Journal of Metamorphic Geology* 25, 991–1009.

Zhang, X.H., Yuan, L.L., Xue, F.H., Zhang, Y., 2012. Contrasting Triassic ferroan granitoids from northwestern Liaoning, North China: magmatic monitor of Mesozoic decratonization and craton–orogen. *Lithos* 144–145, 12–23.

Zhang, X.H., Yuan, L., Xue, F., Yan, X., Mao, Q., 2015. Early Permian A-type granites from central Inner Mongolia, North China: Magmatic tracer of post-collisional tectonics and oceanic crustal recycling. *Gondwana Res.*, 28, 311–327.

Zheng, Y.F., 2009. Fluid regime in continental subduction zones: petrological insights from ultrahigh-pressure metamorphic rocks. *Journal of the Geological Society* 166, 763–782.

Capítulo 5 – Considerações finais

Os estudos de química mineral e de inclusões fluidas no depósito Liberdade-Piçarrão (DLP) e demais áreas de ocorrência de itabirito no Grupo Guanhães propiciaram um maior entendimento a respeito dos processos relacionados à gênese de corpos de minério de ferro de alto teor ($> 65\%$ Fe) na região a leste da Serra do Espinhaço meridional. Estes corpos de minério são compostos por hematita granoblástica e tabular, com menor ocorrência de magnetita (kenomagnetita $\sim 30\%$), e são fortemente foliados. Esta estrutura foliada originou-se durante o evento tectono-termal do orógeno Brasiliiano, o qual promoveu a justaposição de fatias/lascas de unidades do embasamento (Granito Borrachudos e Complexo Guanhães) com sequências sedimentares do Grupo Guanhães ao longo de falhas de orientação aproximadamente N-S e vergência para W. No caso do DLP os corpos de minério possuem espessura média de 20 m, intercalados ao itabirito por aproximadamente 5 km na direção N-S. Corpos de pegmatito com espessuras métricas a centimétricas ocorrem associados às rochas do DLP.

Os resultados dos estudos de geocronologia e de isotópios Lu-Hf no granito Borrachudos na área próximo ao DLP em conjunto aos resultados de química mineral e inclusões fluidas permitem concluir que: (1) fluidos hidrotermais de média a alta salinidade (25-28 wt% NaCl eq.) e temperatura (275-375 °C), com provável assinatura magmática (fusões hidratadas), formaram os veios de quartzo associados com os corpos de minério; (2) eventos metassomáticos foram responsáveis pelas transformações e recristalizações minerais (e.g. magnetita – hematita) durante o processo de lixiviação em sílica que levou ao enriquecimento em ferro nos corpos de alto teor; (3) durante o orógeno Brasiliiano (ca. 614-480 Ma), metamorfismo e anatexia do Granito Açuena originou grande quantidade de fusões hidratadas (pegmatitos) e fluidos hidrotermais; (4) os corpos de alto teor em ferro nos depósitos Piçarrão-Liberdade formaram-se durante o evento tecto-termal Brasiliiano (entre ca. 614-480 Ma) com influência de fluidos hidrotermais originados pela anatexia de rochas do embasamento (principalmente Granito Açuena).

Uma segunda geração de veios de quartzo-martita-II é característica marcante do DLP, os quais contém inclusões fluidas de baixa a média salinidade (1-14 wt% NaCl eq) e temperatura (144-260 °C), e formaram-se devido à interação (mistura) de fluidos meteóricos com fluidos anatéticos enriquecidos em ferro e em alguns elementos traços.

O Granito Açuena representa um evento magnético tipo-A₂, gerado pela fusão de rochas ígneas preexistentes (e.g. Complexo Guanhães) durante o Paleo- Mesoproterozoico (ca. 1740-1650 Ma). Futuros trabalhos de análise de isótopos de O nas áreas dos zircões já datadas e analisadas por Lu-Hf seriam necessários para determinar se houve contribuição de rochas supracrustais na geração

deste magma. Por outro lado, as idades modelo de Hf são consistentes com as idades de cristalização magmática no Complexo Guanhães, sugerindo que a fusão do Complexo Guanhães é a fonte dos magmas Borrachudos. Dados de isótopos Lu-Hf nos cristais de zircão mostram uma evolução complexa (múltiplos pulsos magmáticos) na evolução do magma Açucena, o que juntamente com a assinatura geoquímica tipo-A₂, poderia indicar um contexto tectônico pós-colisional para a formação da Suíte Borrachudos.

Os cristais de esmeralda dos depósitos Piteiras e Belmonte formaram-se devido à interação de fluidos hidrotermais originados durante os eventos de metamorfismo/anatexia do Granito Açucena com as rochas máficas e ultramáficas do Complexo Guanhães.

Capítulo 6 - Referências bibliográficas (dos capítulos 1 e 2 que não foram citadas nos artigos)

Braga, F.C.S., 2012. A sequência portadora de formação ferrífera da Serra do Morro Escuro, Santa Maria de Itabira, Minas Gerais. Diss. Mestrado, UFMG.

Chemale Jr., F., 1987. Gênese das Rochas Graníticas do Tipo Borrachudos. In: SBG, Congr. Bras. Geoquímica, Porto Alegre. 1, 171-186.

Grossi-Sad, J.H., Magualhães, J.M.M., 1989. Reconhecimento geológico do alto e médio vales do Rio Doce, Minas Gerais, Brasil. Rel. DOCEGEO/GEOSOL, inédito, p154.

Knauer, L.G., Grossi-Sad, J.H., 1997. Geologia da Folha Serro. In: Grossi-Sad, J.H, Lobato, L.M., Pedrosa-Soares, A.C., Soares-Filho, B.S. (Org.) Projeto Espinhaço em CD-ROM (textos, mapas e anexos). Belo Horizonte: COMIG. p.2057-2316.

Nasdala, L., Hofmeister, W., Norberg, N., Mattinson, J.M., Corfu, F., Dörr, W., Kamo, S.L., Kennedy, A.K., Kronz, A., Reiners, P.W., Frei, D., Kosler, J., Wan, Y., Götze, J., Häger, T., Kröner, A., Valley, J.W., 2008. Zircon M257, a homogeneous natural reference material for the ion microprobe U-Pb analysis of zircon. *Geostandards and Geoanalytical Research*. v.32, p. 247–265.

Oliveira, A.R.O., 2015. Mineralizações ferríferas (especularíticas) e depósitos do tipo Jacutinga (Au-Pd-Pt), Quadrilátero Ferrífero e sul da Serra do Espinhaço (MG). Tese Doutorado, UFMG.

Pedrosa-Soares, A.C., Dardenne, M.A., Hasui, Y., Castro, F.D.C., Carvalho, M.V.A., 1994. Nota Explicativa dos Mapas Geológico, Metalogenético e de Ocorrências Minerais do Estado de Minas Gerais. Escala 1:1.000.000. Belo Horizonte: SEME/COMIG.

Silva, A.M., Chemale Jr, F., Kuyumjian, R.M., Heaman, L., 1995. Mafic dykes swarms of Quadrilátero Ferrífero and southern Espinhaço. *Revista Brasileira de Geociências*, 25(2), 124-137.

Stern, R.S., Bodorkos S., Kamo S. L., Hickman, A. H., and Corfu F. (2009). Measurement of SIMS instrumental mass fractionation of Pb-isotopes during zircon dating: *Geostandards and Geoanalytical Research*, v. 33, p. 145-168.

Uhlein, A., 1982. Geologia e mineralizações de cromita e itabiritos na Região do Serro, Minas Gerais. Dissertação (Mestrado), Brasília, UnB, p.189.

Anexo 1: Análises LA-ICP-MS em óxidos de ferro no depósito Piçarrão-Liberdade, serra do Morro Escuro e prospectos Guanhães e Dores de Guanhães.

Amostra	Mineral	Mg24	Al27	Ti49	V51	Cr52	Mn55	Co59	Ga71	As75	W182	Pb208
		2.5455	1171.5370	95.4963	33.3589	6.2471	3.2428	0.0430	0.3833	0.4348	2.3177	0.0435
Li1	Kmag	406.2244	0.7624	0.0123	2.3079	2.0688	239.8105	65.4333	1.9504	0.0000	0.0000	0.0000
Li1	Kmag	392.7851	0.7046	0.0290	2.3118	2.8522	228.6063	61.9148	2.2622	0.0000	0.0000	0.0000
Li1	Kmag	419.4226	0.8215	0.0115	2.3382	2.9257	234.5252	63.8336	2.1184	0.0000	0.0000	0.3288
Li1	Kmag	361.9176	0.7237	0.0097	2.3502	3.1754	208.9716	66.5082	2.2088	0.0000	0.0000	0.0000
Li1	Kmag	364.5824	0.7011	0.0149	2.3144	3.1517	200.4115	69.6582	1.8685	0.0000	0.0000	0.0000
Li1	Kmag	376.1555	0.8509	0.0159	2.3264	3.1406	202.4282	63.4769	2.5646	0.5238	0.0000	0.0000
Li1	Kmag	377.1687	0.7096	0.0059	2.2928	2.9836	204.4270	63.5889	2.1404	0.0000	0.0000	0.0000
Li1	Kmag	298.9279	0.7166	0.0194	2.2897	3.1546	173.9799	65.3101	2.0853	0.0000	0.0000	0.0000
Li1	Kmag	252.8694	0.5343	0.0094	2.2695	3.0104	155.0631	64.2341	2.1271	0.0000	0.0000	0.0000
Li3	Mart	5.1234	0.8378	0.0179	0.2886	0.4560	9.9540	6.0879	1.4572	88.1787	0.1409	43.1726
										110.684		
Li3	Mart	5.3356	0.8003	0.0632	0.3230	0.4835	10.0500	6.0491	1.0908	3	0.6431	45.1520
Li3	Mart	5.3082	0.8112	0.0000	0.2157	0.4185	9.3538	5.0795	1.7198	93.8624	0.5614	37.7753
Li3	Mart	4.7522	0.8739	0.0300	0.1234	0.7322	8.9103	4.8145	1.8287	85.2759	0.0343	39.9683
										119.785		
Li3	Mart	5.8908	0.9500	0.0072	0.1425	0.6288	12.0543	6.1225	1.9015	3	0.0986	46.1880
Li3	Mart	6.4634	0.9946	0.0027	0.1561	0.4617	11.7360	6.4571	2.0015	0	0.0617	50.5856
										119.072		
Li3	Mart	5.8156	0.9941	0.0000	0.1587	0.3891	11.5425	6.8076	2.2761	8	0.5442	50.9479
Li3	Mart	5.4150	0.9814	0.0000	0.1428	0.6091	10.5196	6.1175	2.0237	92.8329	1.3755	43.8661
Li3	Mart	4.1902	0.8628	0.0000	0.1877	0.4635	7.7179	3.2706	2.1060	69.5100	0.5524	28.3113
Li3	Mart	4.5909	0.9257	0.0000	0.1678	0.5256	7.9448	4.1532	2.2936	74.0177	1.9586	37.5220
Li3	Mart	4.2403	0.9091	0.0000	0.1711	0.4516	7.9234	4.0908	2.5671	71.0276	0.2012	31.4975
Li3	Mart	5.1279	0.9880	0.0000	0.1495	0.6144	11.2896	5.4741	2.3117	98.6052	1.2006	44.3164
Li3	Mart	5.2847	0.9496	0.0000	0.1459	0.6845	10.7819	6.2668	1.8368	94.5119	0.9692	42.7489
										100.754		
Li3	Mart	5.4538	1.0699	0.0066	0.2081	0.6795	10.4185	5.9676	2.2141	6	0.3135	45.9955
										106.314		
Li3	Mart	4.9125	1.1652	0.0153	0.2244	0.7830	10.9881	6.3354	2.4231	3	0.7935	48.8123
Li3	Mart	5.0262	1.0743	0.0085	0.2283	0.7627	10.9559	6.6237	2.4577	97.5768	0.2175	45.3575

Kenomagnetita: Kmag; martita: Mart; hematita especular: Shem; hematita granoblástica: Gbhem; hematita tabular: Tbhem; hematita microlamelar: Mhem; magnetita: Mag.

Anexo 1 (cont.)

Li3	Mart	4.8417	1.1557	0.0195	0.3201	0.9460	12.4898	6.4277	2.6767	96.9605	0.4456	49.0981
Li3	Mart	5.5153	0.9269	0.0065	0.2358	0.8459	9.9001	6.2588	2.0485	89.3559	0.3816	43.5828
Li3	Mart	5.2373	0.7768	0.0000	0.0674	0.4562	8.6171	4.8247	1.1790	80.8080	0.3215	38.1556
										102.239		
Li3	Mart	5.5217	1.0425	0.0000	0.1472	0.4296	11.8282	7.8870	2.5049	0	0.1503	46.5860
Li3	Mart	5.3557	1.0594	0.0000	0.1672	0.4055	11.4580	7.3779	2.4285	99.9119	0.1179	46.1947
										103.178		
Li3	Mart	5.4027	1.0940	0.0000	0.1921	0.4639	11.9625	6.9507	2.7229	6	0.0930	50.0410
										100.541		
Li3	Mart	5.2278	1.0088	0.0000	0.1800	0.5258	11.9121	8.3616	2.2730	2	0.0528	48.1321
										106.529		
Li3	Mart	5.8571	1.0779	0.0000	0.1913	0.4795	10.6559	5.4819	2.0936	4	0.1006	49.0779
Li3	Mart	5.3216	0.5175	0.0032	0.1595	0.2203	4.7684	2.6111	1.8510	88.5631	10.3122	20.8883
Li3	Shem	0.0000	0.1416	0.0000	0.1056	0.1231	0.0000	0.0000	0.5417	1.1831	0.0981	0.0000
Li3	Shem	0.1702	0.5082	0.0000	0.3415	0.0000	0.0000	0.0000	1.2370	0.8953	1.6568	0.0000
Li3	Shem	0.3379	0.3084	0.0000	0.0902	0.1023	0.0000	0.0000	1.8159	3.2290	0.0491	0.0000
Li3	Shem	0.0678	0.4770	0.0000	0.3186	0.1007	0.0000	0.0000	1.1947	0.6267	1.0643	0.0000
Li3	Shem	0.2710	0.1991	0.0000	0.0670	0.0000	0.0000	0.0000	1.7059	0.6792	0.0361	0.0000
Li3	Shem	0.3058	0.1943	0.0000	0.0818	0.0000	0.0000	0.0000	1.7056	0.4966	0.0160	0.0000
Li3	Shem	0.2979	0.2888	0.0000	0.0986	0.0977	0.0000	0.0000	2.1436	1.5406	0.0696	0.9004
Li3	Shem	0.2793	0.4260	0.0000	0.1504	0.0000	0.0000	0.0000	1.9666	0.0000	0.3172	0.0000
Li3	Shem	0.2196	0.4124	0.0000	0.1807	0.0000	0.0000	0.0000	1.6572	0.0000	0.1852	0.0000
Li3	Shem	0.3570	0.4899	0.0000	0.3662	0.1839	0.0000	0.0000	1.5464	2.6081	0.6388	0.0000
Li3	Shem	0.2380	0.2576	0.0000	0.1100	0.0000	0.0000	0.0000	1.5725	0.0000	0.0411	0.4702
Li3	Shem	0.0660	0.4084	0.0000	0.3207	0.0000	0.2984	0.0000	0.9296	0.0000	1.7329	0.0000
Li3	Shem	0.3037	0.3235	0.0000	0.1198	0.1187	0.4283	0.0000	1.6773	0.6998	0.5935	0.0000
Li5	Gbhem	0.8896	1.4330	0.4337	1.1269	0.8010	1.8465	0.0000	2.7285	1.7789	2.5520	0.0000
Li5	Gbhem	1.1085	1.5083	0.5364	1.1786	0.9134	2.3318	0.0000	3.2181	1.6564	2.2907	0.0000
Li5	Gbhem	0.5989	1.5052	0.5106	1.2261	1.2255	1.4147	0.0000	2.9752	1.1124	2.4574	0.7075
Li5	Gbhem	0.8483	1.4775	0.3975	1.2297	0.6437	2.0540	0.0000	3.0640	1.9241	2.8880	0.6706

Anexo 1 (cont.)

Li5	Gbhem	1.0552	1.4568	0.4310	1.1521	0.8431	2.3432	0.0000	3.2513	1.5750	2.9246	0.0000
Li5	Gbhem	0.7862	0.4193	1.6243	0.9986	4.4367	3.2087	0.5786	0.9181	0.0000	0.9361	1.3340
Li5	Gbhem	0.5290	0.4238	1.7288	1.0141	4.7229	1.8438	0.5344	1.0228	0.6834	0.9722	0.0000
Li5	Gbhem	1.0384	0.4166	1.4646	1.0300	1.2434	4.3410	0.0000	1.0858	1.1319	1.0732	0.0000
Li5	Gbhem	0.5279	0.4190	1.4640	1.0134	1.2213	1.9400	0.4415	0.8802	0.0000	1.2051	0.0000
Li5	Gbhem	0.5422	0.4293	1.7870	0.9660	1.2720	1.8579	0.0000	1.0374	0.0000	0.9328	0.9141
Li5	Gbhem	0.6577	0.4163	1.4183	1.0007	0.9990	2.3915	0.4710	1.0019	0.5951	1.1518	0.0000
Li5	Gbhem	0.6868	0.3989	1.1846	1.1153	1.0719	2.7368	0.4921	0.9277	1.4512	1.2848	0.8709
Li5	Gbhem	0.5905	0.4199	1.5432	1.0587	2.2640	2.1334	0.0000	0.9158	0.8269	1.2516	0.0000
Li5	Gbhem	1.3487	0.6779	0.7788	1.2457	14.8728	4.7261	0.0000	1.5299	1.4597	1.8183	0.0000
Li5	Gbhem	1.1403	0.7558	0.6973	1.2809	9.3800	4.6226	0.4688	1.5725	1.7289	1.8901	0.0000
Li5	Gbhem	1.2427	0.6142	0.7639	1.2013	16.7814	4.6119	0.4376	1.4632	1.1678	1.6726	0.0000
Li5	Gbhem	1.2840	0.6750	0.9003	1.1988	21.2358	4.5011	0.5702	1.4805	1.3436	1.5353	0.0000
Li5	Gbhem	1.3889	0.7299	0.7244	1.2427	12.2631	5.2681	0.6239	1.6729	1.0295	1.6367	0.0000
Li5	Gbhem	1.0915	0.7230	0.5241	1.2341	5.0956	4.2471	0.3396	1.5767	1.0169	1.9761	0.0000
Li5	Gbhem	1.6069	0.6683	0.7241	1.2282	12.4140	5.4520	0.6515	1.0447	1.2260	1.5635	0.9332
Li5	Gbhem	0.2379	0.4320	0.4031	1.2718	1.1453	1.7533	0.0000	0.8549	0.9035	1.6782	0.0000
Li5	Gbhem	0.4520	0.4435	0.4194	1.3002	1.2051	1.7993	0.0000	0.9745	0.9835	1.6731	0.0000
Li5	Gbhem	0.1617	0.4438	0.4256	1.2561	0.9796	1.1424	0.0000	0.9037	0.0000	1.6449	1.5300
Li5	Gbhem	0.1639	0.4277	0.3761	1.2695	1.1192	1.6961	0.0000	1.0219	0.7954	1.8007	0.0000
Li5	Gbhem	0.1916	0.4467	0.4495	1.3041	1.4496	1.6463	0.3540	0.9332	0.7385	1.7316	0.0000
Li5	Gbhem	0.2079	0.4312	0.4145	1.2606	1.3111	1.8568	0.0000	1.2309	0.7524	1.8448	0.0000
Li5	Mart	370.9720	0.2019	0.1575	0.6222	3.5755	1888.8715	1003.0862	2.0947	4.1637	0.0408	138.0151
Li5	Mart	366.7607	0.2622	0.1679	0.5954	3.5064	1711.4289	949.2389	1.8861	6.4647	0.0219	88.4559
Li5	Mart	381.2704	0.2665	0.1864	0.5980	3.5470	1864.9846	994.0701	1.8675	5.9577	0.0271	94.2831
Li5	Mart	399.8726	0.3331	0.1965	0.6203	3.7044	2057.0057	1035.1154	2.0998	4.3424	0.0000	173.7009

Anexo 1 (cont.)

Li5	Mart	379.4695	0.3875	0.1824	0.6067	3.5065	1866.8689	1034.0727	2.4560	7.7546	0.0386	114.2897
Li5	Mart	360.7408	0.2843	0.1566	0.6109	3.4648	1766.0182	978.3186	1.7505	4.0739	0.0276	70.8991
Li5	Mart	249.8478	0.2696	0.1589	0.6091	3.5507	1662.9918	990.7529	1.8983	5.5716	0.0234	95.6763
Li5	Mart	481.0409	0.2883	0.0892	0.4689	1.8236	1398.3780	1081.8016	1.9066	6.5267	0.0000	159.3215
Li5	Mart	641.9229	0.3599	0.0972	0.4698	1.7861	1438.7105	1165.2210	1.8954	7.3452	0.0000	153.3994
Li5	Mart	600.9510	0.3539	0.0889	0.4691	1.6868	1449.9613	1145.8985	2.2099	5.0393	0.0000	130.4515
Li7	Gbhem	0.9135	1.3688	0.9917	2.1737	2.9660	1.2840	0.0000	4.9479	1.2366	5.5135	0.0000
Li7	Gbhem	0.7890	1.2874	0.4720	2.2987	1.4873	1.1437	0.0000	5.1527	1.6229	6.5290	0.0000
Li7	Gbhem	0.8356	1.3258	0.5496	2.2344	1.4161	1.3037	0.0000	4.8706	1.1481	6.5915	0.0000
Li7	Gbhem	0.7398	1.3195	0.2906	2.3280	1.5477	1.3203	0.0000	4.8317	1.5506	6.9809	0.0000
Li7	Kmag	71.8552	0.4192	0.0143	0.8590	2.1706	494.3103	54.9877	8.4976	0.0000	0.0000	0.0000
Li7	Kmag	78.2216	0.4799	0.0174	0.8611	2.0831	494.0048	59.0633	8.4126	0.8084	0.0000	0.6229
Li7	Kmag	82.7253	0.5234	0.0110	0.8569	2.2137	506.1004	61.6208	9.0222	0.7238	0.0000	0.0000
Li7	Kmag	108.4275	0.7111	0.0156	0.8545	2.4946	513.7790	56.1501	8.6223	0.0000	0.0000	0.0000
Li7	Kmag	114.4915	0.7323	0.0072	0.8447	2.5574	513.0111	59.0897	10.4618	0.5979	0.0146	0.0000
Li7	Kmag	96.7367	0.6717	0.0130	0.8607	2.4195	507.8141	56.4064	10.0723	0.8374	0.0000	0.0000
Li7	Mart	113.8286	1.0837	0.0135	0.9065	2.8148	645.2319	63.4081	10.7797	23.8336	0.0000	206.5962
Li7	Mart	96.7980	0.9620	0.0094	0.8745	2.9641	682.6030	59.5142	10.8794	22.5080	0.0000	210.6268
Li7	Mart	117.4397	1.0294	0.0162	0.9286	2.7109	670.1239	63.5719	10.8900	24.7670	0.0000	206.8200
Li7	Mart	103.3617	0.9756	0.0111	0.9320	2.4189	646.3806	65.7921	9.7417	22.6410	0.0000	173.3014
Li7	Mart	93.2360	0.9296	0.0110	0.9418	2.4355	603.4271	57.9494	11.4292	19.9960	0.0000	135.7845
Li7	Mart	61.7432	0.7935	0.0168	0.9236	2.2933	641.0874	62.7891	10.6985	24.8443	0.0000	206.0444
Li7	Tbhem	0.8429	1.0959	0.5680	2.6564	3.0587	1.6175	0.0000	4.4378	5.8923	6.6785	1.1884
Li7	Tbhem	0.8267	1.2070	0.2420	2.6972	2.3305	1.4311	0.0000	4.2281	1.3698	3.8286	0.0000
Li7	Tbhem	0.9318	1.2018	0.4567	2.4833	2.3724	1.4337	0.0000	4.5393	1.2227	6.1549	0.0000
Li7	Tbhem	0.8417	1.2412	0.3160	2.6736	2.6748	1.3889	0.0000	4.1442	1.2755	3.0640	0.0000
Li7	Tbhem	0.8177	1.2090	0.2211	2.8227	2.3969	1.3529	0.0000	3.9751	1.1595	2.7647	0.7226
Li7	Tbhem	0.8343	1.2309	0.3216	2.5225	2.6516	1.4042	0.0000	4.3354	1.2768	5.1349	0.0000
Li7	Tbhem	0.5761	1.2694	0.3558	2.1173	1.2093	1.1162	0.0000	4.8702	1.7264	6.8082	0.4784
Li7	Tbhem	0.7347	1.3053	0.8740	2.0774	2.1914	1.1465	0.0000	4.8997	2.3579	5.2706	0.0000

Anexo 1 (cont.)

Li7	Tbhem	0.6153	1.2684	0.8200	2.1206	4.6388	1.2370	0.0000	4.9121	2.0213	4.4525	0.0000
Li7	Tbhem	0.6754	1.3103	0.6714	2.2111	4.6750	1.4000	0.6884	5.1104	1.7382	4.2008	4.8331
Li7	Tbhem	0.6612	1.2798	0.5212	2.3368	2.5502	1.1045	0.0000	5.0295	1.6938	4.9624	0.0000
Li7	Tbhem	0.2363	1.2886	0.2193	2.3295	1.3462	0.5870	0.0000	5.1736	0.9967	2.6877	0.0000
Li7	Tbhem	0.2801	1.3280	0.3067	2.2776	2.4565	0.6734	0.0000	5.1276	0.9753	3.1025	0.0000
Li7	Tbhem	0.6655	1.3443	0.5215	2.2264	2.6090	1.1695	0.0000	5.2456	0.9310	6.2487	0.0000
Li1Sul	Mart	257.0988	0.7216	0.0607	1.2151	1.2507	311.7186	19.7927	1.9686	1.0173	0.0000	442.4244
Li1Sul	Mart	271.1570	0.7870	0.0340	1.2697	1.3540	310.8233	23.4011	2.0622	0.0000	0.0000	370.6353
Li1Sul	Mart	265.2349	0.7880	0.0412	1.2047	1.2745	317.2507	19.9584	2.0843	1.1903	0.0000	545.4435
Li1Sul	Mart	248.6501	0.7606	0.0366	1.1626	1.9024	310.2997	18.3773	2.1432	1.9455	0.0000	481.4904
Li1Sul	Mart	261.5422	0.6983	0.0409	1.1664	1.7145	311.0986	21.6855	1.8163	1.0701	0.0000	349.1658
Li1Sul	Mart	249.1227	0.6828	0.0476	1.1660	1.6952	310.5826	21.5721	2.3388	1.8521	0.0000	363.1497
Li1Sul	Mart	254.3869	0.6711	0.0585	1.1504	1.9299	304.8808	22.3697	1.8350	0.9661	0.0000	326.9427
Li1Sul	Mart	248.9499	0.7410	0.0692	1.1994	2.0589	304.5111	17.6888	1.8144	1.1755	0.0000	276.8882
Li1Sul	Mart	243.2882	0.7570	0.0616	1.1941	1.9520	311.4975	21.7703	2.2213	2.1380	0.0000	420.5695
Li1Sul	Mart	245.2018	0.7034	0.0404	1.2208	2.5596	302.9092	16.1309	2.4176	2.2520	0.0000	394.9101
Li1Sul	Mart	249.8047	0.7740	0.0485	1.1698	2.1101	301.0489	17.6520	2.5347	1.3571	0.0000	407.9244
Li1Sul	Mart	250.1836	0.7261	0.0573	1.2098	2.3322	306.8221	20.1681	2.2673	1.2183	0.0000	281.1325
Li1Sul	Mart	212.0841	0.7399	0.0655	1.2818	1.1790	314.9378	18.2260	2.8527	1.9216	0.0000	471.7371
Li1Sul	Mart	221.7121	0.7701	0.0780	1.2435	1.4061	321.2405	15.8728	1.8819	1.3095	0.0000	494.5678
Li1Sul	Mart	208.5539	0.7062	0.0687	1.2577	1.0433	306.5010	18.4014	1.8184	1.5628	0.0000	387.3113
Li4Sul	Kmag	271.6918	0.6465	0.5167	1.5408	1.7228	62.2809	32.8682	1.2408	0.0000	0.0000	0.0000
Li4Sul	Kmag	251.3809	0.6155	0.4139	1.5018	2.1418	61.8964	39.6946	1.3269	0.0000	0.0000	0.0000
Li4Sul	Kmag	314.6811	0.4784	0.2266	1.4754	1.7819	71.5273	42.3376	1.1273	0.0000	0.0000	0.0000
Li4Sul	Kmag	348.4107	0.4241	0.2336	1.5175	1.9083	70.2574	44.5820	1.2658	0.0000	0.0000	0.0000
Li4Sul	Kmag	378.6095	0.5590	0.6104	1.5023	1.5826	70.3011	44.2477	1.3712	0.0000	0.0000	0.0000
Li4Sul	Kmag	384.5061	0.5414	0.3026	1.5107	2.0132	68.9636	40.4558	1.5278	0.0000	0.0000	0.0000
Li4Sul	Mart	146.9466	0.6004	0.4417	1.4647	1.8220	31.6816	67.7318	1.1338	0.0000	1.3937	31.2288
Li4Sul	Mart	156.1139	0.8719	0.4029	1.5577	1.8445	19.2997	207.6468	1.3180	0.0000	0.2011	62.4399
ME1A	Mhem	0.7738	0.7194	1.7180	1.0289	3.1743	14.5441	2.8848	2.6545	0.0000	1.0763	1.5372

Anexo 1 (cont.)

ME1A	Mhem	0.6521	0.7033	1.1796	1.1549	3.3723	10.5999	0.7147	2.8274	1.0554	1.0051	1.0395
ME1A	Mhem	0.8696	0.6963	1.8870	0.9459	2.9299	11.2388	1.3939	2.5259	0.0000	1.0042	1.0985
ME1A	Mhem	0.7782	0.7051	1.6354	1.0287	2.7018	11.0649	1.0617	2.6745	0.0000	0.9732	0.0000
ME1A	Mhem	0.6161	0.7034	1.7895	0.9654	2.8612	8.4373	0.0000	2.4124	0.0000	1.0549	0.0000
ME1A	Mhem	0.6264	0.7107	1.6883	1.0198	4.4141	8.8260	0.6505	2.5565	0.0000	1.2492	0.0000
ME1A	Mhem	0.7763	0.7116	1.9902	0.9538	4.9261	9.9437	0.9964	2.5132	0.7716	0.9934	0.0000
ME1A	Mhem	0.7964	0.7396	1.8006	0.9860	4.0201	11.0592	0.6894	2.5878	0.0000	1.1688	0.7425
ME1A	Mhem	0.9102	0.7001	1.9524	0.9735	1.7369	11.3995	0.8570	2.6683	0.0000	0.9792	0.0000
ME1A	Mhem	0.8720	0.6808	2.0166	0.9419	2.4204	10.6897	0.6359	2.4185	0.6573	0.9343	0.9943
ME1A	Mhem	0.7984	0.6957	1.9232	0.9525	2.2432	10.8963	0.8150	2.8121	0.0000	1.0273	0.9042
ME1A	Mhem	0.6914	0.7210	1.9784	0.9385	3.3010	9.8116	0.0000	2.7164	0.0000	0.8862	0.6352
ME1A	Mhem	0.7506	0.7179	2.0735	0.9269	3.3807	9.4589	0.9337	2.4412	0.8057	0.9188	0.0000
ME1A	Mhem	1.1137	0.7511	3.0899	0.8712	3.1733	11.2797	0.5185	2.6335	0.0000	0.5176	0.7016
ME1A	Mhem	1.1596	0.7237	3.4290	0.8541	3.4345	12.1740	1.1218	2.7372	0.0000	0.6018	0.0000
ME1A	Mhem	0.3365	0.6243	1.1234	0.5672	1.0944	7.0492	0.0000	1.9664	0.8359	1.7735	0.4954
ME1A	Mhem	0.4608	0.6005	1.0982	0.5621	0.9607	8.3217	0.0000	1.8224	1.1071	1.8912	0.0000
ME1A	Mhem	0.4439	0.6222	1.0776	0.5911	0.7148	8.6033	0.0000	1.8738	0.8172	2.0990	0.9176
ME1A	Mhem	0.5049	0.6134	1.0746	0.5824	0.6944	12.4628	3.5361	2.0534	0.6927	1.9533	0.0000
ME1A	Mhem	0.5277	0.6189	1.0690	0.5830	0.6282	10.8619	1.4402	2.3929	1.0056	1.8813	0.0000
ME1A	Mhem	0.5225	0.6074	0.9892	0.5811	0.8713	19.8242	12.0244	1.6425	0.9197	2.0208	0.0000
ME1A	Mart	10.0291	0.5918	0.0000	0.6226	0.8184	2366.7544	1261.2343	5.8417	18.4190	1.1112	108.5132
ME1A	Mart	25.9710	1.6517	0.0410	0.4332	1.2713	1743.5776	1706.9433	4.2774	28.1037	1.4228	294.1808
ME1A	Mart	7.6660	0.4198	0.0000	0.4513	1.1373	1878.8973	1722.7131	4.4273	18.1949	1.0379	130.2101
ME1A	Mart	7.2300	0.4641	0.0000	0.6563	2.2228	1681.6360	1360.5763	3.6101	21.4854	0.3522	171.5747
ME1A	Shem	0.0767	0.6660	0.4305	1.1366	0.2537	4.0673	0.0000	2.4302	0.0000	2.5871	5.3285
ME1A	Shem	0.1448	0.6696	0.4109	1.1603	0.2328	4.9598	0.0000	2.3654	1.0136	2.4680	3.3386
ME1A	Shem	0.1077	0.6737	0.4237	1.0452	0.2317	3.7470	0.4384	2.9155	0.6376	2.1712	0.7478
ME1A	Shem	0.1268	0.6724	0.3961	1.1145	0.2187	3.7012	0.0000	2.5799	0.9422	2.5804	0.7488
ME1A	Shem	0.0684	0.6636	0.4442	1.1101	0.2895	3.9327	0.0000	2.5462	0.0000	2.3979	0.0000
ME1A	Shem	0.1040	0.6892	0.4552	1.2609	0.2521	4.5498	0.0000	2.0781	0.0000	2.5146	1.2024

Anexo 1 (cont.)

ME1A	Shem	0.0679	0.5163	0.4223	1.1072	0.1955	3.5457	0.0000	2.9731	1.3183	2.4044	0.7357
ME1A	Shem	0.0999	0.5141	0.4750	1.0714	0.1759	4.1377	0.0000	2.7680	0.0000	2.1514	0.0000
ME1A	Shem	0.0809	0.5202	0.4175	1.1373	0.1817	4.8687	0.0000	3.0022	0.0000	2.2901	0.9615
ME1A	Shem	0.2733	0.5090	0.4432	1.0779	0.2174	7.3939	0.4622	2.4447	1.5549	2.4085	0.9699
ME1A	Shem	0.1568	0.5279	0.4345	1.1146	0.1845	5.1280	0.0000	2.6075	0.0000	1.1428	0.0000
ME1A	Shem	0.1567	0.5169	0.5436	0.9922	0.2584	5.1887	0.0000	2.5589	0.6687	1.2787	0.0000
ME2A	Kmag	10.1783	0.0490	0.0083	2.7836	0.5209	338.8359	105.2359	9.0124	1.1509	0.0000	6.1710
ME2A	Kmag	11.0934	0.0488	0.0167	2.8306	0.5444	350.1105	102.3436	9.3657	1.1115	0.0000	3.6133
ME2A	Kmag	9.2182	0.0404	0.0122	2.8483	0.4924	341.0929	102.3644	8.9143	1.6105	0.0317	8.8897
ME2A	Kmag	10.6897	0.0892	0.0135	2.8466	0.6843	335.0208	100.5452	8.6836	1.1021	0.0000	0.0000
ME2A	Tbhem	27.9707	1.7229	93.0750	4.3350	0.3195	10.0679	2.8457	3.5047	0.0000	0.4658	0.0000
ME2A	Tbhem	17.8712	1.6865	54.4537	4.2111	0.3788	6.1510	1.4256	3.3669	1.2039	0.1966	0.0000
ME2A	Tbhem	32.0774	1.7282	96.0484	4.2690	0.3647	10.8536	2.5275	3.4000	0.8480	0.2762	0.0000
ME2A	Tbhem	7.0038	1.6977	21.3471	4.3375	0.4710	2.7102	0.4318	3.1507	0.0000	0.3131	0.0000
ME2A	Tbhem	11.8305	1.6658	33.1045	4.3406	0.4704	4.0850	1.1712	3.1283	0.0000	0.3578	2.3019
ME2A	Tbhem	4.7606	1.7532	16.6183	4.4713	0.1546	2.3018	0.6209	3.2239	0.0000	0.3207	0.0000
PB1A	Mag	9728.9337	1.2481	1.2428	2.2608	1.8023	1118.6448	122.0672	5.5035	0.0000	0.0000	0.0000
PB1A	Mag	9984.2983	1.4357	1.2711	2.2868	1.1397	1103.0894	121.7969	5.6175	0.0000	0.0000	0.0000
PB1A	Mag	9019.7295	1.5752	1.2123	2.2613	1.2003	1150.8973	117.4620	5.7096	2.7142	0.9769	10.4685
PB1A	Mag	9640.7161	1.0984	1.2574	2.2360	1.1875	1110.1402	120.1912	5.2652	2.4592	0.2487	0.0000
PB1A	Mag	9656.7888	1.0936	1.2301	2.2393	1.9571	1116.7684	121.8786	5.2347	3.8070	0.0000	0.0000
PB1A	Mag	9828.3183	0.7686	1.2226	2.2418	1.3835	1100.6595	115.4074	5.3549	0.0000	0.0000	1.0673
PB1A	Mag	9787.9043	1.0874	1.2766	2.2159	0.6661	1151.2195	117.5023	5.8960	0.0000	0.0000	0.0000
PB1A	Mag	9996.4055	1.0135	1.2155	2.2653	1.7440	1126.9061	122.2270	5.9654	0.0000	0.0000	0.0000
PB1A	Mag	9616.1876	1.1223	1.1779	2.2468	1.9486	1090.1951	122.8671	5.8977	0.0000	0.0904	0.0000
PB3	Mhem	0.1648	0.5954	0.2142	1.1973	0.8715	8.8986	0.0000	3.8253	1.6864	3.4185	0.0000
PB3	Mart	28.8176	0.7117	0.0000	1.0379	0.9133	5727.0099	528.3388	17.4062	34.1179	9.9897	240.7488
PB3	Mart	16.6332	0.5940	0.0000	0.9863	0.9078	4930.1714	462.5489	15.5099	32.5231	8.0995	204.6398
PB3	Mart	21.0035	0.6091	0.0000	0.9715	0.9006	5087.4179	488.2947	16.2721	33.0073	8.5705	222.2443
PB3	Mart	30.2489	0.7097	0.0000	1.0241	0.9051	5784.6690	531.1500	16.6450	31.5464	11.0039	314.8688
PB3	Mart	23.6303	0.7476	0.0000	1.0672	1.1349	5381.2473	522.8624	16.3307	32.4909	8.0790	127.5025
PB3	Mart	27.8146	0.7425	0.0000	1.0792	1.2595	5477.4737	532.6234	16.3817	34.1923	8.3272	119.6913
PB3	Mart	22.5210	0.7495	0.0000	1.0602	1.1483	5272.2360	513.2904	15.0341	32.0506	8.4032	117.7933

Anexo 1 (cont.)

PB3	Mart	13.3607	0.6751	0.0000	1.0470	1.1674	5209.6519	526.0399	15.4238	33.1841	7.7281	152.2114
PB3	Mhem	0.3041	0.5415	0.1619	1.0684	0.9457	27.1216	1.0962	3.2973	1.7417	2.1551	0.0000
PB3	Mhem	0.1845	0.5217	0.1642	1.0591	0.5484	11.7392	0.0000	3.0774	1.9784	3.6161	0.0000
PB3	Mhem	0.2051	0.5412	0.1817	0.9875	0.4356	14.2463	0.0000	2.9268	2.2695	3.8195	0.0000
PB3	Mart	35.0624	0.7220	0.0000	1.2028	0.9021	7551.9030	485.7955	13.2075	43.2718	0.3213	41.8508
PB3	Mart	28.0642	0.6949	0.0000	1.1859	0.8694	7788.9268	496.2179	13.5595	40.7130	0.3491	41.7685
PB3	Mart	25.2749	0.6911	0.0000	1.1659	0.9291	7727.4594	502.1966	13.2942	37.0863	0.2759	37.0696
PB3	Mart	27.9620	0.6843	0.0000	1.2995	0.9505	8237.8842	513.3681	13.6987	50.6631	3.7648	242.6102
PB3	Mart	30.2836	0.7758	0.0000	1.2624	1.0400	8583.0089	523.8772	13.2488	44.9801	3.3041	201.8286
PB3	Mart	18.3987	0.7612	0.0000	1.3668	0.8847	8547.3283	556.3819	12.7588	51.3282	3.8810	199.7073
PB4A	Tbhem	4.5985	3.9254	3.1518	2.3367	6.6526	4.1811	0.0000	15.4930	0.0000	1.7156	0.0000
PB4A	Tbhem	3.1701	3.8701	3.3709	2.2866	9.4376	2.9723	1.7197	15.5186	0.0000	1.6429	0.0000
PB4A	Tbhem	3.7839	4.0986	3.0986	2.2730	2.9816	2.4751	0.0000	15.2350	0.0000	1.5862	0.0000
PB4A	Tbhem	2.5128	4.2854	2.8625	2.2067	3.2089	2.9390	0.0000	14.9663	0.0000	1.6848	0.0000
PB4A	Tbhem	2.4601	3.9775	3.2158	2.2285	2.8963	2.8360	0.0000	15.1552	0.0000	1.5621	0.0000
PB4A	Tbhem	3.2789	3.8283	3.2920	2.2708	2.9635	1.2019	0.9320	15.2031	0.0000	1.6450	0.0000
PB4A	Tbhem	1.9669	3.8842	3.2396	2.2546	2.4105	1.2871	0.0000	14.8911	0.0000	1.6330	0.0000
PB4A	Tbhem	7.6237	3.7926	3.2111	2.2428	2.8604	0.8983	2.5174	15.8323	0.0000	1.6013	0.0000
PB4A	Tbhem	2.8921	3.8683	3.2237	2.2464	2.9261	0.9672	1.2568	16.7238	0.0000	1.8515	0.0000
PB4A	Tbhem	3.6070	3.8576	3.3859	2.1498	3.5957	1.6373	1.8973	14.5825	0.0000	1.3321	0.0000
PB4A	Tbhem	3.3826	3.9622	3.5578	2.2179	3.8899	3.5260	1.2126	15.5927	0.0000	1.3758	0.0000
GA	Gbhem	243.1647	3.8557	41.6177	3.3156	3.8429	11.7500	6.2208	4.7571	0.0000	0.3895	0.0000
GA	Gbhem	166.2354	3.1102	30.7774	2.8638	3.7023	9.2247	4.5665	3.9800	0.0000	0.1828	0.0000
GA	Gbhem	241.5134	3.6869	42.1464	3.3382	3.0853	11.6498	6.0829	4.6680	0.0000	0.8997	0.0000
GA	Gbhem	196.6992	3.5167	35.7423	3.1819	3.0933	10.0177	6.0795	4.4589	1.2257	0.3687	0.0000
GA	Gbhem	97.0427	2.2064	21.8948	2.1983	7.3944	6.6213	3.4911	3.7917	1.1189	0.0464	0.8423
GA	Gbhem	202.8455	3.5429	35.0675	3.2024	4.0619	10.6599	5.1318	4.6949	0.0000	0.3133	0.0000
GA	Gbhem	198.6681	3.7119	33.7094	3.4052	4.0527	10.0355	6.3317	4.9126	0.0000	0.5649	0.0000
GA	Gbhem	138.3805	2.6984	27.3432	2.5342	3.3609	8.1350	4.0487	4.0155	0.0000	0.1688	0.0000
GA	Gbhem	135.2593	2.7170	27.1409	2.4834	3.2031	8.2136	5.1911	3.6689	0.7930	0.1486	0.0000
GA	Gbhem	203.2809	3.4446	34.4859	3.1115	2.9673	10.5533	6.0563	4.8309	1.0390	0.8329	0.0000
GA	Gbhem	140.2603	3.7893	22.4786	3.9539	2.6142	9.4525	3.0877	5.5846	0.0000	2.9474	1.2415
GA	Gbhem	210.7302	3.7244	33.8948	3.3484	3.3001	11.0813	6.7051	4.9694	0.0000	0.9004	0.0000
GA	Gbhem	180.1586	3.2257	31.4561	2.9909	2.9676	10.7441	0.0000	4.6082	0.0000	0.8456	0.0000

Anexo 1 (cont.)

GA	Gbhem	144.3646	2.5438	28.2544	2.3113	3.3455	8.6462	4.8624	4.0396	0.0000	0.0948	0.0000
GA	Gbhem	224.3724	3.3487	37.2888	2.9999	3.0414	11.5537	5.9771	4.3737	0.0000	0.7169	0.0000
GA	Gbhem	231.6865	3.4661	39.1705	3.0524	2.8771	11.6975	5.9874	4.7457	0.0000	0.4811	0.0000
GA	Gbhem	198.2215	3.1839	34.0095	2.8618	3.3763	10.9249	5.0985	4.7580	0.0000	0.3566	0.0000
GA	Gbhem	111.5787	3.6290	18.1857	3.9566	2.8671	7.8398	2.3740	5.0097	1.3300	4.4986	0.0000
GA	Gbhem	64.8020	3.8981	10.7638	5.0100	3.0150	5.9977	1.0198	5.2172	1.2698	4.1361	0.0000
GA	Gbhem	58.8421	3.8866	11.3127	4.6446	2.7816	5.4929	2.0086	5.1284	0.0000	5.9721	0.0000
GA	Gbhem	146.0909	3.7827	23.8359	3.6765	3.3206	9.2599	4.1959	5.5565	0.8174	2.6656	0.0000
GA	Gbhem	143.2547	3.7832	23.5996	3.6305	3.1215	8.8650	3.9634	5.8128	0.0000	1.9100	0.0000
GA	Gbhem	135.5171	2.7633	25.9715	2.5899	2.5795	8.1352	4.0483	3.8994	0.0000	0.1100	0.0000
GA	Gbhem	144.0098	2.5475	27.7632	2.4056	3.1984	8.9128	4.0698	4.0950	0.0000	0.0783	0.0000
GA	Gbhem	178.1663	3.5390	30.6266	3.2504	2.3239	10.0308	4.3535	5.0675	0.9245	0.6404	0.0000
GA	Gbhem	132.2406	4.0412	22.3796	3.7843	1.8740	10.3966	4.0093	5.9091	1.0055	3.6405	0.0000
GA	Gbhem	80.6872	4.2301	8.8671	5.2628	5.6324	7.9810	1.6983	6.2578	0.0000	6.0416	0.0000
GA	Gbhem	60.8078	4.1549	8.5126	5.2800	5.6191	4.8063	1.9909	6.1284	0.8606	8.4925	0.0000
GA	Gbhem	180.2037	3.3114	31.9579	2.9261	2.4221	10.4830	4.4012	4.3347	0.8328	0.4471	1.4007
GA	Kmag	15088.5502	0.7156	0.1843	1.6840	6.0825	1308.9164	674.6797	16.4295	0.0000	0.0000	0.0000
GA	Kmag	14981.8165	3.0125	0.1741	1.6521	6.5168	1231.9318	673.9325	22.2194	0.0000	0.0000	0.0000
GA	Kmag	15398.8937	1.6788	0.2003	1.7160	7.0109	1221.5281	670.1820	20.7124	0.6690	0.0000	0.0000
GA	Kmag	15788.5410	2.5334	0.1761	1.7015	6.3773	1323.8524	689.1078	22.5881	0.0000	0.0000	0.0000
GA	Kmag	14875.1715	0.6974	0.2438	1.7186	6.5229	1360.8998	670.5657	16.4536	0.0000	0.0000	0.0000
GA	Kmag	15048.1257	1.2277	0.3390	1.7221	4.4115	1263.9127	652.8627	18.7077	0.0000	0.0166	0.0000
GA	Kmag	15219.6495	0.8644	0.2281	1.7198	4.2375	1295.2891	684.2601	16.8920	0.7285	0.0000	0.0000
GA	Kmag	15469.1770	1.3580	0.2213	1.6540	4.2748	1258.0006	676.8456	18.7962	0.0000	0.0000	0.0000
GA	Kmag	15880.3448	3.7995	0.2117	1.7207	4.5848	1295.6316	705.9334	19.2790	0.0000	0.0000	0.0000
GA	Kmag	15369.7117	1.1364	0.2232	1.6828	4.3070	1255.7743	681.0078	18.1163	0.7306	0.0000	0.0000
GA	Kmag	15755.7813	3.1772	0.2519	1.7406	4.4024	1259.5006	701.5836	24.8239	0.7295	0.0000	0.0000
GA	Kmag	15227.5014	2.2327	0.2365	1.7510	4.3829	1259.5284	662.2680	21.0059	0.0000	0.0000	0.0000
GA	Kmag	15095.9689	1.5194	0.1715	1.6447	4.8087	1309.0921	663.6641	19.9692	1.0818	0.0000	0.0000
GA	Kmag	15068.7140	1.7682	0.2158	1.7319	4.4741	1292.8718	672.1723	21.6866	1.0219	0.0000	0.0000
GA	Kmag	15037.9291	2.0661	0.2283	1.6784	5.5600	1302.5963	698.9439	23.9733	0.6634	0.0000	0.5847
GA	Kmag	14980.9674	1.2507	0.1995	1.7264	6.0159	1314.5534	684.1435	19.6750	1.2220	0.0000	0.0000
GA	Kmag	15111.6410	0.8504	0.2049	1.6988	5.9062	1360.6185	686.3368	16.9284	0.0000	0.0000	0.0000

Anexo 1 (cont.)

GA	Kmag	15509.1745	1.4519	0.1900	1.7078	5.6194	1337.2203	688.4456	19.6891	0.0000	0.0000	0.0000
GA	Kmag	15021.2620	1.0337	0.1675	1.7364	5.4295	1315.8433	678.5686	18.1793	0.5057	0.0000	0.0000
GA	Kmag	15319.6657	1.1786	0.2085	1.7162	6.0882	1369.9912	710.5109	18.2865	0.0000	0.0000	0.0000
GA	Kmag	14657.4598	1.1116	0.1371	1.6984	4.7195	1272.0026	666.0911	17.7152	1.6702	0.0498	4.2735
GA	Kmag	15204.4269	2.2169	0.1262	1.7282	5.0050	1280.8782	670.4400	21.8533	0.0000	0.0000	0.0000
GA	Kmag	14926.8086	0.7902	0.1191	1.7120	4.8662	1284.3996	681.6634	17.6451	0.6981	0.0000	0.0000
GA	Kmag	15334.4419	1.4134	0.1186	1.7259	5.1623	1297.1095	729.6300	20.5647	0.6092	0.0000	0.0000
GA	Kmag	14948.4311	1.0838	0.1173	1.6917	4.8669	1283.3958	684.8099	18.0705	0.0000	0.0000	0.0000
GA	Kmag	15071.0470	1.5803	0.2644	1.6816	5.2034	1369.5593	670.3594	17.1742	0.0000	0.0000	0.0000
GA	Kmag	14928.8576	1.1950	0.2272	1.6998	5.2737	1311.7071	667.0199	17.3169	0.6131	0.0000	0.0000
GA	Kmag	15029.5714	2.4321	0.2071	1.7204	5.3522	1321.5585	708.4141	22.2419	0.0000	0.0000	0.0000
GA	Kmag	14755.8111	0.7201	0.2124	1.6897	5.2523	1347.6329	671.4689	16.6878	0.7494	0.0000	0.0000
GA	Kmag	14996.2303	1.3723	0.2580	1.6659	5.0622	1310.0672	688.9871	18.9788	0.8050	0.0000	0.0000
GA	Kmag	14819.8515	1.6410	0.2037	1.6478	5.1686	1282.2132	671.0421	20.4868	0.6582	0.0000	0.0000
GA	Kmag	14651.9535	1.1136	0.2106	1.7040	5.1747	1299.2230	678.5288	18.0271	0.0000	0.0000	0.0000
GB	Kmag	9768.4112	1.4502	1.2366	2.1538	0.9490	1118.3214	113.6809	5.9139	1.1057	0.0000	0.0000
GB	Kmag	10081.8826	1.3460	1.1344	2.1811	0.7910	1138.6511	121.2806	6.0934	1.6469	0.0000	0.0000
GB	Kmag	10053.4223	1.0283	1.2288	2.2355	0.8893	1146.3605	122.0860	5.4822	0.8178	0.0000	0.0000
GB	Kmag	10243.0846	1.9839	1.1409	2.2290	0.8341	1122.6679	118.7560	6.0139	0.8164	0.0000	0.0000
GB	Kmag	9966.3639	1.1971	1.2242	2.2459	0.7073	1113.5050	119.3575	5.4922	0.8259	0.0000	0.0000
GB	Kmag	9158.0339	0.6673	0.7792	2.1765	1.1723	1140.6488	119.0624	4.7477	1.4779	0.0000	2.1842
GB	Kmag	9571.7676	0.6844	0.9498	2.2668	1.1958	1161.3497	118.1680	5.1169	1.0062	0.0000	2.4254
GB	Kmag	9302.6977	0.8077	0.8718	2.1652	1.1189	1154.1035	122.2623	4.9784	0.0000	0.0000	3.2811
GB	Kmag	10103.1598	2.0828	1.0668	2.2022	1.1736	1140.3425	114.0571	6.4799	1.0576	0.0000	0.0000
GB	Kmag	9218.2048	0.6125	1.1235	2.2112	1.2094	1134.0129	121.9128	4.8832	1.5004	0.1429	1.8111
GB	Kmag	9431.9183	0.6132	0.8084	2.2146	1.1689	1183.2129	121.5574	4.4722	0.8660	0.0654	3.5080
GB	Kmag	10108.8626	0.9900	1.2227	2.1942	0.9656	1084.9594	120.5360	5.8092	1.1661	0.0000	0.0000
GB	Kmag	10111.8116	1.4099	1.1805	2.1355	1.0030	1104.9782	116.9866	6.5185	0.0000	0.0000	0.0000
GB	Kmag	10133.6283	1.4792	1.2030	2.1496	1.0696	1105.6374	120.7201	5.4987	1.0416	0.0000	0.7017
GB	Kmag	10306.7718	2.3849	1.1201	2.1819	1.0449	1105.2547	119.6808	5.6738	1.0316	0.0000	0.0000
GB	Kmag	9892.7687	1.0855	1.2018	2.1672	0.9660	1168.9493	123.6598	6.0146	1.0430	0.0000	1.1263
GB	Kmag	10045.0845	0.8544	1.0569	2.2341	0.9188	1101.9390	122.0539	5.2160	0.0000	0.0000	1.7850
GB	Kmag	10163.1686	1.5994	1.1334	2.2538	1.0207	1136.2088	121.2030	7.0773	0.8352	0.0000	0.0000
GB	Kmag	9927.4666	0.9412	1.1638	2.2051	0.6920	1079.5376	116.2916	5.5490	1.1246	0.0000	0.0000

Anexo 1 (cont.)

GB	Kmag	10224.4198	1.3513	1.2421	2.2019	0.6701	1103.5315	121.9479	5.7715	0.0000	0.0000	0.0000
GB	Kmag	10027.4180	1.1310	1.1923	2.2020	0.7577	1095.0141	118.6078	5.3415	0.8774	0.0000	0.0000
GB	Kmag	10248.3234	1.0690	1.2711	2.2185	0.7387	1122.8149	118.2261	5.1281	0.0000	0.0000	0.8927
GB	Kmag	9803.2429	1.0201	1.1593	2.1710	0.8135	1094.9144	120.6327	5.5066	0.0000	0.0000	0.5679
GB	Kmag	10269.4483	1.0760	1.1730	2.2677	0.8025	1085.1551	120.7317	5.8310	0.0000	0.0000	0.0000
GB	Kmag	10085.5826	0.9992	1.1665	2.1802	0.6593	1081.7588	128.2555	5.4801	0.6797	0.0000	0.0000
GB	Kmag	9904.8104	0.8245	1.2670	2.2339	0.6914	1178.8018	118.4770	5.4861	0.0000	0.0000	0.8781
GB	Kmag	10009.4487	2.5719	1.1776	2.2219	0.6632	1134.3851	117.0180	5.5691	2.0542	0.0217	0.0000
GB	Kmag	9861.6494	1.1281	1.2506	2.2115	0.7785	1116.6121	114.6516	5.9143	1.6948	0.0000	0.0000
GB	Kmag	9820.7512	1.1084	1.1896	2.1916	0.7046	1118.4744	121.2767	5.5094	2.0154	0.0000	0.0000
GB	Kmag	9548.2933	1.0176	1.1680	2.1214	0.6847	1098.2204	120.9732	5.8856	0.0000	0.2656	4.4940
GB	Kmag	9884.4739	1.2110	1.2125	2.1951	0.7270	1104.6455	119.1897	6.0541	1.2653	0.0000	0.0000
DG1	Mart	349.2560	4.7887	27.6969	8.8777	80.3997	1150.8370	191.2931	20.1621	11.7537	0.1768	1162.3028
DG1	Mart	412.2069	3.0505	30.3664	9.7857	92.6429	1251.4197	190.9127	20.6649	9.3947	0.0617	881.0590
DG1	Mart	329.5806	2.5918	30.0729	9.7724	83.7267	1146.1379	176.7909	16.0704	9.1086	0.0663	858.0837
DG1	Mart	404.6183	3.2253	29.8907	9.8555	113.2565	1227.3393	181.8163	20.3551	9.5315	0.0595	893.8260
DG1	Mart	400.9961	3.0925	27.8982	10.3605	88.4547	1249.7000	195.5558	21.0337	8.9419	0.0748	746.1282
DG1	Mart	364.2744	3.1596	28.9503	9.8389	84.6587	1194.2068	176.1308	18.0411	9.5830	0.0847	910.8429
DG1	Mart	364.8809	3.4502	35.7321	10.4594	13.2404	1175.8441	165.9046	21.8875	4.9371	0.0276	417.8055
DG1	Mart	400.4382	4.2527	33.9003	10.7272	18.2205	1169.0000	176.5055	23.8419	6.1894	0.0306	468.6146
DG1	Mart	310.3026	2.7162	34.7242	10.3839	12.7161	1203.3652	163.2752	17.5741	4.4928	0.0365	372.2783
DG1	Mart	397.3412	4.3770	34.0525	10.7770	15.5343	1235.6380	174.3399	24.4167	4.1447	0.0000	509.1659
DG1	Mart	409.0550	3.4749	33.9267	10.5733	14.3497	1267.1022	171.7353	22.0211	5.6703	0.0445	397.2968
DG1	Mart	417.7516	3.4620	35.6169	10.4200	15.1828	1261.0986	175.0869	24.7674	5.1959	0.0284	387.4679
DG1	Mart	373.6645	3.3555	32.1792	10.7304	13.0204	1251.9779	168.8990	23.7329	6.0806	0.2044	572.3371
DG1	Mart	337.3598	3.0954	30.3421	10.8556	13.8321	1199.2862	173.6122	22.5684	5.1091	0.0546	457.2442
DG1	Mart	367.2009	2.9349	29.6279	10.7450	13.7790	1261.8525	175.8669	26.2116	7.5521	0.0321	427.5726
DG1	Mart	288.2647	2.4504	32.4316	10.5939	10.6097	1198.8587	176.2030	17.3942	5.3149	0.0248	490.3249
DG1	Mart	269.7632	2.4974	32.0355	10.5047	12.4174	1114.7201	179.5495	16.6274	5.2746	0.0288	450.8188
DG1	Mart	370.4953	3.6331	31.9759	10.8270	9.4799	1189.8443	196.4070	23.9323	5.9911	0.0467	441.8074
DG1	Mart	279.4988	2.1468	27.9925	10.2691	9.8127	1039.3512	180.2757	17.2806	4.9100	0.0000	281.7950
DG1	Mart	291.5660	2.2753	26.3025	9.9670	10.5738	1038.0466	182.6610	16.5337	5.1069	0.0730	424.2460
DG2	Gbhem	3.4148	5.7544	3.6299	2.8760	9.4603	2.9391	1.1663	20.4681	1.3658	2.0442	0.0000

Anexo 1 (cont.)

DG2	Gbhem	3.5034	5.6855	3.4740	2.7134	10.6955	2.9386	0.0000	17.9831	0.0000	1.9539	0.0000
DG2	Gbhem	1.9747	5.5692	3.5671	2.8415	12.9232	1.6119	0.0000	19.1448	0.9052	1.6108	0.0000
DG2	Gbhem	1.4727	5.5743	3.5231	2.8803	11.7210	1.3688	0.6544	18.6273	0.9673	1.8924	0.0000
DG2	Gbhem	1.7524	5.6379	3.3161	2.8365	5.7489	1.6673	0.8100	19.3857	1.3181	2.1001	0.0000
DG2	Gbhem	1.7694	5.7098	3.5521	2.7278	10.4542	1.5428	0.6880	17.8656	1.3376	1.6099	0.6107
DG2	Gbhem	3.8579	5.3988	2.9046	2.8736	5.9005	2.4640	1.2303	20.2085	1.6762	2.2848	0.0000
DG2	Gbhem	3.2800	5.5189	3.2955	2.8012	7.8914	2.0375	0.7650	19.6758	1.8527	2.1747	0.0000
DG2	Gbhem	3.6936	5.7427	3.6719	2.8277	13.8656	3.4770	0.8078	17.9700	0.0000	1.7961	0.0000
DG2	Gbhem	4.4559	5.6695	3.5326	2.8813	13.6685	3.6729	0.9088	19.2377	1.5918	1.9077	0.0000
DG2	Gbhem	4.4876	5.6887	3.6062	2.8959	13.0143	4.1246	1.1345	19.2835	2.2123	2.0167	0.0000
DG2	Gbhem	3.6527	5.8137	3.5184	2.8756	15.7995	2.8940	0.6099	19.5500	1.1372	1.8510	0.0000
DG2	Gbhem	3.8210	5.7372	3.4760	2.8197	12.1224	3.6285	0.7818	18.8316	2.0453	2.0121	0.0000
DG2	Gbhem	3.7886	5.6124	3.4511	2.9236	15.8125	3.4485	1.0160	18.8888	1.5145	2.0187	0.0000
DG2	Gbhem	4.5805	5.7191	3.5131	2.8245	14.0502	4.1265	1.1195	19.4030	1.7730	1.8677	0.0000
DG2	Gbhem	1.7547	5.3774	3.5013	2.7338	21.7795	1.6530	0.0000	19.1073	0.9377	2.0240	0.0000
DG2	Gbhem	4.7742	5.3788	3.4366	2.7489	18.6733	3.5950	0.0000	18.5519	1.5381	2.0674	0.0000
DG2	Gbhem	2.4450	5.2431	3.5260	2.8101	17.4823	2.6753	0.7227	18.8829	1.0244	2.1588	0.0000
DG2	Gbhem	4.0216	5.4383	3.5047	2.8710	19.1698	3.2132	0.5598	19.8607	2.0976	1.9691	0.0000
DG2	Gbhem	3.2584	5.5447	3.6591	2.8430	18.3754	2.6478	0.7934	21.8470	1.4120	2.3348	0.0000
DG2	Gbhem	2.2150	5.1820	3.2206	2.7706	18.6673	1.8458	0.8116	19.0224	1.3418	2.0952	0.0000
DG2	Gbhem	4.6951	5.6457	3.7572	2.7264	25.7015	4.5369	1.3812	19.1095	1.5703	1.7708	0.0000
DG2	Gbhem	4.8318	5.8961	3.4224	2.8757	23.8815	4.7201	0.0000	18.5992	1.7611	1.9742	0.0000
DG2	Gbhem	3.7279	5.7865	3.1059	2.9155	17.5939	5.2092	1.6619	18.7717	3.1423	2.1609	5.9681
DG2	Gbhem	3.8081	5.6744	3.1767	2.8736	18.3045	3.5567	0.7311	17.3433	1.6097	2.1404	0.0000
DG2	Gbhem	3.7762	5.8633	3.1678	2.9524	20.2010	3.7126	0.8464	17.4775	2.2758	1.9233	0.0000
DG2	Gbhem	4.2337	5.6982	3.3164	2.8235	24.3754	3.9997	0.0000	18.5507	1.8004	2.0233	0.0000
DG2	Gbhem	1.8975	5.5590	3.1920	2.6848	11.6440	1.7114	0.0000	18.6748	1.6075	2.0033	0.0000
DG2	Gbhem	2.6835	5.4365	3.3642	2.7556	10.7917	2.8564	1.3414	19.5124	1.0698	2.0206	0.0000
DG2	Gbhem	2.5716	5.5750	3.2454	2.7606	10.7705	2.2620	0.9199	19.6012	2.2509	2.0301	0.0000
DG2	Gbhem	3.1605	5.6788	3.5357	2.7909	14.4106	3.0534	0.8463	20.0094	1.6992	2.0031	0.0000
DG2	Gbhem	2.2568	4.5321	3.1531	2.7723	22.1630	2.0405	0.0000	19.5290	0.8810	2.0325	0.0000
DG2	Gbhem	2.6689	5.4811	3.0644	2.9301	19.3090	2.3431	0.0000	19.9722	1.0892	2.0925	0.0000
DG2	Gbhem	2.7634	5.4797	3.2459	2.9474	22.3452	2.6105	0.8483	19.6197	0.7674	2.0297	0.0000
DG2	Gbhem	3.2227	5.6678	3.0953	3.0043	21.8904	2.7079	1.2203	19.3809	1.2935	2.0461	0.5041
DG2	Gbhem	2.1971	5.1722	3.4179	2.8791	25.1651	1.8614	0.0000	19.3934	0.0000	2.1688	0.0000

Anexo 2a: Análises LA-ICP-MS em inclusões fluidas nos veios de quartzo e pegmatito do depósito Piçarrão-Liberdade.

Veio	Na23	Mg24	K39	Ca40	Mn55	Fe56	Cu63	Zn66	Sr88	Ag107	Ba137	La139	Pb208	Li7
Vp2	1	0.75549	2.26947	0.31930		0.59826	0.37386	0.30705	0.00228		0.01057		0.02024	
Vp2	1	5.89143	1.32789	0.76333	0.18299	7.00490	0.23748	0.80814	0.02418		0.00171	2.14067	0.02760	
Vp2	1	0.64885	1.72875	2.03490	0.01548	13.93032	5.40712	11.73257	0.00393		0.01004	0.02378	0.04780	
Vp2	1	0.20005	0.19965	0.16151		0.26421	0.22807	0.02462	0.00258		0.01211	0.00022	0.00099	
Vp2	1	0.12307	0.19468	0.11519		0.09858	0.01819	0.04682	0.00042			0.06615	0.00101	
Vp2	1	1.39584	1.20377	0.58284		0.24832	0.05690	0.04658	0.00813			0.43655	0.00322	
Vp2	1	0.08778	1.07853	1.12610		3.26030	0.21023	0.13964	0.00317		0.01057		0.01289	
Vp2	1	0.24553	1.41785	0.48871		4.34010	0.23766	0.17561	0.00226		0.01561	0.00025	0.00974	
Vp2	1	0.52733	0.27485	0.42668		1.10635	0.22010	0.01588	0.00135		0.00354	0.00078	0.00222	
Vp2	1	1.50573	0.57756	0.44413		0.44982	0.11298	0.09533	0.00390		0.00386	0.47274	0.00269	
Vp2	1	0.09386	1.18947	0.60433		1.71889	0.15079	0.16550	0.00208		0.00776	0.00290	0.00481	
Vp2	1	0.13145	1.10956	4.87539		0.90132	0.87081	0.31256	0.00599		0.00679	0.07141	0.02102	
Vp2	1	0.49643	0.33141	0.78004		0.30856	0.08040	0.05504	0.00595		0.00544	0.00940	0.00185	
Vp2	1	0.02476	4.48322	6.32439	0.02349	11.99493	0.17019	0.06135	0.00225	0.00073			0.00646	
Vp2	1	0.17928	1.23338	0.42382		2.11137	0.18217	0.12833	0.00126		0.00611	0.07230	0.00539	
Vp2	1	3.75456	1.43186	0.09813		0.62780	0.16451	0.10547	0.00084			0.97845		
Vp2	1	2.25121	0.49889	0.40786		0.55704	0.10515		0.00196		0.00665	1.65829		
Vp2	1	1.21952	0.50273	1.14868	0.00558	0.98795	0.06954	0.03210	0.00120	0.00013	0.00822	0.16048	0.00294	
Vp2	1	0.52355	0.71492	0.58064		2.16822	0.16282	0.08852	0.00237		0.00662	0.00038	0.00532	
Vp2	1	0.13253	0.65416	0.87036		1.15924	0.23751	0.21826	0.00390		0.01272			
Vp2	1	0.02133	0.27067	0.18621		0.11218	0.39626	0.02558	0.00039			0.73150	0.00272	
Vp2	1	0.29777	1.05727	0.34643		0.62872		0.67321	0.00230		0.00649	0.00668	0.00346	
Vp2	1	0.70683	1.37554	0.43037	0.04395	13.06615	0.59303	0.24470	0.00301		0.00184	0.04102	0.01179	
Vp2	1	1.29534	0.64252	0.57744		1.25518	0.12792	0.14514	0.01029		0.01037	0.02578	0.01083	
Vp2	1	0.06709	1.19383	0.72635		0.16750	1.02165	2.51335	0.00120	0.00020	0.00099		0.00961	
Vp2	1	0.05288	1.11773	0.51469		0.25957	0.03890	0.00943	0.00172		0.00237	0.00012	0.00228	
Vp2	1		1.84250	0.20696	0.07254	0.17118		0.10611	0.00698					
Vp2	1	0.42673		0.42467	0.01481	0.38247	0.12070	0.03793	0.01404		0.00233	0.14362	0.06386	
Vp2	1	0.00050	0.00079	0.00053		0.00059	0.00390	0.00134	0.00001			0.00134	0.00008	
Vp1	1	0.60000	1.83087	0.64982		5.21259	3.33554	2.22569	0.00460	0.00107	0.01526	0.08885	0.39903	
Vp1	1	2.44830	1.84809	0.66369		3.52200	3.03753	1.07893	0.00281		0.01145	0.17080	0.10598	0.04662
Vp1	1	1.79771	1.21613	0.21132		1.20049	0.25627	0.16367	0.00170		0.00476	0.07821	0.01390	
Vp1	1	1.25416	2.94528	0.08226		0.04784	0.07820	0.09440	0.00018			1.23902	0.01273	
Vp1	1	6.46003						0.14407	0.02003	0.00633		2.54737		
Vp1	1	0.04029	0.88050	0.37402		1.29607	0.29392	0.06722	0.00228	0.00090		9.23323	0.01231	
Vp1	1	1.14070	4.43054	0.08762		0.38480	0.17437	0.06831	0.00338		0.02008	0.00621	0.48873	

Anexo 2a (cont.)

Vp1	1	7.32901	0.41581	0.16745	5.61082	0.22253	0.30620	0.00174		0.02768	2.80983	0.02983		
Vp1	1	0.01626	0.10630	0.04705	0.08231		0.00876	0.00071				0.01227		
Vp1	1	0.00334	0.08750		0.00336		0.00548			0.02152	0.00031	0.01216		
Vp1	1	0.10005	0.08665	0.03055	0.00098	0.02705	0.02232	0.01065	0.00014	0.00023	0.10488	0.00044		
Vp1	1	0.28425	2.14661	0.48088	1.79338	0.17537	0.08681	0.00366		0.01957	0.24093	0.00956		
Vp1	1	0.96878	0.26893	0.03630	0.02441		0.02250	0.00357		0.22102		0.05730		
Vp1	1	0.04495	0.05230	0.03734	0.06111	0.00726	0.01247	0.00028		0.15924	0.00076	0.01769		
Vp1	1	0.16027	0.53061	2.37652	0.02678	1.51343	0.64561	0.36518	0.00410	0.00036	0.00982	0.07157	0.02440	
Vp1	1	1.94977	0.91484	0.52436	0.02517	1.90085	1.07116	0.93816	0.00514	0.00083	0.02683	2.37354	0.08059	0.06270
Vp1	1	0.10947	0.72871	0.05511	0.22188	0.26955	0.02229			0.00296		0.07392		
Vp1	1	0.65135	0.75254	0.23268	0.76905	0.26420	0.17295	0.00184		0.02508	7.61543	0.04899		
Vp1	1	2.47316	30.27630	0.93620	3.10581	2.07897	0.65224	0.34311		0.04062	0.28243	0.16181		
Vp1	1	0.43363	1.12618	0.83231	0.01995	1.19018	0.38161	0.10566	0.00492	0.01312	0.09383	0.02898		
Vp1	1		1.15280	0.79727		0.25056	0.19066	0.00339		0.01405		0.03382		
Vp1	1	0.05963	0.61414	0.52203	1.20960	0.32245	0.10711	0.00429	0.00318	0.01873		0.01689		
Vp1	1	0.06497	0.56642	0.31423	0.70195	0.16058	0.09923	0.00144	0.00116	0.01048	0.04175	0.01223		
Vp1	1	0.98084	2.04776	0.63736	3.51555	0.26905	0.05592	0.00387		0.02483	0.07723	0.04080		
Vp1	1	0.39785	0.05347	0.47859	0.00642		0.00071	0.00266		0.00251	0.03642			
Vp1	1	0.57319	0.25247	0.50794	0.15883	0.10972	0.11478	0.00176	0.00050	0.00150	2.57625	0.00195	0.07857	
Vp1	1	1.27031	0.52737	0.45671	1.61925	0.68592	0.18807	0.00857	0.00086	0.00355		0.03820		
Vp1	1	0.14183	0.28807	0.52570	1.44555	0.74161	0.45334	0.00254		0.00411		0.02190		
Vp1	1	1.17359	0.37626	0.55792	0.60648	0.25325	0.16045	0.00271	0.00301	0.00280	0.51621	0.00539	0.07655	
Vp1	1	0.02856	0.00285		0.00042					0.00000				
Vp1	1	0.05806	0.32511	2.13663	0.00477	2.42406	0.40104	0.96769	0.00233	0.00031	0.00325		1.20766	0.01657
Vp1	1	0.17140	0.49783	0.39348	0.19543	0.15820	0.14876	0.00132		0.01180	0.02411	0.00263		
Vp1	1	0.23319	0.25911	0.50995	0.14140	0.93087	0.25873	0.00207		0.00495	0.00009	0.00789		
Vp1	1	0.07942	1.92526	1.04161	7.00022	0.29072	0.25460	0.00387			0.00305	0.07835		
Vp1	1	0.06916	0.41208	0.88936	0.01611	1.20404	123.50326	0.91132	0.00212	0.00094	0.03069	0.11561	0.02720	0.08288
Vp1	1	0.14095	0.42939	0.45728	0.65320	0.71051	0.16859	0.00258		0.00630	0.00053	0.03664		
Vp1	1	0.04330	0.42636	0.18191	0.57707	3.78226	4.84748	0.00262			0.00021	0.13549	0.10001	
Vp1	1	0.07533	0.58362	0.89160	0.84729	0.42130	0.14790	0.00287		0.01545	0.02967	0.01713		
Vp2	1	0.44278	1.88179	0.71580	0.34674		0.07559	0.00260		0.00324	0.00586	0.00418		
Vp2	1	0.83418	5.89171	0.54720	0.39974		0.09808	0.00448			0.61500	0.00202		
Vp2	1	0.09359	0.52168	0.19554	0.03638		0.01447	0.00141		0.00070	0.01167	0.00083		
Vp2	1	0.19556	0.75224	1.34188	0.08197	0.03572	0.03181	0.00113		0.00104	0.00040	0.00184		
Vp2	1	0.08527	13.98086	0.46082	0.09566	0.01861	0.03064	0.00307		0.00202		0.01066		
Vp2	1	0.06823	1.58801	0.35359	0.02931	0.02508	0.01831	0.00076		0.00059				
Vp2	1	1.01517	0.73913	0.35951	0.16718		0.02419	0.00081		0.37621				

Anexo 2a (cont.)

Vp2	1	0.57611	0.63884	0.17860		0.21044		0.02244	0.00068		1.61297	0.00159	
Vp2	1	0.40244	6.79116	0.31833	0.00412	0.12110	0.03899	0.02307	0.00116	0.00065	0.80209	0.00152	
Vp2	1	0.07485	0.98595	0.16269		0.22309	0.03240	0.02660	0.00054	0.00193		0.00186	
Vp2	1	7.71474	1.51277	0.98176		0.68898		0.15110	0.00206		2.41169	0.01213	
Vp2	1	0.27772	1.48058	0.62586		0.08854		0.00276	0.01112	0.80891	0.58107		
Vp2	1	0.20445	0.02641	0.00489		0.00860	0.05727	0.00092			0.02016		
Vp2	1	2.49560	0.77805	0.20476		0.21273	0.07436	0.01066	0.00075		0.29673		
Vp2	1	0.60680	1.45132	0.54945		0.39831	0.04267	0.01371	0.00061		0.21963		
Vp2	1	0.55948	4.67100	0.03733		0.18236		0.00609	0.00097		1.22502	0.00084	
Vp2	1	0.98807	1.52745	0.19610		0.61538		0.02524	0.00211		2.19111	0.00198	
Vp2	1	3.17696	16.30688	1.28277	0.01773	0.10777		0.00767	0.03117	0.00495	1.41762	0.00156	
Vp2	1	1.84652	1.05632	0.30191		0.49814		0.02708	0.00697	0.00156	0.30869	0.00213	
Vp2	1	49.24152	8.36312	0.28884		0.59409		<0.029013	0.00376	0.01342	5.65244		
Vp2	1	5.34092	5.52361	0.66801		1.16280		0.06149	0.00949		1.05163	0.00301	
Vp2	1	0.68303	1.27897	0.25209		0.50626		0.03511	0.00411	0.00143	0.00655	0.13906	0.00499
Vp2	1	0.55569	2.91331	0.20682		0.89646		<0.025892	0.00481		0.02085		
Vp2	1	0.07669	0.32993	0.08005		0.03371		0.00807	0.00031		0.00929		
Vp2	1	1.10577	1.44336	0.05148		0.30561		0.00901	0.00129		0.17481	0.00130	
Vp2	1	0.05585	0.42819	0.05776		0.16867		0.01747	0.00081				
Vp2	1	0.96950	2.23193	1.66632		0.99072	0.07630	0.03047	0.01267	0.00905	0.03154	0.00968	
Vp2	1	0.62511	2.42573	1.16540		2.18134	0.08177	0.11986	0.00690	0.00845	0.00044	0.00401	
Vp2	1	0.12721	1.92100	0.57202		1.25895		0.03615	0.00243				
Vp2	1	0.05826	3.31966	0.39653		0.15269		0.04917	0.00603				
Vp2	1	0.26885	1.96492	0.28276		0.03057	0.02237	0.02454	0.00175	0.00110	0.00624	0.00085	
Vp2	1	0.64499	1.65039	0.53923	0.01524	4.41748	0.05551	0.06194	0.00704	0.00630		0.00453	
Vp2	1	0.07497	2.04618	0.35895	0.00429	0.98463	0.01411	0.01096	0.00205	0.00164	0.00005	0.00650	0.01299
Vp2	1	0.08547	2.92121	0.73501	0.00899	0.29842	0.03026	0.03084	0.00276	0.00289	0.00008	0.00826	
Vp2	1	0.26351	2.98815	0.58039	0.02673	0.76726		0.02803	0.00378		0.00425		
Vp2	1	0.05260	2.76215	0.73222	0.00875	0.08227	0.01919	0.01868	0.00189	0.00015	0.00087	0.00010	0.00264
Vp2	1	0.17566	2.57938	0.75886	0.00981	0.47857	0.02350	0.04253	0.00694	0.00265	0.00012	0.00712	
Vp2	1	0.10492	4.12673	0.78122	0.01184	0.44206	0.03015	0.02553	0.00372	0.00190		0.00514	
Vp2	1	0.06842	2.48769	0.59462		0.13665	0.02253	0.01625	0.00331	0.00025	0.00121		0.00267
Vp2	1	0.18375	3.26323	0.69374	0.00880	0.43938	0.03438	0.02323	0.00461	0.00011	0.00252	0.00010	0.00473
Vp2	1	0.00831	1.15496	0.11365	0.00041	0.04767	0.00406	0.00175	0.00024	0.00001	0.00014	0.00001	0.00044
Vp2	1	0.15368	2.63599	1.45449		1.00105	0.04148	0.16798	0.00771	0.00389	0.00061	0.00732	
Vp2	1	0.05432	2.02365	0.40513		0.17193	0.01607	0.00990	0.00193	0.00058		0.00178	
Vp2	1	0.25955	2.32240	0.32690		0.65506	0.03137	0.01785	0.00163	0.00157		0.00258	
Vp2	1	0.14412	3.14939	0.66755	0.00538	0.77414	0.01500	0.01871	0.00304	0.00118	0.00004	0.00122	

Anexo 2a (cont.)

Vpe	1	0.13133	0.73753	0.39822	0.42707	0.17544	0.13580	0.00219	0.00049	0.01385	0.26873	0.00316	
Vpe	1	0.05582	0.09599	0.08616	0.00576	0.00420	0.00716	0.00294		0.00580	0.01179		
Vpe	1	0.06892	0.67374	0.14665	0.05520	0.76874	0.24139	0.00068			0.12317	0.01054	
Vpe	1	0.04375	0.77246	0.27427	0.06513	0.11005	0.08325	0.00111		0.00173	0.00301		
Vpe	1	0.37862	0.75047	0.34228	0.28655	0.12483	0.05514	0.00100		0.00404	0.01109	0.00317	
Vpe	1	0.23116	1.75892	1.22813	0.42750	0.32776	0.17305	0.00675		0.01363	0.00081		
Vpe	1	18.86927	9.17808	0.26827	0.03203	0.13727	0.09269	0.24176	0.00424		0.62346	0.00829	
Vpe	1	0.45288	0.66561	0.80800	0.01540	0.96935	0.23284	0.15227	0.00469	0.01500	0.09697	0.01697	
Vpe	1	0.07995	4.20712	0.24534	0.15653	0.12206	0.05043	0.00105		0.00370	0.21253		
Vpe	1	1.04781	1.07184	0.97321	0.42392	0.24195	0.15670	0.00438		0.00804	0.65420		
Vpe	1	1.84365	0.92065	6.92828	0.03225	0.47698	0.41613	0.33084	0.00357		0.00685	0.58779	0.01661
Vpe	1	0.32250	1.01926	0.55057	0.65330	0.34967	0.53423	0.00463	0.00059	0.02272	0.00380	0.00365	
Vpe	1	0.43420	0.91366	0.73653	0.45917	0.42468	0.27562	0.00291		0.01700	0.56651	0.00632	
Vpe	1	1.60291	0.53425	0.22235	0.09277	0.14024	0.06347	0.00111		0.00272	0.93731		
Vpe	1	0.06316	1.22180	0.33127	0.10533	0.24896	0.12087	0.00111	0.00049	0.00646			
Vpe	1	0.19638	0.88271	0.68515	0.48529	0.52072	0.27239	0.00435	0.00154	0.00994	0.12319	0.01181	
Vpe	1	0.13618	1.85005	0.61734	0.01557	1.04494	0.48609	0.32137	0.00599	0.00031	0.01445	0.29488	0.01557
Vpe	1	6.91526	1.02766	0.75251	0.37110	0.58237	0.34501	0.00293	0.00244	0.02132	1.14180		
Vpe	1	0.15088	0.66435	0.24958	0.06864	0.16868	0.06055	0.00144		0.00301	1.17719		
Vpe	1	1.92358	1.23514	0.20083	0.12154	0.11373	0.24855	0.00107		0.00940	0.50584	0.00264	0.04208
Vpe	1	0.03383	0.89156	0.22263	0.09886	0.17767	0.07001	0.00152		0.00620			
Vpe	1	0.05397	0.76162	0.27529	0.23440	0.20837	0.15814	0.00210		0.00698	0.02323	0.00134	
Vpe	1	0.36788	0.30131	0.64447	0.11168	0.08935	0.02375	0.00212		0.00287	0.27328	0.01727	
Vpe	1	0.28871	0.35588	0.08042	0.03353	0.63036	0.28631	0.00104	0.00029	0.00188	0.06141	0.00627	
Vpe	1	0.44000	0.50203	0.85455	0.04307	0.06564	0.03237	0.00403		0.00530	0.00032		
Vpe	1	0.02602	3.39522	0.21972	0.10454	0.10163	0.04399	0.00152		0.00436	1.17671	0.04092	
Vpe	1	0.14677	0.82352	0.37244	1.38690	1.20542	0.10309	0.00225		0.01122	0.01603	0.02205	
Vpe	1	1.40850	0.22935	0.11666	0.06614	0.27338	0.22830	0.00043		0.00213	0.06050	0.06461	0.01249
Vpe	1	0.07024	0.46116	0.30039	0.07727	0.12409	0.04427	0.00067		0.25292	0.00008	0.01488	
Vpe	1	0.33010	2.00121	0.96394	0.04127	0.15629	0.43219	0.08468	0.00438	0.00232	1.14080		
Vpe	1	0.36332	0.32942	0.80997	0.02208	0.01614	0.00526	0.00350		0.00454	0.02433	0.00324	
Vpe	1	0.75815	0.32303	0.43750	0.05167	0.11797	0.06653	0.00209		0.00672	0.15481	0.00135	
Vpe	1	1.95893	0.10616	0.14011	0.03947	0.65127	0.21765	0.00032		0.00143	1.52543	0.00883	

Anexo 2b: Análises LA-ICP-MS em inclusões fluidas nos veios de quartzo da serra do Morro Escuro.

Veio	Na23	Mg24	K39	Ca40	Mn55	Fe56	Cu63	Zn66	Sr88	Ag107	Ba137	La139	Pb208	Li7
Vms	1	0.15127	2.59315	0.23178		0.04036	0.00823	0.00420	0.00062		0.00071	0.13588	0.00502	
Vms	1		1.51512	0.24338		0.10643		0.03214	0.00226			0.47594	0.00521	
Vms	1			0.43553		0.09599	0.03275	0.01491	0.00134		0.00143	0.06449	0.00724	
Vms	1	0.41297	1.04304	0.32296		0.04247	0.01561	0.01644	0.00116			0.27703	0.00190	
Vms	1	0.09245		0.36904		0.08118	0.01520	0.01196	0.00094	0.00054		0.17977	0.00594	
Vms	1	0.16608	2.62929	0.38618	0.00644	0.04907	0.01490	0.00568	0.00102		0.00040	0.02999	0.00463	
Vms	1	0.25383	2.24505	0.55667		0.02796	0.01766	0.00733	0.00209		0.00091	0.23220	0.00563	
Vms	1		1.42159	0.28320		0.05677	0.01467	0.00831	0.00089		0.00051	0.00724	0.00400	
Vms	1		0.81831	0.12635		0.04508		0.01058	0.00097			1.08300	0.00248	
Vms	1		1.77518	0.26696		0.04829		0.02605	0.00096			0.16739	0.00320	0.06827
Vms	1	0.07101	1.74329	0.35362		0.08334	0.02671	0.04023	0.00106		0.00107	0.22654	0.00241	
Vms	1	0.73079	1.19646	0.39291		0.06668		0.02697	0.00154		0.00184	0.13373	0.00318	
Vms	1		1.29992	0.26764		0.04389		0.02424	0.00157				0.00163	
Vms	1	0.25573	1.26737	0.64025		0.12392		0.01976	0.00315					
Vms	1	0.67715	2.31410			0.10536		0.03745	0.00264			1.29133	0.00729	
Vms	1		2.35643	0.58596				0.02993	0.00189			0.22637	0.00257	
Vms	1	0.66060	1.43375	0.43319		0.04964	0.02468	0.02303	0.00180		0.00165	0.49532	0.00173	
Vms	1		1.52214	0.41216		0.07171		0.04173	0.00321			0.86421	0.00467	
Vms	1	0.35512	1.83713	0.80438		0.15067		0.03390	0.00290			0.01700		
Vms	1	0.50828	1.86891	0.52133			0.03866	0.02853	0.00187			0.15950	0.00165	
Vms	1		2.81267	0.47574	0.00147	0.03438	0.00942	0.00704	0.00142	0.00002	0.00102	0.00010	0.00856	
Vms	1	0.07942	1.75627	0.64463		0.08349	0.03325	0.02657	0.00229	0.00010	0.00079	0.00088	0.00324	
Vms	1		1.73116	0.54203	0.00104	0.04765	0.01218	0.00891	0.00191		0.00051	0.00445	0.00324	
Vms	1	0.57182	2.09818			0.03006	0.02630	0.01269	0.00352		0.00162	0.22368	0.00084	
Vms	1	0.30969	1.87410	0.85056		0.13633	0.05417	0.02818				0.17947	0.00311	
Vms	1	0.23251	2.27706	0.33882		0.01732	0.02488	0.00703	0.00088		0.00077	0.08848	0.00092	
Vms	1	0.12715	2.24068			0.02724	0.01939	0.00565			0.00119	0.01581	0.00138	
Vms	1	0.06291	2.03493	0.34089	0.00095	0.01144	0.01892	0.00397	0.00080		0.00025	0.00007	0.00116	
Vms	1		1.95938	0.29807		0.00647	0.01230	0.00349	0.00065		0.00021	0.00018	0.00097	
Vms	1	0.66548	2.12245	0.70967			0.02741	0.01807	0.00278			0.29521	0.00894	
Vms	1	0.06196	2.78888	0.33487		0.02472	0.01881	0.01055	0.00100		0.00048	0.00019	0.00756	

Anexo 2b (cont.)

Vms	1	0.08790	2.18918	0.00479	0.03281	0.02355	0.01032	0.00064	0.00829	0.00376			
Vms	1	2.27996	0.53481	0.00141	0.03374	0.01919	0.02289	0.00111	0.00038	0.01102	0.00748		
Vms	1	2.27965	0.53483	0.00140	0.03377	0.01912	0.02283	0.00111	0.00038	0.01102	0.00749		
Vms	1	0.13617	1.87390	0.43020	0.00187	0.01545	0.01125	0.00339	0.00086	0.01329	0.00150	0.00455	
Vms	1	0.08503	1.94727	0.42515	0.00110	0.03754	0.01126	0.00810	0.00111	0.00095	0.00867	0.00468	0.00233
Vmi	1	0.12897	2.67803	0.84966		0.33152	0.02410	0.01228	0.00251	0.00302	0.00017	0.00301	
Vmi	1	0.06648	1.80295	0.54458		0.11025		0.01149	0.00106	0.00120		0.00212	
Vmi	1	0.09252	3.95213	0.71608	0.00328	0.11426	0.01452	0.00773	0.00147	0.00242	0.00013	0.00232	
Vmi	1	0.10272	2.28998	0.59696		0.15762	0.01921	0.01797	0.00216	0.00196	0.00006	0.00137	
Vmi	1	0.09851	3.92952	0.73093	0.00243	0.14340	0.02892	0.00961	0.00146		0.00008		
Vmi	1	0.06324	1.91695			0.10758		0.00557	0.00239			0.00106	
Vmi	1	0.05719	2.44944	0.44865	0.00555	0.05903	0.01340	0.00425	0.00100		0.00006	0.00164	
Vmi	1	0.07950	2.79788	0.42557		0.06151	0.02183	0.00842	0.00104			0.00110	
Vmi	1	0.12476	2.33373	0.40876		0.08700		0.01159	0.00129				
Vmi	1	0.04987	2.97025	0.48237	0.00115	0.04014	0.01018	0.00458	0.00259	0.00005	0.00003	0.00083	
Vmi	1	0.07896	3.30255	0.25048	0.00250	0.21830	0.00492	0.00404	0.00055		0.00002	0.00055	
Vmi	1	0.12715	2.54024	0.76835	0.01214		0.02008	0.01293	0.00244	0.00318		0.00314	
Vmi	1	0.16259	2.90755	0.42757		0.14059	0.01738	0.01121	0.00266	0.00017	0.00232	0.00009	0.00249
Vmi	1	0.15013	1.53779	0.64426		0.22106		0.00897	0.00131	0.00661	0.00061		
Vmi	1	0.06353	2.03687	0.49264	0.00391	0.12722	0.00956	0.00598	0.00176	0.00011	0.00018	0.00141	
Vmi	1	0.16786	1.67842				0.00788		0.00040				
Vmi	1	0.20788	2.32984	0.34969		0.14192			0.00067				
Vmi	1	0.06025	3.89253	0.40827		0.05371	0.02200	0.01275	0.00087		0.00076		
Vmi	1	0.05784	3.07169	0.59430		0.15478			0.00123	0.00020			
Vmi	1	1.22550	0.19375			0.30866		0.00313		0.13417			
Vmi	1	0.83712	0.10763			0.02623			0.00468	0.07002	0.00120		
Vmi	1	0.17644	0.51118	0.09085		0.20497				0.18124			
Vmi	1	0.56895	0.15281			0.12857		0.00222		0.74858			
Vmi	1	0.64600	0.04731			0.12338				1.04804			
Vmi	1	0.22993	0.87056	0.79551		0.31943	0.03148		0.00175	0.00019	0.00163	0.05143	0.00207
Vmi	1	1.40173	0.14336			0.23002	0.03675		0.00359		1.22924		
Vmi	1					0.31374	0.00320	0.01756	0.00024		0.00003	0.00031	

